

Syracuse University

SURFACE

Physics - Dissertations

College of Arts and Sciences

5-2013

Cell Mechanics: From Cytoskeletal Dynamics to Tissue-Scale Mechanical Phenomena

Shiladitya Banerjee

Follow this and additional works at: https://surface.syr.edu/phy_etd

Recommended Citation

Banerjee, Shiladitya, "Cell Mechanics: From Cytoskeletal Dynamics to Tissue-Scale Mechanical Phenomena" (2013). *Physics - Dissertations*. 131.

https://surface.syr.edu/phy_etd/131

This Dissertation is brought to you for free and open access by the College of Arts and Sciences at SURFACE. It has been accepted for inclusion in Physics - Dissertations by an authorized administrator of SURFACE. For more information, please contact surface@syr.edu.

5-1-2013

Cell Mechanics: From Cytoskeletal Dynamics to Tissue-Scale Mechanical Phenomena

Shiladitya Banerjee
sbanerje@syr.edu

Follow this and additional works at: http://surface.syr.edu/phy_etd

Recommended Citation

Banerjee, Shiladitya, "Cell Mechanics: From Cytoskeletal Dynamics to Tissue-Scale Mechanical Phenomena" (2013). *Physics - Dissertations*. Paper 131.

This Dissertation is brought to you for free and open access by the College of Arts and Sciences at SURface. It has been accepted for inclusion in Physics - Dissertations by an authorized administrator of SURface. For more information, please contact surface@syr.edu.

Abstract

This dissertation explores the mechanics of living cells, integrating the role of intracellular activity to capture the emergent mechanical behavior of cells. The topics covered in this dissertation fall into three broad categories : (a) intracellular mechanics, (b) interaction of cells with the extracellular matrix and (c) collective mechanics of multicellular colonies. In part (a) I propose theoretical models for motor-filament interactions in the cell cytoskeleton, which is the site for mechanical force generation in cells. The models predict in a unified manner how contractility, dynamic instabilities and mechanical waves arise in the cytoskeleton by tuning the activity of molecular motors. The results presented in (a) holds relevance to a variety of cellular systems that behave elastically at long time scales, such as muscle sarcomeres, actomyosin stress fibers, adherent cells. In part (b) I introduce a continuum mechanical model for cells adherent to two-dimensional extracellular matrix, and discuss how cells can sense mechanical and geometrical cues from its surrounding matrix. The model provides an important step towards a unified theoretical description of the dependence of traction forces on cell size, actomyosin activity, matrix depth and stiffness, strength of focal adhesions and makes experimentally testable predictions. In part (c) we combine experiment and theory to reveal how intercellular adhesions modulate forces transmitted to the extracellular matrix. We find that In the absence of cadherin-based adhesions, cells within a colony appear to act independently, whereas with strong cadherin-based adhesions, the cell colony behaves like a liquid droplet wetting the substrate underneath. This work defines the importance of intercellular adhesions in coordinating mechanical activity of cell monolayers and has implications for the mechanical regulation of tissues during development, homeostasis, and disease.

Cell Mechanics

From cytoskeletal dynamics to tissue-scale mechanical phenomena

by

Shiladitya Banerjee

B.Sc. (Hons.) Chennai Mathematical Institute 2008

DISSERTATION

Submitted in partial fulfillment of the requirements for the degree of
Doctor of Philosophy in Physics

Syracuse University

May 2013

Copyright 2013 Shiladitya Banerjee

All rights reserved

Dedicated to my mother Sanchaita

Acknowledgements

I express my sincerest gratitude to my supervisor, Prof. Cristina Marchetti, who instilled in me a strong passion and interest towards biological and soft matter physics. I'm further indebted to Prof. Marchetti and the Department of Physics for their continual support and encouragement through my graduate student years. I have specially cherished mentoring and guidance from Prof. Mark Bowick, Prof. Eric Dufresne, Prof. Tanniemola Liverpool and Prof. Kristian Mueller-Nedebock, who encouraged me to think in diverse ways. I thank my dissertation committee - Prof. Peter Saulson, Prof. Jennifer Schwarz, Prof. Martin Forstner, Prof. James Henderson and Prof. Liviu Movileanu for their critical reading of my dissertation. I specially acknowledge and thank my collaborators, Luca Giomi for valuable contributions to Chapter 6, and Aaron Mertz for performing and analyzing performing experiments described in Chapter 8.

I thank my family for their endless support, love and encouragement, helping me pursue my interests in academics. I specially prize Koel's presence in my life, her enduring love and care, making my everyday joyful and refreshing. Finally I thank all my wonderful friends and colleagues in Syracuse - Sandeep, Auritro, Parvathy, Prayush, Bithika, Jayanth, Anirban, Shrimoy, Yannek, Rastko, Yaouen and Silke, who made my stay here fun and memorable.

Contents

1	Introduction	1
1.1	Scope	1
1.2	Intracellular Mechanics	2
1.2.1	The Cytoskeleton : an <i>active</i> biopolymer gel	2
1.2.2	Collective behavior in motor-filament assemblies	4
1.3	Cell-matrix Interactions	7
1.3.1	Cellular force measurements	9
1.3.2	Mechanical modeling	10
1.4	Towards the Mechanics of Tissues	11
1.5	Outline	12
2	Motor-driven Dynamics of Cytoskeletal Filaments	16
2.1	Collective action of molecular motors	16
2.2	The model	20
2.2.1	Filament dynamics	20
2.2.2	Individual motor dynamics	21
2.2.3	Motor binding and unbinding	24
2.3	Mean field approximation	26
2.4	Active filament sliding in one dimension	28
2.4.1	Steady state and its stability	29
2.4.2	Fluctuation dynamics	35

CONTENTS

2.5	Active filament dynamics in two dimensions	38
2.5.1	Steady state and its stability	39
2.5.2	Fluctuations around the steady state	40
2.6	Summary and Outlook	43
	Appendix 2.A Solution of mean-field equation	43
3	Linear Hydrodynamics and Rheology of Cross-linked Motor-Filament Gels	46
3.1	Active gel approach	46
3.2	Hydrodynamic model	49
3.3	Hydrodynamic modes and linear stability analysis	53
3.3.1	Longitudinal modes	55
3.3.2	Transverse modes	61
3.4	Application to muscle sarcomeres	62
3.5	Linear response	66
3.5.1	Dynamic compressional moduli	66
3.5.2	Creep	69
3.6	Discussion	72
4	Emergent Mechanical Phases of Cross-linked Motor-Filament Gels	75
4.1	Active solids	75
4.2	Nonlinear gel model	77
4.3	Linear stability analysis	80
4.4	One-mode model	83
4.5	Numerical analysis of the continuum nonlinear model	86
5	Rigidity and Geometry Sensing by Adherent Cells on Elastic Substrates	89
5.1	Mechanosensing	89
5.2	Active gel model of an adherent cell	91

CONTENTS

5.3	Adherent cell in one dimension	95
5.3.1	Isotropic cell	95
5.3.2	Polarized Cell	98
5.4	Planar adherent cell	100
5.4.1	Spatial distribution of traction stresses	101
5.4.2	Rigidity dependent cell spreading	102
5.4.3	Curvature-induced traction	104
5.4.4	Mechanical anisotropy is linked to geometric anisotropy	106
6	Optimal Shapes of Adherent Cells	111
6.1	Contractile Film Model	112
6.1.1	Continuous adhesions	114
6.1.2	Discrete adhesions	116
6.2	Inflections, cusps and protrusions	119
	Appendix 6.A Numerical simulations	124
	Appendix 6.B Kinks, cusps and protrusions	125
7	Cohesive Cell Layers on Elastic Substrates of Finite Thickness	127
7.1	Non-local cell-substrate interactions	127
7.2	Contractile cell on a thick substrate	129
7.3	Contractile cell layer	131
7.3.1	Thin substrate	132
7.3.2	Infinitely thick substrate	133
7.3.3	Substrate of finite thickness	135
	Appendix 7.A Green's Function for elastic substrate of finite thickness	136
	Appendix 7.B One dimensional cell layer on elastic half plane	139
	Appendix 7.C Two dimensional cell layers	139
8	Collective Mechanics of Adherent Cell Colonies	141
8.1	Cohesive epithelial cell colonies	142

CONTENTS

8.1.1	Traction stress measurements	142
8.1.2	Effective surface tension	144
8.1.3	Minimal physical model	148
8.2	Role of intercellular adhesions	150
8.2.1	Traction Stresses Systematically Reorganize in High-Calcium Medium	150
8.2.2	Planar model of cell colonies as elastic media	156
8.2.3	Model of cell colonies as elastic media in one dimension	157
Appendix 8.A	Materials and Methods	162
	Bibliography	166

List of Figures

1.1	The Cell Cytoskeleton	3
1.2	Actin motility assay and cross-linked actomyosin gel	5
1.3	Interplay of cell shape, size and mechanics during cell-matrix adhesion	8
1.4	Traction Force Microscopy	10
1.5	Cadherin based intercellular adhesions	12
2.1	Molecular motor binding-unbinding cycle	22
2.2	Force-velocity relation of a single molecular motor	24
2.3	Anomalous Force-velocity relation in motor-driven filaments	32
2.4	Dynamic phases of a motor-driven filament	33
2.5	Hysteresis and bistability in motor-driven filaments	34
2.6	Motor-induced sliding velocity of actin filaments	35
2.7	Mean field motor attachment time as a function of filament velocity	44
2.8	Mean field motor stretch as a function of filament velocity	45
3.1	Propagating waves in passive polymer gels with inertia	57
3.2	Phase diagram for the overdamped active gel	66
3.3	Storage and Loss Moduli as functions of frequency in active gels	69
3.4	Creep response - phase diagram	72
3.5	Evolution of strain field in active gels in response to a step-stress	73

LIST OF FIGURES

4.1	Mechanical phases of a cross-linked active gel obtained by varying the gel compressional modulus and motor activity	77
4.2	Phase diagram of active and passive non-linear gels obtained from linear stability analysis	82
4.3	Nonlinear dynamics of the slowest (longest lived) mode of the active gel.	84
4.4	Numerical phase diagram of the nonlinear active gel model	87
5.1	Traction stress localization and internal stress buildup in adherent cells	97
5.2	Spatial profile of stresses and contraction in polarized active gels . . .	99
5.3	Excess mean polarization in adherent cells as a function of substrate compliance	100
5.4	Traction stress distribution in planar adherent cells	101
5.5	Relationship of cell shape and spread area with substrate stiffness . .	103
5.6	Traction stresses are higher in regions of high-curvatures	105
5.7	Mechanical anisotropy in adherent cells is linked to geometric anisotropy of the adhesion pattern	107
6.1	Cell spread area increases monotonically with substrate stiffness . . .	114
6.2	Geometric properties of a cell anchored onto three pointwise adhesions.	116
6.3	Schematic of the equilibrium shapes of an adherent cell at different values of contractile pressure	119
6.4	Bistability and hysteresis in cell shapes driven by changes in actomyosin contractility	120
6.5	Cell polymorphism by tuning substrate stiffness and actomyosin contractility	122
6.6	Kinks, cusps and protrusions	125
7.1	Schematic of an adherent cell layer on a soft substrate	128
7.2	Contraction, stiffening and traction forces generated by a contractile cell on a thick substrate	130

LIST OF FIGURES

7.3	Internal stress, traction moments and substrate deformations for an adherent cell layer on thick substrates	134
7.4	Approximate Green's function (in fourier space) for a substrate of finite thickness	138
8.1	Traction stresses and strain energies for colonies of cohesive keratinocytes	145
8.2	Spatial distribution of strain energy for colonies of different size . . .	146
8.3	Mechanical output of keratinocyte colonies versus geometrical size. . .	147
8.4	Traction stresses dynamically reorganize in high-calcium medium . .	151
8.5	Traction stresses systematically reorganize in high-calcium medium .	154
8.6	Minimal physical model captures cadherin-dependent organization of traction stresses.	156
8.7	Minimal one-dimensional picture of N cells adhering via cadherin-based adhesions, modeled as linear hookean springs	158
8.8	Internal stress, strain energy and intercellular forces in an adherent cell doublet	159

Chapter 1

Introduction

1.1 Scope

Living cells are highly sensitive to physical, chemical or geometrical cues in the extracellular environment [1]. Environmental determinants such as friction, elastic modulus, chemical potential or geometry of the substrate largely control the emergent behavior of adherent cells. Cellular mechanotransduction and response to extracellular cues are mediated by active intracellular processes. In typical living cells, *activity* originates in the cytoskeleton, where molecular motors perform mechanical work on cytoskeletal filaments, fueled by adenosine triphosphate (ATP) hydrolysis [2]. These motor-filament interactions play a major role in cellular and tissue-scale mechanical phenomena, and are capable of affecting the extracellular environment. The inherent cooperativity and *feedback* between intracellular and extracellular forces determine cell fate, physiology and mechanical functions. Important questions have since opened up at the interface of *soft matter* physics, cell biology and materials science - Can physical interactions between intra- and extracellular components account for emergent behavior on multicellular length scales? Can we identify universal trends and characterize cellular material properties such as elastic modulus, viscosity or surface tension? How can we control cell and tissue behavior by designing

specific substrates? While experiments continue to reveal quantitative biophysical data, the need for theoretical modeling has come forth with an aim to unify cellular mechanics at various length scales. Using tools and ideas from continuum mechanics and non-equilibrium statistical mechanics, this dissertation theoretically investigates the emergent mechanical behavior in cells and tissues, stemming from intracellular activity and controlled by extracellular physical properties.

1.2 Intracellular Mechanics

1.2.1 The Cytoskeleton : an *active* biopolymer gel

The cytoskeleton is a cellular scaffolding dissolved in the cytoplasm, and is responsible for the structural integrity and mechanical force generation in living cells. From the viewpoint of polymer physics, the cytoskeleton can be described as a cross-linked polymer gel made of semiflexible filaments and cross-linking proteins [3, 4]. Semiflexible polymers are associated with a finite energy cost of bending in the presence of thermal fluctuations. An individual semiflexible polymer can be characterized by its *persistence length* L_p , defined as the distance along the polymer beyond which it loses memory of its orientation [5]. Filaments with a persistence length larger than the contour length are essentially rigid, whereas those with a smaller persistence length tend to be flexible, with entropic degrees of freedom. In eukaryotic cells, the cytoskeleton consists of three main kinds of filaments - actin filaments, intermediate filaments and microtubules (Fig. 1.1, top frame). Actin filaments are the thinnest of the cytoskeletal filaments with persistence length of the order of tens of microns ($L_p \sim 17 \mu m$) [6] and interact with myosin molecular motors. They play a key role in muscle contraction, cell motility and mechanotransduction. The actin cytoskeleton is mostly abundant in the cortical layer beneath the plasma membrane, and is also present in membrane protrusions, such as lamellipodia and filopodia during cell motility. Depending on the density of filaments and cross-linking proteins, actin gels can either respond elasti-

cally or flow under mechanical perturbation. Elastic modulus of actin gels have been measured to be of the order of $1 - 10$ kPa [7], with viscous relaxation over timescales of minutes to hours. Microtubules are the stiffest of the cytoskeletal filaments, with $L_p \sim 1$ mm. They are responsible for cytoskeletal rigidity, intracellular transport of organelles via kinesin or dynein motors, and are known to control mitotic spindle formation during cell division. Intermediate filaments on the other hand are the most flexible, with $L_p \sim 1$ μ m. Intermediate filaments are mostly found in the nuclear lamina or cell-cell and cell-matrix junctions during mechanotransduction, and are also associated with maintaining cell shape.

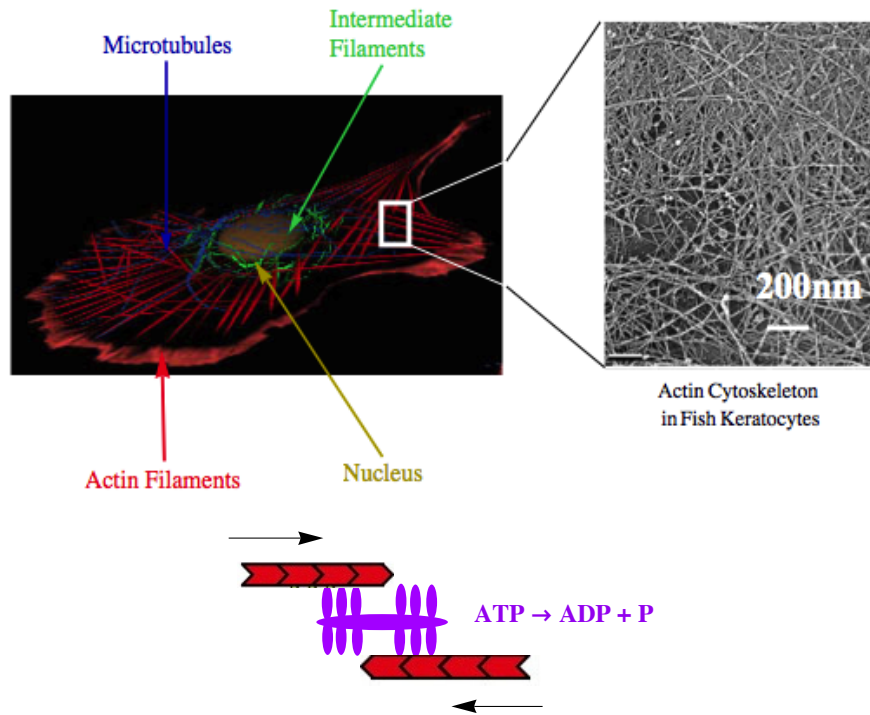


Figure 1.1: Top : (Left) Fluorescent image of an eukaryotic cell with actin labeled in red, microtubule in blue and intermediate filaments in green. (Right) Electron Micrograph image of actin cytoskeleton in fish keratocytes [8]. Bottom : Schematic diagram of a myosin cluster (purple), known as a minifilament, exerting contractile forces (black arrows) on neighboring actin filaments (red), fueled by ATP hydrolysis.

Mechanical processes in the cytoskeleton are largely controlled by *active* molecular motors, that form temporary cross-links between filaments (Fig. 1.1, bottom frame). During a chemical cycle fueled by ATP hydrolysis, molecular motors undergo a conformational change, known as the *power stroke*, and walk along *polar* filaments carrying food and cargo across the cytoskeleton. The total cycle duration is determined by the sum of the time τ_{on} that the protein spends attached to the filament, performing its working stroke, and the time τ_{off} that it spends detached from the filament, making its recovery stroke. Motor proteins are generally characterized by the value of the duty ratio, $r = \tau_{\text{on}}/(\tau_{\text{on}} + \tau_{\text{off}})$. Myosin-II with $r \sim 0.05$, spends most of its time unbound, while two-headed kinesins have values of r close to unity and are classified as *processive* motors that remain attached to the filament for most of the duration of the cycle [2]. Motor-filament gels constantly consume chemical energy, thus maintaining the cytoskeleton out-of-equilibrium. Hereafter we refer to these biopolymer gels as *active gels*, whose internal activity originates from non-equilibrium chemical reactions [9].

1.2.2 Collective behavior in motor-filament assemblies

Molecular motors such as myosin-II do not act individually on actin filaments, but tend to form clusters known as minifilaments. By binding onto actin filaments, these minifilaments generate internal stresses that can lead to macroscopic contraction of the cytoskeleton. Collective effects in molecular motor ensembles have previously been studied and have generically predicted dynamic instabilities [10]. These motor-induced instabilities provide the likely route to traveling density waves and cluster formations, as observed in recent experiments on dense actin motility assays [11]. Motility assays are *in vitro* substrates consisting of molecular motors with their one end tethered to a rigid substrate and the other end free to interact with the filaments [12] (Fig. 1.2, left frame). The assay constitutes an *active* substrate that can spontaneously drive the motion of cytoskeletal filaments through motor attachment-

detachment kinetics. Motor kinetics can induce effective self propulsion, enhanced diffusivity, anomalous force-velocity relations and hysteretic effects on the filament [13]. Motility assay is perhaps the simplest realization of an active system that allows for detailed semi-microscopic modeling and quantitative measurements.

Motor-filament assemblies exhibit a number of rich collective behaviors from self organization into structures with the symmetries of topological defects [14], to ordering into liquid crystalline phases, to dynamic pattern formation [15]. To assess collective properties in these active gels, experimentally controllable and quantifiable set-ups have emerged. In-vitro reconstitution of active gels from purified extracts of cytoskeleton components are now used extensively in experiments, enabling *rheological* measurements [16–18]. These networks consist of filaments, cross-linking proteins and molecular motors (Fig. 1.2, right frame), and are capable of generating controlled contractile forces, sustained oscillations and structural patterns. In addition, experiments have revealed novel rheological properties in these active networks as functions of crosslinking and motor protein concentrations. For example, *in vitro* actomyosin gels can stiffen by orders of magnitude, as one increases cross-link density, actin concentration or motor activity [16, 19].

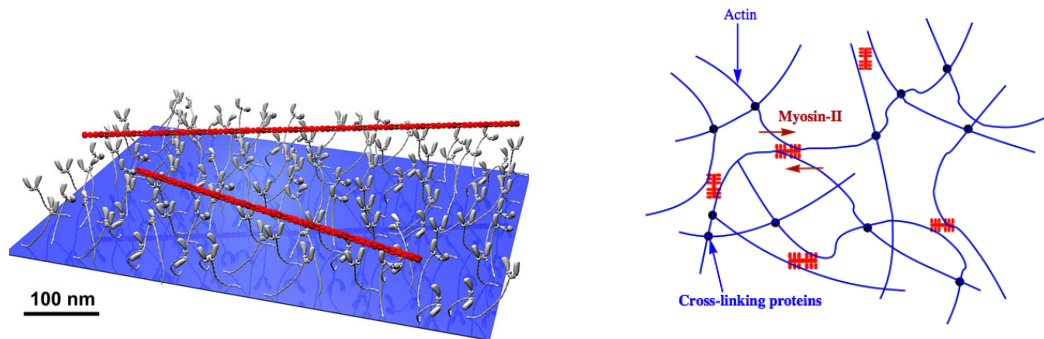


Figure 1.2: Left: Schematic of the experimental set-up for an actin motility assay, with actin filaments (shown in red) propelled by myosin motors underneath (gray) [20]. Right : Schematic of a cross-linked actomyosin gel showing actin filaments (blue lines), myosin-II motors (red) and cross-linking proteins (solid blue dots). Myosin motors exert local contractile forces on the actin network, as indicated by red arrows.

Oscillations are ubiquitous in biological systems [21]. Examples of spontaneous oscillations in active gels include - contraction waves in muscle sarcomeres [22], repositioning of mitotic spindles during asymmetric cell division [23], and *in vitro* cilia like beatings of self assembled microtubule-dynein bundles [24]. Oscillations in these active gels arise from a competition between the network elasticity and the chemical activity of the molecular motors. The origin of contraction and spontaneous oscillations are now fairly well understood for ordered actomyosin structures such as muscle sarcomeres [25]. However it is more challenging to describe the mechanisms of contraction and oscillations in actomyosin systems that lack such highly organized structures, for example, isotropic active networks. During the past decade, continuum models for active polar gels have been constructed by suitable modifications of hydrodynamic equations of liquid crystals to incorporate the effect of chemical activity and filament polarity [26–28]. Specific microscopic models of motor-filament interactions have also been coarse-grained to derive continuum equations that respect the symmetries as required by hydrodynamics [29, 30]. Although these derivations have yielded expressions for the phenomenological parameters in terms of microscopic quantities, these expressions are model dependent, thus rendering quantitative comparisons with experiments challenging. These models describe actomyosin gels as Maxwellian viscoelastic fluids with long-time viscous stress $\sigma \sim \eta \dot{\epsilon}$, where η is a viscosity and $\dot{\epsilon}$ is the local strain rate. In addition, the gels can possess an internal degree of freedom arising from *polarity* in filaments. Permanently cross-linked gels, on the other hand, are more likely to behave as solids at long time scales with elastic stress $\sigma \sim E\epsilon$, where E is the elastic modulus and ϵ is the local strain. These *passive* internal stresses are counteracted by motor-induced contractile stresses that can be estimated as $\sigma_a \sim \rho \xi \langle f \rangle$, where ρ is the density of bound motors, ξ is the network mesh size and $\langle f \rangle$ (> 0) is the average force exerted by molecular motors on a filament. The estimated value for the active stress, as inferred from experiments on crawling keratocytes [31], is found to be ~ 1 kPa, comparable to the elastic modulus

of actin gels [32]. Motor induced stresses depend strongly on the local strains and strain rates in the gel, and are highly dynamical due to binding-unbinding kinetics of individual molecular motors. However, the mechanical and physical properties of active gels have not been theoretically investigated, thus leaving open a lot of key questions in the physics of the cytoskeleton : What are the dynamic steady states and hydrodynamic instabilities in active elastic gels? How sensitive are the steady states to changes in network elastic modulus, filament density or chemical potential during ATP hydrolysis? Are non-linear chemo-mechanical couplings necessary to describe contractility and oscillations?

1.3 Cell-matrix Interactions

Forces that originate in the cytoskeleton are transmitted across the cell and eventually to the extracellular matrix (ECM) through specialized adhesion sites [35]. The actin cytoskeleton plays the most prominent role during cell-ECM force transduction [36]. Interactions of the cell with its surrounding ECM are mediated by *focal adhesions*, which are assemblies of *integrin* receptors, that are linked to actomyosin bundles (stress fibers) in the cell interior (Fig. 1.3, top frame). Integrins bind to specific ligands on the underlying ECM such as fibronectin, collagen, vitronectin or laminin, thus forming a mechanical linkage between the cytoskeleton and the ECM. This interior-exterior connection can modulate actomyosin activity as well as lead to remodeling of integrin-ECM ligand-receptor bonds [37]. The ability of the cells to respond to extracellular cues is strongly linked to myosin activity in the cytoskeleton, whereas the organization of the actin cytoskeleton is in turn controlled by mechanical and geometrical properties of the surrounding matrix. Micropatterning has emerged as a useful tool to study the response of the actin cytoskeleton by spatially controlling the distribution of ECM ligands [34, 38]. These studies have shown that when strongly adhesive patterns force the cell boundary to exhibit regions of high curvature,

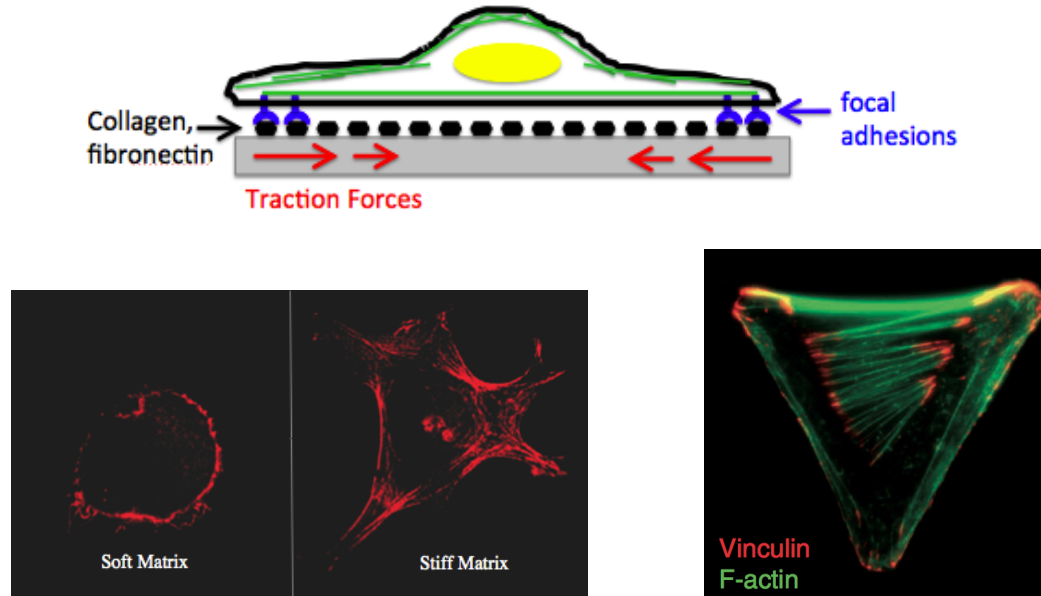


Figure 1.3: Top : Cartoon of an adherent cell, showing nucleus (yellow), actin stress fibers (green), focal adhesions (blue) and contractile traction forces (red arrows). Bottom : (Left) Fluorescently labeled actin cytoskeleton in migrating fibroblasts on soft and stiff matrices. The figure illustrates that substrate stiffness controls cell spread area, shape and cytoskeletal architecture [33]. (Right) Actin organization (green) and focal adhesion distribution (vinculin, shown in red) are also controlled by substrate geometry [34]. Underlying substrate here is a *concave* V-shape, coated with ECM proteins.

contractile forces tend to be concentrated in these regions, while stress fibers develop along cell boundaries linking non-adhesive zones (Fig. 1.3, bottom right). This observation confirms the crucial role of the cytoskeletal contractility and architecture in controlling cellular stresses and morphology [34, 39, 40]. Matrix stiffness also plays a profound role in regulating a myriad of cellular processes, from morphogenesis, motility and spreading, to cell fate and survival [1]. For example, mesenchymal stem cells differentiate into neurons on soft gels whereas on rigid substrates they become bone cells [41]. Cells adhering to softer substrates spread less and prefer to have well rounded morphologies, while they are more likely to exhibit branched patterns on stiffer substrates with greater spread area (Fig. 1.3, bottom left) [33, 42, 43].

1.3.1 Cellular force measurements

Cells exert *traction forces* on the surrounding ECM through focal adhesions causing elastic deformations in the matrix. The traction forces are lateral to the adhesive substrate, directed inward toward the cell center. This was first observed by Harris and coworkers in 1980 as migrating fibroblasts caused wrinkling in the underlying silicon gel [44, 45]. Powerful techniques have been developed in recent years to measure the traction forces exerted by adherent cells on synthetic elastic substrates coated with ECM proteins. To measure forces imparted to an elastic system, the standard technique is to measure the displacements of specified markers and then infer forces from the material's *constitutive* laws. Traction Force Microscopy (TFM) is used to probe the traction stresses exerted by cells on continuous elastic gels. The in-plane traction stresses are inferred from measurements of the displacements of fiducial markers embedded in the gel, before and after cell detachment [46–48] (see Fig. 1.4, left frame). Recent 3D measurements have also accounted for out-of-plane traction stresses in migrating cells via rotational deformations in focal adhesions [49]. In a second technique, cells plated on microfabricated pillar arrays induce bending of the elastic micropillars (Fig. 1.4, right frame). The traction forces are then obtained by assuming a linear Hooke's law relation between the measured bending and the forces [50, 51]. These experimental techniques have revealed a number of important trends in *cell on gel* experiments including localization of traction stresses to the cell edge [46], relationship of cell shape and motility with substrate stiffness [52, 53], role of substrate thickness [54] etc. For instance, traction forces are found to scale linearly with focal contact area in cardiac myocytes [55], giving a value for the stress of the order ~ 1 kPa. In 3T3 fibroblasts, traction forces are found to increase from 1-10 nN upon increasing substrate elastic modulus in the range 1-100 kPa [56]. While the exact correlation between adhesion and actomyosin activity depends on the cell type, recent TFM studies have claimed a biphasic (non-monotonic) relationship between traction forces and actin retrograde flow speed [57].

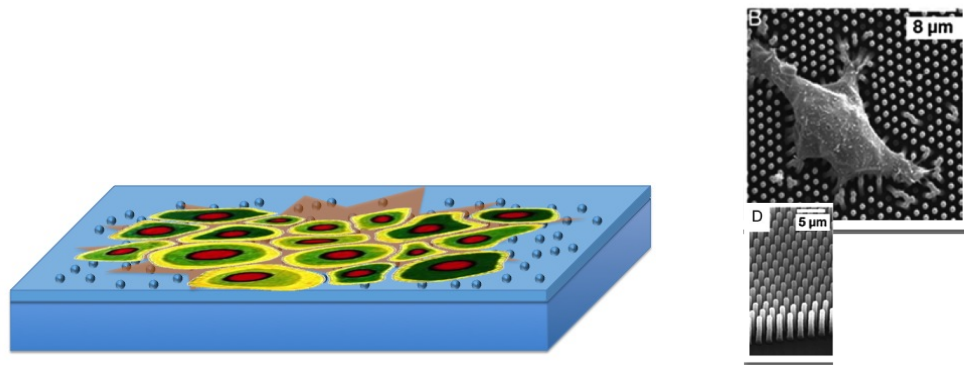


Figure 1.4: Left : Experimental set-up for Traction Force Microscopy. Traction stresses are inferred using *linear elasticity* from displacements of embedded beads [58]. Image courtesy : Eric Dufresne lab. Right : Cell adhering to a bed of micropillars [50]

1.3.2 Mechanical modeling

Motivated by the experimental findings, relating the rigidity of the extracellular environment to traction forces exerted by cells, a number of mechanical models have been proposed over the past decade. These include, studying the relationship of matrix rigidity with the growth and anisotropy of focal contacts [59–62], or analyzing the cooperativity between adhesion dynamics and stress fiber contractility [63, 64]. In addition, a growing class of models, inspired by Eshelby theory [65], have modeled cells as inclusions in an elastic matrix [66, 67], and have successfully captured rigidity induced self polarization of cells. Other continuum mechanical approaches have studied the interplay between cell elasticity and biochemical pathways using Finite Element Modeling [68]. Much simpler approaches, including a two-spring model for focal adhesions have provided key physical insights into cellular rigidity sensing [69]. Despite these significant theoretical contributions a lot of important physical questions have remain unanswered. What factors govern the spatial organization of traction forces? How do cells sense the geometry of their extracellular environment? How deeply do cells feel the substrate underneath? What is the relationship between mechanical anisotropy of cellular stresses and geometrical anisotropy of the substrate?

Cellular force generation is necessarily accompanied by changes in cell shape and

morphology. How do intercellular and extracellular forces cooperate to control the geometry of cell shapes? Previous theoretical models have analyzed the competition between bulk and peripheral contractility by suitable modification of *soap film* models [70, 71]. In analogy with the Laplace law of capillarity, the steady state cell contour is then described by concave circular arcs connecting neighboring adhesion sites, as seen in micropillar experiments [72]. The question then arises of whether these circular arcs are always the stable configuration. As discussed before, recent experiments suggest that on stiff environments, cells attain singular structures such as cusps and protrusions, whereas they maintain rounded shapes on softer substrates [43, 73]. Hence, the need for a comprehensive theoretical model emerges, integrating the geometry of cell shapes with mechanical properties of the extracellular matrix.

1.4 Towards the Mechanics of Tissues

While the mechanical behavior of individual cells has been the topic of inquiry for the past few decades, the focus has recently shifted to understanding the collective mechanics of groups of cells. Emergent mechanics at multicellular scales are particularly important in developmental morphogenesis [74], homeostasis [75], and wound healing [76] in epithelial tissues. Cells exert mechanical force on each other at sites of intercellular adhesion, typically through cadherins [77, 78], as well as on the underlying extracellular matrix (ECM) through integrins [55, 79, 80]. Cadherin-based adhesions can alter physical aspects of cells such as the surface tension of cellular aggregates [81] and the spreading [82] and migration [83] of cells adherent to cadherin-patterned substrates. Integrity of intercellular adhesions may also contribute to metastatic potential, the propensity of cancer cells to spread the disease to their local and non-adjacent neighbours [84]. It has been shown that epithelial cell clusters with strong cell–cell adhesions exhibit coordinated mechanical behavior over length scales much larger than a single cell [85–87]. Earlier cell-doublet studies

reported that during the formation of cadherin based adhesions, actomyosin contractility is down-regulated (decreased) at the cell-cell contact zones and are up-regulated (increased) at the exterior cell boundaries (Fig. 1.5, left) [88]. This is consistent with the claim that there is a direct relationship between cell-ECM traction forces and cell-cell forces [86]. Several studies have implicated crosstalk between cell-ECM and cell-cell adhesions [89, 90] that can be modulated by actomyosin contractility [91]. Recent data suggest that integrin-mediated adhesions can modulate the composition [92] and tension [93, 94] of cell-cell junctions. While cadherins have been shown to modify local traction forces [95] and monolayer contractility [96], the effects of intercellular adhesions on the spatial organization of cell-ECM forces remain unexplored.

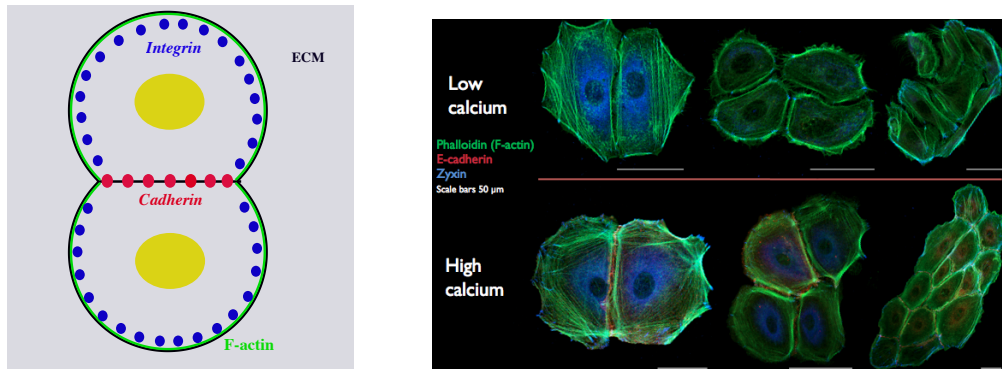


Figure 1.5: Left : Schematic top view of an adherent cell pair anchored onto ECM. The diagram illustrates the spatial organization of integrins (blue), cadherins (red) and F-actin (in green). Right : Calcium alters morphology and cohesiveness of cells.

1.5 Outline

In the chapters that follow, we discuss mechano-chemical models of the cell cytoskeleton, integrating the role of internal cellular activity with the emergent mechanical properties of cells. In chapter 2, we investigate the dynamics of cytoskeletal filaments on a motility assay, randomized by stochastic binding/unbinding kinetics of molecular motors [13]. Motility assay provides a simple mechanical set-up to analyze

in detail the interaction of cytoskeleton filaments with groups of molecular motors. We demonstrate that individual cytoskeletal filaments in a motility assay behave like self-propelled rods, paving the way to formulate simple continuum theoretical models to analyze collective behavior of motor-filament gels. In chapter 3, we propose a generic continuum model describing the dynamics of a permanently cross-linked active gel at hydrodynamic length and time scales, and examine its properties in the *linear* regime [97]. The model allows us to capture the emergent mechanical phases and rheology in actomyosin networks that are not necessarily endowed with well organized structures. In Chapter 4, we further explore the interplay of elasticity and activity in a cross-linked active gel beyond the linear description, and propose a *minimal* nonlinear model of the cytoskeleton as a crosslinked active gel [98]. The model describes in an unified manner, the origin of contractility and spontaneous waves in isotropic networks. Our findings suggest that with increasing motor activity, the active gel passes through periods of softening and stiffening, before settling down to a macroscopic contracted state at high motor activity.

In chapter 5, we adopt the active gel approach to describe the mechanics of cells adhering to elastic substrates. We model the cell as an active elastic medium mechanically coupled to a passive elastic medium [99, 100]. An elastic description of the cell is valid on time scales shorter than cytoskeletal turnovers, that are indeed slowed down by strong adhesion to the substrate. The model naturally leads to localization of traction forces at the cell edge and buildup of tensile stresses at the cell center - two features that are ubiquitously observed in TFM experiments. In addition, the model has yielded key analytical results, capturing the relationship between traction forces and substrate stiffness, substrate geometry and cell spread area, in quantitative agreement with experimental trends [101, 102]. Furthermore, changes in the mechanical properties of cells and in the matrix stiffness can reorganize cytoskeletal architecture such that actin stress fibers may reorient in response to matrix strains. This can lead to emergence of macroscopic *polar* order in actin organization. Since

myosin clusters exert active dipolar stresses when attached to actin stress fibers, the coupling of activity with adhesion can induce buildup of stress fiber polarization in cells. We introduce an active polar gel model for an adherent cell, where local mechanical strains are slaved to changes in orientational order. Our study demonstrates how cells can sense orientational cues with an optimal substrate stiffness for maximal stress fiber polarization [99]. The optimal substrate stiffness is comparable to that of the cell, as suggested by experiments on stem cells [66].

In chapter 6, we analyze the effect of mechanosensing on optimal cellular shapes. We describe an adherent cell as a contractile film bounded by an elastic cortex and connected to the substrate through compliant links, with bending elasticity in the cortical layer [103]. Our analysis suggests that cells can indeed be driven through *geometric phase transitions* by artificially tuning substrate stiffness or actomyosin contractility. The contractile film model is equivalent to the adherent active gel model when the substrate is much stiffer than the cell.

Going beyond the single cell description, in chapter 7, we introduce a coarse-grained model of a cohesive cell monolayer. We discuss in detail the impact of substrate thickness and non-local elastic interactions of the cells with the substrate on traction stress generation. We provide justifications to the fact that non-local elastic effects do not influence force generation in single cells but are important in large cell sheets.

Chapter 8 describes a combined theoretical and experimental approach to analyze the role of intercellular and extracellular adhesions in tissue-scale force generation, using primary mouse keratinocytes as the model system [104, 105]. Our studies claim that adherent cells in a tissue form a mechanically integrated system where cadherins and integrins are mechanically coupled through the actomyosin cytoskeleton. Cell-cell cohesion in a colony can be tuned by changing extracellular-calcium concentration (Fig. 1.5, right). In a high-calcium environment cadherin based *adherens junctions* form between cells, leading to strong cell-cell coupling. Whereas in a low calcium

environment, cells in a colony are weakly coupled and react independently to integrin mediated force transduction. Traction stresses were measured in colonies of 1-27 keratinocyte cells adherent to a fibronectin coated soft silicon gel *. Irrespective of the number of constituent cells, it is found that traction stresses strongly localize to periphery of the colony when cell-cell interaction is strong. In low-calcium environment when the cadherin based adhesions do not form, traction stresses distribute in a disorganized fashion with strong traction stresses underneath the cell-cell junctions and at the colony periphery. We investigate a mechanical model of the cell colony, where cells are modeled as contractile elastic sheets adhering to a soft substrate and to the neighboring cells through elastic links. The model quantitatively and qualitatively captures the spatial distribution of traction stresses as measured in experiments in low and high calcium extracellular environments. Interestingly, we find that that traction forces exerted by strongly cohesive cell colonies do not correlate with the number of constituent cells but with the geometrical size of the colony. Furthermore, for large colonies, total traction force scales linearly with the colony size. This scaling suggests emergence of a scale-free material property in large sized colonies, namely an *effective* surface tension (force per unit length), of the order of 10^{-3} N/m. The theoretical model supports the scaling and implies that the effective surface tension originates from actomyosin contractility. The measured value for the surface tension in *these* epithelial colonies is of the same order as reported for adherent endothelial cells [71] and 3D non-adherent cellular aggregates [106]. It is then tempting to think of the adherent cell colonies as cohesive aggregates that wet the substrate underneath, whose effective surface tension originate not only from the interfaces between different ambient phases but also from actomyosin activity.

*Experiments were performed by Aaron Mertz at the Soft Matter Lab of Eric Dufresene (Yale University)

Chapter 2

Motor-driven Dynamics of Cytoskeletal Filaments

2.1 Collective action of molecular motors

There has recently been renewed interest in motility assays where semiflexible actin filaments are driven to slide over a “bed” of myosin molecular motors. Recent experiments at high actin density have revealed that the collective behavior of this simple active system is very rich, with propagating density waves and large scale swirling motion [11, 107], not unlike those observed in dense bacterial suspensions [108]. In an actin motility assay the polymeric tails of myosin motor proteins are anchored to a surface, while their heads can bind to actin filaments [12]. Once bound, the motor head exerts forces and drives the filament’s motion. This system provides possibly the simplest realization of an active system that allows detailed semi-microscopic modeling.

Stochastic models of the collective action of motor proteins on cytoskeletal filaments in *one dimension* have been considered before by several authors, with emphasis on the acto-myosin system in muscles and on the mitotic spindle [109]. When working against an elastic load, the motor assemblies have been shown to drive periodic

spontaneous activity in the form of oscillatory instabilities, which in turn have been observed ubiquitously in a variety of biological systems [25, 110–113]. These instabilities arise in the model from the collective action of the motors and the breaking of detailed balance in their dynamics and manifest themselves as a negative effective friction of the filament. When free to slide under the action of an external force, the filament can exhibit bistability that manifests itself as hysteresis in the force velocity-curve [10, 114]. A large body of earlier work has modeled the motors as rigid two-state systems attached to a backbone and bound by the periodic potential exerted by the filament on the motor head [10, 110, 115]. In a second class of models the motors have been modeled as flexible springs [116, 117]. The motor heads bind to the filament and unbind at a load-dependent rate. In this case the dynamic instability arises from the dependence of the unbinding rate on the tension exerted by springs [118–120]. Recent work by Guérin et al. [121] has generalized the two-state model by taking into account the flexibility of the motors, showing that both models can be obtained in a unified manner for different values of a parameter that compares the stiffness of the motors to the stiffness of the periodic potential provided by the filament.

In this chapter we consider a model of a rigid filament, free to slide in *two dimensions* under the driving action of motor proteins uniformly tethered to a two-dimensional plane. The model considered is a modification of the “crossbridge” model first introduced by Huxley in 1957 to describe motor-induced contractile behavior of muscle fibers [122]. The motor proteins’ polymeric tails are modeled as linear springs that pull back on the bound motor heads. After attachment, the motor heads slide along the filament at a velocity that depends on the load exerted by the flexible motor tails. The sliding and subsequent detachment play the role of the motor’s power stroke. The binding/unbinding dynamics of the motor heads and the dependence of the transition rates on the load exerted by the motor tails play a crucial role in controlling the dynamics of the filament, effectively yielding non-Markovian noise sources on the filament. Related models have been studied numerically [116, 117, 123]. The

results presented here are obtained by generalizing to two dimensions the mean field approximation for the motor dynamics described for instance in Ref. [111]. The mean-field theory neglects convective nonlinearities in the equation for the probability of bound motors and correlations in the motors on/off dynamics, but it is expected to be adequate on time scales large compared to that of the motor on/off dynamics and for a large number of motors. This is supported by the results of [10] for a model of rigid two-state motors.

We begin by revisiting the one-dimensional problem. We discuss the steady-state response of the filament to an external force and present new results on the dynamics of fluctuations about the sliding steady state. The force-velocity curve is evaluated analytically and exhibits bistability and hysteresis, as obtained in Ref. [10] for a rigid two-state motor model. A new result is an expression for the effective propulsion force on the filament due to the motors in terms of physical parameters characterizing the motor proteins. Next, we analyze the fluctuations about the steady state by evaluating the mean-square displacement of the filament. We show that the coupling to the motor binding/unbinding dynamics yields non-Markovian noise sources with time correlations controlled by the duration of the motors' binding/unbinding cycle. Since the filament has a finite motor-induced velocity even in the absence of applied force, the mean-square displacement is ballistic at long time. The fluctuations of displacement about this sliding state are, however, diffusive at long times with an enhanced diffusion constant. This enhancement is controlled by the dependence of the motors' unbinding rate on the load exerted on the bound motors' heads by the tethered tails and vanishes for unloaded motors.

We then consider the case of a filament in two dimensions, to analyze the effect of the coupling of translational and rotational degrees of freedom in controlling the dynamics. At steady state, motors yield an effective propulsion force along the long axis of the filament, as in one dimension, but no effective torque. This is in contrast to phenomenological models considered in the literature [124] that have considered

the dynamics of active rod-like particles in the presence of both effective internal forces and torques. As a result, in the steady-state the filament slides along its long axis and the dynamics in this direction is essentially one dimensional, with a motor-induced negative friction instability and bistability and hysteresis in the response to an external force. Motors do enhance both the transverse and the rotational friction coefficients of the filament. The enhancement of rotational friction could be probed by measuring the response to an external torque. Since the finite motor-induced propulsion is along the filament axis, whose direction is in turn randomized by rotational diffusion, the mean velocity of the filament is zero in the absence of external force, unlike in the one-dimensional case. The mean square displacement is therefore diffusive at long times, with behavior controlled by the interplay of non-Markovian effects due to the coupling to motor dynamics with coupled translational and rotational diffusions. The filament performs a persistent random walk that consists of ballistic excursions at the motor-induced propulsion speed, randomized by both rotational diffusion and the motor binding/undinding dynamics. The crossover to the long-time diffusive behavior is controlled by the interplay of motor-renormalized diffusion rate and duration of the motor binding/unbinding cycle. The effective diffusion constant is calculated in terms of microscopic motor and filament parameters. Its dependence on activity, as characterized by the rate of ATP consumption, could be probed in actin assays.

Finally, this work provides a microscopic justification of a simple model used in the literature [125] that describes a cytoskeletal filament interacting with motor proteins tethered to a plane as a “self-propelled” rod, although it also shows that the effective noise is rendered non-Markovian by the coupling to the motors’ binding/unbing dynamics. It also provides microscopic expressions for the self-propulsion force and the various friction coefficients in terms of motor and filament parameters and shows that this effective model fails beyond a critical value of motor activity, where the effective friction changes sign and the filament exhibits bistability and hysteresis.

2.2 The model

In this model the motor proteins are described as composed of polymeric tails attached permanently to a two-dimensional fixed substrate and motor heads that can bind reversibly to the filament. Once bound, a motor head moves along the filament thereby stretching the tail. This gives rise to a load force on the motor head and on the filament. Eventually excessive load leads to detachment of the motor head.

2.2.1 Filament dynamics

The actin filament is modeled as a rigid polar rod of length L that can slide in two dimensions. It is described by the position \mathbf{r} of its center of mass and a unit vector $\hat{\mathbf{u}} = (\cos(\theta), \sin(\theta))$ directed along the rod's long axis *away* from the polar direction of the rod, which is in turn defined as the direction of motion of bound motors. In other words, bound motors move along the rod in the direction $-\hat{\mathbf{u}}$. In contrast to most previous work [110, 111, 115, 121], and given our interest in modeling actin motility assays, we assume the substrate is fixed and consider the dynamics of the filament. The goal is to understand the role of the cooperative driving by motors in controlling the coupled rotational and translational dynamics of the rod.

The dynamics of the filament is described by coupled equations for the translational and orientational degrees of freedom, given by

$$\underline{\underline{\boldsymbol{\Gamma}}} \cdot \partial_t \mathbf{r} = \mathbf{F}_a + \mathbf{F}_{\text{ext}} + \boldsymbol{\chi}(t) , \quad (2.1a)$$

$$\Gamma_\theta \partial_t \theta = T_a + T_{\text{ext}} + \chi_\theta(t) . \quad (2.1b)$$

Here we have grouped the forces and torques into the effects due to the motors, *i.e.* the activity, \mathbf{F}_a and T_a , external forces and torques \mathbf{F}_{ext} and T_{ext} and the stochastic noise not due to motors. The friction tensor is given by $\underline{\underline{\boldsymbol{\Gamma}}} = \Gamma_\parallel \hat{\mathbf{u}} \hat{\mathbf{u}} + \Gamma_\perp (\underline{\underline{\boldsymbol{\delta}}} - \hat{\mathbf{u}} \hat{\mathbf{u}})$ with Γ_\parallel and Γ_\perp the friction coefficients for motion longitudinal and transverse to the long direction of the rod, and Γ_θ is the rotational friction coefficient. For the case of a long, thin rod of interest here, $\Gamma_\parallel = \Gamma_\perp/2$. The random force $\boldsymbol{\chi}(t)$ and random torque

$\chi_\theta(t)$ describe noise in the system, including nonthermal noise sources. For simplicity we assume that both $\boldsymbol{\chi}(t)$ and $\chi_\theta(t)$ describe Gaussian white noise, with zero mean and correlations $\langle \chi_i(t)\chi_j(t') \rangle = 2A_{ij}\delta(t-t')$ and $\langle \chi_\theta(t)\chi_\theta(t') \rangle = 2A_\theta\delta(t-t')$, where $A_{ij} = A_{\parallel}\hat{u}_i\hat{u}_j + A_{\perp}(\delta_{ij} - \hat{u}_i\hat{u}_i)$.

2.2.2 Individual motor dynamics

We model the interaction cycle of an individual motor protein with the filament as shown in Fig. 2.1 for a one-dimensional system. The tail of a specific motor is fixed at position \mathbf{x}_t in the plane. At a time t_0 the head of this motor attaches to a point on the filament. The position of the motor head at the time of attachment is $\mathbf{x}_h(t_0) = \mathbf{r}(t_0) + s_0\hat{\mathbf{u}}(t_0)$, where $\mathbf{r}(t_0)$ and $\hat{\mathbf{u}}(t_0)$ denote the position of the center of the filament and its orientation $t = t_0$ and $s_0 \in [-L/2, L/2]$ parametrizes the distance of the point of attachment from the center of the filament (cf. Fig. 2.1(b)). We assume that motor proteins will attach to parts of the filament which are within a distance of the order of the size of the motor protein. The stretch of the motor tail at the time of attachment is then of order of the motor size and will be neglected, *i.e.* $\mathbf{x}_h(t_0) - \mathbf{x}_t = 0$, or motors attach to the part of the filament directly overhead without any initial stretch.

For $t > t_0$ the motor head remains attached to the filament and walks along it towards the polar head ($-\hat{\mathbf{u}}$ direction) until detachment. The tails, modeled as a linear spring of force constant k , exert a load $\mathbf{f} = -k\boldsymbol{\Delta}(t, \tau; s_0)$ on the head, where $\boldsymbol{\Delta}(t, \tau; s_0) = \mathbf{x}_h(t) - \mathbf{x}_t$ is the stretch at time t of a motor protein that has been attached for a time τ , *i.e.* $t = t_0 + \tau$ (cf. Fig. 2.1(c)). Since we assume $\boldsymbol{\Delta}(t_0) = 0$, we can also write

$$\begin{aligned} \boldsymbol{\Delta}(t, \tau; s_0) &= \mathbf{r}(t) - \mathbf{r}(t - \tau) + \sigma(t, \tau)\hat{\mathbf{u}}(t) \\ &\quad + s_0 [\hat{\mathbf{u}}(t) - \hat{\mathbf{u}}(t - \tau)] , \end{aligned} \tag{2.2}$$

where $\sigma(t, \tau) = s(t) - s(t - \tau)$ is the distance traveled along the filament at time t by

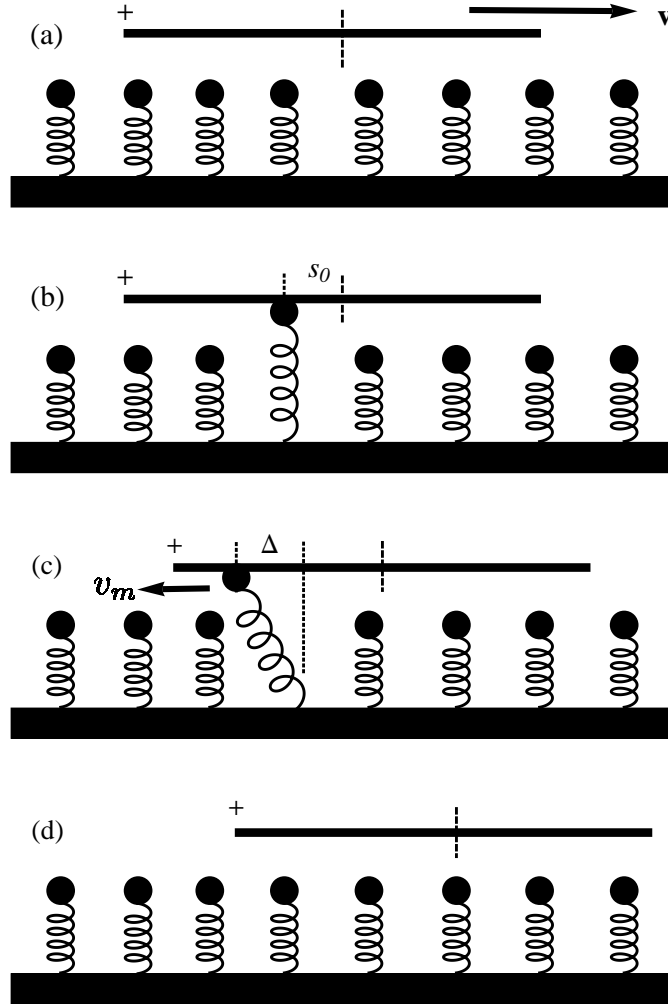


Figure 2.1: The figure shows the four steps of a motor cycle. In (a) a filament is sliding with velocity v over a uniform density of unbound motors with tails tethered to the substrate. In (b) a motor attaches to the filament at a position s_0 from the filament's mid-point. The stretch of the motor tails at the time of attachment is neglected. In (c) the motor has walked towards the polar head of the filament, stretching the tails by an amount Δ . Finally, in (d) the bound motor detaches and relaxes instantaneously to its unstretched state. The filament has undergone a net displacement in the direction opposite to that of motor motion.

a motor head that has been attached for a time τ , measured from the initial attachment position, s_0 . The kinematic constraint imposed by the condition of attachment requires

$$\begin{aligned} \partial_t \Delta(t, \tau; s_0) &= \mathbf{v}(t) - \mathbf{v}(t - \tau) + \hat{\mathbf{u}}(t) [v_m(t) - v_m(t - \tau)] \\ &\quad + \boldsymbol{\Omega}(t) \sigma(t, \tau) + s_0 [\boldsymbol{\Omega}(t) - \boldsymbol{\Omega}(t - \tau)] , \end{aligned} \quad (2.3)$$

where $\boldsymbol{\Omega}(t) = \partial_t \hat{\mathbf{u}}(t) = \dot{\theta} \hat{\mathbf{n}}(t)$ is the angular velocity of the rod and $v_m(t) = \partial_t s(t)$ the velocity of the motor head along the filament. We have introduced a unit vector $\hat{\mathbf{n}} = \hat{\mathbf{z}} \times \hat{\mathbf{u}}$ normal to the long axis of the filament. Then $(\hat{\mathbf{z}}, \hat{\mathbf{u}}, \hat{\mathbf{n}})$ defines a right-handed coordinate system with in-plane axes longitudinal and transverse to the filament. We note that Eq. (2.3) can also be written as

$$\begin{aligned} \partial_t \Delta(t, \tau; s_0) + \partial_\tau \Delta(t, \tau; s_0) &= \mathbf{v}(t) + v_m(t) \hat{\mathbf{u}}(t) \\ &\quad + \boldsymbol{\Omega}(t) \sigma(t, \tau) + s_0 \boldsymbol{\Omega}(t) . \end{aligned} \quad (2.4)$$

While the motor remains bound, the dynamics of the motor head along the filament is described by an overdamped equation of motion

$$\Gamma_m \dot{s}(t) = -f_s + \hat{\mathbf{u}} \cdot \mathbf{f} \quad (2.5)$$

where $f_s > 0$ is the stall force, defined as the force where the velocity $v_m = \dot{s}$ of the loaded motor vanishes. Since motors move in the $-\hat{\mathbf{u}}$ direction, generally $v_m = \dot{s} < 0$. Letting $f_{\parallel} = \hat{\mathbf{u}} \cdot \mathbf{f} = -k \Delta_{\parallel}$, Eq. (2.5) can also be written as

$$v_m(t) = -v_0 \left(1 - \frac{f_{\parallel}(\Delta_{\parallel})}{f_s} \right) , \quad (2.6)$$

where $v_0 = f_s / \Gamma_m \sim \Delta \mu > 0$ is the load-free stepping velocity, with $\Delta \mu$ the rate of ATP consumption. The motor velocity is shown in Fig. (2.2) as a function of the load f_{\parallel} . The motor head velocity also vanishes for $f_{\parallel} < -f_d$, when the motor detaches. The linear force-velocity relation for an individual motor is consistent with experiments on single kinesin molecules [126].

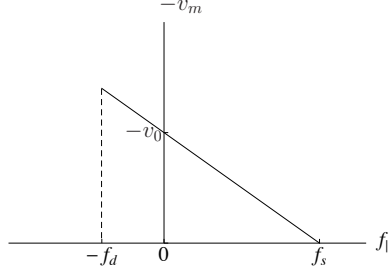


Figure 2.2: The velocity $-v_m$ of a loaded motor head as a function of the load $f_{\parallel} = \hat{\mathbf{u}} \cdot \mathbf{\Delta}$. The figure shows the stall force f_s where $v_m = 0$ and the detachment force $-f_d$.

The active force and torque on the filament due to an individual bound motor can then be expressed in terms of these quantities as

$$\mathbf{f}_a(t, \tau; s_0) = -k\mathbf{\Delta}(t, \tau; s_0) , \quad (2.7a)$$

$$\tau_a(t, \tau; s_0) = -\hat{\mathbf{z}} \cdot [(s_0 + \sigma(t, \tau))\hat{\mathbf{u}}(t) \times k\mathbf{\Delta}(t, \tau; s_0)] . \quad (2.7b)$$

Finally, after traveling along the filament for a time τ_{detach} , the motor head detaches and the head position relaxes instantaneously back to the fixed position \mathbf{x}_t of the tail.

We note that we shall not be considering the possibility of direct interactions of motors with each other. We have also not considered stochastic aspects of the motor motion along the filament (Eq. (2.5)).

2.2.3 Motor binding and unbinding

Next we need to describe the stochastic binding/unbinding dynamics of the motor heads. We assume the motor tails are attached to the substrate with a homogeneous surface density ρ_m , such that for a rod of length L and width b a maximum of $N = \rho_m Lb$ motors can be bound at any given time. Following Guérin et al. [121], we denote by $\mathcal{P}_b(t, \tau; s_0)$ the probability that a motor head that has attached at s_0 at a time t_0 , has remained attached for a duration τ at time t . For simplicity in the following we assume that the probability that a motor attaches at any point along

the filament is uniform, i.e., $\mathcal{P}_b(t, \tau; s_0) = \frac{1}{L}P_b(t, \tau)$. We further assume that when motors unbind they relax instantaneously to the relaxed state. The time evolution of the binding probability is then given by

$$\begin{aligned} \partial_t P_b(t, \tau) + \partial_\tau P_b(t, \tau) = & - \langle \omega_u(\mathbf{\Delta}(\tau)) \rangle_{s_0} P_b(t, \tau) \\ & + \omega_b \delta(\tau) p_u(t), \end{aligned} \quad (2.8)$$

where $p_u(t)$ is the probability that a motor be unbound at time t . The probability distribution is normalized according to

$$\int_0^\infty d\tau \int_{-L/2}^{L/2} ds_0 \mathcal{P}_b(t, \tau; s_0) + p_u(t) = 1. \quad (2.9)$$

In Eq. (2.8), $\omega_u(\mathbf{\Delta}(\tau))$ and ω_b are the rates at which a motor head with tails stretched by an amount $\mathbf{\Delta}(t, \tau)$ unbinds from and binds to the filament, respectively. The binding rate ω_b will be assumed to be constant. In contrast, the unbinding rate ω_u is a strong function of the stretch of the motor tails, that has to be obtained by solving Eq. (2.4), with initial condition $\Delta(t = 0, \tau) = 0$. We will see below that the nonlinear dependence of the unbinding rate plays an important role in controlling the filament dynamics. In two dimensions the unbinding rate ω_u also depends on the initial attachment point s_0 along the filament. To be consistent with our ansatz that the probability that the motor attaches at any point along the filament is uniform, we have replaced the rate in Eq. (2.8) with its mean value $\langle \omega_u \rangle_{s_0}$, where $\langle \dots \rangle_{s_0} = \int_{-L/2}^{L/2} \frac{ds}{L} \dots$ denotes an average over the initial attachment points.

The unbinding rate is controlled by the work done by the force (load) acting on the motor head, which in turn is a linear function of the stretch $\mathbf{\Delta}$. A form that has been used extensively in the literature for one-dimensional models is an exponential, $\omega_u = \omega_0 e^{\alpha|\Delta|}$, where ω_0 is the unbinding rate of an unloaded motor and α is a characteristic length scale that control the maximum stretch of the tails above which the motor unbinds *. The exponential form represents an approximation for the result of a

* α can be estimated to be equal to $ka/k_B T$, where a is a microscopic length scale of the order of a few nm. Experiments are carried out at room temperatures which leads to $k_B T \sim$ pN nm.

detailed calculation of the average time that a motor moving along a polar filament spends attached to the filament as a function of a tangentially applied load [127] and is consistent with experiments on kinesin [128]. This form can easily be generalized to the case of a filament sliding in two dimensions where the motor load had both components tangential and transverse to the filament. It is, however, shown in the Appendix that within the mean-field approximation used below the exponential form yields a steady-state stretch Δ that saturates to a finite value at large velocity v of the filament. This is unphysical as it does not incorporate the cutoff described by the detachment force f_d in Fig. 2.2. For this reason in the mean-field treatment described below we use a parabolic form for the unbinding rate as a function of stretch,

$$\omega_u(\Delta) = \omega_0 [1 + \alpha^2 |\Delta|^2] , \quad (2.10)$$

where for simplicity we have assumed an isotropic dependence on the magnitude of the stretch in terms of a single length scale, α^{-1} . An explicit comparison of the two expressions for the unbinding rates is given in the Appendix.

The total active force and torque on the filament averaged over the original positions and the times of attachment can be written as

$$\mathbf{F}_a(t) = -Nk \int_0^\infty d\tau \langle P_b(t, \tau) \mathbf{\Delta}(t, \tau; s_0) \rangle_{s_0} , \quad (2.11a)$$

$$T_a(t) = -Nk \int_0^\infty d\tau \langle P_b(t, \tau) \hat{\mathbf{z}} \cdot [(s_0 + \sigma(t, \tau)) \hat{\mathbf{u}}(t) \times \mathbf{\Delta}(t, \tau; s_0)] \rangle_{s_0} . \quad (2.11b)$$

2.3 Mean field approximation

To proceed, we introduce several approximations for the motor dynamics. First, we restrict ourselves to the dynamics on times scales large compared to the attachment time τ of individual motors. For $t \gg \tau$ we approximate

$$\sigma(t, \tau) \simeq v_m(t) \tau , \quad (2.12a)$$

$$\mathbf{\Delta}(t, \tau; s_0) \simeq [\mathbf{v}(t) + v_m(t) \hat{\mathbf{u}}(t) + s_0 \mathbf{\Omega}(t)] \tau . \quad (2.12b)$$

This approximation becomes exact for steady states where the filament and motor velocities are independent of time. We also stress that in Eqs. (2.12a) and (2.12b) σ and Δ are still nonlinear functions of τ due to the dependence of v_m on the load force.

Secondly, we recall that we have assumed that the attachment positions s_0 are uniformly distributed along the filament and can be treated as independent of the residence times τ . Finally, we make a mean field assumption on the probability distribution of attachment times, which is chosen of the form $P(t, \tau) = \delta(\tau - \tau_{\text{MF}})p_b(t)$, with $p_b(t)$ the probability that a motor be attached at time t regardless of the its attachment time. The mean-field value of the attachment time is determined by requiring

$$\tau_{\text{MF}} = [\langle \omega_u (\Delta(\tau_{\text{MF}})) \rangle_{s_0}]^{-1} . \quad (2.13)$$

In previous literature a similar mean field assumption has been stated in terms of the stretch, Δ [25, 111]. In the present problem, however, where filaments can slide in two dimensions, it is necessary to restate the mean-field theory in terms of the residence time τ as the active forces and torques depend on both the stretch Δ of the motor tails and the distance σ traveled by a bound motor head along the filament. These two quantities are in turn both controlled by a single stochastic variable, identified with the residence time τ . The rate of change of the probability $p_b(t)$ that a motor be bound at time t is then described by the equation

$$\partial_t p_b(t) = -\tau_{\text{MF}}^{-1} p_b(t) + \omega_b [1 - p_b(t)] , \quad (2.14)$$

The mean field active force and torque due to the motors are then given by

$$\mathbf{F}_a^{\text{MF}} = -kN \langle \Delta(t, \tau_{\text{MF}}; s_0) p_b(t) \rangle_{s_0} , \quad (2.15)$$

$$T_a^{\text{MF}} = -kN \langle p_b(t) \hat{\mathbf{z}} \cdot [(s_0 + \sigma(t, \tau_{\text{MF}})) \hat{\mathbf{u}}(t) \times \Delta(t, \tau_{\text{MF}}; s_0)] \rangle_{s_0} . \quad (2.16)$$

In the following we will work in the mean-field approximation and remove the label MF from the various quantities.

2.4 Active filament sliding in one dimension

We first consider the simplest theoretical realization of a motility assay experiment, where the actin filament is sliding over a one dimensional track of tethered motor proteins. A closely related model, where the filament is elastically coupled to a network, has been used extensively in the literature to study the onset of spontaneous oscillations arising from the collective action of the bound motors [10, 110, 111]. Previous studies of freely sliding filaments, as appropriate for the modeling of motility assays, have also been carried out both analytically and numerically [120]. Our work contains some new results on the response to an external force of a filament free to slide under the action of active crosslinkers and also on the filament fluctuations.

The Langevin equation for the center of mass coordinate x of the filament is given by

$$\Gamma \dot{x} = F_a(t) + F_{\text{ext}} + \chi(t) , \quad (2.17)$$

where \dot{x} is the center-of-mass velocity of the filament and the mean-field active force is given by

$$F_a^{\text{MF}}(t) = -kNp_b(t)\Delta(\dot{x}, \tau) . \quad (2.18)$$

In one dimension the dependence on s_0 drops out and Eq. (2.12b) simply gives $\Delta \simeq (\dot{x} + v_m)\tau$. Substituting Eq. (2.6) for v_m , we can solve for Δ as a function of \dot{x} and τ ,

$$\Delta(\dot{x}, \tau) = \frac{(\dot{x} - v_0)/\omega_0}{\tilde{\tau}^{-1} + \epsilon} , \quad (2.19)$$

and Eq. (2.13) for the mean attachment time becomes

$$\tilde{\tau}^{-1}(\dot{x}) = 1 + \frac{(\dot{x} - v_0)^2 \alpha^2}{[\tilde{\tau}^{-1}(\dot{x}) + \epsilon]^2 \omega_0^2} , \quad (2.20)$$

where $\tilde{\tau} = \omega_0 \tau$ and $\epsilon = kv_0/f_s \omega_0$. The parameter ϵ is the ratio of the length $\ell_0 = v_0/\omega_0$ traveled by an unloaded motor that remains attached for a time ω_0^{-1} to the stretch

Parameters	Myosin-II	Kinesin
ℓ_0	~ 2 nm	~ 8 nm
δ_s	~ 1 nm	~ 25 nm
ϵ	~ 2	~ 0.32

Table 2.1: Typical values of the length scales $\ell_0 = v_0/\omega_0$ and $\delta_s = f_s/k$ introduced in the text and the ratio ϵ for myosin II and kinesin. The parameters are taken from Refs. [2] and [116].

$\delta_s = f_s/k$ of the motor tails at the stall force, f_s . Typical values for these length scales and the parameter ϵ are given in Table 2.1.

It is convenient to rewrite the mean residence time $\tilde{\tau}$ as

$$\tilde{\tau}^{-1} = 1 + \frac{(u-1)^2 \Lambda^2}{[\tilde{\tau}^{-1} + \epsilon]^2}, \quad (2.21)$$

where $u = \dot{x}/v_0$ and we have introduced a dimensionless parameter $\Lambda = \ell\alpha$ that controls the dependence of the unbinding rate on the load exerted on the bound heads by the stretched motor tails, with

$$\frac{1}{\ell} = \frac{1}{\ell_0} + \frac{1}{\delta_s} \quad (2.22)$$

the geometric mean of the two length scales introduced earlier. For stiff motors, with $\epsilon \gg 1$ or $\ell_0 \gg \delta_s$, $\ell \sim \delta_s$, while for floppy, easy to stretch motors, corresponding to $\epsilon \ll 1$ or $\ell_0 \ll \delta_s$, $\ell \sim \ell_0$. Setting $\Lambda = 0$ corresponds to neglecting the load dependence of the unbinding rate. The exact solution to Eq. (2.21) for the mean residence time $\tilde{\tau}(\dot{x})$ as a function of the filament velocity can be determined and is discussed in the Appendix. Clearly τ has a maximum value at $\dot{x} = v_0$, where $\tau = \omega_0^{-1}$ and decays rapidly as $|\dot{x} - v_0|$ grows.

2.4.1 Steady state and its stability

We begin by characterizing the steady state dynamics of the filament in the absence of noise. Incorporating for generality an external force F_{ext} , the steady state velocity

v of the filament is obtained from the solution of the nonlinear equation

$$\Gamma v = F_{\text{ext}} + F_a(v) \quad (2.23)$$

where $F_a(v) = -kNp_{bs}(v)\Delta(v)$. The steady state stretch $\Delta(v)$ is given by Eq. (2.19) with $\dot{x} = v$ and

$$p_{bs}(v) = \frac{\omega_b \tau(v)}{1 + \tau(v)\omega_b}, \quad (2.24)$$

with $\tau(v)$ given by Eq. (2.21) for $\dot{x} = v$. To gain some insight in the behavior of the system, we expand the active force as $F_a(v) \simeq F_p + \left(\frac{\partial F_a}{\partial v}\right)_{v=0} v + \mathcal{O}(v^2)$, with $F_p = F_a(v=0)$. Retaining only terms linear in v this gives a steady state force/velocity relation of the form

$$(\Gamma + \Gamma_a)v = F_{\text{ext}} + F_p \quad (2.25)$$

with a filament ‘‘propulsion’’ force F_p

$$F_p = \frac{Np_{bs0}k\ell_0}{\epsilon + \tilde{\tau}_0^{-1}}, \quad (2.26)$$

where $p_{bs0} = r/[r + (1-r)\tilde{\tau}_0^{-1}]$, with $r = \omega_b/(\omega_0 + \omega_b)$ the duty ratio, and $\tilde{\tau}_0 = \tilde{\tau}(v=0)$.

The active contribution $\Gamma_a = -\left(\frac{\partial F_a}{\partial v}\right)_{v=0}$ to the friction is given by

$$\Gamma_a = Np_{bs0} \frac{k|\Delta_0|}{v_0} \left[1 - \left(\frac{|\Delta_0|}{\ell_0} + p_{bs0} \frac{1-r}{r} \right) \frac{2\alpha^2 \Delta_0^2 \ell_0}{\ell_0 + 2\alpha^2 |\Delta_0|^3} \right], \quad (2.27)$$

where $\Delta_0 = \Delta(v=0) = -\ell_0/(\tilde{\tau}_0^{-1} + \epsilon)$. In the absence of external force, the filament will slide at a velocity

$$v_s = F_p/(\Gamma + \Gamma_a) \quad (2.28)$$

due to the action of the motor proteins. This motion is in the polar direction of the filament and opposite to the direction of motion of bound motors along the filament. Phenomenological models of motility assays have described the actin filaments as ‘‘self-propelled’’ Brownian rods. Our model yields a microscopic calculation of such

a “self-propulsion” force F_p in terms of microscopic parameters characterizing the motor proteins. We note that $-F_p$ can also be interpreted as the “stall force” of the filament, *i.e.* the value of F_{ext} required to yield $v = 0$. This is a quantity that may be experimentally accessible using optical force microscopy.

If we neglect the load dependence of the unbinding rate by letting $\Lambda = 0$, the mean number of bound motors is simply Nr and $F_p^0 = Nrkl$, with ℓ given by Eq. (2.22). In this limit the sliding velocity v_s^0 in the absence of external force can be written as

$$v_s^0 = \frac{v_0}{1 + \Gamma/\Gamma_a^0}. \quad (2.29)$$

where the active friction $\Gamma_a^0 = Nrkl/v_0 > 0$ is always positive. The sliding velocity vanishes when $v_0 \rightarrow 0$ and it saturates to its largest value v_0 when the number Nr of bound motors becomes very large and $\Gamma_a^0 \gg \Gamma$. The behavior is controlled by the parameter ϵ . If the motors are easy to stretch, *i.e.*, $\epsilon \ll 1$, then the propulsion force is determined entirely by the elastic forces exerted by these weak bound motors, with $F_p^0 \simeq Nrkl_0$. On the other hand stiff motors, with $\epsilon \gg 1$, stall before detaching. The propulsion force is then controlled by the motor stall force, with $F_p^0 \simeq Nrf_s$.

The load-dependence of the unbinding rate changes qualitatively the behavior of the system. In particular, the net friction $\Gamma + \Gamma_a$ can become negative, rendering the steady state unstable. This instability was already noted in Ref. [10] for a two-state model of active linkers and in Ref. [121] for a two state “soft” motor model. The full nonlinear force-velocity curves are shown in Fig. 2.3 for various values of the motor stiffness k , for parameters appropriate for acto-myosin systems. In the steady state, as we increase the active parameter k while keeping the substrate friction Γ constant, the $F_{\text{ext}} - v$ curve becomes non-monotonic, and two distinct regions of bistability emerge. To understand the increase of the bistability region with motor stiffness, we note that the active force is simply proportional to k , hence naively one would indeed expect its effect to be more pronounced for stiff motors. The detailed behavior is, however, determined by the interplay of the mean residence time τ that motors spend bound to the filament and the stretch, Δ . Soft, floppy motors have large stretches, controlled

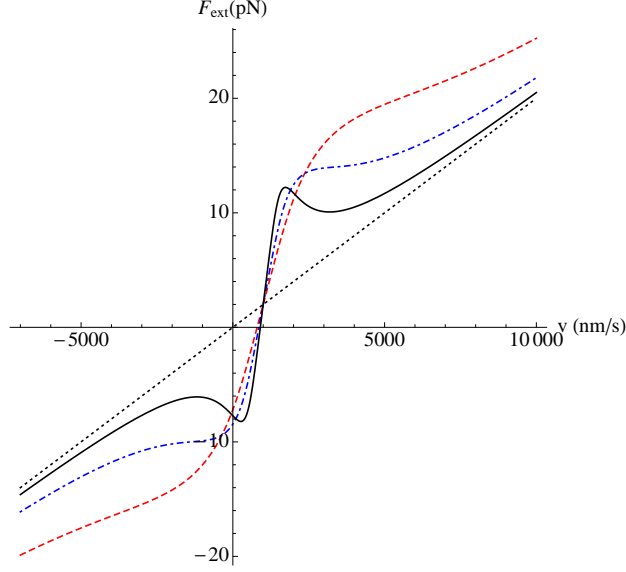


Figure 2.3: Force-velocity curves for $\Gamma = 0.002 \text{ pNnm}^{-1}\text{s}$ and various values of the motor stiffness k , showing the transition to non-monotonicity as k increases. The values of the stiffness k (in pN/nm) and the corresponding values for α^{-1} (in nm) and ϵ are as follows: $k = 0$, $\alpha^{-1} = 0$, $\epsilon = 0$ (black dotted line); $k = 1$, $\alpha^{-1} = 0.75$, $\epsilon = 0.5$ (red dashed line); $k = 2$, $\alpha^{-1} = 1.5$, $\epsilon = 1$ (blue dashed-dotted line); $k = 8$, $\alpha^{-1} = 6$, $\epsilon = 4$ (black solid line). At high velocities the curves merge into the linear curve $F_{\text{ext}} = \Gamma v$ (black dotted line), corresponding to the case where no motors are present. The remaining parameters have the following values: $N = \rho_m L b = 100$, $v_0 = 1000 \text{ nm/s}$, $f_s = 4 \text{ pN}$, $\omega_0 = 0.5 \text{ (ms)}^{-1}$, $r = 0.06$.

mainly be the length ℓ_0 traveled by an unloaded motors advancing at speed v_0 . On the other hand, their residence time is small and the overall effect of the active force remains small. In contrast, stiff motors have a small stretch, of order of the stretch $\delta_s = f_s/k$ of a stalled motor, but long residence times and are collectively capable of slowing down the filament and even holding it in place against the action of the external force, driving the negative friction instability. At even larger values of the external force motors are effectively always unbound due to the fast sliding of the filament and the velocity-force curve approaches the linear form obtained when no motors are present. This behavior is best seen from Fig. 2.5.

The region of non-monotonicity of the force-velocity curve and associated bista-

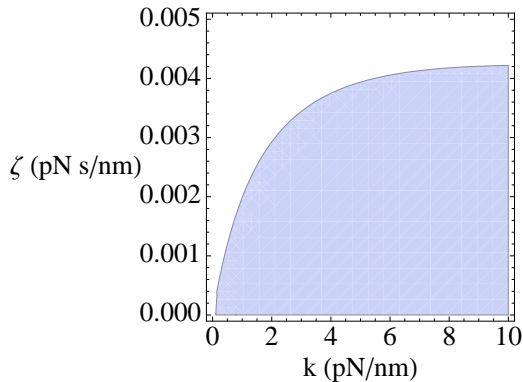


Figure 2.4: Phase diagram in k - Γ plane showing the region where the $F_{\text{ext}}-v$ curves exhibit non-monotonic behavior (blue shaded region) for $N = \rho_m Lb = 100$ and $v_0 = 1 \mu\text{m s}^{-1}$, $f_s = 4 \text{ pN}$, $\alpha/k = 1.33 \text{ pN}$, $\omega_0 = 0.5 \text{ (ms)}^{-1}$, $r = 0.06$.

bility can also be displayed as a phase diagram, as shown in Fig. 2.4. The stiffness of myosins is about 5 pN/nm and the actin filament friction was estimated to be of order 0.003 pNs/nm in Ref [12]. In actomyosin systems the negative friction instability should therefore be observable in a range of experimentally relevant parameters. Kinesin motors have floppier tails and a smaller stiffness of about 0.5 pN/nm . In this case bistability effects should be prevalent only at very low filament friction, $\Gamma \ll 0.001 \text{ pNs/nm}$. A proper estimate of the region of parameters where the instability may be observable is rendered difficult by the fact that the onset of negative friction is also a strong function of the density of motors tethered to the substrate, which in turn affects the value of the friction Γ . In general, we expect that a high motor density will be needed for the instability to occur. On the other hand, if the density of motors is too high, the friction Γ will be enhanced and the instability suppressed.

We stress that the force-velocity curves displayed in Fig. 2.3 have been obtained by calculating F_{ext} as a function of v . In an experiment one would tune the applied force and measure the resulting velocity. The system would not access the unstable regions of negative friction, but rather follow the hysteretic path sketched in Fig. 2.5.

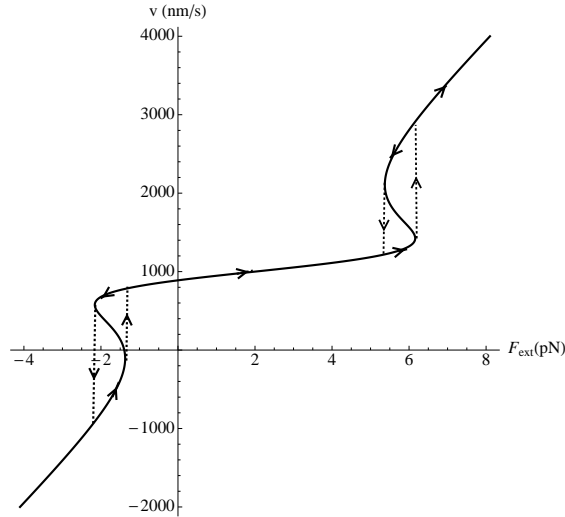


Figure 2.5: The figure sketches the hysteretic behavior that may be obtained in an experiment where an external force F_{ext} is applied to a filament in a motility assay. The response of the filament will generally display two regions of hysteresis, at positive and negative forces.

The discontinuous jump may occur at the boundary of the stability region, as shown in the figure, or before such a boundary is reached, corresponding to what is known as “early switching”.

To summarize, motors have two important effects on the steady state dynamics of the filament. First, they make the filament self-propelled, in the sense that in the absence of an external force the filament will slide at a velocity v_s given by Eq. (2.28). The value of v_s increases with increasing motor stiffness and of course vanishes for $v_0 = 0$, corresponding to the vanishing of the rate of ATP consumption $\Delta\mu$. The sliding velocity v_s is shown in Fig. 2.6 as a function of the parameter ϵ inversely proportional to the motor stall force for a few values of the maximum number of motors that can bind to the filament. A second important effect of motor activity is the discontinuous and hysteretic response to an external force displayed in Fig. 2.5. When $F_{\text{ext}} = 0$ the filament slides at the motor-induced velocity v_s . If a small force $F_{\text{ext}} > 0$ is applied, the filament velocity remains an approximately linear function of the applied force, but with an effective friction greatly enhanced by motor

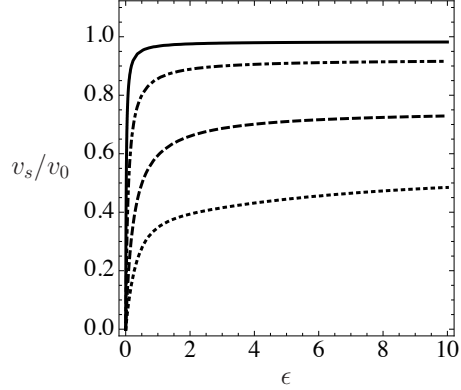


Figure 2.6: The motor-induced sliding velocity v_s of an actin filament in the absence of external force is shown as a function of $\epsilon = \ell_0/\delta_s$ for $N = 10$ (dotted line), $N = 25$ (dashed line), $N = 100$ (dashed-dotted line) and $N = 500$ (solid line). We observe that $v_s \rightarrow v_0$ for stiff motors as N is increased. Parameter values: $\Gamma = 0.002 \text{ pN (nm)}^{-1}\text{s}$, $r = 0.06$, $\alpha/k = 1.33 \text{ pN}$.

binding/unbinding. This enhancement of friction is also termed in the literature as protein friction [129]. At high velocity, only a few motors are attached to the filament and the filament velocity approaches the value it would have in the absence of motors as the applied force is increased beyond a characteristic value. When the external force is ramped down the filament velocity jumps to the lower branch corresponding to a lower value of the force, resulting in hysteresis.

2.4.2 Fluctuation dynamics

We now examine the dynamics of noise-induced fluctuations about the steady state by letting $\delta\dot{x} = \dot{x} - v$, where v is the steady state velocity, given by the solution of Eq. (2.23) discussed in the previous section. The dynamics of the fluctuation $\delta\dot{x}$ is then described by the equation

$$\Gamma\delta\dot{x} = -kN\Delta(v)\delta p_b - kNp_{bs}\delta\Delta + \chi(t), \quad (2.30)$$

where both $\delta\Delta = [\partial_v\Delta(v)]\delta\dot{x}$ and $\delta p_b(t)$ depend on noise only implicitly through the velocity \dot{x} , with

$$\partial_t\delta p_b = - \left[\frac{1}{\tau(v)} + \omega_b \right] \delta p_b - p_{bs}(v) \frac{\partial}{\partial v} \left[\frac{1}{\tau(v)} \right] \delta\dot{x} \quad (2.31)$$

The random force $\chi(t)$ in Eq. (2.30) describes noise on the filament, with $\langle\chi(t)\rangle = 0$ and $\langle\chi(t)\chi(t')\rangle = 2A\delta(t-t')$. Noise can arise in the system from a variety of sources, including the fluid through which the filament moves and the motor on/off dynamics. For simplicity we assume the spectrum is white, albeit with a non-thermal strength B . By solving Eq. (2.31) with initial condition $\delta p_b(t=0) = 0$ and substituting in Eq. (2.30), we obtain a single equation for $\delta\dot{x}$,

$$[\Gamma + \Gamma_a(v)]\delta\dot{x}(t) + \omega_0\Gamma'_a(v) \int_0^t dt' e^{-\Omega(t-t')}\delta\dot{x}(t') = \chi(t) \quad (2.32)$$

where we have introduced an effective frequency $\Omega(v) = \tau^{-1}(v) + \omega_b$ and active frictions

$$\Gamma_a(v) = kNp_{bs}(v)\partial_v\Delta(v) \quad (2.33)$$

$$\Gamma'_a(v) = kNp_{bs}(v)\Delta(v)\frac{\partial}{\partial v}\left(\frac{1}{\tilde{\tau}}\right). \quad (2.34)$$

In all the parameters defined above v has to be replaced by the steady state solution obtained in the previous section. The time scale Ω^{-1} represent the duration of the cycle of a loaded motor. Note that $\Gamma_a(v=0) = \Gamma_a$, with Γ_a given by Eq. (2.27). It is evident from Eq. (2.32) that motor dynamics yields a non-Markovian contribution to the friction.

If we neglect the load dependence of the unbinding rate by letting $\Lambda = 0$, hence $\tau^{-1} = \omega_0$, then $\Gamma_a(v) = \Gamma_{a0} = Nrk\ell/v_0$ and $\Gamma'_a(v) = 0$. In this limit $\langle[\delta x(t) - \delta x(0)]^2\rangle = 2D_{a0}t$ and is diffusive *at all times*, with an effective diffusion constant $D_{a0} = \frac{A}{(\Gamma+\Gamma_{a0})^2}$.

When Λ is finite we obtain

$$\langle[\delta x(t) - \delta x(0)]^2\rangle = 2D_a t + 4D_a \left[\frac{\Gamma'_a(v)\omega_0}{[\Gamma + \Gamma_a(v)]\Omega_a} \right]^2 \left(t - \frac{1 - e^{-\Omega_a t}}{\Omega_a} \right), \quad (2.35)$$

where $D_a = A/[\Gamma + \Gamma_a(v)]^2$ and $\Omega_a(v) = \Omega(v) + \omega_0 \Gamma'_a(v)/[\Gamma + \Gamma_a(v)]$. The characteristic time scale Ω_a^{-1} controls the crossover from ballistic behavior for $t \ll \Omega_a^{-1}$ to diffusive behavior for $t \gg \Omega_a^{-1}$. It is determined by the smaller of two time scales: Ω^{-1} , defined after Eq. (2.32), that represents the duration of the cycle of a loaded motor, and the active time $(\omega_0 \Gamma'_a/[\Gamma + \Gamma_a])^{-1}$ that represents the correlation time for the effect of motor on/off dynamics on the filament. At long times the mean-square displacement is always diffusive, with an effective diffusion constant

$$D_{\text{eff}} = D_a \left[1 + \left(\frac{\Gamma'_a \omega_0}{[\Gamma + \Gamma_a(v)] \Omega_a} \right)^2 \right] \quad (2.36)$$

This result only describes the behavior of the system in the stable region, where the effective friction remains positive. At the onset of negative friction instability $\Gamma + \Gamma_a(v) \rightarrow 0$ and the effective diffusivity diverges. In other words the instability is also associated with large fluctuations in the rod's displacements due to the cooperative motor dynamics.

To leading order in Λ the frequency Ω_a that controls the crossover to diffusive behavior is simply $\Omega \simeq \omega_0 + \omega_b + \mathcal{O}(\Lambda^2)$. For non-processive motors such as myosins $\omega_0 \gg \omega_b$ and $\Omega \sim \omega_0$. The effective diffusion constant is given by

$$D_{\text{eff}} \simeq D_a \left[1 + \frac{2\Gamma^2 \Gamma_{a0}}{(\Gamma + \Gamma_{a0})^3} \left(\frac{v_0 \alpha}{\omega_0(1 + \epsilon)} \right)^2 + [(v_0 \alpha / \omega)^4] \right]. \quad (2.37)$$

This expression indicates that the enhancement of the diffusion constant comes from the competition of the ballistic motor-driven motion of the filament at speed $\sim v_0 \Gamma_{a0}/(\Gamma + \Gamma_{a0})$ and the randomization of such motion by the motor on/off dynamics on time scales $\sim \omega_0^{-1}$. The result is that the filament dynamics is diffusive at long times, but with an enhanced diffusion constant.

Finally, we stress that the correlation function $\langle [\delta x(t) - \delta x(0)]^2 \rangle$ describes the fluctuations about the steady state value vt . If we write $x(t) = vt + \delta x(t)$ the actual mean square displacement of the center of mass of the rod is given by $\langle (x(t) - x(0))^2 \rangle = v^2 t^2 + \langle [\delta x(t) - \delta x(0)]^2 \rangle$ and is ballistic at long times in one dimension due to the mean

motion of the rod. In addition, due to nonlinearity of the Langevin equation (2.17) the mean value $\langle x \rangle$ in the presence of noise will in general differ from the steady state solution vt obtained in the absence of noise due to renormalization by fluctuations $\langle F_a(\dot{x}, t) \rangle - F_a(v, t)$. These fluctuations are neglected in mean field theory.

2.5 Active filament dynamics in two dimensions

In two dimensions the coupled translational and rotational dynamics of the filament is described by Eqs. (2.1a) and (2.1b). It is convenient to write the instantaneous velocity of the center of the filament in terms of components longitudinal and transverse to the long axis of the filament, $\dot{\mathbf{r}} = V_{\parallel} \hat{\mathbf{u}} + V_{\perp} \hat{\mathbf{n}}$. Similarly the stretch is written as $\Delta = \Delta_{\parallel} \hat{\mathbf{u}} + \Delta_{\perp} \hat{\mathbf{n}}$, where (see Eq. (2.12b))

$$\Delta_{\parallel} = \hat{\mathbf{u}} \cdot \Delta = (V_{\parallel} + v_m) \tau, \quad (2.38a)$$

$$\Delta_{\perp} = \hat{\mathbf{n}} \cdot \Delta = (V_{\perp} + s_0 \dot{\theta}) \tau. \quad (2.38b)$$

It is then clear that Δ_{\parallel} has the same form as in one dimension

$$\Delta_{\parallel} = \frac{(V_{\parallel} - v_0)/\omega_0}{\tilde{\tau}^{-1} + \epsilon}, \quad (2.39)$$

and the mean-field value of the attachment time τ is given by

$$\tilde{\tau}^{-1}(V_{\parallel}, V_{\perp}, \dot{\theta}) = 1 + \frac{(V_{\parallel} - v_0)^2 \alpha^2}{(\tilde{\tau}^{-1} + \epsilon)^2 \omega_0^2} + \frac{V_{\perp}^2 \tilde{\tau}^2 \alpha^2}{\omega_0^2} + \frac{L^2 \dot{\theta}^2 \tilde{\tau}^2 \alpha^2}{12 \omega_0^2}, \quad (2.40)$$

where we have carried out the average over s_0 . Inserting these expressions in Eqs. (2.15) and (2.16), the mean field active force and torque exerted by bound motors on the filament can then be written as

$$\mathbf{F}_a = -kNp_b(t) \left[\frac{(V_{\parallel} - v_0)/\omega_0}{\tilde{\tau}^{-1} + \epsilon} \hat{\mathbf{u}} + V_{\perp} \tau \hat{\mathbf{n}} \right], \quad (2.41a)$$

$$T_a = -kNp_b(t) \tau \left[\frac{L^2 \dot{\theta}}{12} + V_{\perp} v_m \tau \right]. \quad (2.41b)$$

2.5.1 Steady state and its stability

The steady state of the motor-driven filament in two dimensions in the absence of noise is characterized by the center of mass velocity $\mathbf{v} = v_{\parallel}\hat{\mathbf{u}} + v_{\perp}\hat{\mathbf{n}}$ and angular velocity $\dot{\vartheta}$. In the absence of any external force or torque, $\dot{\vartheta}$ and v_{\perp} are identically zero, whereas the longitudinal dynamics described by v_{\parallel} is identical to that obtained in one-dimension: the filament will slide along its long axis at a steady longitudinal velocity $v_{\parallel} = F_p/(\Gamma + \Gamma_a)$, with F_p and Γ_a given by Eqs. (2.26) and (2.27), respectively.

To gain some insight into the stability of the system under application of external forces or torques, we expand \mathbf{F}_a and T_a to linear order in velocities \mathbf{v} and $\dot{\vartheta}$ as, $\mathbf{F}_a(\mathbf{v}, \dot{\vartheta}) \simeq \mathbf{F}_p + \left(\frac{\partial \mathbf{F}_a}{\partial v_{\parallel}}\right)_0 v_{\parallel} + \left(\frac{\partial \mathbf{F}_a}{\partial v_{\perp}}\right)_0 v_{\perp} + \left(\frac{\partial \mathbf{F}_a}{\partial \dot{\vartheta}}\right)_0 \dot{\vartheta}$, and $T_a(\mathbf{v}, \dot{\vartheta}) \simeq \left(\frac{\partial T_a}{\partial v_{\parallel}}\right)_0 v_{\parallel} + \left(\frac{\partial T_a}{\partial v_{\perp}}\right)_0 v_{\perp} + \left(\frac{\partial T_a}{\partial \dot{\vartheta}}\right)_0 \dot{\vartheta}$, where $\mathbf{F}_p = \mathbf{F}_{a,0} = F_p\hat{\mathbf{u}}$, is the tangential propulsion force due to the motors. The subscript ‘0’ indicates that the expressions are evaluated at $\mathbf{v} = 0$ and $\dot{\vartheta} = 0$. This leads to steady state force/velocity and torque/velocity relations of the form

$$\left(\underline{\underline{\Gamma}} + \underline{\underline{\Gamma}}_a\right) \cdot \mathbf{v} = \mathbf{F}_{\text{ext}} + F_p\hat{\mathbf{u}}, \quad (2.42a)$$

$$(\Gamma_{\theta} + \Gamma_{\theta a})\dot{\vartheta} = T_{\text{ext}} - g_a v_{\perp}, \quad (2.42b)$$

where we have introduced an active ‘‘momentum’’ g_a given by $g_a = -\left(\frac{\partial T_a}{\partial v_{\perp}}\right)_0$. The active contributions to the longitudinal, transverse and rotational friction coefficients are defined as $\Gamma_{\parallel a} = -\hat{\mathbf{u}} \cdot \left(\frac{\partial \mathbf{F}_a}{\partial v_{\parallel}}\right)_0$, $\Gamma_{\perp a} = -\hat{\mathbf{n}} \cdot \left(\frac{\partial \mathbf{F}_a}{\partial v_{\perp}}\right)_0$, and $\Gamma_{\theta a} = -\left(\frac{\partial T_a}{\partial \dot{\vartheta}}\right)_0$. The longitudinal friction coefficient $\Gamma_{\parallel a}$ is identical to the active friction Γ_a given in Eq. (2.27) for a rod in one dimension, with $\Delta \rightarrow \Delta_{\parallel}$. The transverse and rotational friction coefficients are enhanced by motor activity. Their active components are given by

$$\Gamma_{\perp a} = \frac{kNr\tau_0}{r + (1-r)\tilde{\tau}_0^{-1}} \quad (2.43a)$$

$$\Gamma_{\theta a} = \frac{kNr\tau_0 L^2/12}{r + (1-r)\tilde{\tau}_0^{-1}}. \quad (2.43b)$$

Finally we have, $g_a = \frac{kNr\tau_0 v_0 (\tau_0 + \epsilon |\Delta_{\parallel}^0|)}{r + (1-r)\tilde{\tau}_0^{-1}}$. When the load dependence of the unbinding rate is neglected ($\Lambda = 0$), all friction coefficients are enhanced by motor activity.

When the force/velocity and torque/angular velocity curves are calculated to non-linear order, we find that the only instability is the negative longitudinal friction instability obtained in one dimension. No instabilities are obtained in the angular dynamics. We expect this will change if we include the semiflexibility of the filament [130, 131].

2.5.2 Fluctuations around the steady state

We now examine the dynamics of noise-induced fluctuations about the steady state by letting $\delta\dot{\mathbf{r}} = \dot{\mathbf{r}} - \mathbf{v}$ and $\delta\dot{\theta} = \dot{\theta} - \dot{\vartheta}$ where \mathbf{v} and $\dot{\vartheta}$ are the steady state velocity and angular frequency in the absence of external force and torque. As noted in the previous section when $\mathbf{F}_{\text{ext}} = 0$ and $T_{\text{ext}} = 0$, $v_{\parallel} = v \neq 0$, with v given by the solution of Eq. (2.23), and $v_{\perp} = \dot{\vartheta} = 0$. Projecting velocity fluctuations longitudinal and transverse to the filament, $\delta\dot{\mathbf{r}} = \hat{\mathbf{u}}\delta V_{\parallel} + \hat{\mathbf{n}}\delta V_{\perp}$, the dynamics of fluctuations is described by the coupled equations,

$$[\Gamma_{\parallel} + \Gamma_{\parallel a}(v)] \delta V_{\parallel} = -kN\Delta_{\parallel}(v)\delta p_b(t) + \chi_{\parallel} , \quad (2.44a)$$

$$[\Gamma_{\perp} + \Gamma_{\perp a}(v)] \delta V_{\perp} = \chi_{\perp} , \quad (2.44b)$$

$$[\Gamma_{\theta} + \Gamma_{\theta a}(v)] \delta\dot{\theta} = -kNp_{bs}(v)\tau(v)v_m(v)\delta V_{\perp} + \chi_{\theta} , \quad (2.44c)$$

with

$$[\Gamma_{\theta} + \Gamma_{\theta a}(v)] \delta\dot{p}_b = -\Omega(v)\delta p_b - p_{bs}(v)\frac{\partial}{\partial v} \left[\frac{1}{\tau(v)} \right] \delta V_{\parallel} , \quad (2.45)$$

where the effective frequency $\Omega(v) = \tau^{-1}(v) + \omega_b$ and the longitudinal active friction $\Gamma_{\parallel a}(v)$ are as in one dimension, $\Gamma_{\perp a}(v) = kNp_{bs}(v)\tau(v)$ and $\Gamma_{\theta a}(v) = kNp_{bs}(v)\tau(v)L^2/12$. In all the parameters, $v \equiv v_{\parallel}$ has to be replaced by the steady state solution obtained in one dimension in the absence of external force or torque.

The time-correlation function of orientational fluctuations, $\Delta\theta(t) = \delta\theta(t) - \delta\theta(0)$, can be calculated from Eqs. (2.44b) and (2.44c), with the result

$$\langle \Delta\theta(t)\Delta\theta(t') \rangle = 2D_{\theta a} \min(t, t') . \quad (2.46)$$

The effective rotational diffusion constant is enhanced by the transverse diffusivity and is given by

$$D_{\theta a}(v) = \frac{A_{\theta}}{[\Gamma_{\theta} + \Gamma_{\theta a}(v)]^2} + \frac{A_{\perp}/\ell_p^2(v)}{[\Gamma_{\perp} + \Gamma_{\perp a}(v)]^2} \quad (2.47)$$

with $\ell_p(v) = [\Gamma_{\theta} + \Gamma_{\theta a}(v)]/kNp_{bs}(v)\tau(v)v_m(v)$. Using Eq. (2.46), one immediately obtains the angular time-correlation function as [132],

$$\langle \hat{\mathbf{u}}(t') \cdot \hat{\mathbf{u}}(t'') \rangle = e^{-D_{\theta a}|t'-t''|}. \quad (2.48)$$

The fluctuations in the probability of bound motors are driven by their coupling to the stochastic longitudinal dynamics of the filament. Assuming $\delta p_b(0) = 0$, we obtain

$$\langle \delta p_b(t) \delta p_b(t') \rangle = \left(\frac{\Gamma'_a \omega_0}{v_p} \right)^2 \frac{A_{\parallel}}{\Omega_a} \left[e^{-\Omega_a|t-t'|} - e^{-\Omega_a(t+t')} \right], \quad (2.49)$$

where $\Omega_a(v) = \Omega(v) + \omega_0 \frac{\Gamma'_a(v)}{\Gamma_{\parallel} + \Gamma_{\parallel a}(v)}$, $\Gamma'_a(v) = kNp_{bs}(v)\Delta_{\parallel}(v)\frac{\partial}{\partial v}\left(\frac{1}{\tau}\right)$, and $v_p(v) = \frac{Nk\Delta_{\parallel}(v)}{[\Gamma_{\parallel} + \Gamma_{\parallel a}(v)]}$ is a longitudinal propulsion velocity. Notice that $v_p(v=0) = v_s/p_{bs0}$, with v_s given in Eq. (2.28). Finally, we can compute the correlation function of the fluctuation $\delta \dot{\mathbf{r}}$ of the filament's position. In the laboratory frame the dynamics of $\delta \dot{\mathbf{r}}$ can be recast in the form of a simple equation,

$$\delta \dot{\mathbf{r}} = -v_p \delta p_b(t) \hat{\mathbf{u}} + [\underline{\underline{\Gamma}} + \underline{\underline{\Gamma}}^a(v)]^{-1} \cdot \boldsymbol{\chi} \quad (2.50)$$

Fluctuations in the probability of bound motors do not couple to orientational fluctuations to linear order. It is then straightforward to calculate the correlation function of displacement fluctuations, with the result

$$\begin{aligned} \langle [\delta \mathbf{r}(t) - \delta \mathbf{r}(0)]^2 \rangle &= 2D_{\text{eff}} t + \\ &\frac{D_{\parallel a} \Gamma_a'^2 \omega_0^2 / \Omega_a^2}{(D_{\theta a}^2 - \Omega_a^2)(\Gamma_{\parallel} + \Gamma_{\parallel a})^2} \left[-(D_{\theta a} + \Omega_a) (1 - e^{-2\Omega_a t}) + \frac{4\Omega_a^2}{D_{\theta a} + \Omega_a} (1 - e^{-(\Omega_a + D_{\theta a})t}) \right] \end{aligned} \quad (2.51)$$

where effective longitudinal and transverse diffusion constants have been defined as

$$D_{\parallel a} = A_{\parallel} / [\Gamma_{\parallel} + \Gamma_{\parallel a}(v)]^2, \quad (2.52a)$$

$$D_{\perp a} = A_{\perp} / [\Gamma_{\perp} + \Gamma_{\perp a}(v)]^2. \quad (2.52b)$$

Finally, using $\mathbf{r}(t) = \delta\mathbf{r}(t) + \int_0^t dt' v \hat{\mathbf{u}}(t')$, the mean square displacement (MSD) can be written as,

$$\langle [\mathbf{r}(t) - \mathbf{r}(0)]^2 \rangle = \langle [\delta\mathbf{r}(t) - \delta\mathbf{r}(0)]^2 \rangle + \frac{v^2}{D_{\theta a}} \left[t - \frac{1 - e^{-D_{\theta a} t}}{D_{\theta a}} \right]. \quad (2.53)$$

The MSD is controlled by the interplay of two time scales, the rotational diffusion time, $D_{\theta a}^{-1}$, that is decreased by activity as compared to its bare value, D_{θ}^{-1} , and the time scale Ω_a^{-1} , which is turn controlled by the duration of the motor binding/unbinding cycle. If $D_{\theta a}^{-1} \gg \Omega_a^{-1}$, which is indeed the case for actomyosin systems [†] then on times $t \gg \Omega_a^{-1}$ the MSD is given by

$$\langle [\mathbf{r}(t) - \mathbf{r}(0)]^2 \rangle = 2D_{\text{eff}} t + \frac{v^2}{D_{\theta a}} \left[t - \frac{1 - e^{-D_{\theta a} t}}{D_{\theta a}} \right], \quad (2.54)$$

with

$$D_{\text{eff}} = D_{\parallel a} + D_{\perp a} + \frac{D_{\parallel a} \Omega_a}{D_{\theta a} + \Omega_a} \left(\frac{\Gamma'_a \omega_0}{[\Gamma_{\parallel} + \Gamma_{\parallel a}(v)] \Omega_a} \right)^2. \quad (2.55)$$

In other words the rod performs a persistent random walk consisting of ballistic segments at speed v randomized by rotational diffusion. The behavior is diffusive both at short and long times, albeit with different diffusion constants, D_{eff} and $D_{\text{eff}} + v^2/(2D_{\theta a})$, respectively. This is indeed the dynamics of a self-propelled rod. If the noise strengths B_{\parallel} , B_{\perp} and B_{θ} are negligible, then Eq. (2.54) reduces to

$$\langle [\mathbf{r}(t) - \mathbf{r}(0)]^2 \rangle \simeq \frac{v^2}{D_{\theta a}} \left[t - \frac{1 - e^{-D_{\theta a} t}}{D_{\theta a}} \right]. \quad (2.56)$$

and the MSD exhibits a crossover from ballistic behavior for $t \ll D_{\theta a}^{-1}$ to diffusive at long times.

It is worthwhile to note that if one neglects load dependence of unbinding rate by taking $\Lambda = 0$, effective diffusivity at long time is enhanced with, $D_{\text{eff}}^0 = D_{\parallel a}^0 + D_{\perp a}^0 + (v^0)^2/2D_{\theta a}^0$, due to the interplay between ballistic motion driven by the tethered motors and rotational diffusion, unlike the situation in one dimension.

[†]A naive estimate for actin-myosin systems (neglecting the load dependence of the unbinding rate) gives $\Omega_a^0 \simeq 5 \text{ ms}^{-1}$ and $D_{\theta a}^0 \simeq 0.17 \text{ s}^{-1}$ for $N = 1$.

2.6 Summary and Outlook

We have investigated in this chapter the dynamics of a single cytoskeletal filament modeled as a rigid rod interacting with tethered motor proteins in a motility assay in two dimensions. Motor activity yields both an effective propulsion of the filament along its long axis and a renormalization of all friction coefficients. The longitudinal friction can change sign leading to an instability in the filament's response to external force, as demonstrated by previous authors [10]. The effective propulsion force and filament velocity in the steady state are calculated in terms of microscopic motor and filament parameters.

We also considered the fluctuations of the filament displacement about its steady state value and demonstrated that the coupling to the binding/unbinding dynamics of the the motors yields non-Markovian fluctuations and enhanced diffusion. Future work in this direction should investigate the interplay between stochasticity in motor displacements and semiflexibility of filaments, which is expected to lead to buckling instabilities [133] and anomalous fluctuations [134].

Appendix 2.A Solution of mean-field equation

Here we discuss the solution of the mean-field equation (2.13) for the attachment time τ , For simplicity, we consider the one-dimensional case in detail. The discussion is then easily generalized to two dimensions. The mean-field equation for the residence time τ is rewritten here for clarity:

$$\tau_{MF} = \omega_u^{-1}(\Delta(\tau_{MF})) . \quad (2.57)$$

The solution clearly depends on the form chosen to describe the dependence of the motor unbinding rate on the stretch Δ , in turn given by $\Delta(\tau_{MF}) = (\dot{x} - v_0)/(\tau_{MF}^{-1} + \epsilon\omega_0)$. The mean-field equation must be inverted to determine τ_{MF} as a function of the filament velocity $\dot{x} = v$. For compactness we drop the label 'MF'. It is clear that

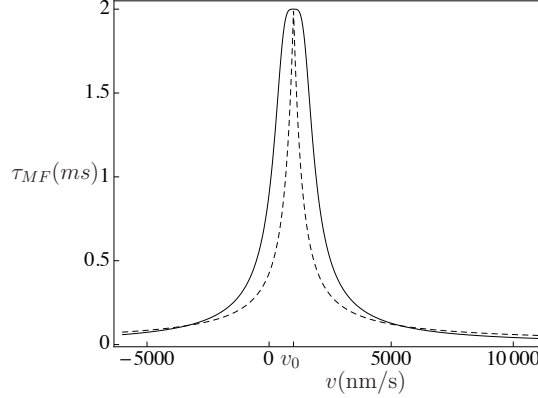


Figure 2.7: Mean field attachment time τ_{MF} as a function of v for parameter values appropriate for acto-myosin systems: $v_0 = 1000 \text{ nm s}^{-1}$, $k = 10 \text{ pN nm}^{-1}$, $f_s = 4 \text{ pN}$, $\alpha^{-1} = 7.5 \text{ nm}$, $\omega_0 = 0.5 \text{ (ms)}^{-1}$, $r = 0.06$, corresponding to $\epsilon = 5$. The dashed line is the numerical solution of Eq. (2.57) obtained using the exponential dependence of the unbinding rate on the stretch. The solid line is obtained using the parabolic ansatz given in Eq. (2.59).

τ has a maximum at $v = v_0$, where $\tau = \omega_0^{-1}$. This simply corresponds to the fact that the time a motor protein spends attached to the actin filament is largest when the motors' tails are unstretched ($\Delta = 0$) and the motors advance at the unloaded motor velocity, v_0 .

It is convenient to use the dimensionless variable and parameters introduced in the text and write the stretch Δ as

$$\Delta = \frac{(u - 1)\ell_0}{\tilde{\omega}_u + 1}, \quad (2.58)$$

where $u = v/v_0$, $\tilde{\omega}_u = \omega_u/\omega_0$ and $\ell_0 = v_0/\omega_0$. A form commonly used in the literature is the exponential form $\omega_u(\Delta) = \omega_0 e^{\alpha|\Delta|}$, with α^{-1} a characteristic length scale. The dimensionless combination $\alpha\Delta$ can then be written in terms of the parameter $\Lambda = \alpha\ell_0/(1+\epsilon)$ and setting $\Lambda = 0$ corresponds to neglecting the load dependence of the unbinding rate. The numerical solution of Eq. (2.57) for the mean attachment time as a function of v is shown as a dashed line in Fig. 2.7 for parameter values appropriate for acto-myosin systems. As expected it has a sharp maximum at $v = v_0$. At large v the attachment time decays logarithmically with velocity. As a result, the

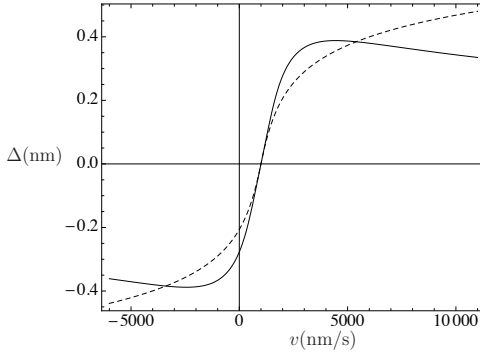


Figure 2.8: Stretch Δ as a function of velocity v obtained using the mean-field value of the attachment time displayed in Fig. 2.7. The parameter values are the same as in Fig. 2.7. The dashed line is obtained using the exponential dependence of the unbinding rate on the stretch. The solid line is obtained using the parabolic ansatz given in Eq. (2.59).

stretch is found to saturate at large velocity, as shown by the dashed curve in Fig. 2.8. This behavior is unphysical as it does not incorporate the fact that when the stretch exceeds a characteristic value of the order f_d/k , the motor head simply detaches, as shown in Fig. 2.2. Instead of incorporating this cutoff by hand, we have chosen to use a simple quadratic form for the dependence of the unbinding rate on the stretch, given by

$$\omega_u(\Delta) = \omega_0 [1 + \alpha^2 \Delta^2] . \quad (2.59)$$

With this form the mean field equation (2.57) can be solved analytically, although the explicit solution is not terribly informative and will not be given here. The resulting attachment time is shown as a solid line in Fig. 2.7. The quadratic form reproduces the sharp maximum of τ at $v = v_0$ and yields $\tau \sim v^{-3/2}$ at large v . The stretch then decays with velocity, as shown in Fig. 2.8.

Chapter 3

Linear Hydrodynamics and Rheology of Cross-linked Motor-Filament Gels

3.1 Active gel approach

In the previous chapter we studied in detail the dynamics of a single cytoskeletal filament interacting with groups of molecular motors. In this chapter we consider the limit when the filaments form a network, cross-linked by specific binding proteins and are driven by molecular motors. As discussed in the introductory chapter, the cytoskeleton is a highly heterogeneous polymer gel, mainly composed of filamentous actin crosslinked by a myriad of globular proteins [135]. These include proteins that preserve the isotropic nature of the network (e.g., filamin), proteins that induce bundle formation (e.g., fascin or villin), and molecular motor proteins, such as kinesins and myosins, that are capable of transforming chemical energy into mechanical work [2]. Motor proteins hydrolyze adenosine-tri-phosphate (ATP) and convert it to adenosine-di-phosphate (ADP) and inorganic phosphate(P). The free energy released from this chemical reaction is used to generate conformational changes of the

motor proteins that yield mechanical forces along cytoskeletal filaments. The dynamics of the resulting polymer network is controlled by active process on a range of time scales, including the polymerization/depolymerization of the polar filaments, the force-generation from crosslinking motor proteins, and the load-dependent dynamics of these active crosslinkers.

Theoretical work has modeled the cytoskeleton via generic continuum hydrodynamics as an *active liquid*, where the effect of activity is incorporated via suitable modification of the hydrodynamic equations of equilibrium liquid crystals [27, 28, 136]. The continuum theory has led to several predictions, including the onset of spontaneous deformation and flow in active films [137, 138], the formation of spiral and aster patterns reminiscent of those observed in in-vitro extracts of cytoskeletal filaments and motor proteins [14, 27, 136, 139–143], and activity-induced thinning and thickening in sheared active suspensions [144–147]. Viscoelasticity has also been incorporated in the continuum theory using the Maxwell model that modifies the response of the liquid by introducing a characteristic time scale controlling the crossover from fluid behavior at long times to elastic behavior at short times [9]. Given, however, that the active liquid viscoelastic model cannot support elastic stresses at long times, its direct relevance for the understanding of the crawling dynamics of the lamellipodium and of active contractions in living cells remains to be established. In addition, the active liquid model is inadequate to describe cross-linked contractile systems, such as stress fibers (cross-linked bundles of actin filaments and myosin minifilaments that play a crucial role in controlling the ability of non-muscle animal cells to generate and resist forces) [148] or muscle sarcomeres that often exhibit spontaneous oscillations [22]. Such oscillations require long-wavelength elastic restoring forces [25, 110] not accounted for in an active (even viscoelastic) liquid. This suggests that the long-wavelength properties of stress fibers or sarcomeres may be better described as those of an active elastic medium or *active solid*. Polarity is generally expected to also play an important role in these systems indicating that a suitable continuum model maybe

that of an active polar elastomer gel.

Passive polymer gels are often classified on the basis of the nature of the crosslinking forces [149]. Chemical gels have strong cross-links bound by covalent bonds. These crosslinks have an essentially infinite lifetime on all experimentally relevant time scales and the gel behaves elastically at long times, with a finite shear modulus. At short times, however, dissipation induced by internal frictional processes can result in “liquid-like” response, with the loss (viscous) component of the elastic moduli exceeding the storage (elastic) component. In physical gels, in contrast, the crosslinks are held together by weaker interactions (e.g., dipolar or ionic) and have finite lifetimes, ranging from minutes to a fraction of a second. This yields a broad spectrum of behavior, from strong physical gels, that are similar to chemical gels, to weak physical gels, with reversible links formed by temporary associations between chains. The latter are liquids at long time and exhibit elasticity on short time scales.

Similarly, active polymer gels also may or may not exhibit low frequency elasticity, depending on the nature of the crosslinkers. Cross-linked reconstituted actin networks exhibit some of the properties of strong physical gels and display large active stiffening driven by molecular motors [19]. It has been showed that elastic networks with contractile forces induced by myosin II motors, described as static force dipoles, can account for both the large scale contractility and stiffening observed in experiments [150–152]. In a recent paper Günther and Kruse [25] also demonstrated that a continuum theory obtained by coarse graining a specific microscopic model of coupled sarcomeres does yield oscillatory states, as observed ubiquitously in these systems, provided the load-dependent on/off dynamics of motor proteins is included in the hydrodynamic model. Motor proteins are also directly involved in controlling mechanical oscillations and instabilities in cilia and flagella [113, 118] and in the mitotic spindle during cell division [111]. In all these cases the elastic nature of the network at low frequency is crucial to provide the restoring forces need to support oscillatory behavior, i.e., these systems are best modeled as active solids, rather than active

liquids.

In this chapter we formulate a generic continuum theory of *isotropic* cross-linked active gels that incorporates the on/off dynamics of crosslinking motor proteins. We model the gel as a two-component system composed of an elastic network coupled frictionally to a permeating fluid. The active forces arising from motor proteins are incorporated phenomenologically through an active contribution to the stress tensor of the elastic network and are controlled by the load-dependent on/off dynamics of the motors. We then proceed to examine the hydrodynamic modes of the active gel and show that a large activity can change the sign of the effective compressional modulus, yielding a contractile instability. Spontaneous oscillations are obtained in the regime of weak activity where the compressional modulus is softened by bound motors, but remains positive. Next, we consider the case of an overdamped gel relevant to muscle fibers and show that it can exhibit propagating waves and oscillatory instabilities as parameters are varied. We describe the macroscopic homogeneous response of the active medium as probed in creep experiments and by macroscopic rheology measurements. The two-component gel model exhibits viscous response on short time scales and elastic response at long times [153] even in the absence of activity, when the time scale controlling the crossover between these two responses is set by the ratio of the viscosity and the compressional modulus of the network. Activity renormalizes the time scale controlling this crossover.

3.2 Hydrodynamic model

We adopt a phenomenological symmetry-based approach to formulate a continuum hydrodynamic description of a cross-linked gel (e.g., a network of actin filaments crosslinked by filamins or other "passive" linkers) under the influence of active forces exerted by clusters of crosslinking motor proteins (e.g., myosin II minifilaments). Hydrodynamics is a systematic method to study the behavior of extended systems

on long times and length scales by focusing on the dynamics of conserved and broken symmetry fields. We consider a three-dimensional isotropic polymer gel of mesh size ξ , viscously coupled to an incompressible permeating Newtonian fluid [153]. This two component model has been used previously to determine viscoelastic response of a filamentous isotropic network in solution [150, 151, 153, 154], and more recently to discuss mechanical response of a coupled network-solvent system when probed by an active agent [155]. At length scales larger than ξ the deformations of the polymer network can be described by isotropic elasticity in terms of a continuum displacement field, $\mathbf{u}(\mathbf{r}, t)$ and an elastic free energy given by

$$F_e = \frac{1}{2} \int_{\mathbf{r}} (\lambda u_{ii}^2 + 2\mu u_{ij}u_{ij}) , \quad (3.1)$$

with λ and μ the usual bulk and shear Lamé coefficients and $u_{ij} = \frac{1}{2}(\partial_i u_j + \partial_j u_i)$ the strain tensor. The permeating viscous fluid is characterized by a velocity field $\mathbf{v}(\mathbf{r}, t)$ and the coupling between the network and the fluid is controlled by a friction per unit volume, Γ . The equation of motion for the displacement field can be written as

$$\rho \ddot{\mathbf{u}} = -\Gamma(\dot{\mathbf{u}} - \mathbf{v}) + \nabla \cdot \boldsymbol{\sigma} , \quad (3.2)$$

where ρ is the mass density of the network and $\boldsymbol{\sigma}$ is the stress tensor of the gel. The permeating fluid is described by the Navier-Stokes equation,

$$\rho_f \dot{\mathbf{v}} - \eta \nabla^2 \mathbf{v} + \nabla P = \Gamma(\dot{\mathbf{u}} - \mathbf{v}) \quad (3.3)$$

where ρ_f is the mass density of the fluid, η the fluid shear viscosity, and P is the pressure. We have assumed a low Reynolds number regime for the fluid and omitted the convective term from the Navier-Stokes equation. It is also assumed that motor proteins do not exert any direct forces on the permeating fluid. As discussed elsewhere [153], the friction Γ between the elastic network and the permeating fluid can be estimated by considering a polymer strand of length ξ moving relative to the background fluid at a velocity $v = \dot{u}$. By equating the viscous force density $\sim \eta v / \xi^2$ on the strand to the viscous friction $\sim \Gamma v$ due to the permeating fluid, one obtains

an estimate of the friction as $\Gamma \sim \eta/\xi^2$. The frictional drag per unit volume Γ is then determined by the force density required to drive a fluid of viscosity η through network pores of characteristic cross section ξ^2 .

The stress tensor of the gel can be written as the sum of elastic, dissipative and active parts,

$$\boldsymbol{\sigma} = \boldsymbol{\sigma}^e + \boldsymbol{\sigma}^d + \boldsymbol{\sigma}^a . \quad (3.4)$$

The elastic contribution is given by $\sigma_{ij}^e = \frac{\delta F}{\delta u_{ij}}$, with

$$\sigma_{ij}^e = \left(\lambda + \frac{2\mu}{3} \right) \delta_{ij} \boldsymbol{\nabla} \cdot \mathbf{u} + 2\mu \left(u_{ij} - \frac{1}{3} \delta_{ij} \boldsymbol{\nabla} \cdot \mathbf{u} \right) . \quad (3.5)$$

The dissipative component $\boldsymbol{\sigma}^d$ is given by

$$\sigma_{ij}^d = \eta_b \delta_{ij} \boldsymbol{\nabla} \cdot \dot{\mathbf{u}} + 2\eta_s \left(\dot{u}_{ij} - \frac{1}{3} \delta_{ij} \boldsymbol{\nabla} \cdot \dot{\mathbf{u}} \right) , \quad (3.6)$$

where η_b and η_s are bulk and shear viscosities arising from internal friction in the gel. Changes in the density ρ of the network are slaved to changes in volume, thus $\delta\rho = -\rho_0 \boldsymbol{\nabla} \cdot \mathbf{u}$, with ρ_0 the mean mass density of the elastic network. In addition, we neglect here for simplicity energy fluctuations and assume that the fluid surrounding the network serves as a heat bath and maintains the temperature constant. This approximation is not adequate to describe real muscle fibers that heat upon contraction.

The active contribution, $\boldsymbol{\sigma}^a$, to the stress tensor arises from the forces exerted by motor proteins bound to the filaments. We assume a total concentration $c = c_b + c_u$ of motor proteins in the gel, with c_b and c_u the concentrations of bound and unbound motors, respectively. In an isotropic network the active contribution to the stress tensor can generically be written as [27],

$$\sigma_{ij}^a = \delta_{ij} \zeta(\rho, c_b) \Delta\mu , \quad (3.7)$$

where $\Delta\mu$ is the change in chemical potential due to the hydrolysis of ATP and $\zeta(\rho, c_b)$ is a scalar function with dimensions of number density describing the stress per unit change in chemical potential due to the action of active crosslinkers.

To complete the hydrodynamic description we need equations describing the dynamics of bound and unbound motors. We assume unbound motors diffuse in the permeating fluid, while bound motors are convected with the polymer network. Their dynamics is controlled by prescribed binding and unbinding rates, k_b and k_u according to first-order reaction kinetics. The resulting equations are

$$\partial_t c_b + \nabla \cdot (c_b \dot{\mathbf{u}}) = -k_u c_b + k_b c_u, \quad (3.8)$$

$$\partial_t c_u = D \nabla^2 c_u + k_u c_b - k_b c_u, \quad (3.9)$$

where D is the diffusion coefficient for free motors. The rates k_b and k_u depend of course on the specific type of motor protein considered. Each motor protein undergoes a conformational transformation during a cycle fueled by a chemical reaction, generally the hydrolysis of ATP [2]. The total cycle duration is determined by the sum of the time τ_{on} that the protein spends attached to the filament, doing its working stroke, and the time τ_{off} that it spends detached from the filament, making its recovery stroke. The binding and unbinding rates are then estimated as $k_u \sim 1/\tau_{\text{on}}$ and $k_b \sim 1/\tau_{\text{off}}$. For individual myosins II, $\tau_{\text{on}} \sim 2$ ms and $\tau_{\text{off}} \sim 40$ ms [2], corresponding to $k_b \ll k_u$. During the working stroke and in the absence of external load, the protein moves along the filament at a speed $v_0 \sim \Delta\mu$. The time $\tau_{\text{on}} \sim 1/v_0 \sim 1/\Delta\mu$ depends on motor activity, while τ_{off} is essentially independent of $\Delta\mu$. For myosin-II this gives $k_u \sim \Delta\mu \gg k_b$.

Finally, we assume that the four-component active gel described by the set of coupled equations (3.2), (3.3), (3.8) and (3.9) is incompressible. This requires

$$\nabla \cdot [(1 - \phi_p) \mathbf{v} + \phi_p \dot{\mathbf{u}}] = 0, \quad (3.10)$$

where ϕ_p denotes the combined volume fraction of the polymer network with bound motors. We assume that the volume fraction of the network is very small, i.e. $\phi_p \ll$

1. In this case Eq. (3.10) reduces to the condition of incompressibility of the ambient fluid, $\nabla \cdot \mathbf{v} \simeq 0$.

In the homogeneous steady state the network and fluid densities have constant values ρ_0 and ρ_f , respectively. The relative concentrations of bound and free motors are controlled by the binding/undinding rates and are given by

$$c_{b0} = \frac{k_b}{k_b + k_u} c_{m0} , \quad (3.11a)$$

$$c_{u0} = \frac{k_u}{k_b + k_u} c_{m0} , \quad (3.11b)$$

with c_{m0} the total steady state concentration of motor proteins. In the following we are mainly interested in non-processive motors like myosins II that are mostly unbound on average, with $c_{b0} \ll c_{u0}$. In this case we neglect the dynamics of free motors that essentially provide a "motor reservoir" and assume that $c_u \sim c_{u0}$ in (3.8). In addition, we expand $\zeta(\rho, c_b)$ to linear order in fluctuations of the network density and motor concentration from their equilibrium values, $\delta\rho = \rho - \rho_0$ and $\delta c_b = c_b - c_{b0}$, as

$$\zeta(\rho, c_b) = \zeta_0 + \zeta_1 \frac{\delta\rho}{\rho_0} + \zeta_2 \frac{\delta c_b}{c_{b0}} . \quad (3.12)$$

The microscopic parameter ζ_0 is related to a stall force, but will not play a role in the following. The parameter ζ_1 arises from spatial variations in the motor density. Both ζ_1 and ζ_2 are expected to be positive for contractile systems.

3.3 Hydrodynamic modes and linear stability analysis

In this section we consider the linear stability of the homogeneous stationary state, with $\mathbf{u} = \mathbf{v} = 0$, $\rho = \rho_0$ and $c_b = c_{b0}$ by examining the hydrodynamic modes of the incompressible gel. The fluid density ρ_f is fixed due to the condition of incompressibility. Using (3.12) for the active parameter ζ , the linearized hydrodynamic

equations are given by

$$\begin{aligned} \rho_0 \ddot{\mathbf{u}} - \mu \nabla^2 \mathbf{u} - (\lambda + \mu - \zeta_1 \Delta \mu) \nabla (\nabla \cdot \mathbf{u}) &= \Gamma (\mathbf{v} - \dot{\mathbf{u}}) \\ + \eta_s \nabla^2 \dot{\mathbf{u}} + \left(\eta_b + \frac{\eta_s}{3} \right) \nabla (\nabla \cdot \dot{\mathbf{u}}) + \zeta_2 \Delta \mu \nabla \phi, \end{aligned} \quad (3.13a)$$

$$\rho_f \dot{\mathbf{v}} - \eta \nabla^2 \mathbf{v} + \nabla P = \Gamma (\dot{\mathbf{u}} - \mathbf{v}), \quad (3.13b)$$

$$\dot{\phi} + \nabla \cdot \dot{\mathbf{u}} = -k_u \phi, \quad (3.13c)$$

with $\phi = \delta c_b / c_{b0}$ and the condition $\nabla \cdot \mathbf{v} = 0$.

We now discuss the hydrodynamic modes of the three-component system described by Eqs. (3.13a-3.13c) obtained by neglecting fluctuations in free motors. We expand the fluctuations $\delta y_\alpha = (\mathbf{u}, \mathbf{v}, \phi)$ in Fourier components according to

$$\delta y_\alpha(\mathbf{r}, t) = \int_{\mathbf{q}} e^{-i\mathbf{q}\cdot\mathbf{r}} \delta \tilde{y}_\alpha(\mathbf{q}, t) \quad (3.14)$$

and look for solutions with time dependence of the form $\delta \tilde{y}_\alpha(\mathbf{q}, t) \sim e^{-i\omega t} \delta \tilde{y}_\alpha(\mathbf{q})$. We also write $\tilde{\mathbf{u}}$ into its components transverse and longitudinal to \mathbf{q} by letting $\tilde{\mathbf{u}} = \hat{\mathbf{q}} u_L + \tilde{\mathbf{u}}_T$, with $\hat{\mathbf{q}} = \mathbf{q}/q$ and $\hat{\mathbf{q}} \cdot \tilde{\mathbf{u}}_T = 0$. Due to incompressibility of the background fluid, $\tilde{\mathbf{v}}$ does not have any longitudinal component, and incompressibility allows us to eliminate the pressure P from (7.9). In Fourier space, dropping for simplicity of notation the tilde on the Fourier components of the fluctuations, the equations for the longitudinal fluctuations are given by

$$[-\rho_0 \omega^2 + (B - \zeta_1 \Delta \mu) q^2 - i\omega(\Gamma + \eta_L q^2)] u_L = -iq \zeta_2 \Delta \mu \phi, \quad (3.15a)$$

$$(-i\omega + k_u) \phi = \omega q u_L, \quad (3.15b)$$

where we have defined the longitudinal modulus of the gel as $B = \lambda + 2\mu$ and a longitudinal viscosity of the network as $\eta_L = \eta_b + (4/3)\eta_s$. The longitudinal part of the displacement couples to motor density, but not to the velocity of the permeating fluid in the incompressible limit considered here. Fluctuations in the longitudinal displacement are slaved to fluctuations in the network density, with $\delta \rho = \rho_0 i q u_L$. The longitudinal equations (3.15a) and (3.15b) can then also be rewritten as coupled

equations for fluctuations in the network and bound motor densities,

$$\left[-\rho_0\omega^2 + (B - \zeta_1\Delta\mu)q^2 - \imath\omega(\Gamma + \eta_Lq^2)\right] \frac{\delta\rho}{\rho_0} = \zeta_2\Delta\mu q^2\phi, \quad (3.16a)$$

$$(-\imath\omega + k_u)\phi = -\imath\omega \frac{\delta\rho}{\rho_0}, \quad (3.16b)$$

Finally, the equations for the transverse components are given by

$$\left[-\rho_0\omega^2 - \imath\omega(\Gamma + \eta_sq^2) + \mu q^2\right] \mathbf{u}_T = \Gamma \mathbf{v}, \quad (3.17)$$

$$(-\imath\omega\rho_f + \Gamma + \eta q^2) \mathbf{v} = -\imath\omega\Gamma \mathbf{u}_T. \quad (3.18)$$

and are decoupled from the equations for the longitudinal modes. We therefore proceed to analyze the two groups separately.

3.3.1 Longitudinal modes

In the incompressible limit considered here, the only role of the permeating fluid is to provide the frictional damping Γ . The longitudinal deformations of the polymer network do, however, couple to fluctuations in the bound motor density. It is instructive to first review the behavior of a passive gel, as obtained by letting $\Delta\mu = 0$ in Eq.(3.15a).

Passive gel.

In the absence of motor proteins, longitudinal fluctuations in an incompressible gel are controlled by a single equation, given by

$$\left\{-\rho_0\omega^2 + Bq^2 - \imath\omega [\Gamma + \eta_Lq^2]\right\} u_L = 0. \quad (3.19)$$

We stress that this equation also describes the behavior of fluctuations in the network density, as $\delta\rho = \imath q\rho_o u_L$. The hydrodynamic modes are the roots of the quadratic polynomial in curly brackets in Eq. (3.19) and are given by

$$\omega = -\frac{\imath}{2\rho_0} \left[\Gamma + \eta_Lq^2 \pm \sqrt{(\Gamma + \eta_Lq^2)^2 - 4\rho_0 Bq^2} \right]. \quad (3.20)$$

The behavior is controlled by the interplay of two length scales, $\xi_d = \sqrt{\eta_L/\Gamma}$, the length scale over which intrinsic viscous dissipation within the network is comparable to dissipation due to friction with the permeating fluid, and $\ell_\Gamma = 2\sqrt{\rho_0 B}/\Gamma$ controlling the ratio of elastic restoring forces in the network to viscous drag from the permeating fluid. At small wavevector ($q \ll \ell_\Gamma^{-1}$) the dispersion relations are always imaginary, corresponding to diffusive modes, and take the form

$$\omega_{L,\Gamma}^0 = -i \left[\frac{\Gamma}{\rho_0} + \left(\frac{\eta_L}{\rho_0} - \frac{B}{\Gamma} \right) q^2 \right] + O(q^4), \quad (3.21)$$

$$\omega_L^0 = -i \frac{B}{\Gamma} q^2 + O(q^4), \quad (3.22)$$

where the superscript 0 is used to denote the passive gel limit. The mode $\omega_{L,\Gamma}^0$ is non-hydrodynamic and describes the relative motion of the polymer network and the permeating fluid. The mode ω_L^0 describes the diffusive relaxation of network density fluctuations. In the two-fluid incompressible gel model considered here there are no propagating longitudinal sound waves [153] and the network density $\delta\rho$ relaxes diffusively, while the solvent density ρ_f remains fixed. The limit $q \ll \ell_\Gamma^{-1}$ holds if $\ell_\Gamma < \xi_d$. On the other hand, when $\ell_\Gamma > \xi_d$, the modes are diffusive as given in Eqs. (3.21) for $q \ll \ell_\Gamma^{-1}$, but there is an intermediate regime of $\ell_\Gamma^{-1} < q < \xi_d^{-1}$ where the gel can support propagating sound-like density waves. Propagating density waves exist if the argument of the square root on the right hand side of Eq. (3.20) is positive, i.e., $4\rho_0 B q^2 > [\Gamma + \eta_L q^2]^2$. It is convenient to scale lengths by ξ_d , with $\tilde{q} = q\xi_d$. The condition for the existence of propagating waves can then be written as

$$B^* \geq \frac{(1 + \epsilon \tilde{q}^2)^2}{4\tilde{q}^2}, \quad (3.23)$$

where $B^* = \frac{B\rho_0}{\Gamma^2 \xi_d^2}$ and $\epsilon = \eta_L/\eta$. The propagating waves are controlled by the interplay of inertia and elasticity and decay on time scales of the order of the relaxation time $\tau_\Gamma = \rho_0/\Gamma$, which is set by the frictional damping from the solvent. The equality sign in Eq. (3.23) defines the critical line shown in Fig. 3.1 separating the region of diffusive density relaxation from the region where the system supports propagating sound-like

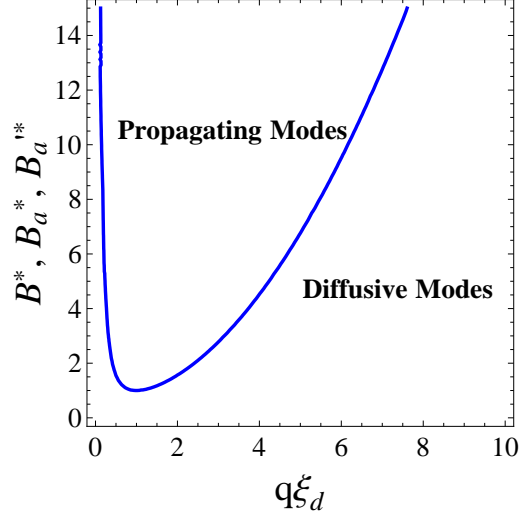


Figure 3.1: The critical line $B^*(\tilde{q})$ given in Eq. (3.23) for $\epsilon = 1$ separating the region of parameters where density fluctuations in a passive incompressible gel relax diffusively, from the region where the system supports propagating density waves. In the chosen dimensionless units, the same line also describes the boundary $B_a^*(\tilde{q})$ obtained for the case $k_u \rightarrow \infty$ and boundary $B_a'^*(\tilde{q})$ obtained for the case $k_u = 0$.

waves. No propagating waves exist for $B < \Gamma^2 \xi_d^2 / \rho_0$, corresponding to the minimum of the curve in Fig. 3.1. We stress that the modes are always diffusive at the longest wavelengths, when $q \rightarrow 0$. These finite wavevector sound-like waves persist down to very small wavevector in the limit of vanishing friction Γ with the surrounding fluid. This is seen by setting $\Gamma = 0$ first, followed by the small wavevector approximation. The dispersion relations then take the form

$$\omega_{\pm}^0 = \pm q \sqrt{\frac{B}{\rho_0} - vq^2 \frac{\eta_L}{2\rho_0}}. \quad (3.24)$$

These are indeed sound waves propagating at the longitudinal sound speed $\sim \sqrt{B/\rho_0}$.

Neglecting bound motor fluctuations ($k_u \rightarrow \infty$).

We now proceed to incorporate the effect of motor proteins. We first consider the case of stationary bound motors. This can be obtained in two ways, either by letting

$k_u \rightarrow \infty$, which corresponds to neglecting bound motor fluctuations, or by letting $k_u = 0$, which corresponds to neglecting the motor on/off dynamics. In both limits motor activity can yield a contractile instability of the system, but no spontaneous oscillations [25].

When $k_u \rightarrow \infty$, then $\phi = 0$ and the concentration of bound motors is constant, $c_b = c_{b0}$. We then obtain a single decoupled equation for fluctuations in the longitudinal displacement (or equivalent, in the network density $\delta\rho$) of the form

$$\{-\rho_0\omega^2 + (B - \zeta_1\Delta\mu)q^2 - i\omega [\Gamma + \eta_L q^2]\} u_L . \quad (3.25)$$

In this limit the only effect of motor activity is a contractile reduction of the compressional modulus, which is given by

$$B_a = B - \zeta_1\Delta\mu . \quad (3.26)$$

The hydrodynamic modes are identical to those described in the previous subsection, with the replacement $B \rightarrow B_a$. If $B_a < 0$ the imaginary part of the mode ω_L^0 changes sign, signaling a contractile instability of the system driven by motor activity. When $B_a > 0$, the modes can be real at finite wavevector, corresponding to propagating waves. The condition for the existence of propagating waves is precisely as given in Eq. (3.23) for the passive gel, with the replacement $B \rightarrow B_a$. A plot of $B_a^* = B_a\rho_0/(\Gamma^2\xi_d^2)$ as a function of \tilde{q} is that identical to that shown in Fig. 3.1 for the passive case. We stress that the existence of these propagating density waves is *not* a consequence of activity. There is in fact a maximum value of activity, given by $\zeta_1\Delta\mu_c = B - \Gamma\xi_d^2/\tau_\Gamma$, and corresponding to the minimum of the curve plotted in Fig. 3.1 above which there are no propagating modes. In addition, since $\ell_\Gamma \sim \sqrt{B_a}$ *decreases* with increasing activity $\Delta\mu$, the range of wavevectors where propagating waves exist for a fixed B_a^* decreases with increasing activity and is given by $\Delta\tilde{q} = 2[B_a^*(B_a^* - 1)]^{1/4}$.

Neglecting bound motor dynamics ($k_u = 0$).

In this case bound motors remain bound at all times and bound motor fluctuations are slaved to network density fluctuations, with $\phi = \delta\rho/\rho_0$. The relaxation of longitudinal fluctuations is described by

$$\{-\rho_0\omega^2 + [B - (\zeta_1 + \zeta_2)\Delta\mu]q^2 - i\omega[\Gamma + \eta_L q^2]\}u_L = 0. \quad (3.27)$$

and the only effect of static bound motors is a further downward renormalization of the elastic modulus, which is now given by

$$B'_a = B - (\zeta_1 + \zeta_2)\Delta\mu. \quad (3.28)$$

The modes are again formally identical to those obtained for the passive gel, but with $B \rightarrow B'_a$. The gel exhibits a contractile instability for $B'_a < 0$ and finite wavevector propagating density waves for $B'_a > 0$. Note that the limit where all motors are bound can be obtained for instance after full hydrolysis of ATP to ADP. Myosin has a high affinity to actin, hence in a pure ADP environment it will act as a “permanent” bound crosslinker [156]. In this case, however, there will also be no reduction of the elastic modulus due to activity, hence no contractile instability. In fact muscles become rigid as ATP runs out, which is one of the causes of *rigor mortis*.

Including bound motors dynamics (finite k_u).

We now incorporate the dynamics of the bound motors and consider the hydrodynamic modes of the the two coupled equations (3.16a) and (3.16b). These yield a cubic eigenvalue equation, given by

$$\begin{aligned} i\rho_0\omega^3 - \omega^2(\Gamma + k_u\rho_0 + \eta_L q^2) - i\omega\left\{k_u(\Gamma + \eta_L q^2) \right. \\ \left. + [B - (\zeta_1 + \zeta_2)\Delta\mu]q^2\right\} + k_u B_a q^2 = 0. \end{aligned} \quad (3.29)$$

The behavior is now controlled by the competition of two time scale, the network relaxation time $\tau_\Gamma = \rho_0/\Gamma$ and the time scale $\tau_{on} = k_u^{-1}$ characterizing the motors

on/off dynamics. Solving perturbatively for small wave numbers q , the three modes are given by

$$\omega_L = -\imath \frac{B_a}{\Gamma} q^2 + O(q^4), \quad (3.30)$$

$$\omega_b = -\imath k_u + \imath q^2 \frac{\zeta_2 \Delta\mu}{\Gamma - k_u \rho_0} + O(q^4), \quad (3.31)$$

$$\omega_{L,\Gamma} = -\imath \frac{\Gamma}{\rho_0} + \imath q^2 \left(\frac{B_a}{\Gamma} - \frac{\zeta_2 \Delta\mu}{\Gamma - k_u \rho_0} - \frac{\eta_L}{\rho_0} \right) + O(q^3) \quad (3.32)$$

The mode ω_L describing the relative mass diffusion of network and solvent in the gel is unchanged at small wavevector. Again, it changes sign when $\Delta\mu > B/\zeta_1$, corresponding to a contractile instability of the gel that occurs when the active stresses exceed the elastic restoring forces from the passive elements of the polymer network. The other two modes are non-hydrodynamic and always stable at long wavelengths. The mode with relaxation rate ω_b describes the decay of fluctuations in the density of bound motors. The mode with relaxation rate $\omega_{L,\Gamma}$ describes the damping of the network due to its motion with respect to the permeating fluid. Even when the on/off dynamics of the bound motors is taken into account, no spontaneous oscillations are generated by motor activity *in the long wavelength limit*. Oscillatory solutions do, however, occur at finite wavevector, as described below. We note that, although the modes always remain stable, the coupling to motor activity can yield a change in sign of the $\mathcal{O}(q^2)$ damping in ω_b and $\omega_{L,\Gamma}$. This effective "negative viscosity" due to motors occurs when the time scale of the motor on/off dynamics is fast compared to the frictional relaxation of the network, i.e., for $\tau_\Gamma > \tau_{on}$. This "negative friction" effect of motors will become important below and was also discussed in Prost et al [10].

As in the passive case, the dispersion relations of the hydrodynamic modes of our model viscoelastic gel depend on the order in which the limits $\Gamma \rightarrow 0$ and $q \rightarrow 0$

are taken. Above we considered the small q limit for fixed Γ . If in contrast we take $\Gamma \rightarrow 0$ first, followed by $q \rightarrow 0$ we obtain propagating modes (for $B_a > 0$). The mode ω_b describing relaxation of bound motor fluctuations is qualitatively unchanged and takes the form

$$\omega_b = -ik_u - iq^2 \frac{\zeta_2 \Delta\mu}{k_u \rho_0} + O(q^4). \quad (3.33)$$

The two modes ω_L and $\omega_{L,\Gamma}$ describing the dynamics of network density fluctuations are replaced by two propagating modes (for $B_a > 0$), with dispersion relation

$$\omega_{L,\pm} = \pm q \sqrt{\frac{B_a}{\rho_0}} + i \frac{q^2}{2\rho_0} \left(\eta_L - \frac{\zeta_2 \Delta\mu}{k_u} \right). \quad (3.34)$$

In contrast to the case of a passive gel or a gel with static bound motors, these oscillatory density waves can now become unstable when the (negative) viscosity induced by the motors overcome the internal viscous dissipation of the network, i.e., for $\zeta_2 \Delta\mu \tau_{on} \geq \eta_L$. Above the critical value of activity defined by the vanishing of the damping in Eq. (3.34), the propagating waves become unstable and the uniform state is presumably replaced by a state that supports spontaneous oscillations.

3.3.2 Transverse modes

The transverse equations (3.17) and (3.18) do not couple to motor dynamics. They yield a cubic eigenvalue equation. There are therefore three transverse modes in the system. Of these two are propagating shear waves, with dispersion relation for small q given by

$$\omega(\mathbf{q}) = \pm q \sqrt{\frac{\mu}{\rho_g}} - \frac{iq^2}{2\rho_g} \left(\eta + \eta_s + \frac{\mu \rho_f^2}{\Gamma \rho_g} \right) + O(q^3), \quad (3.35)$$

with $\rho_g = \rho_0 + \rho_f$ the mass density of the gel. The third transverse mode is a non-hydrodynamic mode with a finite decay rate at $\mathbf{q} = 0$. It describes the relative motion of the polymer network and the permeating fluid. The dispersion relation is given by

$$\omega(\mathbf{q}) = -\frac{i\Gamma\rho_g}{\rho_0\rho_f} - \frac{iq^2}{\rho_g} \left(\frac{\eta\rho_0^2 + \eta_s\rho_f^2}{\rho_0\rho_f} - \frac{\mu\rho_f^2}{\Gamma\rho_g} \right) + O(q^4). \quad (3.36)$$

Transverse fluctuations always decay and to linear order do not destabilize the stationary homogeneous state. Finally, if B and μ are comparable, the speed of propagation of the transverse waves given in Eq. (3.35) is generally much smaller than that of the longitudinal waves given in Eq. (3.24), since $\rho_f \gg \rho_0$.

3.4 Application to muscle sarcomeres

In the overdamped limit of large friction Γ , the inertial term in Eq. (3.13a) is negligible and the relaxational dynamics of the fiber density is controlled by the viscous coupling to the permeating fluid. This is the limit that is relevant to most biological systems, such as muscle sarcomeres. We show here that in this limit the on/off dynamics of bound motor yields an effective inertia that results in spontaneous oscillations even in this overdamped limit.

The approximation of neglecting the inertial terms can be quantified as follows. The inertial term in Eq. (3.13a) can be neglected relative to the frictional damping from the fluid provided $\rho_0\omega^2 \ll \Gamma\omega$ or $\omega \ll \Gamma/\rho_0 \sim \eta/(\xi^2\rho_0)$, which is simply the condition of low Reynolds number for an object of typical size ξ moving in a medium of kinematic viscosity η/ρ_0 at a typical speed $\sim \xi\omega$. A sarcomere of typical rest length $\xi \sim 2.5 \mu\text{m}$ [135], moves in an ambient viscous medium of viscosity $\eta \sim 10 \text{ pNs}/\mu\text{m}$. The mass density ρ_0 of a sarcomere is approximately 10^3 kgm^{-3} [157]. Inertial effects can be neglected if the velocity of a sarcomere unit, typically of order $10 \mu\text{m}/\text{s}$, is small compared to $\eta/\xi\rho_0$. From the known values of sarcomere parameters, as quoted above, $\eta/\xi\rho_0 \sim 10^{-2} \text{ m/s}$, which is three orders of magnitude higher than the typical velocity of a sarcomere. Hence the ignoring of the inertial forces is justified.

A sarcomere chain can be described as a one dimensional elastic system in terms of a displacement field $u(z, t)$, with z the coordinate along the sarcomere's length. In

the overdamped limit the equation for the displacement field and the deviation of the fraction of bound motor from the steady state value are given by

$$(\Gamma - \eta_L \partial_z^2) \partial_t u = B_a \partial_z^2 u + \zeta_2 \Delta \mu \partial_z \phi, \quad (3.37)$$

$$\partial_t \phi = -\partial_z [(1 + \phi) \partial_t u] - k_u \phi. \quad (3.38)$$

We note that in the overdamped limit discussed in this section our model is formally similar to the model introduced by Murray and Oster [158] to describe the role of the mechanochemistry of the cytoskeleton in epithelium movements (albeit with calcium dynamics taking the place of motor dynamics), but with one important difference: here we consider a gel frictionally coupled to a permeating fluid, while Refs. [158, 159] consider a gel elastically coupled to a substrate. As shown below, both models yield oscillations and traveling waves.

When linearized by approximating the convective term on the right hand side of Eq. (4.3) as $\sim -\partial_z \partial_t u$, these equations are identical to those derived by Günther-Kruse [25] from a microscopic model of muscle sarcomeres. Here we show that the same equations can be obtained by a purely phenomenological approach that includes both the dissipation due to the coupling to the permeating fluid and the on/off motor dynamics. We also note that the bound motor fraction can be eliminated from the linearized equations by transforming them into a single differential equation for the displacement. Solving the linearized form of Eq. (4.3) for ϕ with $\phi(z, t = 0) = 0$, substituting in Eq (7.1a) and differentiating with respect to time, we obtain a single differential equation for the displacement $u(z, t)$, albeit second order in time, given by

$$\tau_{on} (\Gamma - \eta_L \partial_z^2) \partial_t^2 u + [\Gamma - \eta_L \partial_z^2 - \eta_a \partial_z^2] \partial_t u = B_a \partial_z^2 u \quad (3.39)$$

where

$$\eta_a = \tau_{on} [B - (\zeta_1 + \zeta_2) \Delta \mu]. \quad (3.40)$$

It is clear from Eq. (3.39) that the effect of motor on/off dynamics is to provide an "inertial" contribution to the dynamics of the network. On length scales large

compared to ξ_d we can neglect the internal dissipation intrinsic to the network proportional to the viscosity η_L compared to the friction Γ with the permeating fluid. Eq. (3.39) then simplifies to

$$\tau_{on}\Gamma\partial_t^2u + [\Gamma - \eta_a\partial_z^2] \partial_tu = B_a\partial_z^2u \quad (3.41)$$

In this limit Eq. (3.41) describing deformations of the active network is formally identically to Eq. (3.19) for the passive gel, with $\tau_{on}\Gamma$ playing the role of a mass density, and a viscosity η_a and an elastic modulus B_a , both renormalized by activity. The effective viscosity and the elastic modulus can change sign at high activities, yielding instabilities.

First we consider the hydrodynamic modes of the systems described by the linearized form of Eqs. (7.1a) and (4.3) or by Eq. (3.39). These are given by the solutions of the eigenvalue equation, given by

$$\omega^2(\Gamma + \eta_Lq^2) + i\omega k_u [\Gamma + (\eta_L + \eta_a)q^2] - k_u B_a q^2 = 0. \quad (3.42)$$

The general solutions of the eigenvalue equation are

$$\omega = \frac{k_u}{2(\Gamma + \eta_Lq^2)} \left\{ -i [\Gamma + (\eta_L + \eta_a)q^2] \pm \sqrt{-[\Gamma + (\eta_L + \eta_a)q^2]^2 + \frac{4B_aq^2}{k_u}(\Gamma + \eta_Lq^2)} \right\} \quad (3.43)$$

For small wavevector ($q \rightarrow 0$) we obtain two modes,

$$\omega_b = -ik_u + i\frac{\zeta_2\Delta\mu}{\Gamma}q^2 \quad (3.44)$$

$$\omega_L = -i\frac{B_a}{\Gamma}q^2 \quad (3.45)$$

describing motor and network density relaxation, respectively. Again, the system exhibit a contractile instability when $B_a < 0$, but there are no oscillatory waves in the long wavelength limit.

Propagating wave solutions exist if the argument of the square root on the right hand side of Eq. (3.43) is positive. The active viscosity can be written as $\eta_a =$

$(B_a - \zeta_2 \Delta\mu)/k_u$, hence it depends on the renormalized elastic modulus B_a . If we choose to treat $\tilde{B}_a = B_a/(\Gamma\xi_d^2 k_u)$ and $\tilde{\zeta}_2 = \zeta_2 \Delta\mu/(\Gamma\xi_d^2 k_u)$ as independent parameters the condition for existence of propagating waves can be written as $\tilde{B}_a^-(\tilde{q}) \leq \tilde{B}_a \leq \tilde{B}_a^+(\tilde{q})$, with

$$\tilde{B}_a^\pm(\tilde{q}) = \frac{1}{\tilde{q}^2} \left[1 + \tilde{q}^2 + \tilde{\zeta}_2 \tilde{q}^2 \pm 2\sqrt{\tilde{q}^2(1 + \tilde{q}^2 + \tilde{\zeta}_2 \tilde{q}^2)} \right], \quad (3.46)$$

where we assumed $\eta_L \sim \Gamma\xi_d^2$. Propagating waves then exist in a band in the (\tilde{B}_a, \tilde{q}) plane, as shown in Fig. 3.2. The width of the band is $\Delta\tilde{B}_a = 4\sqrt{1 + \tilde{\zeta}_2 + 1/\tilde{q}^2}$. It vanishes at small wavevectors and goes to the constant value $4(1 + \tilde{\zeta}_2)^{1/2}$ at large wavevectors. In contrast to the propagating density waves obtained in a damped passive gel, the oscillatory behavior results here from motor activity and the range of parameter where it exists grows with the time τ_{on} that characterizes motor dynamics. Since $\tau_{on} \sim 1/\Delta\mu$ to leading order $\tilde{\zeta}_2$ is independent of activity for small activity. In addition, the propagating waves are unstable when the imaginary part of the eigenvalues given by Eq. (3.43) is positive. This corresponds to

$$\tilde{B}_a \leq \tilde{\zeta}_2 - \frac{1 + \tilde{q}^2}{\tilde{q}^2} \quad (3.47)$$

and defines a region where the overdamped active gel exhibits an oscillatory instability. We expect that when nonlinear terms are included in the equations, the gel will exhibit spontaneous oscillations in this region of parameters. The transition from diffusive to oscillatory behavior is controlled by the interplay between τ_{on} and the characteristic time $\tau_d \sim \xi_d^2 \Gamma/B$ for the diffusive relaxation of a network fluctuation of size ξ_d . If $\tau_{on} \gg \tau_d$ the on/off motor dynamics provides an "inertial drag" to the network that opposes the elastic restoring forces, yielding propagating waves. Alternatively, the result can be understood in terms of two length scales in the problem, ξ_d and $l_b \sim \sqrt{B/(k_u \Gamma)}$. If $\xi_d > l_b$ then density relaxation is always diffusive in the range of wavevectors ($q\xi_d \ll 1$) described by the present theory. If in contrast $l_b > \xi_d$ the network supports propagating density waves in the wavevector range $l_b^{-1} \leq q \leq \xi_d^{-1}$.

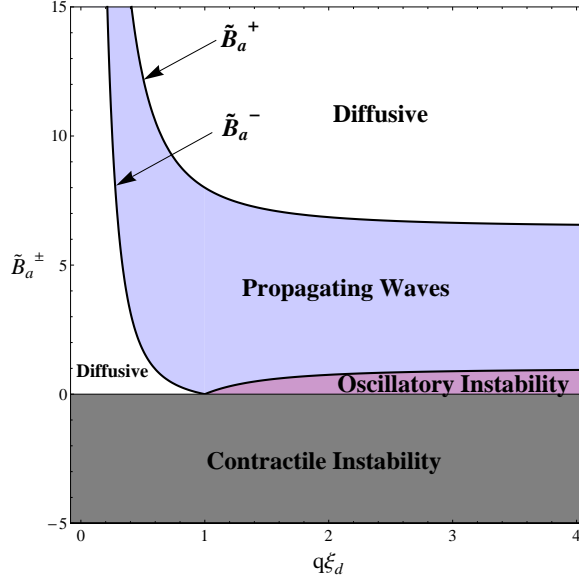


Figure 3.2: A phase diagram for the overdamped active gel. The vertical axis is $\tilde{B}_a = B_a/(\Gamma\xi_d^2k_u)$ and the horizontal axis is $q\xi_d$. The boundaries separating the regions of diffusive relaxation of network density fluctuations from the region where traveling waves exist are given by Eq. (3.46), plotted here for $\tilde{\zeta}_2 = 2$. Below the horizontal line $\tilde{B}_a = 0$, the system exhibits a contractile instability.

3.5 Linear response

3.5.1 Dynamic compressional moduli

In this section we characterize the macroscopic homogeneous viscoelastic response of the active gel in frequency space in terms of the dynamical compressional modulus. To describe a traditional compressional experiment, we consider a slab the three-fluid active gel model with only longitudinal degrees of freedom, held between two plates at $z = 0$ and $z = L$ and unbounded in the other two directions. We imagine applying a harmonic compressive strain at one end, where $u(z = L) = u_0 e^{-i\omega t}$, while holding the other end fixed, i.e., $u(z = 0) = 0$. In general, both the cases of an oscillating boundary that is permeable or impermeable to the permeating fluid are experimentally relevant. To implement a calculation that allow to treat both cases one needs to include a finite compressibility so that the longitudinal elasticity equations

couple to the fluid velocity v . Here we limit ourselves to a permeable boundary and impose no boundary conditions on v . With these boundary conditions we calculate the stress $\sigma(z = L)$ required at the oscillating boundary and define the complex compressional modulus $B_{expt}(\omega)$ measured in experiments as the ratio of the stress to the applied compressional strain, u_0/L . We will see below that at low frequency we recover the complex bulk compressional modulus, $B(\omega) = B - i\omega\eta_L$, obtained assuming an affine compression over the entire sample.

First we analyze for comparison the case of the passive gel with inertia and damping. The elastic response is governed by the equation

$$\rho_0 \partial_t^2 u + \Gamma \partial_t u = B \partial_z^2 u + \eta_L \partial_t \partial_z^2 u. \quad (3.48)$$

We assume a solution of the form $u(z, t) = f(z)e^{-i\omega t}$, where $f(z) = f_i e^{\lambda_i z}$, yielding a characteristic equation for the eigenvalues λ ,

$$\lambda^2 = -\frac{\omega^2 \rho_0 + i\omega\Gamma}{B(\omega)} \quad (3.49)$$

Boundary conditions, $f(0) = 0$ and $f(L) = u_0$ lead to the solution,

$$f(z) = u_0 \frac{\sinh(\lambda z)}{\sinh(\lambda L)} \quad (3.50)$$

The complex dynamic compressional modulus is then given by $B_{expt}(\omega) = \frac{L}{u_0} B(\omega) \left(\frac{df}{dz} \right)_{z=L}$ which gives

$$B_{expt}(\omega) = B(\omega) \lambda L \coth(\lambda L) \quad (3.51)$$

The eigenvalue can be written as

$$\lambda^2 L^2 = -\left[\frac{\omega L}{v_s(\omega)} \right]^2 + i \left[\frac{L}{\delta(\omega)} \right]^2 \quad (3.52)$$

where we have defined the frequency dependent sound speed, $v_s(\omega) = \sqrt{B(\omega)/\rho_0}$, and the penetration depth $\delta(\omega) = \sqrt{B(\omega)/\omega\Gamma}$ which controls the penetration of rarefaction/compression waves of frequency ω [151]. At low frequency, where $|\lambda L| \ll$

1, we recover $B_{expt}(\omega) \rightarrow B(\omega)$, provided $\omega L/v_s(\omega) \ll 1$ and $L \ll \delta(\omega)$. The first condition means that the frequency of applied oscillations is small compared to the frequency of sound wave propagation across the entire sample. When this is not satisfied there is an appreciable time lag between the imposed deformation at one end of the sample and the deformations realized at other material points across the sample, resulting in nonuniform strain and preventing the experimental determination of a macroscopic compressional modulus. The second condition demands that the boundary compressional waves fully penetrated the sample, which is again necessary to achieve a uniform compressional strain. For a similar discussion of shear rheological experiments see Appendix C of Ref. [153]. Finally, the compressional modulus to second order in frequency as measured in a macroscopic experiment is given by

$$B_{expt}(\omega) = B - \omega^2 \rho_0 L^2 / 3 - i\omega(\eta_L + \Gamma L^2 / 3) + O(\omega^3) \quad (3.53)$$

We now turn to the compressional response of an active gel. In this case we ignore the inertial contributions relative to the damping from the permeating fluid and look for solutions of the linearized version of Eqs. (7.1a) and (4.3) of the form $u(z=L) = u_0 e^{-\omega t}$ and $\phi(z,t) = g(z)e^{-\omega t}$, with $f(z) = f_i e^{\lambda_i z}$ and $g(z) = g_i e^{\lambda_i z}$. The eigenvalues are given by

$$\lambda^2 L^2 = -i \left[\frac{L}{\delta_a(\omega)} \right]^2 \left[1 + \frac{i\omega \zeta_2 \Delta\mu / B_a(\omega)}{-i\omega + k_u} \right]^{-1}, \quad (3.54)$$

where $\delta_a(\omega) = \sqrt{B_a(\omega)/\omega\Gamma}$ and $B_a(\omega) = B_a - i\omega\eta_L$. Using, $-i\omega f'(z) = (-i\omega + k_u)g(z)$ and the boundary conditions on $f(z)$ and proceeding as in the passive case, we obtain

$$B_{expt}^a(\omega) = \left[B_a(\omega) + \zeta_2 \Delta\mu \frac{i\omega\tau_{on}}{1 - i\omega\tau_{on}} \right] \lambda L \coth(\lambda L). \quad (3.55)$$

The real and imaginary parts of $B_{expt}^a(\omega) = B'_{expt}(\omega) - iB''_{expt}(\omega)$ representing the storage and loss moduli, respectively, are shown in Fig.(3.3) for generic values of parameters. The storage or elastic modulus has a frequency independent plateau at frequencies lower than the motor's unbinding rate, indicating that the system

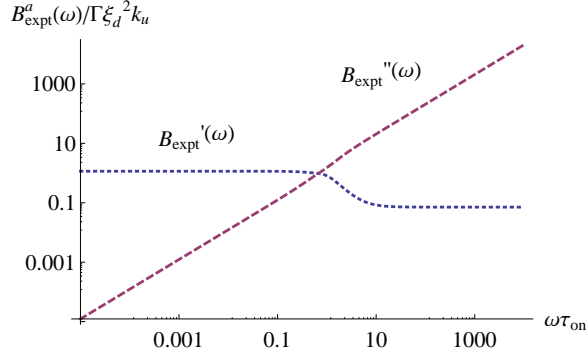


Figure 3.3: Storage ($B'_{expt}(\omega)$) and loss ($B''_{expt}(\omega)$) moduli, for $\tilde{B}_a = 1.15$, $\tilde{\zeta}_2 = 1.1$ and $\xi_d/L = 0.5$.

behaves like an elastic gel in this region. The linear frequency dependence of the loss modulus is the hallmark of a dissipative gel. At low frequency $B'_{expt} > B''_{expt}$ and the system behaves elastically, while at high frequency $B''_{expt} > B'_{expt}$ and the response is dominated by viscous losses. This response is reminiscent of the Kelvin-Voigt model of viscoelasticity. Finally, at low frequency the compressional modulus is given by

$$B_{expt}^a(\omega) = B_a - \omega^2 \tau_{on}^2 \zeta_2 \Delta\mu - i\omega \left(\eta_L + \frac{\Gamma L^2}{3} - \tau_{on} \zeta_2 \Delta\mu \right) + O(\omega^3), \quad (3.56)$$

whereas, at high frequencies since $\lambda \sim \sqrt{\Gamma/\eta_L} = 1/\xi_d$, we obtain

$$B_{expt}^a(\omega) \sim (B_a - \zeta_2 \Delta\mu - i\omega \eta_L) (L/\xi_d) \coth(L/\xi_d). \quad (3.57)$$

3.5.2 Creep

Here we study the macroscopic behavior of our active elastic medium by considering the creep response, i.e., the time evolution of the average strain $\varepsilon(t) = 1/L \int_0^L dz \partial_z u$ in response to a homogeneous external stress, $\sigma(t)$. In particular we are interested in characterizing the load and recovery creep of the material following the sudden application and removal, respectively, of a constant stress. Both responses are measured experimentally in cells [160, 161].

Consider a muscle fiber of length L with free boundary conditions at the ends $z = 0$ and $z = L$, i.e. $\partial_z u(z = 0, L) = 0$, and no fluctuation in motor densities being imposed at the ends. Hence one assumes normal mode expansions for u and ϕ to be of the form $u(z, t) = \sum_{m=0}^{\infty} u_m(t) \cos(\hat{m}z)$, and $\phi(z, t) = \sum_{m=1}^{\infty} \phi_m(t) \sin(\hat{m}z)$, where $\hat{m} = m\pi/L$.

Neglecting nonlinearities, the evolution of the normal modes $u_m(t)$ and $\phi_m(t)$ in the material in response to a small external stress $\sigma(t)$ is governed by the equations

$$(\Gamma + \eta_L \hat{m}^2) \dot{u}_m(t) + B_a \hat{m}^2 u_m(t) - \zeta_2 \Delta \mu \hat{m} \phi_m(t) = f_m(t) , \quad (3.58a)$$

$$\dot{\phi}_m(t) = \hat{m} \dot{u}_m(t) - k_u \phi_m(t) . \quad (3.58b)$$

With, $f_m(t) = \frac{2\sigma(t)}{L^2} \int_0^L dz \sin(\hat{m}z)$.

Eliminating the fluctuations $\phi_m(t)$ in the density of bound motor, we obtain an effective equation for $u_m(t)$, given by

$$\begin{aligned} \tau_{on}(\Gamma + \eta_L \hat{m}^2) \ddot{u}_m(t) + [\hat{m}^2 (\tau_{on}(B_a - \zeta_2 \Delta \mu) + \eta_L) + \Gamma] \dot{u}_m(t) \\ + B_a \hat{m}^2 u_m(t) = \tau_{on} \dot{f}_m + f_m , \end{aligned} \quad (3.59)$$

where $\tau_{on} = k_u^{-1}$. The decay rates of the individual modes are

$$2g(m) = k_u + \frac{B_a - \zeta_2 \Delta \mu}{\eta_L \left(1 + \frac{L^2}{m^2 \xi_d^2 \pi^2}\right)} . \quad (3.60)$$

Eq. (3.60) shows that $g(m)$ is an increasing function of m , hence the higher modes decay at a faster rate. For simplicity we then consider only the first mode, $m = 1$. Thus we approximate the averaged strain developed in the material as $\varepsilon(t) \simeq -2u_1\pi/L$. Also note that neglecting viscous coupling to the fluid Γ amounts to considering the limit of the fastest mode $m \rightarrow \infty$.

In the limit $\tau_{on} \rightarrow 0$, when motors are unbound at all times, Eq. (3.59) reduces to the familiar Kelvin-Voigt viscoelastic equation [162]. In this case the creep following application of a sudden load at $t = 0$, $\sigma(t) = \sigma_0 \Theta(t)$ has the familiar form

$$\varepsilon(t) = \frac{8\sigma_0/\pi}{\eta_L \pi^2 + \Gamma L^2} (1 - e^{-t/(\tau_B + \Gamma L^2/\pi^2 B_a)}) ,$$

where $\tau_B = \eta_L/B_a$ is the Kelvin-Voigt relaxation time.

For finite values of τ_{on} , the creep response is controlled by the interplay of the two times scales τ_B and τ_{on} . We assume $B_a > 0$, corresponding to weak activity. When $B_a < 0$ the system exhibits a contractile instability and the strain becomes arbitrarily large at long times for any applied $\sigma(t)$. The evolution of the strain in response to an applied stress is then controlled by the two eigenvalues of Eq. (3.59) for $m = 1$, given by

$$\lambda_{\pm} = -g \pm \sqrt{g^2 - \frac{\tau_B}{J(L)\tau_{on}}}, \quad (3.61)$$

where time is measured in units of τ_B , and

$$2g = \left(1 - \frac{\zeta_2 \Delta\mu}{B_a} + \frac{\tau_B}{\tau_{on}} + \frac{\Gamma L^2}{\pi^2 B_a \tau_{on}}\right) / J(L),$$

$$J(L) = \left[1 + \left(\frac{L}{\pi \xi_d}\right)^2\right].$$

The linear creep response of the active gel can then be classified as follows:

- I. $g > 0$, $g^2 > \frac{\tau_B}{J(L)\tau_{on}}$: stable monotonic behavior
- II. $g > 0$, $g^2 < \frac{\tau_B}{J(L)\tau_{on}}$: stable oscillatory behavior
- III. $g = 0$: sustained oscillations
- IV. $g < 0$, $g^2 > \frac{\tau_B}{J(L)\tau_{on}}$: unstable oscillatory growth
- V. $g < 0$, $g^2 < \frac{\tau_B}{J(L)\tau_{on}}$: unstable monotonic growth

The behavior is summarized in the phase diagram of Fig. 3.4 displaying the various regions in the (τ_{on}, ζ_2) plane for fixed $J(L)$. We note that when τ_{on}/τ_B is increased for fixed $\zeta_2 \Delta\mu/B_a \geq 1$, the material eventually becomes unstable to stretching. Figures 3.5(a) and 3.5(b) show the time evolution of the strain in response to a step stress of height σ_0 and duration T , $\sigma(t) = \sigma_0 [\Theta(t) - \Theta(t - T)]$, with initial condition $\varepsilon(0) = 0$.

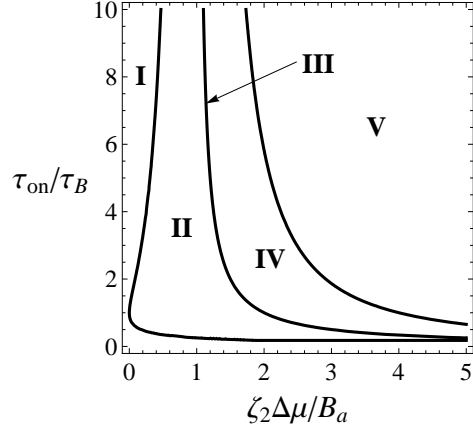


Figure 3.4: A phase diagram displaying the various types of creep response obtained for $B_a > 0$. I) Stable Monotonic Decay, II) Stable Oscillatory, III) Line of Sustained Oscillations, IV) Unstable Oscillatory Growth, V) Unstable Monotonic Growth.

The response in region I of stable monotonic decay is similar to conventional Kelvin-Voigt response. In region II of stable oscillatory decay the interplay of the two time scales τ_{on} and τ_B yields the possibility of a strain overshoot. For finite τ_{on} we also need to specify an additional initial condition determined by the initial distribution of bound motors, since $\dot{\epsilon}(0) = \dot{\phi}(0) - \phi(0)/\tau_{on}$. Fig. 3.5(b) displays the response in region III of sustained oscillations.

3.6 Discussion

We have presented a generic continuum theory of active gels, modeled as a viscoelastic solid with bound motor proteins that induce active stresses in the medium. In the limit where the inertia of the network is neglected and the equations are specialized to one dimension, the model is equivalent to that proposed by Günther and Kruse [25] by coarse-graining of a specific mechanical model of coupled muscle sarcomeres. For large values of the motor activity as measured by the rate of ATP consumption, $\Delta\mu$, the contractile action of bound motors yields a diffusive (contractile) instability of

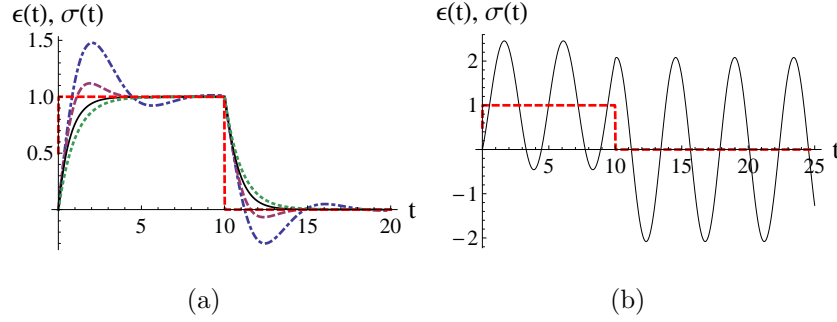


Figure 3.5: Strain $\epsilon(t)$ in response to a step-stress $\sigma(t)$ (dashed line, red online) with $T = 10$. Strain and stress are measured in units of σ_0 and σ_0/B_a , respectively and time is in units of τ_B . The various curves correspond to different values of τ_{on} , spanning the regimes described above. Left frame: $\tau_{on} = 0$ (dotted line, green online), corresponding to a passive gel with Kelvin-Voigt response; $\tau_{on}/\tau_B = 0.2$ (solid line, black online), corresponding to region I of monotonic stable response; $\tau_{on}/\tau_B = 0.5$ (dashed line, purple online), and $\tau_{on}/\tau_B = 1$ (dashed-dotted line, blue online), corresponding to region II of oscillatory stable response. All curves are for $\zeta_2/B_a = 1$. Right frame: $\tau_{on}/\tau_B = 0.5$ and $\zeta_2/B_a = 3$, corresponding to region III of sustained oscillations.

the gel. This result has been obtained earlier in models of muscle sarcomeres [25] and actin bundles [163]. Here we show that it is a generic property of active elastic media. For smaller values of motor activity the interplay of solid elasticity and the binding/unbinding dynamics of the motor proteins yields propagating waves and eventually oscillatory instabilities in the linear theory. Both stable and unstable oscillatory modes are obtained even in the case of an overdamped gel, as relevant to muscle fibers. We show that the finite time scale of motor on/off dynamics yields an effective *inertial* contribution to the dynamics of the elastic medium controlled by the time τ_{on} that motors spend bound to filaments (see Eq. (3.39)). One of the new results of the paper is the phase diagram displayed in Fig. 3.4 for the macroscopic response of the system to external stresses. In the linear model sustained oscillations are only obtained for special parameter values corresponding to a line in the (τ_{on}, ζ_2) phase diagram. It is expected that nonlinearities neglected in the present work will have a stabilizing effect and replace the unstable oscillatory response with stable

self-sustained oscillations. The model considered is relevant for the description of motor-induced spontaneous oscillations in muscle sarcomeres and other active elastic media, and may provide a useful framework for the understanding of lamellipodium crawling.

Our linear elasto-hydrodynamic model can be extended in various ways. First, an analysis of the effect on nonlinearities is needed. Two classes of nonlinear terms are important in our model of an active gel. The first is provided by nonlinear convective terms in the equation describing the dynamics of bound motors, as shown in Eq. (4.3), and also including dependence of the unbinding rate k_u on the elastic strain $\partial_z u$ developed in the gel. These are the simplest continuum manifestation of the highly nonlinear load dependence of the microscopic motor unbinding rate, which in turn plays an important role in controlling the motor-induced negative friction induced by the cooperative action of motor proteins on biological systems elastically coupled to their environment [10, 111, 115]. A second class of nonlinearities arise from higher order terms in the expansion of the active parameter ζ given in Eq. (3.7). A preliminary estimate of the effect of these terms suggest that they stabilize the oscillatory growing modes and yield stable sustained oscillations. A detailed study of the nonlinear active gel model will be presented in Chapter 4.

In the liquid state of an active system the polarity of actin filaments plays an important role. The coupling of polarity and flow has been shown to yield spontaneous flow [137], banded states of inhomogeneous concentration, and oscillatory states [138]. It is similarly expected that the coupling of polarity and elasticity will yield new phenomena in active solids, including spontaneous deformations and oscillations. To incorporate the effect of polarity we have begun to consider the properties of an active polar elastomer, where the orientational order can be induced either by elongated passive crosslinkers [164] or by the myosin minifilaments themselves. In addition, the latter exert active force dipoles on the medium that induce active stresses coupled to the orientational order.

Chapter 4

Emergent Mechanical Phases of Cross-linked Motor-Filament Gels

4.1 Active solids

There is great variation in the organization of actin, myosins, and other cross-linking proteins in the actomyosin structures found in cells. Myofibrils in striated muscle cells are examples of highly organized structures [135], composed of repeated subunits of actin and myosin, known as sarcomeres, arranged in series. Each sarcomere consists of actin filament of alternating polarity bound at their pointed end by large clusters of myosins, known as myosin “thick filaments”. The periodic structure of the myofibril allows it to generate forces on large length scales due to the collective dynamics of individual units of microscopic size, giving rise to muscle oscillation and contraction. More difficult is to understand the origin of spontaneous oscillations and contractility in cytoskeletal filament-motor assemblies that lack such a highly organized structure [23, 165].

In this chapter we consider a nonlinear version of the generic continuum model of an isotropic active solid discussed in Chapter 3. We go beyond the linear stability analysis and show that the presence of nonlinearities leads to both stable contracted

and oscillatory states in different regions of parameters. The acto-myosin network is modeled as an elastic continuum, as appropriate for a cross-linked polymer gel embedded in a permeating viscous fluid, with elastic response at *long times* and liquid-like dissipation at short times. The active solid model describes the various phases of acto-myosin systems as a function of motor activity, including spontaneous contractility and oscillations. It provides a unified description of both phenomena and a minimal model relevant to many biological systems with motor-filament assemblies that behave as solids at low frequencies. When the active solid is isotropic, as assumed in the present work, the coupling to a non-hydrodynamic mode provided by the binding and unbinding kinetics of motor proteins is essential to generate spontaneous sustained oscillations.

The main results are summarized in Fig. 4.1, where we sketch the steady states of the system as we tune the activity, defined as the difference $\Delta\mu$ between the chemical potential of ATP and its hydrolysis products, and the compressional modulus B of the passive gel. For a fixed value of B we find a regime where the active gel supports sustained oscillating states and a contracted steady state as $\Delta\mu$ is increased. For fixed $\Delta\mu$ spontaneous contractility is only observed below a critical network stiffness. This is consistent with experiments on isotropic acto-myosin networks with additional cross-linking α -actinin where spontaneous contractility was seen only in an intermediate range of α -actinin concentration [17]. Our model does not, however, yield a lower bound on B below which the contracted state does not exist. This may be because, in contrast to the experiments where a minimum concentration of α -actinin is required to provide integrity to the network, our system is always by definition an elastic solid, even at the lowest values of B . The phase diagram resulting from our model also resembles the state space diagram of a muscle sarcomere obtained experimentally [166].

Interestingly, we find that a simplified dynamical system obtained by a one-mode approximation to our continuum theory corresponds to the half-sarcomere model pro-

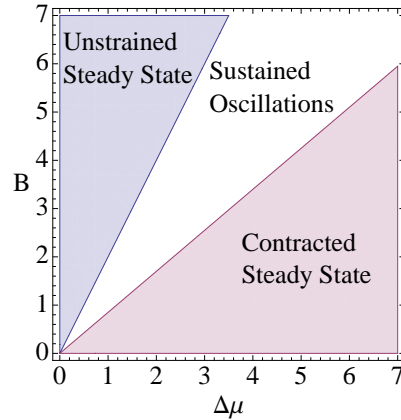


Figure 4.1: Mechanical phases of a cross-linked active gel obtained by varying the gel compressional modulus B and motor activity $\Delta\mu$.

posed recently [25], for a particular set of parameters. Our analysis shows, however, that the phase behavior described above is generic and can be expected in a wide variety of active elastic systems, as it relies solely on symmetry arguments. It provides a unified description of both oscillatory and contracted states and predicts their regions of stability as a function of the elastic properties of the network and motor activity.

4.2 Nonlinear gel model

In the previous chapter, on the basis of symmetry arguments, we formulated a phenomenological hydrodynamic model of a cross-linked gel (a network of actin filaments crosslinked by filamins or other "passive" linkers) under the influence of active forces exerted by clusters of crosslinking motor proteins (e.g., myosin II minifilaments). Only linear terms were retained in the continuum equations, where the linear modes of the system and their stability were analyzed. Here we consider a nonlinear continuum model and show how nonlinearities can stabilize oscillatory and contracted states. The active gel consists of a polymer network in a permeating fluid. On length scales large compared to the network mesh size, the gel can be described as a continuum

elastic medium, viscously coupled to a Newtonian fluid. The model follows closely that formulated for a passive gel [153]. We focus on compressional deformations and consider for simplicity a one-dimensional model. We assume the permeating fluid to be incompressible and consider the case of small volume fraction of the gel. In this limit the permeating fluid simply provides a frictional drag to the polymer network. The hydrodynamic description is then obtained in terms of two conserved fields: the density $\rho(x, t)$ of the gel and the one-dimensional displacement field, $u(x, t)$. The momentum density of the gel is not conserved due to drag exerted by the permeating fluid. In addition, density variations are determined by the local strain, with $\delta\rho = \rho - \rho_0 = -\rho_0\partial_x u$ and ρ_0 the equilibrium mean density. The elastic free energy density of the gel can be expanded in the strain $s = \partial_x u$ about the state $s = 0$. To describe the possibility of swelling and collapse of a gel (even a passive one) one needs to keep terms up to fourth order in s in the elastic free energy density (dropping a linear term that can be eliminated by redefining the ground state) [167, 168]

$$f_e = \frac{B}{2}s^2 + \frac{\alpha}{3}s^3 + \frac{\beta}{4}s^4, \quad (4.1)$$

where B is the longitudinal compressional modulus of the gel and $\alpha, \beta > 0$ are phenomenological parameters capturing the effects of many-body interactions and nonlinear elasticity of the components [16, 169].

It is straightforward to show that within mean-field theory the free energy given in Eq. (4.1) yields a line of first order phase transitions at $B \equiv B_c = 2\alpha^2/(9\beta)$ between an unstrained state with $s = 0$ for $B > B_c$ and a strained state with finite s for $B < B_c$. The stable strained state is one of higher density ($s < 0$) for $\alpha > 0$, corresponding to a contracted state, and one of lower density ($s > 0$) for $\alpha < 0$, corresponding to an expanded state. The transition line terminates at a critical point at $\alpha = 0$.

Activity is induced by the presence of a concentration $c(x, t)$ of bound active cross-linkers that undergo a cyclic binding/unbinding transformation fueled by ATP, exerting forces on the gel. The dynamics of the active gel on time scales larger than

the Kelvin-Voigt viscoelastic relaxation time is described by coupled equations for $u(x, t)$ and $c(x, t)$, given by

$$\Gamma \partial_t u = \partial_x \sigma_e - \partial_x p_a, \quad (4.2)$$

$$\partial_t c = -\partial_x (c \partial_t u) - k(s)(c - c_0) \quad (4.3)$$

where $\sigma_e = \frac{\partial f_e}{\partial s} = Bs + \alpha s^2 + \beta s^3$ is the elastic stress, Γ is a friction constant describing the coupling of the polymer network to the permeating fluid, and $p_a(\rho, c)$ is the active contribution to the pressure, describing the isotropic part of the active stresses induced by myosins. Equation (4.3) allows for convection of bound motors by the gel at speed $\partial_t u$ and incorporates the binding/unbinding dynamics, with $k(s)$ the strain-dependent motor unbinding rate and c_0 the equilibrium concentration of bound motors. Since highly non-processive motor proteins such as myosins are on average largely unbound, we neglect the dynamics of free motors that provide an infinite motor reservoir.

The active pressure is taken to be linear in the rate $\Delta\mu$ of ATP consumption, with $p_a = \Delta\mu \zeta(\rho, c)$. This is a reasonable approximation for weakly active systems, where the number of active elements make up a small fraction of the total mass of the gel, as is the case in most experiments. * We then expand

$$\zeta(\rho, c) \simeq -\zeta_0 - \zeta_1 \delta\tilde{\rho} - \zeta_2 \phi - \zeta_3 (\delta\tilde{\rho})^2 + \zeta_4 \delta\tilde{\rho} \phi + \zeta_5 \phi^2 + \zeta_6 (\delta\tilde{\rho})^3 \dots \quad (4.4)$$

with $\delta\tilde{\rho} = \delta\rho/\rho_0$ and $\phi = (c - c_0)/c_0$ the fluctuations in the gel and bound motor concentrations, respectively, and all parameters ζ_i defined positive. The positive sign of ζ_0 , ζ_1 and ζ_2 corresponds to a contractile acto-myosin system and describes the reduction in the longitudinal stiffness of the gel from contractile forces exerted by motor proteins. The parameters ζ_3 , ζ_4 and ζ_5 describe excluded volume effects. A positive ζ_3 favors contracted over expanded states. A positive ζ_6 guarantees the stability of the network in regions of negative effective compressional modulus.

*We note that the effects of nonlinearities in $\Delta\mu$ can taken account of by expanding in $\delta\mu = \Delta\mu - \Delta\mu_0$ about a stationary state with finite $\Delta\mu_0$.

There are several sources of nonlinearities in Eqs. (4.2,4.3): the nonlinear strain dependence of the elastic free energy, the nonlinear terms in the active pressure, and the dependence of the motor unbinding rate k on the load force on bound motors, which in turn is proportional to the strain s of the elastic gel. We assume an exponential dependence of the form $k(s) = k_0 e^{\epsilon s}$ [127], with k_0 the unbinding rate of unloaded motors and ϵ a dimensionless parameter determined by microscopic properties of the motor-filament interaction. In the following we expand the unbinding rate for small strain as $k(s) \simeq k_0 \left[1 + \epsilon s + \frac{\epsilon^2}{2} s^2 + \mathcal{O}(s^3) \right]$. Keeping higher order terms in ϵ does not change qualitatively the behavior described below. Finally, the first term on the rhs of Eq. (4.3) contains a convective nonlinearity that does not affect the key features of dynamics observed and will be neglected in most of the following. The equations for the active gel can then be written as

$$\Gamma \partial_t u = \partial_x \sigma_e^a + \Delta \mu \partial_x [\zeta_2 \phi + \zeta_4 s \phi - \zeta_5 \phi^2] , \quad (4.5a)$$

$$\partial_t \phi = -\partial_x [(1 + \phi) \partial_t u] - k_0 \left[1 + \epsilon s + \frac{\epsilon^2}{2} s^2 \right] \phi , \quad (4.5b)$$

where $\sigma_e^a = B_a s + \alpha_a s^2 + \beta_a s^3$, with renormalized elastic constants, $B_a = B - \zeta_1 \Delta \mu$, $\alpha_a = \alpha + \zeta_3 \Delta \mu$ and $\beta_a = \beta + \zeta_6 \Delta \mu$.

We render our equations dimensionless by letting $u \rightarrow u/L$ and $t \rightarrow t k_0^{-1}$. We then define dimensionless parameters as $\tilde{B} = \frac{B}{\Gamma k_0 L^2}$, $\tilde{\alpha} = \frac{\alpha}{\Gamma k_0 L^2}$, $\tilde{\beta} = \frac{\beta}{\Gamma k_0 L^2}$, $\Delta \tilde{\mu} = \frac{\Delta \mu}{\Gamma k_0 L^3}$ and $\tilde{\zeta}_i = \zeta_i L$. In the following we drop the tilde to simplify notation and all quantities should be understood as dimensionless.

4.3 Linear stability analysis

There are three steady state solutions of Eqs. (7.1b,4.5b): an unstrained state, with $(u_s, \phi_s) = (0, 0)$, and two strained states, with $(u_s, \phi_s) = (s_{\pm} x, 0)$ and $s_{\pm} = \left(-\alpha_a \pm \sqrt{\alpha_a^2 - 4B_a \beta_a} \right) / 2\beta_a$, provided $B_a < \alpha_a^2 / 4\beta_a$. For concreteness we choose $\alpha_a, \beta_a > 0$. Then if $B_a > 0$, $s_{\pm} < 0$ and $\delta \tilde{\rho}_{\pm} > 0$, so that both strained solutions

correspond to contracted states. If $B_a < 0$, then $s_- < 0$ and $s_+ > 0$, corresponding to contracted and expanded states, respectively.

In this section we examine the linear stability of each of these states. Letting $s = s_0 + \delta s$, where $s_0 = (0, s_\pm)$ represents the constant value of strain in the steady state and $\delta s = \partial_x \delta u$, the linearized equations for the displacement and motor concentration fluctuations are given by

$$\partial_t \delta u = \mathcal{B} \partial_x^2 \delta u + Z \partial_x \phi, \quad (4.6a)$$

$$\partial_t \phi = -\partial_x \partial_t \delta u - \kappa \phi, \quad (4.6b)$$

where

$$\mathcal{B} = B_a + 2\alpha_a s_0 + 3\beta_a s_0^2, \quad (4.7a)$$

$$Z = \Delta\mu(\zeta_2 + \zeta_4 s_0), \quad (4.7b)$$

$$\kappa = 1 + \epsilon s_0 + \epsilon s_0^2/2. \quad (4.7c)$$

Looking for solution of the form $\delta u, \phi \sim e^{zt+iqx}$ we find that the dynamics of fluctuations is controlled by two eigenvalues, with dispersion relations

$$z_{u,\phi}(q) = -\frac{b(q)}{2} \pm \frac{1}{2} \sqrt{[b(q)]^2 - 4\kappa\mathcal{B}q^2} \quad (4.8)$$

where $b(q) = \kappa + (\mathcal{B} - Z)q^2$ and $z_u(q)$ and $z_\phi(q)$ correspond to the root with the plus and minus signs, respectively.

If motor fluctuations are neglected ($\phi = 0$), corresponding to letting $Z = 0$ in Eq. (4.8), one finds $z_u = -\mathcal{B}q^2$ and the linear stability of the steady states is entirely determined by the sign of \mathcal{B} , with $\mathcal{B} > 0$, corresponding to a linearly stable state. When $\phi = 0$ the problem is equivalent to an equilibrium problem, with $q^2\mathcal{B}$ being the curvature of a free energy of the form given in Eq. (4.1), albeit with elastic constants renormalized by activity. In this case the unstrained state $s = 0$ is the global minimum of the free energy for $B_a > 2\alpha_a^2/(9\beta_a)$, while the contracted state $s = s_-$ is the global minimum for $B_a < 2\alpha_a^2/(9\beta_a)$. The line $B_a = 2\alpha_a^2/(9\beta_a)$ defines

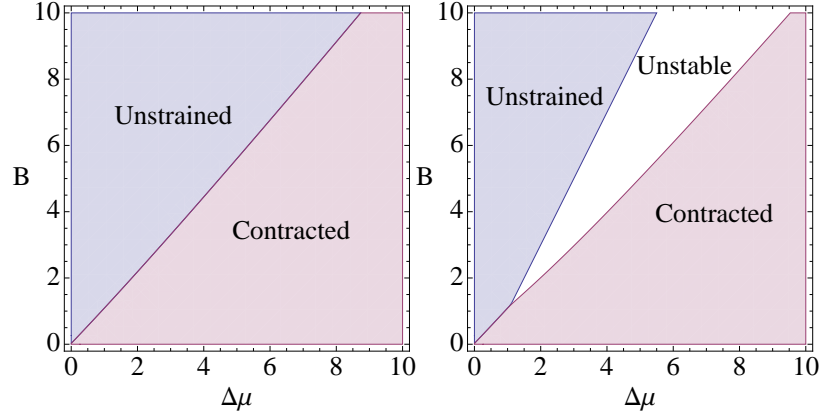


Figure 4.2: Phase diagram obtained by analyzing the linear stability of the modes. The left frame is for $\zeta_2 = \zeta_4 = 0$, corresponding to $\phi = 0$. The right frame is obtained including motor fluctuations, with $\zeta_2 = \zeta$ and $\zeta_4 = \eta\zeta$. The other parameter values are $\alpha = 0.1$, $\beta = 0.1$, $\zeta_1 = \zeta = 1$, $\zeta_3 = \eta\zeta$, and $\zeta_6 = \eta^2\zeta$, with $\eta = 0.1$.

a line of first order phase transitions in the $(B, \Delta\mu)$ (see Fig. 4.2, left frame). If, on the other hand, we consider the problem dynamically, the condition of stability of linear fluctuations given by $\mathcal{B} > 0$ is a necessary, but not a sufficient condition to identify the stable steady states of the system, as multiple fixed points with different basins of attraction coexist in the same region of parameters. In particular, both the unstrained $s = 0$ state and the contracted $s = s_-$ state are linearly stable for $B_a < B < \alpha_a^2/(4\beta_a)$, while both the contracted and expanded states ($s = s_{\mp}$) are stable for $B_a < 0$. If we assume that among these linearly stable states the system dynamically selects the steady state with the fastest decay rate $q^2\mathcal{B}$, then we recover the linear phase diagram of Fig. 4.2 obtained from the equilibrium analysis.

When the coupling to motor concentration fluctuations is included, we find a region of parameters where $\text{Re}[z_{u,\phi}] > 0$ for all three homogeneous solutions $s = (0, s_{\pm})$. This is the white region in Fig. 4.2 (right frame), where the dynamical system is linearly unstable. The instability occurs in a region where the modes are complex, describing oscillatory states, and $Z - \kappa/q^2 > \mathcal{B} > 0$. The linear stability diagram for the system is shown in Fig. 4.2 for the shortest wavevectors $\sim 1/L$, with L the

system size. The phase diagram is constructed again by assuming that the system will relax to linearly stable states characterized by the fastest relaxation rates. To linear order, the coupling to motor fluctuations yields oscillatory or propagating (as opposed to purely diffusive) fluctuations. Some of these oscillatory states are linearly unstable in a region of parameters, as shown in the phase diagram in Fig. 4.2.

Next we consider the effect of nonlinearities by first examining a minimal model that only retains the longest wavelength mode in the Fourier expansion of the nonlinear equations, Eqs. (4.2,4.3), and then comparing the latter to the numerical solution of the full nonlinear partial differential equations.

4.4 One-mode model

We begin by incorporating only the nonlinearities in the unbinding rate, while neglecting convective, elastic and pressure nonlinearities. We impose boundary conditions $[\partial_x u]_{x=0} = [\partial_x u]_{x=L} = 0$ and $[\phi]_{x=0} = [\phi]_{x=L} = 0$, and seek a solution of Eqs. (4.2,4.3) in the form of a Fourier series as, $u(x, t) = \sum_{m=0}^{\infty} u_m(t) \cos(\hat{m}x)$ and $\phi(x, t) = \sum_{m=1}^{\infty} \phi_m(t) \sin(\hat{m}x)$, where, $\hat{m} = m\pi/L$. We perform a 1-mode Galerkin truncation, and only consider the dynamics of the first nontrivial mode, $m = 1$ (setting $u_m = \phi_m = 0, \forall m \neq 1$). This corresponds to approximating the system by only its longest wavelength excitations, ignoring all the shorter wavelength modes.

The coupled equations for u_1 and ϕ_1 are given by

$$\dot{u}_1 = -B_a \pi^2 u_1 + \zeta_2 \Delta \mu \pi \phi_1, \quad (4.9a)$$

$$\dot{\phi}_1 = \pi \dot{u}_1 - \left(1 - \frac{8}{3} \epsilon u_1 + \frac{3}{8} \pi^2 \epsilon^2 u_1^2 \right) \phi_1. \quad (4.9b)$$

These equations can be recast into an effective second order differential equation for u_1 that has the structure of the equation for a Van der Pol oscillator [170] coupled to a nonlinear spring, of the form

$$\ddot{u}_1 + \dot{u}_1 [\lambda - f(u_1)] + u_1 B_a [1 - f(u_1)] = 0, \quad (4.10)$$

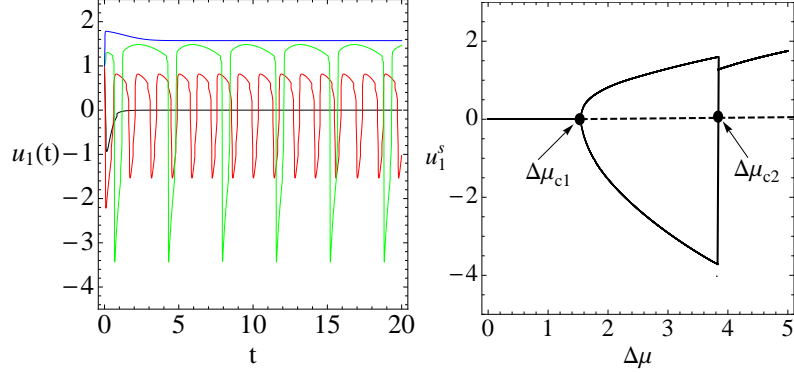


Figure 4.3: Left frame : Time evolution of $u_1(t)$ for various values of activity : $\Delta\mu = 1.0$ (black), corresponding to an unstrained steady state, $\Delta\mu = 2.0$ (red) and $\Delta\mu = 3.5$ (green), corresponding to the region of sustained oscillations and $\Delta\mu = 4.5$ (blue), corresponding to the contracted steady state. Right frame: Bifurcation diagram obtained from the 1-mode model. The figure shows a plot of the value u_1^s of u_1 at long times ($t = 100$) vs $\Delta\mu$. A supercritical Hopf bifurcation occurs at $\Delta\mu = \Delta\mu_{c1} \simeq 1.5$. As one increases $\Delta\mu$ within the range $\Delta\mu_{c1} < \Delta\mu < \Delta\mu_{c2}$, the amplitude of oscillations grows continuously. At $\Delta\mu = \Delta\mu_{c2}$ the limit cycle disappears and the system settles into a contracted steady state for $\Delta\mu > \Delta\mu_{c2}$. The dashed line indicates unstable fixed point. Parameters : $B = 3.0$, $\epsilon = 0.1$. Other parameter values are same as in Fig. 4.2.

with $f(u_1) = \frac{8\epsilon}{3}u_1 - \frac{3\epsilon^2\pi^2}{8}u_1^2$ and friction $\lambda = \pi^2(B_a - \zeta_2\Delta\mu) + 1$. Equations (4.9a) and (4.9b) admit one fixed point $(u_1, \phi) = (0, 0)$. Linear stability analysis about this null fixed point shows that the fixed point is unstable (a repeller) when $\lambda < 0$ and is stable for positive λ . From a global analysis [170] of Eqs. (4.9a) and (4.9b) with the ϵ nonlinearity, we find that the existence of the unstable fixed point signals the appearance a stable limit cycle as λ crosses zero. In other words the system undergoes a supercritical Hopf bifurcation at $\Delta\mu = \Delta\mu_{c1} = (B + \pi^{-2})/(\zeta_1 + \zeta_2)$, with sustained oscillations for $\Delta\mu > \Delta\mu_{c1}$ and stable spirals or nodes in the two-dimensional, (u_1, ϕ_1) phase space, otherwise. We now consider the role of pressure and elastic nonlinearities, while letting $\epsilon = 0$. Within the one-mode model we find that in this case if $\beta_a = \alpha_a = 0$ and $B_a > 0$ there is again only one fixed point at $(u_1, \phi) = (0, 0)$ and the linear stability analysis is identical to that of the model with only rate nonlinearity. In other words, if $\epsilon = 0$, the pressure nonlinearities do not

stabilize the system for $\lambda < 0$. When $\alpha_a \neq 0, \beta_a \neq 0$ and $B_a < 16\alpha_a^2/27\beta_a\pi^2$, we have two new nonzero fixed points $(u_1, \phi) \equiv (u_{\pm}, 0)$, describing a contracted and an expanded state of the gel, respectively, with

$$u_{\pm} = \frac{8\alpha_a}{9\pi^2\beta_a} \pm \frac{2}{3\beta_a\pi^2} \sqrt{\frac{16\alpha_a^2}{9} - 3\pi^2\beta_a B_a}. \quad (4.11)$$

Since $\delta\rho \simeq \pi\rho_0 u_1$, u_+ corresponds to a contracted state whereas u_- corresponds to an expanded state when $B > \zeta\Delta\mu$. The contracted/expanded state is linearly unstable when $\lambda_{\pm}^* = -B_a + \frac{8\alpha_a u_{\pm}}{3} - \frac{9\beta_a\pi^2 u_{\pm}^2}{4} + \zeta_2 - \frac{8\zeta_4 u_{\pm}}{3} - \frac{1}{\pi^2} > 0$. For $\lambda_{\pm}^* < 0$ the nonzero fixed points are unstable if $B_a > 16\alpha_a^2/27\beta_a\pi^2$. When $B_a < 16\alpha_a^2/27\beta_a\pi^2$ and $\lambda_{\pm}^* < 0$ the nonzero fixed points are stable and the orbits in the two-dimensional, (u_1, ϕ_1) phase-space describe nodes or spirals settling at long times to $(u_{\pm}, 0)$. When $\lambda_{\pm}^* > 0$, the contracted/expanded states are linearly unstable. The nonlinearities in the active pressure stabilize these unstable states into stable asymmetric limit cycles. A supercritical Hopf bifurcation occurs when $\Delta\mu > \Delta\mu_{c1} = (B + \pi^{-2})/(\zeta_1 + \zeta_2)$, which terminates to a stable contracted steady state for $\Delta\mu > \Delta\mu_{c2}$ ($\Delta\mu_{c2}$ is determined by the solution of $\lambda_{\pm}^*(B, \Delta\mu) = 0$).

It is instructive to note that when $\alpha_a = \beta_a = 0$, our 1-mode model corresponds to that of a half-sarcomere derived in Ref. [25]. The bifurcation diagram for the complete 1-mode model is shown in Fig. 4.3, with all the nonlinearities incorporated. The diagram summarizes the steady state crossovers of the system as we increase $\Delta\mu$ keeping B fixed. Finally, the steady states of the nonlinear gel within the 1-mode approximation are shown in the phase diagram in Fig. 4.4 (indicated by dashed lines), in the $(B, \Delta\mu)$ plane. The unstrained state of the gel is stable when $\lambda > 0$ whereas the contracted state is stable for $\lambda_+^* > 0$. When $\lambda < 0$ and $\lambda_+^* < 0$ the gel exhibits sustained oscillations.

4.5 Numerical analysis of the continuum nonlinear model

In this section we discuss the numerical solution of the nonlinear PDEs given in Eqs. (7.1b,4.5b) (but with no convective nonlinearities) with boundary conditions $[\partial_x u(t)]_{x=0,L} = 0$ and $[\phi]_{x=0,L} = 0$ and an initial strained state. We spatially discretize the PDEs using finite difference method and then integrate the resulting coupled ODEs using the rkf45 method.

The behavior of the system as we vary B and $\Delta\mu$, keeping all other parameters constants, is summarized in the numerically constructed phase diagram, shown in Fig. 4.4. Assuming $\zeta_1 = \zeta_2 = \zeta$, the system settles into an unstrained state for $B > B_{c1} \simeq 2\zeta\Delta\mu$ and Hopf bifurcates to sustained oscillations for $B < B_{c1}$. We note that the phase boundary in the 1-mode model $B = 2\zeta\Delta\mu - 1/\pi^2$, although different from the numerical phase boundary $B = B_{c1}$, lies within the error bar of the numerics. For $B < B_{c2} \simeq 0.85\zeta\Delta\mu$ the system settles into a stable contracted state. The basin of attraction of the expanded state is much smaller than that of the contracted state. This is due to the choice of the sign of the coupling constants, α_a and ζ_4 . The regimes predicted by our continuum phenomenological model may be used to classify the behavior seen in a number of experimental systems [17, 18, 166]. To estimate the parameter in real systems we assume $\Gamma \sim \eta/\xi^2$, with η the viscosity of the permeating fluid and ξ the gel mesh size [153] and use experimental values of B . For muscle fibers, using $B \sim 2$ kPa [171], $\eta \sim 2 \times 10^{-3}$ Pa s [2], $\xi = 0.5 \mu\text{m}$, $L \sim 100 \mu\text{m}$ and $k_0^{-1} = 40$ ms, we estimate the dimensionless modulus $\tilde{B} = B/\Gamma L^2 k_0$ as $\tilde{B} \sim 1$. For isotropic cross-linked actomyosin gels only direct measurements of the low frequency shear modulus G are available, with $G \sim 1 - 10$ Pa [18]. It has been argued, however, that these networks may support much higher compressional forces, of the order of buckling forces on the scale of the mesh-size, yielding a value of B comparable to that of muscle fibers [172]. For $B \sim 1-10^3$ Pa and η comparable to that

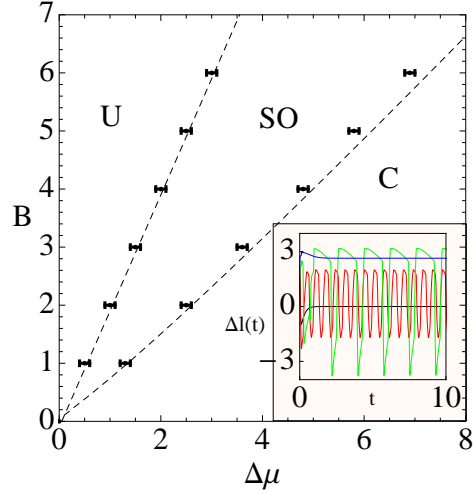


Figure 4.4: Phase diagram in the $(B, \Delta\mu)$ plane for the continuum nonlinear model described by Eqs. (7.1b) and (4.5b). U : Unstrained, SO : Sustained Oscillations, C : Contracted. The points are obtained by numerical solution of the full PDE's; the error bars are determined by the step size used in the $\Delta\mu$ increments. The dashed lines indicate the 1-mode phase boundaries. Inset : Plot of extension $\Delta\ell(t) = u(0, t) - u(L, t)$ for $B = 3.0$ and $\Delta\mu = 1.0$ (black), $\Delta\mu = 2.0$ (red), $\Delta\mu = 3.5$ (green) and $\Delta\mu = 4.5$ (blue). Parameter values are same as in Fig. 4.3.

of water, we obtain $\tilde{B} \sim 10^{-3} - 1$. The active coupling $\zeta\Delta\mu$ can be estimated as [25] $\zeta\Delta\mu \sim \xi n_b k_m \Delta_m$, where n_b is the number density of bound motors, k_m is the stiffness of the myosin filaments and Δ_m is the steady state stretch of the bound motor tails. Using $n_b \sim 10^2 - 10^4 \mu m^{-3}$, $k_m = 4$ pN/nm and $\Delta_m \sim 1$ nm, we obtain $\zeta\Delta\mu \sim 0.1 - 10$ in dimensionless units. In the phase diagram in Fig. 4.4, these parameter values would put muscle fibers in the regions U, SO and C respectively as we increase n_b . Isotropic actomyosin networks may have a much lower value of \tilde{B} , possibly corresponding to the contracted region. Indeed, while spontaneous contractility has been observed in vitro in reconstituted actomyosin networks [17], no experimental evidence has yet been put forward of spontaneous oscillations in these systems.

In summary, we have presented a generic continuum model of a cross-linked active gel which can be used to describe a wide variety of isotropic elastic active systems. We find an elastic active gel system can, in general, be tuned through three classes of

dynamical states by increasing motor activity: an unstrained steady state of homogeneous constant density, a state where the local density exhibits sustained oscillations, and a spontaneously contracted steady state, with a uniform mean density. The continuum model is not strictly hydrodynamic due to presence of the fast variable ϕ , describing the dynamics of motor proteins. The motor binding/unbinding kinetics plays a crucial role in generating oscillating states at finite wavevectors. The one-mode model is in excellent qualitative agreement with the results described by the solutions to the nonlinear continuum equations and is comparable to a variety of one dimensional models for active elastic systems. Quantitative agreement in the phase boundaries between the one-mode model and the continuum model fails due to the non hydrodynamic nature of the model and we expect the oscillatory and/or contractile behaviour to depend on system size [173, 174].

Chapter 5

Rigidity and Geometry Sensing by Adherent Cells on Elastic Substrates

5.1 Mechanosensing

A variety of cellular properties, including cell shape, migration and differentiation, are critically controlled by the strength and nature of the cell's adhesion to a solid substrate and by the substrate's mechanical properties [1]. For instance, it has been demonstrated that cell differentiation is optimized in a narrow range of matrix rigidities [52] and that the stiffness of the substrate can direct lineage specification of human mesenchymal stem cells [41]. In endothelial cells, adhesion to a substrate plays a crucial role in guiding cell migration and controlling a number of physiological processes, including vascular development, wound healing, and tumor spreading [175]. Fibroblasts and endothelial cells seem to generate greater traction forces and develop a broader and flatter morphology on stiff substrates than they do on soft but equally adhesive surfaces [73, 176]. They show an abrupt change in their spread area within a narrow range of substrate stiffnesses. This spreading also coincides with the appear-

ance of stress fibers in the cytoskeleton, corresponding to the onset of a substantial amount of polarization within the cell [73]. Finally, such cells preferentially move from a soft to a hard surface and migrate faster on stiffer substrates [177]. The mechanical interaction of cells with the surrounding matrix is to a great extent controlled by contractile forces generated by interactions between actin cytoskeleton and myosin proteins in the cytoskeleton. Such forces are then transmitted by cells to their surroundings through the action of focal adhesions that produce elastic stresses both in the cell and in the surrounding matrix. Cells in turn are capable of responding to the substrate stiffness by remodeling their own adhesion and elastic properties [1, 178].

In this chapter we present a simple mechanical model of the coupling between cells and substrate that accounts for some of the observed substrate-stiffness dependence of cell properties. The cell itself is modeled as an elastic active gel, adapting recently developed continuum theories of active viscoelastic fluids [27, 136]. In these models the transduction of chemical energy from ATP hydrolysis into mechanical work by myosin motor proteins pulling on actin filaments yields active contractile contributions to the local stresses. As discussed before, the continuum theory of such *active liquids* has led to several predictions, including the onset of spontaneous deformation and flow in active films [137, 138] and the retrograde flow of actin in the lamellipodium of crawling cells [32]. Active liquids cannot, however, support elastic stresses at long times, as required for the understanding of the crawling dynamics of the lamellipodium and of active contractions in living cells. Models of *active elastic solids* on the other hand have been shown to account for the contractility and stiffening of in-vitro actomyosin networks [19, 150, 152] and the spontaneous oscillations of muscle sarcomeres [25]. Very recently a continuum model of a one-dimensional polar, active elastic solid has also been used to describe the alternating polarity patterns observed in stress fibers [179]. In all these cases the elastic nature of the network at low frequency is crucial to provide the restoring forces needed to support deformations and oscillatory behavior.

The role of adhesion geometry in controlling traction force distribution has been addressed theoretically using network models and continuum mechanical models [68, 180]. Network models of the contractile cytoskeleton have also been used to describe the relation between force distribution and shape of adherent cells [180, 181], including networks of Hookean springs as well as cable networks that incorporate the asymmetry of the elastic response of biopolymers such as filamentary actin to compression and extension, with and without the explicit inclusion of contractility. In particular, the active cable network reproduces the arc morphology of cell boundaries pinned by strong local adhesions that has been seen in experiments [72]. The relationship between cell shape and adhesion geometry has also been studied by modeling cells as contractile films bounded by the elastic cortex [70, 71].

We model the adherent cell as an elastic active film anchored to a solid substrate and study the static response of the film to variations in the strength of the anchoring. Although in the following we refer to our system as a cell, we stress that, on different length scales, the active elastic gel could also serve as a model for a cohesive cell monolayer on a substrate. The coupling of the cell to the substrate enters via a boundary condition controlled by a *substrate rigidity parameter* that depends on both the cell/substrate adhesion as well as the matrix stiffness. The description is macroscopic and applies on length scales large compared to the typical mesh size of the actin network in the cell lamellipodium (or large compared to the typical cell size in the case of a cell monolayer).

5.2 Active gel model of an adherent cell

The cell is modeled as an active gel described in terms of a density, $\rho(\mathbf{r}, t)$, and a displacement field, $\mathbf{u}(\mathbf{r}, t)$, characterizing local deformations. In addition, to account for the possibility of cell polarization as may be induced by directed myosin motion and/or filament treadmilling, we introduce a polar orientational order parameter field,

$\mathbf{P}(\mathbf{r}, t)$. Although we are describing a system out of equilibrium, it is convenient to formulate the model in terms of a local free energy density $f = f_{el} + f_P + f_w$, with

$$f_{el} = \frac{B}{2}u_{kk}^2 + \mu\tilde{u}_{ij}^2, \quad (5.1a)$$

$$f_P = \frac{a}{2}|\mathbf{P}|^2 + \frac{b}{4}|\mathbf{P}|^4 + \frac{K}{2}(\partial_i P_j)(\partial_j P_i), \quad (5.1b)$$

$$f_w = \frac{w}{2}(\partial_i P_j + \partial_j P_i)u_{ij} + w'(\nabla \cdot \mathbf{P})u_{kk}, \quad (5.1c)$$

Here f_{el} is the energy of elastic deformations, with B and μ the compressional and shear elastic moduli of the gel, respectively. Alternatively, cellular elastic constants can also be formulated in terms of Young's modulus E and Poisson ratio ν with the relations, $B = E(1 - \nu)/(1 + \nu)(1 - 2\nu)$ and $\mu = E/2(1 + \nu)$. $u_{ij} = \frac{1}{2}(\partial_i u_j + \partial_j u_i)$ represents the symmetrized strain tensor, with $\tilde{u}_{ij} = u_{ij} - \frac{1}{3}\delta_{ij}u_{kk}$ representing the deviatoric strain tensor. The first two terms in Eq. (5.1b), with $b > 0$, allow the onset of a homogeneous polarized state when $a < 0$; the last term is the energy cost for spatially inhomogeneous deformations of the polarization. We have used an isotropic elastic constant approximation, with K a stiffness parameter characterizing the cost of both splay and bend deformations. Finally, the contribution f_w couples strain and polarization and is unique to polar systems [138, 179]. It describes the fact that in the active polar system considered here, like in liquid crystal elastomers, a local strain is always associated with a local gradient in polarization. Such gradients will align or oppose each other depending on the sign of the phenomenological parameters w and w' , which are controlled by microscopic physics. A positive sign indicates that an increase in gel density is accompanied by a positive splay (or enhanced polarization in one dimension). In active actomyosin systems filament polarity can be induced by both myosin motion and actin treadmilling. If the polarization is defined as positive when pointing towards the plus (barbed) end of the filament, i.e., the direction towards which myosin proteins walk, the forces transmitted by myosin procession will yield filament motion in the direction of negative polarization, corresponding to $w < 0$ [142]. In contrast, treadmilling, where polarization occurs at the pointed end,

corresponds to $w > 0$. Density variations $\delta\rho = \rho - \rho_0$ from the equilibrium value, ρ_0 , are slaved to the local strain according to $\delta\rho/\rho_0 = -\nabla \cdot \mathbf{u}$. The stress tensor is written as the sum of reversible and active contributions as $\sigma_{ij} = \sigma_{ij}^r + \sigma_{ij}^a$, where $\sigma_{ij}^r = \frac{\partial f}{\partial u_{ij}}$. The two contributions are given by

$$\sigma_{ij}^r = \delta_{ij} B u_{kk} + 2\mu \tilde{u}_{ij} + \frac{w}{2} (\partial_i P_j + \partial_j P_i) + w' \nabla \cdot \mathbf{P} , \quad (5.2a)$$

$$\sigma_{ij}^a = \sigma_a \delta_{ij} + \alpha P_i P_j . \quad (5.2b)$$

Active stresses arise because the gel is driven out of equilibrium by continuous input of energy from the hydrolysis of ATP, characterized by the chemical potential difference $\Delta\mu$ between ATP and its products. For simplicity, we assume here $\Delta\mu$ to be constant, although situations where inhomogeneities in $\Delta\mu$ may arise, for instance, from inhomogeneous myosin distribution within the actin lamellipodium are also of interest. The experimentally observed contractile effect of myosin corresponds to positive values of the coefficients σ_a and α , that characterize the isotropic and anisotropic stress per unit $\Delta\mu$, respectively, due to the action of active myosin crosslinkers [26, 27, 144]. In polar gels there are also active stresses proportional to $(\partial_i P_j + \partial_j P_i)$ [138, 182]. We neglect these terms here as terms of similar structure already arise from the coupling terms in f_w . Finally, we note that the parameters a , w and w' may also in general depend on $\Delta\mu$ as cell polarity is induced by ATP-driven processes. For simplicity we keep these parameters fixed below.

In mechanical equilibrium, the condition of local force-balance translates to

$$\partial_\beta \sigma_{\alpha\beta} = 0 ,$$

where the greek indices take values x, y and z . For a thin cellular film we average the cellular force-balance equation over the cell thickness h . In-plane force balance is given by

$$\partial_j \sigma_{ij} + \partial_z \sigma_{iz} = 0 , \quad (5.3)$$

with i, j denoting in-plane coordinates. We assume that the top surface of the cell is stress free, $\sigma_{iz}(\mathbf{r}_\perp, z = h) = 0$, whereas at the cell-substrate interface $z = 0$, the cell experiences lateral traction stresses given by $\sigma_{iz}(\mathbf{r}_\perp, z = 0) = Y u_i(\mathbf{r}_\perp, z = 0)$. Here, Y denotes the substrate rigidity parameter, representing the cell-substrate anchoring strength, and $\mathbf{u}(\mathbf{r}_\perp, z)$ is the in-plane deformation field of the cellular medium. The thickness-averaged force balance equation then reads,

$$h \partial_j \bar{\sigma}_{ij} = Y u_i, \quad (5.4)$$

where $\bar{\sigma}_{ij}(\mathbf{r}_\perp) = \int_0^h (dz/h) \sigma_{ij}(\mathbf{r}_\perp, z)$. It is worthwhile to mention that the assumption of in-plane traction forces is a good approximation for fully spread stationary cells making almost zero contact angle with the substrate. During the early stages of spreading and migration, cells can exert appreciable out-of-plane traction forces via rotation of focal adhesions [49]. In the following we will drop the overbar indicating the average and refer to thickness averaged quantities throughout. The quantity $T_i = Y u_i$ is a stress in three dimensions, i.e., a force per unit area. It describes the in-plane traction force per unit area that the cell exerts on the substrate. The assumption of local elastic interactions with the substrate strictly holds on elastic substrates that are much thinner than the lateral size of the cell or on micropillar substrates. The substrate rigidity parameter Y depends on the stiffness of the underlying substrate as well as on the density ρ_f and stiffness k_f of focal adhesions. For an elastic substrate of shear modulus μ_s and thickness h_s , Y takes the simple form, $Y^{-1} = \frac{1}{k_f \rho_f} + \frac{1}{\mu_s / h_s}$. A detailed calculation of the rigidity parameter Y in various limits is provided in Chapter 7. Anisotropic substrates are not considered here, but can be described by a generalized boundary condition where Y is a tensor quantity. Finally, variations in the polarization are described by the equation

$$\partial_t \mathbf{P} + \beta (\mathbf{P} \cdot \nabla) \mathbf{P} = \Gamma \mathbf{h}, \quad (5.5)$$

with β an advective coupling arising from ATP driven processes, such as treadmilling [138, 182], Γ an inverse friction, and $\mathbf{h} = -\frac{\delta f}{\delta \mathbf{P}}$ the molecular field, given

by

$$h_i = - (a + b|\mathbf{P}|^2) P_i + K\nabla^2 P_i + w\partial_j u_{ij} + w'\partial_i u_{kk} . \quad (5.6)$$

Here β is an active velocity and is controlled by actomyosin activity.

Equations (5.4), (5.2a), (5.2b) and (5.5), subject to the boundary condition $\sigma_{ij}n_j|_{\Omega} = 0$, with Ω the cell boundary and \mathbf{n} the outward unit normal on Ω , completely describe the equilibrium of an adherent cell. As a consequence of the stress-free boundary condition, the net traction force transmitted by the cell to the substrate vanishes, i.e., $\int_A d^2\mathbf{r} Y u_i = \oint_{\Omega} ds \sigma_{ij}n_j = 0$. It is instructive to consider two limiting cases for the anchoring strength Y . First, when the cell is rigidly anchored onto the substrate, corresponding to $Y \rightarrow \infty$, we find $\mathbf{u} = 0$, defining the reference state for elastic deformations. In our model the reference cell shape is then dictated by the geometry of the adhesion patch, which can be controlled in experiments by micropatterning substrates by adhesion proteins. In contrast, when $Y \rightarrow 0$, the cell does not adhere to the substrate and the equilibrium state is uniformly contracted state, with a density enhancement $\delta\rho = -\nabla \cdot \mathbf{u} = \sigma_a(1 + \nu)(1 - 2\nu)/E(1 - \nu)$.

5.3 Adherent cell in one dimension

5.3.1 Isotropic cell

We begin by considering the case of an isotropic cell and neglect the coupling to polarization. For simplicity, we consider a quasi-one-dimensional model where the cell is a thin sheet of active gel of thickness z extending from $x = 0$ to $x = L$, with $L \gg h$. The substrate is flat and located at $z = 0$. Although this is of course a gross simplification, we will see below that it captures the substrate-induced stresses and deformations and their dependence on substrate stiffness, as observed in experiments.

In this 1D situation cellular constitutive relation and force balance is given by :

$$\sigma(x) = B\partial_x u + \sigma_a \quad (5.7a)$$

$$h\partial_x \sigma = Y u \quad (5.7b)$$

Combining then the expression for the internal stress, σ with the force-balance condition we obtain

$$\sigma = \ell_p^2 \frac{d^2 \sigma}{dx^2} + \sigma_a, \quad (5.8)$$

where $\ell_p = \sqrt{Bh/Y}$ is a length scale controlled by the ratio of cell and substrate stiffness, describing the length upto which traction forces penetrate inside the cell. The solution of this equation with boundary conditions $\sigma(x=0) = \sigma(x=L) = 0$ is given by :

$$\sigma(x) = \sigma_a \left(1 - \frac{\cosh [(L-2x)/2\ell_p]}{\cosh (L/2\ell_p)} \right). \quad (5.9)$$

The deformation field (proportional to traction stress) is then given by

$$u(x) = \frac{\sigma_a \ell_p}{B} \frac{\sinh [(L-2x)/2\ell_p]}{\cosh (L/2\ell_p)}. \quad (5.10)$$

A finite activity $\sigma_a \neq 0$ generates stresses and deformations in the cell, as shown in the left frame of Fig. 5.1. In an isotropic gel, both the stress and the displacement profiles are symmetric about the cell's mid point and the cell is uniformly contracted. The deformation is localized near the cell's boundaries. From the plots, it is clear that the length scale ℓ_p determined by the ratio of cell to substrate stiffness controls the penetration of the deformation to the interior of the cell. If $\ell_p \sim L$, corresponding to a substrate rigidity $Y \sim Bh/L^2$, the active stresses and deformation extend over the entire cell. For an isolated cell of length $10 \mu m$, thickness $0.1 \mu m$ and elastic modulus $B \sim 10 \text{ kPa}$, the substrate rigidity parameter Y can be estimated to be $\sim 10 \text{ Pa}/\mu m$. The total deformation $\Delta \ell = u(0) - u(L)$ grows with activity and is shown in Fig. 5.1 (middle frame) as a function of $\ell_p/L \sim 1/\sqrt{Y}$. The contraction

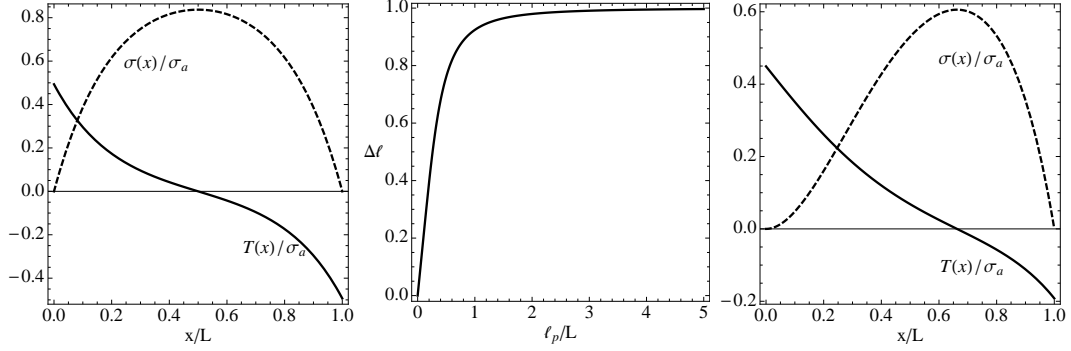


Figure 5.1: Left: stress $\sigma(x)/\sigma_a$ (dashed line) and traction stress $T(x) = Yu(x)/\sigma_a$ (solid line) profiles as functions of the position x inside a cell of length L . Middle: the cell's total deformation $\Delta\ell = u(0) - u(L)$ as a function of ℓ_p/L . In the plot the net contraction $\Delta\ell$ is normalized by its maximum value $\sigma_a L/B$. Right: The stress $\sigma(x)/\sigma_a$ (dashed line) and traction stress $T(x)/\sigma_a$ (solid line) profiles of a cell on a substrate a constant stiffness gradient, described by $Y(x) = Y_0 x/L$ are shown as functions of the position x inside the cell. The profiles are asymmetric and the stress is localized near $x = L$ where the stiffness is largest. Parameters : $\ell_p/L = 0.25$

decreases with increasing substrate stiffness and saturates to a finite value for soft substrates.

It is also interesting to consider a substrate of varying stiffness, as such substrates can be realized in experiments [1]. We consider a constant stiffness gradient, corresponding to $Y(x) = Y_0 x/L$. In this case Eq. (5.8) becomes

$$\sigma = \frac{\ell_p^2 L}{x} \left(\frac{d^2 \sigma}{dx^2} - \frac{1}{x} \frac{d\sigma}{dx} \right) + \sigma_a \quad (5.11)$$

A closed solution can be obtained in terms of hypergeometric functions. The corresponding stress and displacement profiles are now asymmetric and are shown in Fig. 5.1 (rightmost frame). The stress is largest in the region of stiffest substrate, with a correspondingly smaller cell deformation. In other words, the largest cell deformation is obtained in the boundary region where the substrate is softest. In real cells the region where the substrate is softer and the resulting stresses in the cell are smaller may correspond to region of reduced focal adhesions. Hence the gradient stiffness may yield a gradient in the strength of cell-substrate adhesion, providing a

possible driving force for durotaxis, the tendency of cells to move from softer to stiffer regions [176, 183].

5.3.2 Polarized Cell

We now consider the case of a polarized cell, described by the full free energy f . The cell is modeled again as a thin film of length L in the quasi-1d geometry described earlier. We are interested in steady state configurations. In the chosen geometry these are given by the solutions of the equations

$$h \frac{d\sigma}{dx} = Y u \quad (5.12a)$$

$$\sigma = B \frac{du}{dx} + \sigma_a + \alpha p^2 + 2w \frac{dp}{dx} \quad (5.12b)$$

$$\beta' L p \frac{dp}{dx} = K \frac{d^2 p}{dx^2} + 2w \frac{d^2 u}{dx^2} - (a + b p^2) p \quad (5.12c)$$

where $\mathbf{P} = p(x)\hat{\mathbf{x}}$ and we have let $w' = w$ and $\beta/(L\Gamma) = \beta'$. In the following we scale lengths with the cell's length L and stresses with the cell's compressional modulus B . By combining Eqs. (5.12a)-(5.12c), we can eliminate u and rewrite them as coupled equations for $\tilde{\sigma} = \sigma/B$ and p as

$$\tilde{\sigma} = \frac{\ell^2}{L^2} \tilde{\sigma}'' + \zeta_0 + \zeta_\alpha p^2 + \tilde{w} p' \quad (5.13a)$$

$$(\zeta_\beta + 2\zeta_\alpha \tilde{w}) p p' = \tilde{K} p'' + \tilde{w} \tilde{\sigma}' - (\tilde{a} + \tilde{b} p^2) p \quad (5.13b)$$

where the prime denotes a derivative with respect to x/L , $\zeta_0 = \sigma_a/B$, $\zeta_\alpha = \alpha/B$ and $\zeta_\beta = \beta'/B$, $\tilde{w} = 2w/BL$, $\tilde{a} = a/B$, $\tilde{b} = b/B$, and $\tilde{K} = K/(BL^2) - \tilde{w}$. Thermodynamic stability requires $\tilde{K} > 0$. As discussed in Ref. [179] there could be possible active contributions to the coupling w , which at high activity leads to an alternating polarity pattern in the gel. Here we restrict ourselves to $\tilde{K} > 0$.

In the absence of contractility ($\zeta_{0,\alpha,\beta} = 0$) Eqs. (5.13a) and (5.13b) have two homogeneous solutions that satisfy the boundary condition $\sigma(0) = \sigma(L) = 0$, corresponding to an isotropic state for $a > 0$, with $p(x) = u(x) = 0$ and to a polarized state for $a < 0$, with $p(x) = p_0 = \sqrt{-a/b}$ and $u(x) = 0$. In both cases $\sigma(x) = 0$.

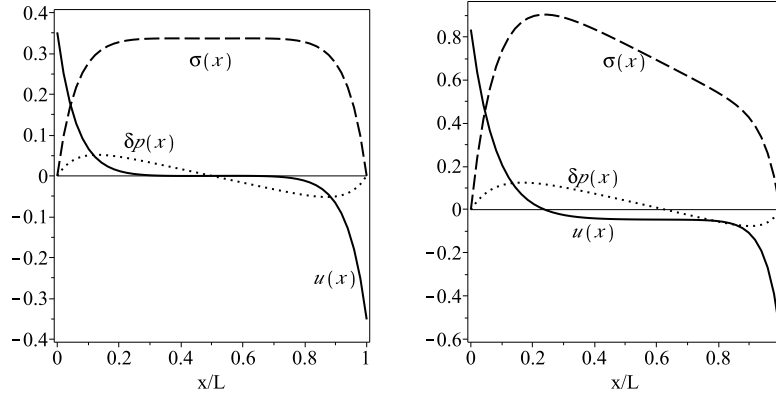


Figure 5.2: Stress $\sigma(x)/B$ (dashed line), deformation field $u(x)/L$ (solid line), and polarization $\delta p(x) = p(x) - p_0$ (dotted line) profiles obtained by numerical solution of Eqs. (5.13a) and (5.13b) for two sets of boundary conditions on the polarization: $p(0) = p(L) = 0$ (left frame) and $p(0) = p(L) = p_0$ (right frame). Both plots are for $\ell_p/L = 0.25$, $\tilde{w} = 4$, $\zeta_0 = \zeta_\alpha = \zeta_\beta = 1$, $\tilde{a} = \tilde{b} = 1$, $\tilde{K} = 1$.

For finite contractility ($\zeta_{0,\alpha,\beta} \neq 0$), we find two qualitatively different solutions, depending on the boundary conditions used for the polarization. When Eqs. (5.13a) and (5.13b) are solved with boundary condition $p(0) = p(L) = 0$, consistent with an isotropic state in the limit $\zeta_{0,\alpha,\beta} = 0$, the stress is an even function of x , as shown in the left frame of Fig. 5.2. It exhibits a maximum at $x = L/2$ and is symmetric about the mid point of the cell. Both the displacement and the polarization vanish at $x = L/2$ and are odd functions of x about this point. For $a < 0$ we solve the nonlinear equations with boundary condition $p(0) = p(L) = \sqrt{-a/b}$, consistent with a polarized state in the limit $\zeta_{0,\alpha,\beta} = 0$. In this case the stress, deformation and polarization profiles are all asymmetric, as shown in the right frame of Fig. 5.2. The sign of the anisotropy is controlled by the sign of the polar coupling w . The figure displays the case $w > 0$, corresponding to filament convection towards the direction of positive polarization.

To quantify the distinct properties of these two states, we define an excess mean polarization averaged over the cell as $\langle \delta p \rangle = \int_0^L \frac{dx}{L} [p(x) - p_0]$. The excess polarization $\langle \delta p \rangle$ is zero for the symmetric polarization profiles obtained with the bound-

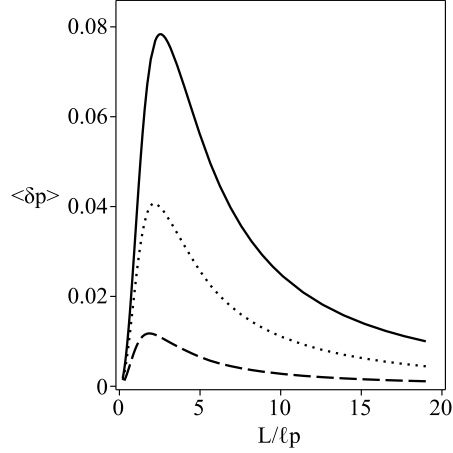


Figure 5.3: Excess mean polarization $\langle \delta p \rangle$ as a function of $L/\ell_p \sim \sqrt{Y}$ obtained from averaging the numerical solutions of Eqs. (5.13a) and (5.13b) for three different values of contractility $\zeta = \zeta_0 = \zeta_\alpha = \zeta_\beta$: $\zeta = 0.5$ (dashed line), $\zeta = 1.0$ (dotted line) and $\zeta = 1.5$ (solid line). The plots are for $\tilde{w} = 4$, $\tilde{a} = \tilde{b} = 1$ and $\tilde{K} = 1$.

any condition $p(0) = p(L) = 0$, whereas $\langle \delta p \rangle$ obtained for the boundary condition $p(0) = p(L) = \sqrt{-a/b}$ is a non-monotonic function of substrate stiffness, as shown in Fig. 5.3 for three different *values* of contractility. The excess polarization is largest at a characteristic substrate stiffness, comparable to the stiffness of the cell, suggesting that enhancement of stress fiber and resulting cell polarization may be obtained for an optimal substrate rigidity, as reported in Ref. [66]. The excess polarization $\langle \delta p \rangle$ vanishes in the absence of contractile activity and its maximum value increases with contractility.

5.4 Planar adherent cell

In this section, we investigate force distribution in planar adherent cells and study the role of extracellular geometry in controlling cell-matrix traction forces. For simplicity, we ignore any feedback of elastic stresses with polarization, and drop the role of \mathbf{P} altogether. This is the limit when polarization relaxes at a time scale faster than internal elastic stress relaxation.

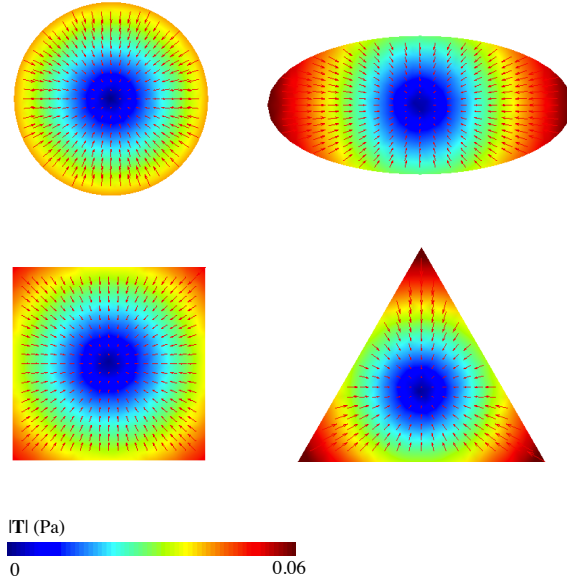


Figure 5.4: Equilibrium cell shapes for various adhesion patterns : Circle (top left), ellipse (top right), square (bottom left) and equilateral triangle (bottom right). The color map indicates magnitude of the traction $|\mathbf{T}| = Y|\mathbf{u}|$, and the arrows demote the direction of the traction vectors. The reference shapes for all the four patterns have an equal area of $1000 \mu m^2$. The other parameters are: $E = 1$ kPa, $\nu = 0.4$, $\sigma_a = 1$ kPa, $\mu_s = 10$ kPa, $h_s = 30 \mu mm$, $h = 0.2 \mu m$.

5.4.1 Spatial distribution of traction stresses

The spatial distribution of traction stresses exerted by cells on substrate and the corresponding organization of stress and deformation inside the cell are affected by the geometry of adhesive patterns. Using micropatterning techniques, cell shapes can be constrained to adhere to controlled geometrical patterns [34, 184]. In our model the shape determined by the pattern in the limit of infinite adhesion strength provides the reference shape for the cell. Here we investigate four reference cell shapes: circle, ellipse, square and equilateral triangle. These are chosen to have the same reference area but different perimeters. The case of a circular cell can be treated analytically, as described below. For the other shapes the force-balance equations (5.4) are solved numerically using the MATLAB pde toolbox. We assume the contractility σ_a to be uniform and of order of the cellular Young's modulus. *Heatmap* of traction stresses

are shown in Fig. 5.4. In all cases the traction stresses are concentrated at the cell periphery, irrespective of the reference shape. The magnitude of the local traction stress is, however, higher in regions of high curvatures or at sharp corners.

For a circular cell, Eq. (5.4) can be solved analytically. Assuming in-plane rotational symmetry, it is convenient to use polar coordinates r and θ , denoting radial and angular coordinates, and demand that no quantity depend on θ . The equation for the radial displacement u_r about a circular reference state of radius R_0 , is then given by

$$r^2 \partial_r^2 u_r + r \partial_r u_r - (1 + r^2/\ell_p^2) u_r = 0, \quad (5.14)$$

where the penetration length ℓ_p describes the localization of traction stresses at the cell boundary. It is given by : $\ell_p^2 = Bh/Y$. The penetration length is short on stiff substrates and increases with decreasing substrate rigidity. The solution of Eq. (8.4) with the boundary conditions $\sigma_{rr}(r = R_0) = 0$ and $u_r(r = 0) = 0$ is given in terms of modified Bessel functions of the first kind as,

$$u_r(r) = -\frac{\sigma_a R_0}{B} I_1(r/\ell_p) g(R_0/\ell_p), \quad (5.15)$$

with $g(s) = [sI_0(s) - \frac{1-2\nu}{1-\nu} I_1(s)]^{-1}$. As anticipated, the deformation u_r vanishes for all r when $Y \rightarrow \infty$, when the adherent circular cell is maximally spread and has its largest undeformed radius R_0 .

5.4.2 Rigidity dependent cell spreading

The optimal spread area of the cell is controlled by the interplay between cell contractility, as described by the active pressure σ_a , and the traction forces on the substrate. In the case of a circular cell, where the deformation induced by adhesion is given by Eq. (5.15), the steady state cell area is given by,

$$A = \pi(R_0 + u(R_0))^2, \quad (5.16)$$

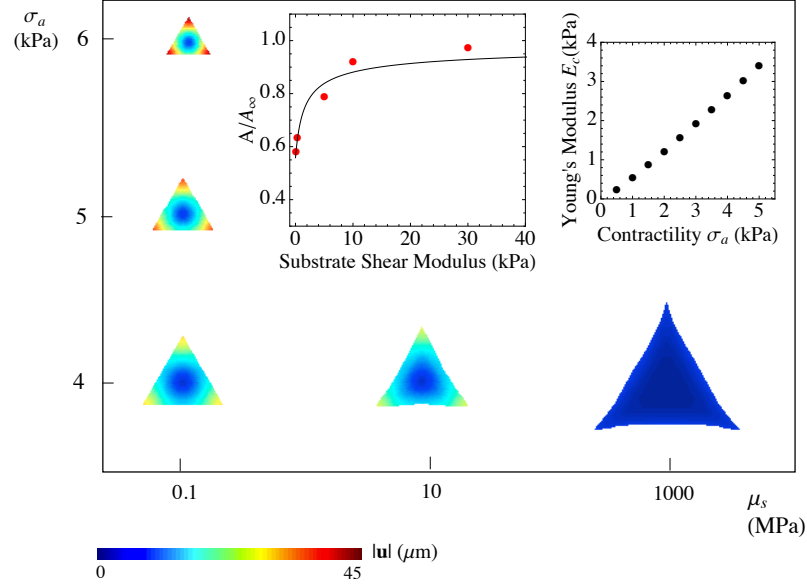


Figure 5.5: Optimal shape of a triangular cell for different values of the active pressure σ_a and the substrate shear modulus μ_s , with $E = 1$ kPa. The color map represents the magnitude of the displacement vector $|\mathbf{u}|$ (proportional to the traction force) about an equilateral triangular reference shape of area $1000 \mu\text{m}^2$. The cell spread area increases with increasing substrate stiffness and decreases with increasing σ_a . Inset (Left) : Least-square fit of the relative cell spread area A/A_∞ obtained from the model using Eq. (5.16) (solid) to the experimental data reported in Ref. [43] (solid red circles). The fitting parameters are $E = 911$ Pa and $\sigma_a = 1589$ Pa. Inset (Right) : Relationship between cellular Young's modulus E and contractility σ_a . Here we tune σ_a to desired values and then determine the fitting parameter E using data in Ref. [43]. Other parameters : $\nu = 0.4$, $h_s = 30 \mu\text{m}$, $h = 0.2 \mu\text{m}$.

with R_0 the reference radius corresponding to the maximal spread area $A_\infty = \pi R_0^2$ attained on an infinitely rigid substrate, where $u_r(r) = 0$. To make contact with experiments, we investigate the ratio A/A_∞ , the relative cell spread area, as a function of substrate stiffness and contractility.

On stiff substrates, where $R_0 \gg \ell_p$, i.e., the traction stress extends over a length much smaller than the reference cell radius, $u_r(R_0) \simeq -\sigma_a \ell_p / B$. The relative spread area then takes the simple form $A/A_\infty \simeq \left(1 - \frac{\sigma_a}{R_0} \sqrt{h/BY}\right)^2$. Letting $Y \simeq \mu_s / h_s$, we note that increasing substrate stiffness increases relative spread area, with $A/A_\infty \rightarrow 1$

as $\mu_s \rightarrow \infty$, in qualitative agreement with experiments [43, 56, 73]. In contrast, increasing the contractile pressure σ_a reduces the optimal cell spread area, consistent with the experimental observation that myosin-II activity retards cell spreading [185]. To make a quantitative comparison with experiments, we fit Eq. (5.16) to experimentally reported data on the projected area of cardiac myocytes cultured on N-cadherin coated Polyacrylamide gels of varying stiffnesses [43]. Here the maximal spread area A_∞ is taken to be equal to the cell projected area on a glass substrate (shear modulus ~ 30 GPa), which is $\simeq 690 \mu m^2$. The fit, shown in the left inset of Fig. 6.1, is obtained using the active contractility σ_a and the cellular Young's modulus E as the fitting parameters. A least-square fit gives us $E = 911$ Pa and $\sigma_a = 1589$ Pa. Although the strength of contractility is likely to depend on cell type, it is worth highlighting that the fit value for σ_a is of the same order of magnitude as used in later in Chapter 8 to fit the measured value of the surface tension of a colony of epithelial cells. Next, we tune the contractility σ_a , which can be artificially controlled through pharmacological interventions, and determine the corresponding best fit value of the cellular Young's modulus E . Our result (Fig. 6.1, right inset) indicates a linear relationship between the cellular Young's modulus and the contractile stress. There are indeed experimental data available [186] that show that the cell stiffness increases linearly with contractility for adherent cells. This suggests that our model could be used to infer contractility from measurements of cellular stiffness. Figure 6.1 also demonstrates the competing roles of contractility and adhesion in controlling optimal cell shapes for a chosen triangular reference state. On softer substrates the triangular cell retains its topology and contracts by an amount proportional to σ_a , whereas on stiffer substrates the corners tend to form protrusions.

5.4.3 Curvature-induced traction

When the boundaries of the adhesion pattern exhibits non-uniform curvature, the traction stresses are higher at regions of high curvatures. This is seen for example

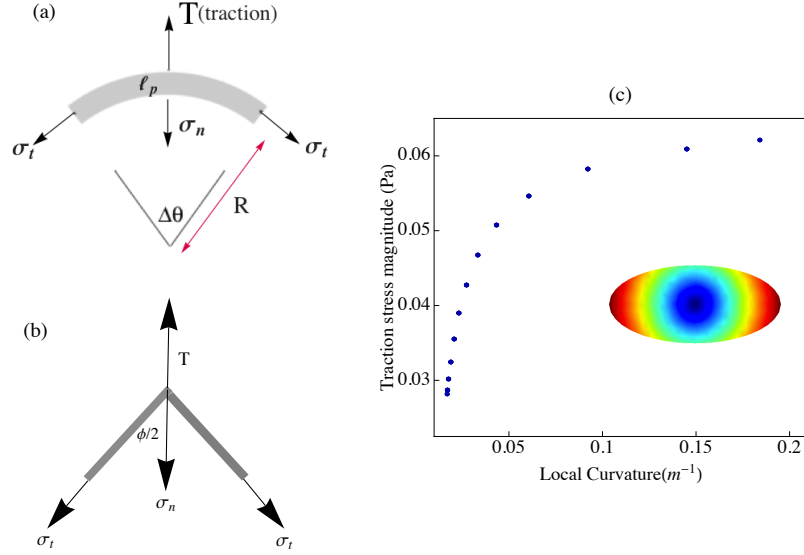


Figure 5.6: (a) Force-balance on a thin slice of cellular material at the cell boundary. (b) Force-balance at a generic sharp corner with opening angle ϕ . (c) Traction stress magnitude at the cell edge as a function of the local curvature κ for the elliptical cell of Fig. 5.4.

in Fig. 5.4 for the case of an elliptical reference shape. To justify this we propose a simple analytical argument based on local force balance. Consider a thin slice of cellular material at the cell periphery of width comparable to penetration length ℓ_p and arc length $R\Delta\theta$ much less than the cell perimeter (Fig. 5.6(a)), with $1/R$ the local curvature of the cell element. At the outer edge of this element, the only force on the cell is the reaction to the traction by the cell on the substrate traction, of areal density $-\mathbf{T}$, with $\mathbf{T} = Y\mathbf{u}$. This yields an outward total force on the outer edge of the cell element of magnitude $TR\Delta\theta\ell_p$, with $T > 0$. At the interior edge, the cellular element experiences a contractile force of magnitude $\sigma_n(R - \ell_p)\Delta\theta\ell_p$, where σ_n is the normal stress pulling the inner contour inwards and has contributions from active as well as passive elastic stresses. The lateral stresses σ_t contributes to an effective line tension $\sigma_t\ell_p R\Delta\theta$ of the cell element. Due to the curvature of the boundary element, the line tension generates an inward Laplace pressure of magnitude $\sigma_t\ell_p/R$. Local

balance of forces then yields,

$$TR\Delta\theta\ell_p - \sigma_n(R - \ell_p)\Delta\theta\ell_p = R\Delta\theta\ell_p\sigma_t\frac{\ell_p}{R}. \quad (5.17)$$

The above law can be written down in a compact form as,

$$T = \sigma_n + (\sigma_t - \sigma_n)\ell_p\kappa, \quad (5.18)$$

with $\kappa = 1/R$, the local curvature of the boundary element. Equation (5.18) then tells us that local magnitude of traction increases linearly with increasing boundary curvature. The lateral and normal stresses σ_t and σ_n can be expressed in terms of the local cellular stresses in polar coordinates as $\sigma_t = \sigma_{\theta\theta} - \partial_\theta\sigma_{r\theta}$ and $\sigma_n = \sigma_{rr}$. The linear dependence of T on κ strictly holds in the limit $\ell_p\kappa \ll 1$. In addition, non-local elastic interactions can also affect the dependence of traction magnitude on local curvature. Figure. 5.6(c) shows the dependence of the magnitude of the traction stress at the cell boundary on local curvature for an elliptical cell as shown in Fig. 5.4. For low κ , the traction stress magnitude increases linearly with κ before reaching a plateau at higher values of κ .

When the cell boundary exhibits a sharp corner with opening angle ϕ , as shown in Fig. 5.6(b), the local force-balance is given by,

$$T = \sigma_n + 2\sigma_t \cos(\phi/2), \quad (5.19)$$

where σ_n acts along the bisecting line of the corner. Hence smaller the opening angle, the larger is the traction force.

5.4.4 Mechanical anisotropy is linked to geometric anisotropy

The spatial distribution of internal stresses σ_{ij} within the cell depends on cell shape, which is in turn controlled by the geometry of the adhesive region. Experimentally $\boldsymbol{\sigma}(x, y)$ can be obtained from the measured distribution of traction stresses $\mathbf{T}(x, y)$, inverting the local force-balance condition $\partial_j\sigma_{ij} = T_i$ [87]. The elasticity equations

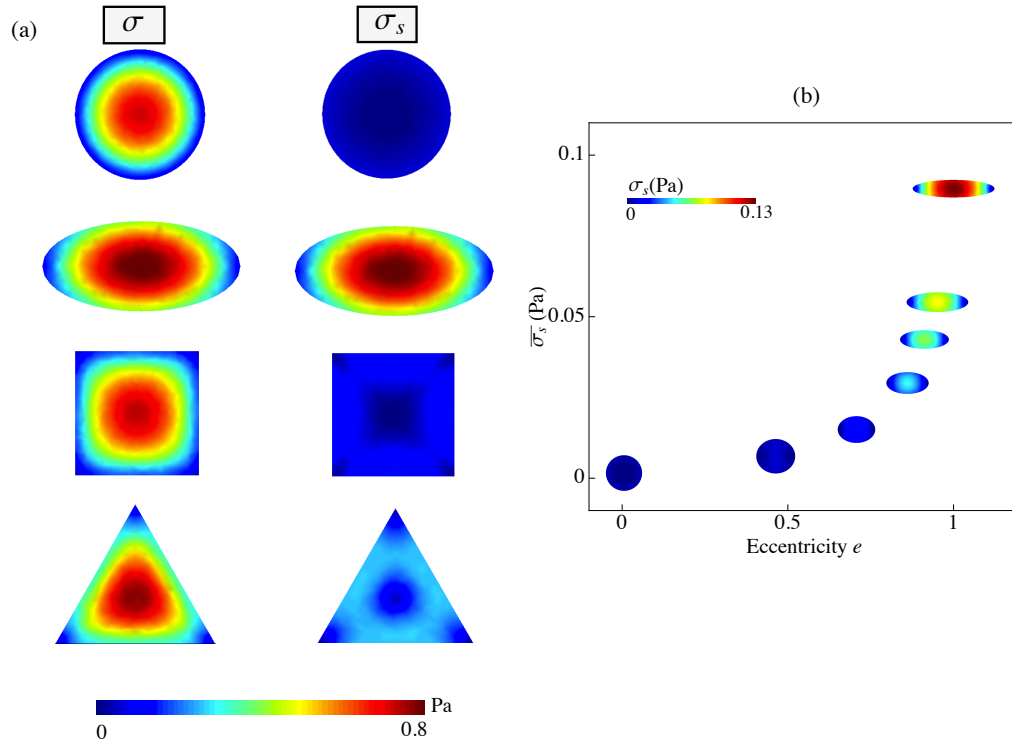


Figure 5.7: Cell shape anisotropy correlates with internal stress anisotropy. (a) Heatmap of internal compressive stress σ (left) and maximum shear stress σ_s (right) corresponding to various reference shapes : circle, ellipse, square and equilateral triangle. The reference shapes all have an equal area of $1000 \mu m^2$. (b) Average maximum shear $\bar{\sigma}_s$ as a function of eccentricity e for elliptical cells of same reference area ($1000 \mu m^2$). Equilibrium shapes with colorplot of μ are given as plot markers. Parameters : $E = 1$ kPa, $\nu = 0.4$, $\sigma_a = 1$ kPa, $\mu_s = 10$ kPa, $h_s = 30 \mu m$, $h = 0.2 \mu m$.

can be recast as a single partial differential equation for the internal stress tensor σ_{ij} , given by

$$\ell_p^2 [\partial_i \partial_k \sigma_{kj}]^S + \delta_{ij} \sigma_a = \sigma_{ij} + \frac{1 - 2\nu}{\nu} \delta_{ij} (\sigma_{kk} - 2\sigma_a) , \quad (5.20)$$

where $[\dots]^S$ denotes symmetrization with respect to indices that are not summed over, i.e., $[\partial_i \partial_k \bar{\sigma}_{kj}]^S = \frac{1}{2} [\partial_i \partial_k \bar{\sigma}_{kj} + \partial_j \partial_k \bar{\sigma}_{ki}]$. We have investigated numerically the solution of Eq. (5.20) with stress free boundary condition $\sigma_{ij} n_j = 0$. To understand the role of shear and compressional deformations in different geometries, it is instructive to diagonalize the stress tensor and display the results in terms of linear combinations of the eigenvalues σ_1 and σ_2 . The sum $\sigma = \frac{1}{2}(\sigma_1 + \sigma_2)$ is simply half the trace of the stress tensor and describes compressional deformations. The difference $\sigma_s = \frac{1}{2}|\sigma_1 - \sigma_2| = \sqrt{[\sigma_{xx} - \sigma_{yy}]^2 + 4\sigma_{xy}^2}$, is controlled by normal stress $\sigma_{xx} - \sigma_{yy}$ and shear stress σ_{xy} . For an isotropic reference shape, such as the circle, $\sigma_1 = \sigma_2$ and $\sigma_s = 0$, whereas for anisotropic shapes such as the ellipse, one expects nonzero values for the local maximum shear σ_s .

Fig. 5.7(a) shows heatmaps of the spatial distribution of σ and σ_s for various reference shapes - circle, ellipse, square and equilateral triangle. Irrespective of the shape of the adhesion geometry, σ is maximum at the cell center, indicating build-up of compressive stresses. The compressional stress σ always vanishes at the boundary, and it does so more rapidly at regions of high curvature or at sharp corners. In contrast, the shear stress σ_s is identically zero for isotropic shapes, defined as those that have a gyration tensor that is diagonal, with equal eigenvalues. The circle, triangle and square are all in this class. Local stress anisotropy as measured by σ_s is nonzero for elliptical shapes and shear stresses build up at the center of the ellipse. The shape anisotropy of ellipses can be quantified by their eccentricity $e = \sqrt{1 - (b/a)^2}$, with a and b the semi-major and semi-minor axes. Figure 5.7(b) shows the spatial average of σ_s over the area A of the cell, defined as $\bar{\sigma}_s = \frac{1}{A} \int_A d^2\mathbf{r} \sigma_s$, as a function of the eccentricity e . The average shear stress $\bar{\sigma}_s$ increases with e with a sharp rise as $e \rightarrow 1$, indicating a positive relationship between geometrical and mechanical anisotropy in

adherent cells. Our theoretical model thus confirms the experimental result that cell mechanical anisotropy increases with increasing aspect ratio, as previously reported for single endothelial cells with the same spread area [39].

In summary, we have proposed a continuum model of an adherent cell on a substrate as an active contractile medium to study the role of adhesion geometry in controlling cell shape, cell spreading and the spatial distribution of traction stresses. More realistic future modeling should take into account that a cell is a highly heterogeneous material with spatially varying stiffness [187]. It is however intriguing to note that the simplified assumption of homogeneity and isotropy in the underlying cytoskeletal network can reproduce several of the known experimental results. The central input of the model is the cell contractility or activity σ_a , a negative contribution to the pressure that enters the constitutive equation for the cellular material. In general, σ_a will be determined by the concentration and activity of myosin proteins cross linking the actin cortex and controlling the formation of stress fiber. In our model σ_a is assumed to be a constant parameter, to be determined by fitting experiments. We consider cells adhering to flat substrates that have been patterned with adhesive patches, consisting for instance of fibronectin coatings, of specific geometry and examine the role of the geometry of the adhesive patch in controlling the spatial distribution of stresses in the cellular material. The reference state for our cell is the limit of infinitely strong adhesion, where the cell shape and lateral extent are determined entirely by the shape and size of the adhesive patch. For finite adhesion strength, cell elasticity and contractility yield deviations from this reference state. We restrict ourselves to considering continuous or densely spaced adhesion sites. As discussed in the next chapter, for discrete or sparsely distributed adhesion sites, non-adherent segments in the cell boundary could likely exhibit morphological transitions induced by contractile activity and substrate stiffness. In agreement with experimental observations, we find that cells spread more on stiff substrates and we provide an expression for the cell area versus substrate stiffness for the case of a circular cell.

We show that this expression fit the data for spread areas of cardiac myocytes on substrates of various stiffness values. We demonstrate analytically and numerically that strong traction stresses correlate with regions of high cell boundary curvature, in agreement with experimental observations. Further, as reported in experiments on single endothelial cells, our model demonstrates that cell mechanical anisotropy is higher on elongated cells than on rounded ones for fixed area [39].

Understanding the relation between cell morphology, the cell's mechanical response and cell fate is an important question in cellular biophysics. Our simple model highlights the correlation between the geometry of adhesion sites and cell morphology and demonstrates that traction forces by cells can be tuned by controlling the geometry of adhesive regions. An important open question not addressed by our model is how cell morphology is determined by the interplay of cell-substrate adhesion and dynamical reorganization of the cytoskeletal architecture in response to the adhesion stimulus. To understand this it will be necessary to incorporate the dynamical feedback between actin reorganization and adhesion kinetics.

Chapter 6

Optimal Shapes of Adherent Cells

Cellular response to extracellular determinants is strongly linked to myosin dependent activity of the cell cytoskeleton [188]. While myosin activity can influence force transmission by regulating the growth of focal adhesions [189], it can also drive changes in cell morphology, as seen by pharmacologically disrupting the cell cytoskeleton [70, 190] or by inhibiting myosin-II activity [34]. In this chapter we present a minimal mechano-geometric model for isolated adherent cells that addresses a fundamental question in cell mechanics and morphogenesis: How do intercellular and extracellular forces cooperate to control the geometry of cell shapes? At time scales when the cell is fully spread and develops stronger focal adhesions, the dominant forces in the cell stem from surface tension induced by actomyosin contractility and elasticity in the actomyosin cortex. These intracellular forces act in opposition to receptor-mediated adhesive forces in determining optimal cell shapes [191, 192]. Although chemical pathways can trigger a feedback between cell activity and cell-substrate adhesion [193], we instead focus on their mechanical cooperativity in regulating cell shapes. Tuning stiffness of the matrix and acto-myosin contractility, we discuss how cells can be driven through a series of morphological transitions - convex, concave, cusps and protrusions with associated hysteresis. In addition, we provide several analytical results relating geometrical properties of cells e.g. curvature, spread radius to mechanical properties

such as substrate stiffness and contractile surface tension, that are amenable to experimental verification and quantitative comparison.

6.1 Contractile Film Model

We consider a thin film of an adherent cell subject to internal contractile forces. The shape of the cell contact line is parametrized by the contour $\mathbf{r}(s)$, where s represents arc-length. The total mechanical energy of the cell can be approximated, on the basis of symmetry arguments, in the form:

$$E = \gamma \int dA + \oint ds (b\kappa^2 + \lambda) + k_s \oint ds \rho |\mathbf{r} - \mathbf{r}_0|^2, \quad (6.1)$$

where γ is the *effective* surface tension in the cell due to cytoskeletal contractility, κ is the local curvature of the cell boundary, b the associated bending rigidity and λ represents line tension at the cell boundary. The last term in Eq. (6.1) represent the strain energy induced by the cell on a substrate of stiffness k_s through focal adhesions localized at the cell edge, with density $\rho(s)$, so that the total number of adhesions is $N_A = \oint ds \rho$. For cells adhering to a thin continuous substrate, \mathbf{r}_0 can be considered as the position of the cell boundary once the cell is fully spread and forces are predominately contractile, while for cells cultured on elastomeric pillars, this is simply the pillar's rest position at the adhesion points. In the analytical framework presented here, we will generally treat the reference shape as an adjustable parameter to investigate different experimental situations.

The model assumes that the overall effect of acto-myosin contractility, that pulls the cell contour inwards reducing its contact area with the substrate, can be described by an *effective* surface tension γ . Thus the first term in Eq. (6.1) should not be interpreted as the classic hydrostatic tension that occurs at the interface between two fluids, but as an *active* normal stress resulting from the action of the motors. In order to estimate the order of magnitude of γ , we assume that the *active* myosin motors cross-linked with the cortical F-actin gel of mean thickness $h \simeq 0.1 \mu\text{m}$,

are distributed with an average areal density $\rho_m \simeq 10^4 \mu m^{-2}$, with effective stiffness $k_m \simeq 1$ pN/nm and mean stretch $\Delta_m \simeq 1$ nm [2]. Surface tension γ can then be estimated as $\gamma \simeq h\rho_m k_m \Delta_m \simeq 1$ nN/ μ m. This estimate comes to the same order of magnitude as reported for endothelial cells [71, 72] and epithelial cells [104].

The second term in Eq. (6.1) describes the elasticity of the cell cortex. This consists of a bending energy density $b\kappa^2$, reflecting the resistance of cortical actin in response of a change in curvature, and an effective line tension λ that, similarly to the bulk tension γ , embodies the contractile forces due to the actin fibers lining the cell periphery [71, 194]. The Euler-Lagrange equations for the shape that minimizes the energy (6.1) can be derived with standard methods [195, 196]. This yields:

$$b(2\kappa'' + \kappa^3) - \lambda\kappa - \gamma + 2k_s\rho(\mathbf{r} - \mathbf{r}_0) \cdot \mathbf{n} = 0 \quad (6.2)$$

Here prime denotes derivative with respect to arc-length s and $\mathbf{n} = \mathbf{r}''/|\mathbf{r}''|$ is the normal vector. Eq. (6.2) expresses the balance between the total stress acting on a cross-section of the cortex and the body force $\mathbf{K} = 2k_s\rho(\mathbf{r} - \mathbf{r}_0)$ due to adhesion:

$$\frac{d}{ds}(\mathbf{F} + \mathbf{\Sigma} + \mathbf{A}) + \mathbf{K} = 0 \quad (6.3)$$

where $\mathbf{F} = b\kappa^2\mathbf{t} + 2b\kappa'\mathbf{n}$ (with \mathbf{t} the tangent vector) is the elastic stress resultant, $\mathbf{\Sigma} = -\gamma[(\mathbf{r} \cdot \mathbf{t})\mathbf{n} - (\mathbf{r} \cdot \mathbf{n})\mathbf{t}]$ is the stress contribution of bulk contractility and $\mathbf{A} = -\lambda\mathbf{t}$ that of peripheral contractility.

Previous theoretical models [70, 71, 194] have analyzed the competition of bulk and peripheral contractility and ignored the bending elasticity of the actin cortex (i.e. $b = 0$). In analogy with the Laplace law of capillarity, the steady state cell contour is then described by concave circular arcs of radius λ/γ connecting adhesion sites. Here we focus on the opposite limit and consider the regime in which the force balance is dominated by the competition between cortex elasticity and bulk contractility, while the effect of peripheral contractility is negligible (i.e. $\lambda = 0$). In this scenario, the curvature is generally non-uniform, especially in the neighborhood of adhesion sites. As we will see in the remainder of this chapter, incorporating bending elasticity leads

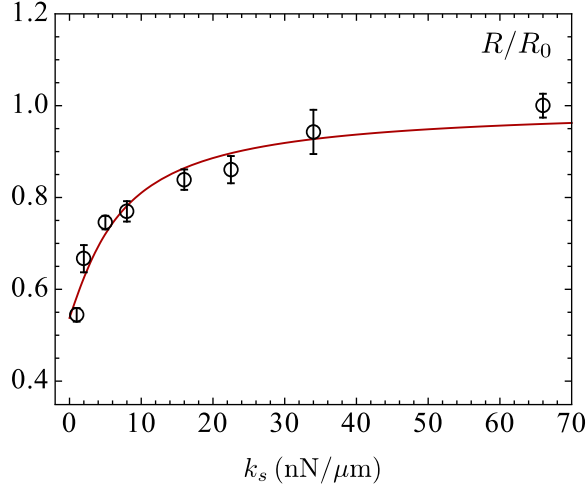


Figure 6.1: Relative cell size R/R_0 as a function of substrate stiffness k_s (solid black circles) for smooth muscle cells, 4 hours after plating on continuous elastic gels [52]. Cell radius is estimated from the projected cell area reported in [52] as $R = \sqrt{\text{area}}/\pi$. Substrate stiffness k_s is determined from substrate Young's modulus E_s as : $k_s = aE_s$, where a is the characteristic focal adhesion size, with $a \sim 1 \mu\text{m}$. Solid (red) line represents the solution to Eq. (6.4) with $\gamma = 1.05 \text{ nN}/\mu\text{m}$ and $b/R_0^3 = 0.16 \text{ nN}/\mu\text{m}$.

to an extremely rich polymorphism and allows for a transition from purely convex to purely concave cell shape reminiscent of that observed in experiments on cardiac myocytes [43].

6.1.1 Continuous adhesions

In this case the periphery of the cell forms contact with a single continuous adhesion site, so that $\rho = 1/\mathcal{L}$ with $\mathcal{L} = \oint ds$ the perimeter of the cell. In presence of a uniform and isotropic substrate, we can assume the reference configuration to be a circle of radius R_0 so that a natural minimizer of the energy (6.1) would be a circle of radius R . Thus, setting $\lambda = 0$, $\kappa = R^{-1}$ and $\rho^{-1} = 2\pi R$ in Eq. (6.2) yields the following cubic equation:

$$(k_s + \pi\gamma)R^3 - k_s R_0 R^2 - \pi b = 0, \quad (6.4)$$

The equation contains two length scales, R_0 and $\xi = (b/\gamma)^{1/3}$, and a dimensionless control parameter k_s/γ expressing the relative amount of adhesion and contraction. For very soft anchoring $k_s \ll \gamma$ and Eq. (6.4) admits the solution $R = \xi$. Thus in non-adherent cell segments, corresponding to the limit $k_s = 0$, radius of curvature scales with surface tension as $R \sim \gamma^{-1/3}$. The same scaling law is also predicted using *active cable network* models of an adherent cell [180]. If the cell is rigidly pinned at adhesion sites, $k_s \gg \gamma$ and $R \rightarrow R_0$. For intermediate values of k_s/γ the optimal radius R interpolates between ξ and R_0 and is an increasing function of the substrate stiffness k_s , in case $\xi < R_0$, or a decreasing function if $\xi > R_0$. For $\xi = R_0$, the lower and upper bound coincide, and the solution is $R = R_0$. In particular, the case $R_0 > \xi$ reproduces the experimentally observed trend that cell projected area increases with increasing substrate stiffness before reaching a plateau at higher stiffnesses [43, 52, 73]. We fit the solution to Eq. (6.4) to the measured projected areas of smooth muscle cells (SMCs) adhering to continuous elastic gels of varying substrate elastic modulus [52], as shown in Fig. 6.1. Data for the spread area of SMCs are taken 4 hours after plating onto the substrate, when they retain rounded morphologies. The fitted value for surface tension $\gamma = 1.05 \text{ nN}/\mu\text{m}$ comes to the same order of magnitude as reported for endothelial cells [71, 72], epithelial cells [104] and is consistent with the numerical estimate provided earlier. The fit also provides a value for the bending rigidity $b = 4.62 \times 10^{-16} \text{ Nm}^2$. The asymptotic behavior and various limits of the solution are well captured by the interpolation formula:

$$R \approx \frac{k_s R_0 + 3\pi\gamma \xi}{k_s + 3\pi\gamma} \quad (6.5)$$

indicating that larger surface tension, hence larger cell contractility γ leads to lesser spread area, consistent with the experimental observation that myosin-II activity retards the spreading of cells [185]. Standard stability analysis of this solution under a small periodic perturbation in the cell radius shows that the circular shape is always stable for any values of the parameters γ , k_s and R_0 .

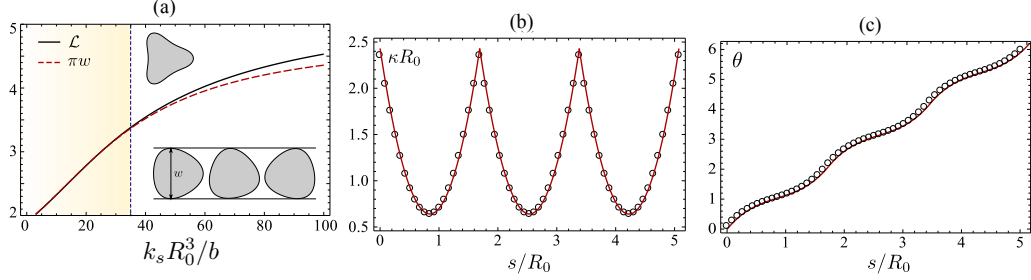


Figure 6.2: Cell anchored onto three pointwise adhesions located at the vertices of an equilateral triangle. (a) The total cell length \mathcal{L} as a function of adhesion stiffness. For small stiffnesses the cell boundary form a curve of constant width (lower inset) and $\mathcal{L} = \pi w$, with w the width of the curve. This property breaks down for larger stiffnesses when inflection points develops (upper inset). The curvature (b) and the tangent angle (c) as function of arc-length for $\gamma R_0^3/b = 10$, $k_s R_0^3 = 50$ and $N_A = 3$. The circles are obtained from a numerical minimization of a discrete version of the energy (6.1), while the solid lines are obtained respectively from our analytical approximation.

6.1.2 Discrete adhesions

For cells adhering to discrete number of adhesion sites, one can show that the circular solution for the cell boundary is never stable and there is always a non-circular configuration with lower energy. For simplicity, we assume that N_A adhesion sites are located at the vertices of a regular polygon of circumradius R_0 , with density $\rho(s) = \sum_{i=0}^{N_A-1} \delta(s - iL)$, and L the distance between subsequent adhesions. Optimal cell shape is given by the solution of the equation:

$$b(2\kappa'' + \kappa^3) - \gamma + 2k_s \sum_{i=0}^{N_A-1} \delta(s - iL) (\mathbf{r} - \mathbf{r}_0) \cdot \mathbf{n} = 0. \quad (6.6)$$

Due to the N_A -fold symmetry of the adhesion sites, adhesion springs stretch by an equal amount Δ in the direction of the normal vector: $(\mathbf{r}_i - \mathbf{r}_{0i}) \cdot \mathbf{n}_i = \Delta$, $i = 1, 2, \dots, N_A$. As a consequence of the localized adhesion forces, the curvature is non-analytical at the adhesion points. Integrating Eq. (6.6) along an infinitesimal neighborhood of a generic adhesion point i , one finds the following condition for the derivative of the curvature at the adhesion points:

$$\kappa'_i = -\frac{k_s}{2b} \Delta. \quad (6.7)$$

The local curvature of the segment lying between adhesion points is on the other hand determined by the equation $b(2\kappa'' + \kappa^3) - \gamma = 0$, with the boundary conditions : $\kappa(iL) = \kappa((i+1)L) = \kappa_0$. Without loss of generality we consider a segment located in $s \in [0, L]$. Although an exact analytic solution of this nonlinear equation is available (see Ref. [197]), an excellent approximation can be obtained by neglecting the cubic nonlinearity (Fig. 6.2b-c). With this simplification, Eq. (6.6) admits a simple solution of the form:

$$\kappa(s) = \kappa_0 + \frac{\gamma}{4b} s(s - L) . \quad (6.8)$$

Eqs. (6.8) and (6.7) immediately allow us to derive a condition on the cell perimeter: $L = 2k_s\Delta/\gamma$. Furthermore, the latter condition leads to a linear relation between traction force $T = 2k_s\Delta$, and cell size :

$$T = \gamma L , \quad (6.9)$$

which is indeed observed in traction force measurements on large epithelial cells [104].

To determine the end-point curvature κ_0 , we use the turning tangents theorem for a simple closed curve [198], which requires $\int_0^L ds \kappa = 2\pi/N_A$. This leads to following relation between local curvature and segment length, or equivalently traction force, at the adhesion sites :

$$\kappa_0 = \frac{\gamma L^2}{24b} + \frac{2\pi}{N_A L} = \frac{T^2}{24b\gamma} + \frac{2\pi\gamma}{N_A T} . \quad (6.10)$$

Finally, to determine the optimal length of the cell segment L , we are going to make use of a remarkable geometrical property of the curve obtained from the solution of Eq. (6.6) with discrete adhesions: the fact of being a *curve of constant width* [198]. The width of a curve is the distance between the uppermost and lowermost points on the curve (see lower inset of Fig. 6.2a). In general, such a distance depends on how the curve is oriented. There is however a special class of curves, where the width is the same regardless of their orientation. The simplest example of a curve of constant width is clearly a circle, in which case the width coincides with the diameter. A

fundamental property of curves of constant width is given by the Barbier's theorem [198], which asserts that the perimeter \mathcal{L} of any curve of constant width is equal to width w multiplied by π : $\mathcal{L} = \pi w$. As illustrated in Fig. 6.2a, this is confirmed by numerical simulations for low to intermediate values for contractility and stiffness. With our setting, the cell width is given by:

$$w = (R_0 - \Delta)(1 + \cos \pi/N_A) + h(L/2), \quad (6.11)$$

where $h(s) = \int_0^s ds' \sin \theta(s')$ is the height of the curve above a straight line connecting subsequent adhesions and

$$\theta(s) = \int_0^s ds' \kappa(s') = \theta_0 + \kappa_0 s + \frac{\gamma}{24b} s^2(2s - 3L) \quad (6.12)$$

the angle formed by the tangent vector with the x -axis of a suitable oriented Cartesian frame (Fig. 6.3b). For small angles h can be approximated as : $h(s) \approx s(L - s) [\pi/(N_A L) - (\gamma/48b) s(L - s)]$. Using this together with Eq. (6.11) and the Barbier's theorem with $\mathcal{L} = N_A L$ allow us to obtain a quartic equation for the cell length and the traction force, whose approximate solution is given by:

$$T \simeq \frac{\gamma R_0}{\left(g_0 + \frac{\gamma}{2k_s}\right) \left[1 + \frac{7\gamma R_0^3}{bg_1} \left(g_0 + \frac{\gamma}{2k_s}\right)^{-4}\right]^{1/7}}, \quad (6.13)$$

where, $g_0 = (4N_A^2 - \pi^2)/[4\pi N_A(1 + \cos \pi/N_A)]$ and $g_1 = 768(1 + \cos \pi/N_A)$. Eq. (6.13) supports the experimental trend that traction force increases monotonically with substrate stiffness k_s before plateauing to a finite value for higher stiffnesses [56, 161]. The plateau value increases with increasing contractility (Fig. 6.4a). Traction force grows linearly with increasing contractility for $\gamma R_0^3/b \ll 1$, before saturating to the value $2k_s R_0$ at large contractility $\gamma R_0^3/b \gg 1$, as shown in Fig. 6.4b. Eq. (6.13) is also consistent with experimentally observed trend that reducing contractility by increasing the dosage of myosin inhibitor Blebbistatin, leads to monotonic drop in traction forces [161].

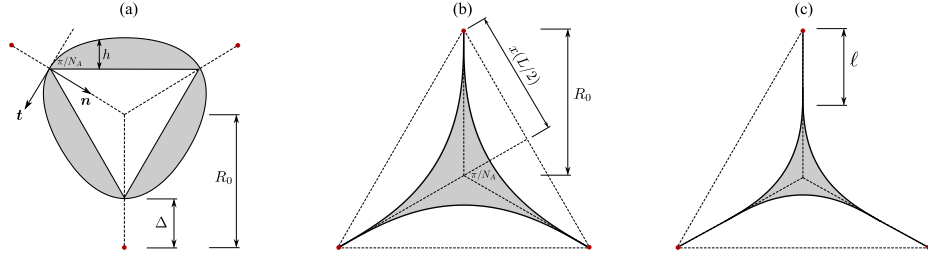


Figure 6.3: Cell anchored onto three pointwise adhesions located at the vertices of an equilateral triangle. (a) $\gamma < \gamma_{c1}$, cell contour is everywhere convex with constant width. (b) $\gamma = \gamma_p$, cell contour is purely concave with cusps at adhesion points and without protrusions. (c) $\gamma > \gamma_{c2}$, cusps are connected to the substrate by means of a protrusion of length ℓ .

In the calculation presented in this section we have neglected the contribution of peripheral contractility embodied in the effective line tension λ . From the point of view of force balance, increasing λ has the effect of rotating the stress resultant toward the tangential direction. This creates a boundary layer between the adhesion points, where the curvature κ_0 is dictated by the balance between adhesion and bending, and the central region, where the curvature $\kappa \approx \gamma/\lambda$ is dominated by the balance between normal and tangential contractility. The size of the boundary layer is approximatively $\sqrt{b/\lambda}$.

6.2 Inflections, cusps and protrusions

For low to intermediate values of γ and k_s , cell shape is convex and has constant width. Upon increasing γ above a k_s -dependent threshold γ_{c1} , however, the cell boundary becomes inflected (see Fig. 6.5 and upper inset of Fig. 6.2a). Initially a region of negative curvature develops in proximity of the mid point between two adhesions, but as the surface tension is further increased, the size of this region grows until positive curvature is preserved only in a small neighborhood of the adhesion points. Due to the presence of local concavities, the cell boundary is no longer a curve of constant width. Convex and concave regions are separated by inflection points, given by the

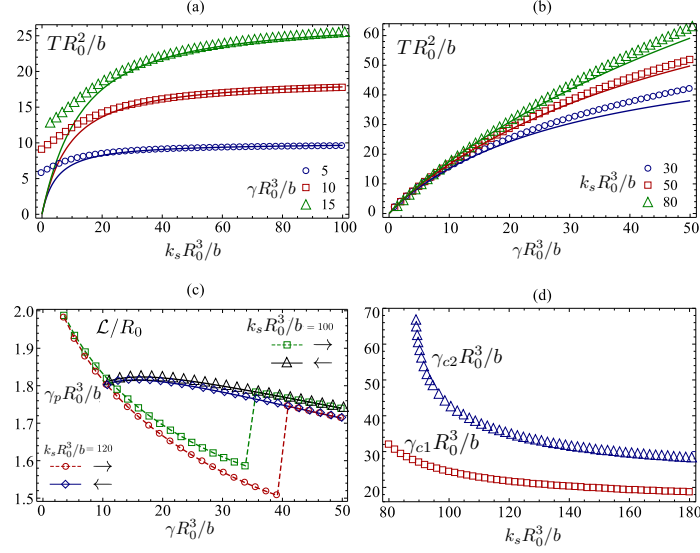


Figure 6.4: Traction force as a function of substrate stiffness (a) and contractility (b) obtained from a numerical minimization of a discrete analog of Eq. (6.1). Solid curves denote the approximate traction values obtained from Eq. (6.13). (c) Boundary length \mathcal{L} obtained by increasing (squares) and then decreasing (triangles) the contractility for substrate stiffnesses $k_s R_0^3/b = 100$ (green squares, black triangles) and $k_s R_0^3/b = 120$ (red squares, blue triangles). The diagram shows bistability in the range $\gamma_p < \gamma < \gamma_{c2}$. (d) The critical contractility γ_{c1} and γ_{c2} as functions of substrate stiffness.

solution to $\kappa = 0$, or explicitly: $s^2 - Ls + 4b\kappa_0/\gamma = 0$. In order for this equation to have real solutions one needs $\gamma L^3 > 96\pi b/N_A$. Fig. 6.4d shows γ_{c1} as a function of k_s .

Upon increasing γ above a further threshold value γ_{c2} , the inflected shape collapses giving rise to the star-shaped configurations shown in upper right corner of Fig. 6.5. These purely concave configurations are made by arcs whose ends meet in a cusp. The cusp is then connected to the substrate by a protrusion consisting of a straight segment of length ℓ that extends until the adhesion point rest position, so that $\Delta \approx 0$ (Fig. 6.3c) (see Appendix B). The cell boundary becomes pinned at adhesion sites as a result of having to satisfy force-balance, Eq. (6.6), and adhesion-induced boundary condition, Eq. (6.7), while accommodating large contractile tensions at its neighbourhood. This results in spontaneous expansion in the cell perimeter. Unlike

the previous transition from convex to non-convex shapes, this second transition occurs discontinuously and is accompanied by a region of bistability in the range $\gamma_p < \gamma < \gamma_{c2}$, where $\gamma_p < \gamma_{c2}$ is the value of γ at which the protrusions have zero length and the shape of the cell is that sketched in Fig. 6.3b. This is clearly visible in the hysteresis diagram in Fig. 6.4c showing the optimal length obtained by numerically minimizing a discrete analog of Eq. (6.1) in a cycle and using as initial configuration the output of the previous minimization. The onset of bistability is regulated by substrate stiffness as shown in Fig. 6.4d, with stiffer substrates promoting transition to cusps at lower γ_{c2} . Away from the protrusion, the curvature has still the form given in Eq. (6.8), with $\kappa_0 = 0$ so that the boundary is everywhere concave or flat and the bending moment $\mathbf{M} = 2b\kappa\hat{\mathbf{z}}$ does not experience any unphysical discontinuity at the protrusion's origin.

From the shape of the cell at $\gamma = \gamma_p$ we can construct all the shapes at $\gamma > \gamma_p$ by mean of a *similarity* transformation. To see this, let us set $\ell = 0$ at $\gamma = \gamma_p$ so that the shape of the cell will be of the kind illustrated in Fig. 6.3b. In the following we will refer to this as the *reference shape*. The approximated expression for the curvature is the same as given in Eq. (6.8), but with $\kappa_0 = \Delta = 0$ and κ' unconstrained since the last term in Eq. (6.6) vanishes identically. The quantities γ_p and the length L_p of the reference shape are left to determine. To achieve this, a first condition can be obtained by observing that: $x(L_p/2) = R_0 \sin \pi/N_A$, where $x(s)$ is the projection of the curve on the edge of the circumscribed polygon (see Fig. 6.3b). A second condition is given by the theorem of turning tangents for a simple closed curve with N_A cusps: $\int_0^{L_p} ds \kappa = \pi(2 - N_A)/N_A$. In the case $N_A = 3$, for instance, the right-hand side is equal to $-\pi/3$, corresponding to the fact that the tangent vector rotates clockwise by 60° as we move counterclockwise along the curve from one cusp to the next. These

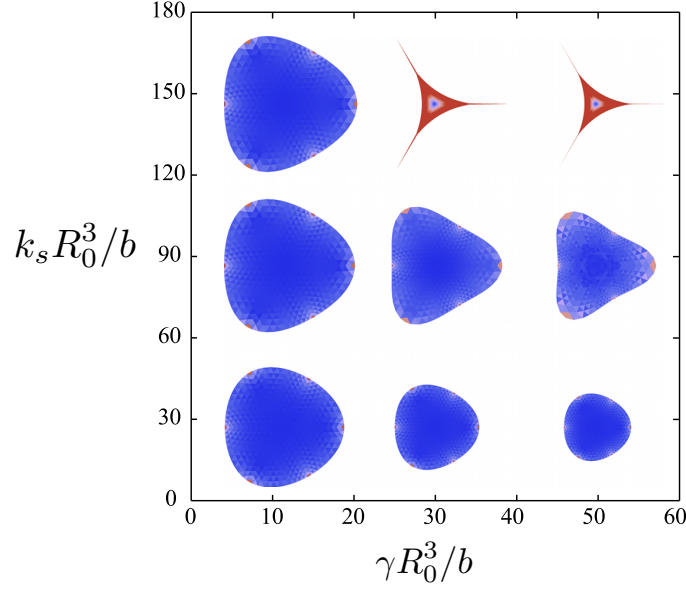


Figure 6.5: Phase diagram in γ - k_s plane showing optimal configuration obtained by numerical minimization of the energy (6.1) for $N_A = 3$.

allow us to approximate:

$$L_p \approx \frac{2N_A R_0}{\pi(N_A - 2)} \sin \frac{\pi}{N_A}, \quad (6.14a)$$

$$\gamma_p \approx \frac{3b\pi^4}{R_0^3 \sin^3 \frac{\pi}{N_A}} \left(\frac{N_A - 2}{N_A} \right)^4, \quad (6.14b)$$

which define the *reference shape* shown in Fig. 6.3b.

Next, following Ref. [199, 200], we notice that the force balance equation $2\kappa'' + \kappa^3 - \gamma/b = 0$ is invariant under the scaling transformation:

$$(s, \kappa, \gamma) \rightarrow \left(\Lambda s, \frac{\kappa}{\Lambda}, \frac{\gamma}{\Lambda^3} \right). \quad (6.15)$$

Consequently, the equilibrium shape obtained for a given value of $\gamma > \gamma_p$ are similar to the reference shape with a scaling factor $\Lambda = (\gamma_p/\gamma)^{1/3} < 1$. Accordingly, the closed curve is rescaled so that $L = \Lambda L_p$ and $A = \Lambda^2 A_p$ with A_p the area of the reference shape. This beautiful geometric property immediately translates into the following algorithm to construct shapes with protrusion (Fig. 6.3c): 1) Given the surface

tension $\gamma > \gamma_p$ we calculate the scaling factor Λ . 2) We rescale the reference curve so that $L = \Lambda L_p$. 3) Finally, we fill the distance between the adhesion points and the cusps with straight segments of length $\ell = R_0(1 - \Lambda)$ (since R_0 is the circumradius of the reference shape and ΛR_0 that of the rescaled shape). This latter step, ultimately allows us to formulate a scaling law for the length of protrusions that can be tested in experiments:

$$\ell/R_0 = 1 - (\gamma_p/\gamma)^{1/3}. \quad (6.16)$$

It should be stressed that our knowledge of the convex/concave transition is still very preliminary. This instability is different from the classical Euler buckling [201], which originates from the trade-off between compression and bending and is a supercritical pitchfork bifurcation. The appearance of cusps is reminiscent, to some extent, of the *sulcification* instability in neo-Hookean solids [202–205], but there is far from being a precise mapping. One of the fundamental aspects that distinguishes our model from classical elasticity relies on the fact that the perimeter is not hardly constrained, but only subject to a soft constraint by mean of the adhesion springs. The length of an elastic object affects its overall flexibility (i.e. long filaments are floppy and easy to bend, while short filaments are stiff), thus, when the effective surface tension is increased, the whole cell boundary becomes shorter and stiffer. Because stiff materials are difficult to bend, but easy to break, a possible interpretation could be the following. For sufficiently large adhesion, increasing the surface tension has the effect of bending and stiffening the cell boundary in proximity of the adhesion sites, until, above a certain surface tension, the cell boundary is too stiff to continue bending and fractures. The cracks are localized at the adhesion points, where the curvature initially focuses, giving rise to the cusps observed in the simulations. However, a thorough understanding of this phenomenon remains a challenge for the future.

Appendix 6.A Numerical simulations

The data shown in Figs. 6.1 and 6.4a,b,d have been obtained by numerically minimizing the following discrete version of the energy (6.1):

$$E_1 = \frac{\gamma}{2} \sum_{i=1}^{N-1} (x_i y_{i+1} - x_{i+1} y_i) + b \sum_{i=1}^N \langle s_i \rangle \kappa_i^2 + k_s \sum_{i=1}^{N_A} |\mathbf{r}_i - \mathbf{r}_{0i}|^2 \quad (6.17)$$

where the first term corresponds to the area of the irregular polygon of vertices $\mathbf{r}_i = (x_i, y_i)$, with $i = 1, 2, \dots, N$, and the third sum represents the energetic contribution of the N_A adhesion points. κ_i is the unsigned curvature at the vertex i : $\kappa_i = |\mathbf{t}_i - \mathbf{t}_{i-1}| / \langle s_i \rangle$ with $\mathbf{t}_i = (\mathbf{r}_{i+1} - \mathbf{r}_i) / |\mathbf{r}_{i+1} - \mathbf{r}_i|$ the tangent vector at i and $\langle s_i \rangle = (s_i + s_{i-1})/2$, with $s_i = |\mathbf{r}_{i+1} - \mathbf{r}_i|$. The discrete energy (6.17) was minimized using a standard conjugate gradient algorithm. Using (6.17) allows a direct comparison between simulations and the analytical results presented in the previous sections. However, for very large substrate stiffness, the discrete curve develops self-intersections and the energy becomes ill-defined. In this regime, it is more convenient to approximate the cell as a simplicial complex consisting of mesh M of equilateral triangles. The edges of the triangles can then be treated as elastic springs of zero rest-length, so that the total energy of the mesh is given by:

$$E_2 = \Sigma \sum_{e \in M} |e|^2 + b \sum_{v \in \partial M} \langle s_v \rangle \kappa_v^2 + k_s \sum_{i=1}^{N_A} |\mathbf{r}_i - \mathbf{r}_{0i}|^2 \quad (6.18)$$

where v and e represent respectively the vertices and the edges of the mesh and Σ is a spring constant. If the triangles in the mesh are equilateral, this yields a discrete approximation of the interfacial energy γA , with the spring stiffness proportional to the surface tension: i.e. $\gamma \approx 4\Sigma\sqrt{3}/(2 - B/E)$, where B/E is the ratio between the number of boundary edges B and the total number of edges E of the triangular mesh [196].

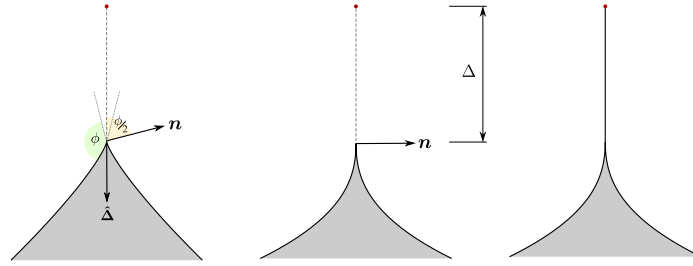


Figure 6.6: Example of singular points: kink (left), cusps (center), protrusion (right). The red dot indicated the adhesion point rest position \mathbf{a} , while $\hat{\Delta} = (\mathbf{r} - \mathbf{r}_0)/|\mathbf{r} - \mathbf{r}_0|$. For a cusp $\mathbf{n} \cdot \hat{\Delta} = 0$, while for a protrusion, the normal vector is undefined at the point of adhesion.

Appendix 6.B Kinks, cusps and protrusions

We present here some additional mathematical aspect on the occurrence of cusps and formation of protrusions in the large contractility and stiffness regime. In particular we show that the shape consisting of N_A cusps that extend until the adhesion rest point through a set of straight protrusions, is the only regular convex N_A -fold star shape to be mechanically stable within the Contractile Film Model.

A kink is a singular point on a curve where the tangent vector switches discontinuously between two orientations (Fig. 6.6, left). The magnitude of the discontinuity can be measured from the external angle ϕ . A cusp, is a kink with $\phi = \pi$, so that the tangent vector switches between equal and opposite orientation (rotation by a larger angle would give rise to self-intersections). In the case of a simple closed curve with kinks, the theorem of turning tangents can be reformulated as follows:

$$\oint ds \kappa + \sum_i \phi_i = 2\pi, \quad (6.19)$$

where the summation runs over all the kinks. In the case of a convex polygon, for instance, $\kappa = 0$ and (6.19) asserts that the sum of the external angle of a polygon is equal to 2π . In a convex N_A -fold star, the external angle is bounded in the range $\phi \in [2\pi/N_A, \pi]$, where $\phi = 2\pi/N_A$ corresponds to a regular polygon. As described in

the main text, Euler-Langrange equation for cellular force-balance is given by:

$$b(2\kappa'' + \kappa^3) - \gamma + 2k_s \sum_{i=1}^{N_A} \delta(s - s_i)(\mathbf{r} - \mathbf{r}_0) \cdot \mathbf{n} = 0 . \quad (6.20)$$

Let $s_1 = 0$ be the position of a generic adhesion point. Then, integrating Eq. (6.20) in the range $s \in [-\epsilon, \epsilon]$ and taking the limit $\epsilon \rightarrow 0$ yields:

$$2b\kappa'(0) + k_s \mathbf{n}(0) \cdot \mathbf{\Delta}(0) = 0 , \quad (6.21)$$

which expresses that the elastic restoring force originating in the boundary must balance the body force $k_s \mathbf{n} \cdot \mathbf{\Delta}$ due to the adhesion spring. For a kink, as that shown on the left of Fig. 6.6, $\mathbf{n} \cdot \mathbf{\Delta} = \Delta \cos(\pi - \phi/2) = -\Delta \cos(\phi/2)$, force balance gives us:

$$\kappa'(0) = \frac{k_s}{2b} \Delta \cos(\phi/2) , \quad (6.22)$$

Now, in a configuration consisting of a regular convex N_A -fold star, the signed curvature is everywhere negative and has *single* minimum at the midpoint between kinks. The latter property implies $\kappa'(0) < 0$, which however contradicts Eq. (6.22) being the right-hand side always positive for any positive value of k_s , b and Δ . From this we conclude that such a configuration cannot be a possible equilibrium shape.

In the case of a cusp, $\mathbf{n} \cdot \mathbf{\Delta} = 0$ and the adhesion force is all exerted along the tangent direction, hence $\kappa'(0) = 0$. Using the full nonlinear equation it can be shown that Eq. (6.20) has no solution with $\kappa'(0) = 0$ that satisfies (6.19) with $\phi = \pi$. The only case left is then that illustrated on the right of Fig. 6.6, in which the cusp extends through a straight protrusion until the adhesion rest position, so that $\Delta = 0$. In this configuration, the adhesion force exerted by the substrate is zero and so is the elastic force acting in the protrusion, this being straight. In other words, the cell is pinned at the adhesion rest position while the elastic force is zero. The case in which the protrusion has zero length, is a special instance of this scenario from which one can construct all the shapes having nonzero protrusion length by mean of a *similarity* transformation.

Chapter 7

Cohesive Cell Layers on Elastic Substrates of Finite Thickness

7.1 Non-local cell-substrate interactions

In this chapter we examine the effect of substrate thickness and stiffness on traction forces exerted by strongly adherent cell layers. We build on the model introduced in Chapter 5, where we described the cell or cell layer as a contractile elastic medium, with local elastic response of the substrate (as appropriate for micropillar arrays or very thin substrates). In contrast, here we consider substrates of finite thickness where the nonlocality of the elastic response must be included. It is found that traction stresses by isolated fibroblasts and epithelial cells on pillar arrays are localized near the cell edge, while contractile stresses (referred to below as cellular stresses) build-up inside the cellular material and is largest near the cell center [46, 56], as shown schematically in Fig. 7.1. This behavior, also observed in adherent cell sheets and in migrating cell colonies [85, 206], is predicted by our model. Further, both substrate thickness and stiffness affect cellular and traction stresses [207]. The magnitude of the traction stress increases with substrate stiffness, saturating at large stiffness [56], and it decreases sharply with substrate thickness, indicating that cell

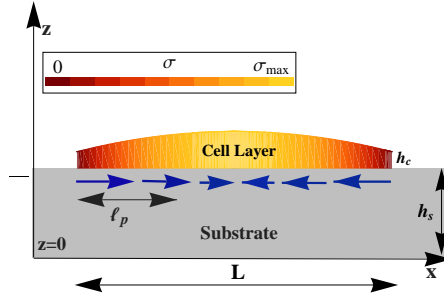


Figure 7.1: Schematic of a cell layer of lateral extent L and thickness $h_c \ll L$ adhering to a substrate of thickness h_s . The build-up of contractile stress σ in the cell layer is indicated by the color map, while the traction stresses in the substrate are shown as vectors (blue online). The spatial variation of both traction and cellular stresses in the lateral (x) direction are characterized by the length scale ℓ_p , referred to as the penetration length.

colonies on thick substrates only probe a portion of substrate of effective depth comparable to the lateral extent of the cell colony [208]. While previous studies have analyzed the deformations of finite-thickness substrates due to point traction forces on their surface [209, 210], our work considers the inhomogeneous traction due to an extended contractile cell layer. A central result for our work is the expression for the scaling parameter referred to as the lateral penetration length ℓ_p (Fig. 7.1). This length scale characterizes the in-plane spatial variations of both adhesion-induced traction stresses on the substrate and cellular stresses within the cell layer in terms of cell and substrate elastic and geometrical properties. Our model also quantifies the experimentally-observed role of substrate thickness h_s in controlling the mechanical response of adhering cell layers [207]. If h_s is small compared to the lateral extent L of the cell sheet, the substrate elasticity plays a negligible role in determining the mechanical response of the cell. This may explain why traction forces exerted by cell colonies with $L \gg h_s$ appear insensitive to substrate stiffness [85]. If, in contrast, $L \ll h_s$, then substrate nonlocality controls stress build-up in the cell sheet. This crossover may be observable in large cell colonies on thick substrates. Finally, the importance of long-range substrate elasticity has also been emphasized in recent models

of cells as active dipoles on a soft elastic matrix, where it is crucial in controlling cell adhesion [211, 212]. Long-range interfacial elastic stresses coupled with gel thickness have also been shown to have a profound effect on focal adhesion growth [61] and to enhance cell polarization [213, 214]. These important effects will not be discussed here.

7.2 Contractile cell on a thick substrate

To illustrate the importance of substrate nonlocality, we first analyze a single cell, modeled as a contractile spring of stiffness k_c and rest length ℓ_{c0} , adhering to a continuum substrate (described as an elastic continuum of Young's modulus E_s and Poisson's ratio ν_s) via two focal adhesion bonds (linear springs of stiffness k_a) located at x_1 and x_2 (Fig. 7.2, top left) [69]. This is motivated by the experimental observation that in adhering cells focal adhesions tend to be localized near the cell periphery [215]. For simplicity we consider a one dimensional model, where the cell lies on the x axis and the substrate lies in the $0 \leq z \leq h_s$ region of the xz plane. Contractile actomyosin fibers connect the focal adhesions and exert active forces of magnitude F_A . Once the cell has fully adhered, the cell-substrate system is in mechanical equilibrium. Force balance at x_1 and x_2 yields

$$k_a [u_1 - u^s(x_1)] = F_A - k_c(u_1 - u_2) , \quad (7.1a)$$

$$k_a [u_2 - u^s(x_2)] = -F_A + k_c(u_1 - u_2) , \quad (7.1b)$$

with u_i the displacements of the contact points x_i from their unstretched positions $x_2^0 - x_1^0 = \ell_{c0}$, and $u^s(x_i)$ the displacement of the substrate's surface at x_i . All displacements are defined with respect to an initial state where the cell has length ℓ_{c0} . The net contraction is then $\Delta\ell = \ell_{c0} - (x_2 - x_1) = u_1 - u_2$. The traction force by the cell on the substrate is localized at x_1 and x_2 , yielding a traction force density $f_T(x) = F_T\delta(x - x_1) - F_T\delta(x - x_2)$, with $F_T = F_A - k_c\Delta\ell$. Assuming linear elasticity,

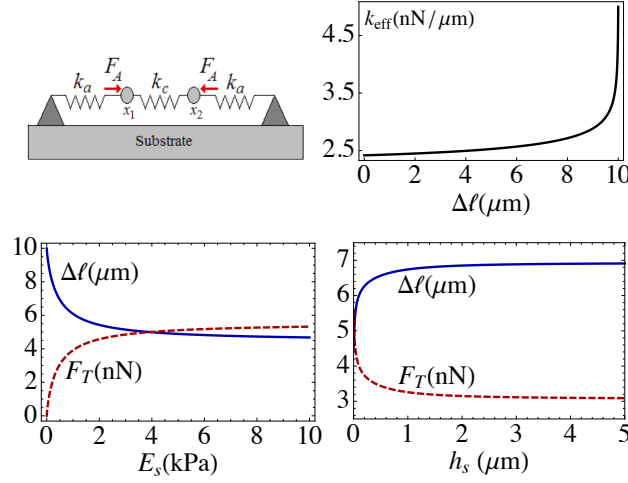


Figure 7.2: Top : Schematic of a contractile cell adhering to a soft substrate (left) and effective spring constant k_{eff} versus cellular strain $\Delta\ell$, showing strain stiffening (right). Bottom : Cell contraction $\Delta\ell$ (solid blue line) and traction force F_T (red dashed line) vs substrate stiffness (left) for $h_s = 10 \mu\text{m}$ and as a function of substrate thickness (right) for $E_s = 500 \text{ Pa}$. Other parameters : $F_A = 10 \text{ nN}$, $k_c = 1 \text{ nN}/\mu\text{m}$, $k_a = 2.5 \text{ nN}/\mu\text{m}$, $E_s = 1 \text{ kPa}$, $h_s = 10 \mu\text{m}$, $\ell_{c0} = 10 \mu\text{m}$, $\nu_s = 0.4$.

the substrate deformation is [216],

$$u^s(x) = \int_{-\infty}^{\infty} dx' G(x-x') f_T(x'), \quad (7.2)$$

where $G(x)$ is the elastic Green's function at $z = h_s$. For a substrate of thickness h_s we use the approximate form *

$$G(x) = \frac{2}{\pi \ell_{c0} E_s} K_0 \left[\frac{a + |x|}{h_s(1 + \nu_s)} \right] \quad (7.3)$$

derived in the Appendix, with a the size of adhesion complexes, providing a short-distance cut-off, and K_0 denotes the modified Bessel function of the second kind. We obtain $F_T(\Delta\ell) = \frac{1}{2} k_{\text{eff}}(\Delta\ell) \Delta\ell$, with $k_{\text{eff}}^{-1} = k_a^{-1} + [G(0) - G(\ell_{c0} - \Delta\ell)]$ the effective stiffness of the cell-substrate adhesions. For $\Delta\ell \ll \ell_{c0}$, k_{eff} is independent of $\Delta\ell$ and F_T scales linearly with $\Delta\ell$. Stiffening sets in for $\Delta\ell > \ell_{c0} |1 - h_s(1 + \nu_s)/\ell_{c0}|$, as shown

*To enable a direct comparison between the penetration lengths obtained below and experimentally accessible parameters, E_s is the Young modulus of a three dimensional elastic medium.

in Fig. 7.2 (top right), with a crossover controlled by the thickness of the substrate h_s .

Using $F_T = F_A - k_c \Delta \ell$, we solve for both $\Delta \ell$ and F_T , shown in Fig. 7.2 (bottom) as functions of the substrate thickness and stiffness. For very thin ($h_s \rightarrow 0$) or infinitely rigid substrates, where the substrate elasticity becomes local, $\Delta \ell = F_A / (k_c + k_a/2)$, corresponding to a spring k_c in parallel with a series of two focal adhesions springs k_a . In this limit the traction force saturates to $F_T = k_a F_A / (2k_c + k_a)$. Conversely, for a very soft substrate with $E_s \rightarrow 0$, the contraction is maximal and given by F_A / k_c , and $F_T \rightarrow 0$. The substrate thickness above which both cell contraction and traction force saturate is controlled by the cell size and the substrate elasticity, in qualitative agreement with experiments [207].

7.3 Contractile cell layer

The continuum limit can be obtained by considering a multi-mer of $N = [L/l_{c0}]$ contractile elemental “cells”, connected by springs representing cell-cell interactions. The outcome is a set of coupled equations for a contractile elastic medium. For a cell layer of thickness $h \ll L$ (Fig. 7.1), the force balance equation, averaged over the cell thickness, is

$$Y_a [u(x) - u^s(x)] = h \partial_x \sigma(x), \quad (7.4)$$

where $Y_a = k_a / (L l_{c0})$ describes the effective strength of the focal adhesions, $u(x)$ is the displacement field of the cellular medium at $z = h_s$, and σ is the thickness-averaged cellular stress tensor, $\sigma(x) = 1/h \int_{h_s}^{h_s+h} dz \sigma_{xx}(x, z)$, given by $\sigma(x) = B \partial_x u + \sigma_a$, with B the longitudinal elastic modulus of the cell layer. The one dimensional model presented here may be relevant to wound healing assays, where the cell layer is a strip with y -translational invariance. Although we have neglected components of the cellular displacements and spatial variations along z , the cell elastic constants are those of a three-dimensional cellular medium.

The active stress $\sigma_a = F_A/(Lh)$ arises from acto-myosin contractility. The substrate deformation at the surface is

$$u^s(x) = h \int dx' G(x - x') \partial'_x \sigma(x'), \quad (7.5)$$

with $G(x)$ the elastic Green's function of a substrate of infinite extent in x , occupying the region $0 \leq z \leq h_s$, evaluated at $z = h_s$. Eqs. (7.22)-(7.23) can be reduced to integro-differential equations for the cellular stress, as

$$\ell_a^2 \partial_x^2 \sigma + \sigma_a = \sigma - BLh \partial_x^2 \int_0^L dx' G(|x - x'|) \sigma(x'). \quad (7.6)$$

The length scale $\ell_a = \sqrt{Bh/Y_a}$ controls spatial variations of cellular stresses induced by the stiffness of the focal adhesions. It is the size of a region where the areal elastic energy density $Y_a \ell_a^2$ associated with focal adhesions is of order of the areal elastic energy density Bh of the cell layer. For a cell monolayer with $B = 1$ kPa, $h = 0.1$ μm , $L = 100$ μm , $\ell_{c0} = 10$ μm and $k_a = 2.5$ nN/ μm [55], we get $\ell_a \simeq 6.3$ μm , comparable to traction penetration length seen in experiments on stiff microposts [217, 218]. The second term on the right hand side of Eq. (7.6) describes spatial variations in the cellular stress due to the (generally nonlocal) coupling to the substrate. In the following we examine solutions to Eq. (7.6), considering various limiting cases for the substrate thickness and analyze the dependence of traction stresses on cell size, substrate stiffness and substrate depth. The equation governing stress distribution in two dimensional cell layers is derived in the Appendix.

7.3.1 Thin substrate

For completeness we revisit the case of a thin elastic substrate as was discussed in detail in Chapter 5. If the substrate's elastic response can be approximated as local, as it is the case for $h_s \ll L$ or for cells on micropillar arrays, the Green's function is given by

$$G(x) = \frac{2h_s(1 + \nu_s)}{LE_s} \delta(x).$$

Eq. (7.6) can then be written as $\ell_p^2 \partial_x^2 \sigma + \sigma_a = \sigma$, where, $\ell_p = \sqrt{Bh/Y_{\text{eff}}}$ and $Y_{\text{eff}}^{-1} = Y_a^{-1} + 2h_s(1 + \nu_s)/E_s$ describes the combined action of the focal adhesions and the substrate, acting like two linear elastic components in series. Assuming zero external stresses at the boundary, i.e., $\sigma(0) = \sigma(L) = 0$, the internal stress profile is $\sigma(x) = \sigma_a (1 - \cosh[(L - 2x)/2\ell_p] / \cosh[L/2\ell_p])$. The traction stress $T(x) = Y_{\text{eff}} u(x)$, is localized within a length ℓ_p from the edge of the cell layer. The penetration length ℓ_p can be written as $\ell_p = \sqrt{\ell_a^2 + \ell_s^2}$, with $\ell_s = \sqrt{\frac{2Bhh_s}{E_s/(1+\nu_s)}}$ the square root of the ratio of the cell's elastic energy to the elastic energy density of the substrate. This form highlights the interplay of focal adhesion stiffness and substrate stiffness in controlling spatial variation of stresses in the lateral (x) direction. The two act like springs in series, where the weaker spring controls the response. If $Y_a \ll \frac{E_s}{2(1+\nu_s)h_s}$, then $\ell_p \simeq \ell_a$ and the stiff substrate has no effect. Conversely, if the focal adhesions are stiffer than the substrate, then $\ell_p \simeq \ell_s$. For an elastic substrate with $h_s = 10 \mu\text{m}$, $\nu_s = 0.4$ and E_s in the range $0.01 - 100 \text{ kPa}$, ℓ_s lies in the range $0.2 - 17 \mu\text{m}$. This leads to typical values of ℓ_p in the range $6.3 - 18 \mu\text{m}$ for a cell layer of length $100 \mu\text{m}$, consistent with experimentally observed traction penetration lengths on thin continuous substrates [104] and on microposts [206].

7.3.2 Infinitely thick substrate

If $h_s \gg L$, the substrate Green's function can be approximated as that of an elastic half plane,

$$G(x) = -\frac{2}{\pi L E_s} [\gamma + \log(|x|/L)] ,$$

with γ the Euler constant [219]. The solution of Eq. (7.6) with boundary conditions $\sigma(0) = \sigma(L) = 0$ can be obtained by expanding $\sigma(x)$ in a Fourier sine series as, $\sigma(x) = \sum_{n=1}^{\infty} \sigma_n \sin(n\pi x/L)$ and solving the coupled algebraic equations for the Fourier amplitudes σ_n given in the Appendix. The effect of the nonlocal elasticity of the substrate is controlled by yet another length scale $\ell_{s\infty} = \sqrt{\frac{4BhL}{\pi E_s}}$ that can be obtained from the length ℓ_s introduced in the case of thin substrate by the replacement

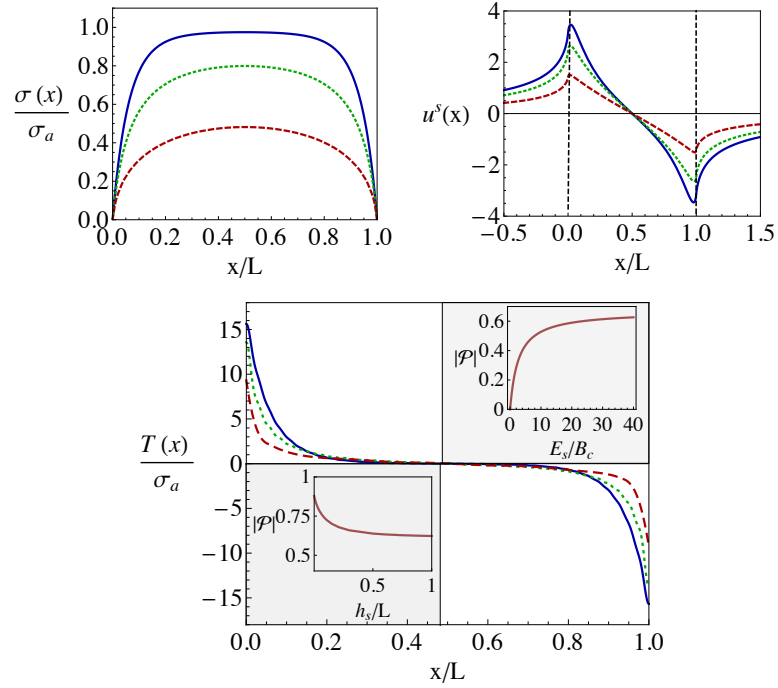


Figure 7.3: Internal stress $\sigma(x)/\sigma_a$ (top left), substrate displacement $u^s(x)$ (top right) and traction stress $T(x)/\sigma_a$ (bottom) vs position x along the cell layer, for $E_s = 500$ Pa (solid, blue), 50 Pa (dotted, green) and 10 Pa (dashed, red). The vertical dashed lines in the top right frame denote the cell layer's edges. Inset (bottom right): magnitude of contractile moment $|\mathcal{P}|$ vs E_s/B . Inset (bottom left): $|\mathcal{P}|$ as a function of substrate thickness for $E_s = 10$ Pa. Other parameters: $B = 1$ kPa, $h = 0.1 \mu\text{m}$, $\ell_a = 6.3 \mu\text{m}$, $L = 100 \mu\text{m}$, $\nu_s = 0.4$.

$h_s \rightarrow L$ and $(1+\nu_s) \rightarrow 2/\pi$. This highlights the known fact that cells or cell layers only “feel” the substrate up to a thickness comparable to their lateral size L . For parameter values quoted in the preceding paragraphs, $\ell_{s\infty}$ takes values between $0.35 - 35 \mu\text{m}$ for E_s in the range $0.01 - 100 \text{ kPa}$, indicating that the thin/thick substrate crossover, although not observable in isolated cells, should be seen experimentally in cohesive cell layers where the lateral extent can exceed $100 \mu\text{m}$. The cellular stress and substrate displacement profiles obtained numerically by summing the Fourier series are shown in Fig. 7.3 (top). The lateral variation of stresses is now controlled by the length scale $\ell_p = \sqrt{\ell_a^2 + \ell_{s\infty}^2}$. One consequence of nonlocal substrate elasticity is that the substrate deformation shown in the top right frame of Fig. 7.3 extends outside the region occupied by the cell layer, indicated by the two vertical dashed lines. The profile of the local traction stress displayed in Fig. 7.3 (bottom frame) shows that the traction stress is localized near the edge of the cell layer and its magnitude increases with substrate stiffness. The inset to Fig. 7.3 (bottom right) shows the magnitude of the net contractile moment defined as $\mathcal{P} = \int_{-\infty}^{\infty} dx x T(x)$. This quantity is negative, as expected for contractile systems. Its magnitude increases with E_s at a rate consistent with experiments, with a 25% rise in $|\mathcal{P}|$ upon increasing the substrate stiffness by 40% [186], and saturates for very stiff substrates.

7.3.3 Substrate of finite thickness

Finally, we consider a substrate of finite thickness, h_s . The calculations are carried out using the approximate Green’s function given in Eq. (7.3), with the replacement $\ell_{c0} \rightarrow L$. The variation of the net contractile moment with h_s for $E_s = 10 \text{ Pa}$ is shown in Fig. 7.3 (bottom left inset). As seen previously in experiments [207], $|\mathcal{P}|$ drops sharply with increasing substrate thickness, quickly reaching the asymptotic value corresponding to infinitely thick substrates. Thinner substrates are effectively stiffer than thick ones, inducing larger contractile moments. Our analysis suggests a general expression for the penetration length ℓ_p that interpolates between the thin

and thick substrates limits,

$$\ell_p = \sqrt{\frac{Bh}{Y_a} + \frac{Bh}{\pi E_s} h_{\text{eff}}} . \quad (7.7)$$

Stress penetration is controlled by a substrate layer of effective thickness $h_{\text{eff}}^{-1} = \frac{1}{h_s 2\pi(1+\nu_s)} + \frac{1}{L}$ given by the geometric mean of the actual substrate thickness h_s and the lateral dimension L of the cell or cell layer. If $h_s \ll L$, then $h_{\text{eff}} \approx 2\pi h_s(1+\nu_s)$ and stress penetration is not affected by cell layer size. On the other hand, if $h_s \gg L$, then cells only feel the effect of the substrate down to an effective depth L .

Appendix 7.A Green's Function for elastic substrate of finite thickness

Here we outline the derivation of the Green's function at the surface of the elastic substrate using Fourier techniques. We assume that the substrate is an isotropic and homogeneous elastic material in two dimensions, with Young's modulus E_s^{2d} [†] and Poisson ratio ν_s . The substrate displacement field is denoted by \mathbf{v} . In the plane stress approximation, the constitutive relation for the substrate stress is given as,

$$\sigma_{ij}^s = \frac{E_s^{2d}}{1+\nu_s} \left[\frac{\nu_s}{1-\nu_s} \nabla \cdot \mathbf{v} \delta_{ij} + \frac{1}{2} (\partial_i v_j + \partial_j v_i) \right] . \quad (7.8)$$

In equilibrium, the substrate deformations \mathbf{v} are governed by the standard equation of elastostatics for plane stress deformations,

$$\left(\frac{1-\nu_s}{1+\nu_s} \right) \nabla^2 \mathbf{v} + \nabla(\nabla \cdot \mathbf{v}) = 0 . \quad (7.9)$$

[†]The Young modulus E_s^{2d} of an elastic sheet has dimensions of force per unit length. In the preceding sections we express our results in terms of the Young modulus E_s of a three dimensional elastic medium, with dimensions of force per unit area. The reason for this choice is to express the various length scales in terms of experimentally accessible quantities. In general the two quantities can be related via a length scale d as $E_s^{2d} = E_s d$, with d describing the thickness of the substrate in the y direction normal to the direction of linear extent of the putative one-dimensional cell. We choose $d = \ell_{c0}$ when describing an individual cell and $d = L$ when describing a cell layer. The results do not depend on this length.

Turning to boundary conditions, we assume that there are negligible normal stresses at the substrate surface letting $\sigma_{zz}^s(z = h_s) = 0$. Assuming that the substrate is plated on a rigid surface, displacements at the bottom of the substrate are zero, $\mathbf{v}(z = 0) = 0$. The x -displacements at the top layer of the substrate, denoted by $u^s(x) = v_x(x, z = h_s)$, can then be written in terms of the Green's function of Eq. (7.9) as,

$$u^s(x) = \int_{x'} G(|x - x'|) \sigma_{xz}^s(x', z = h_s) . \quad (7.10)$$

The shear stress at the cell-substrate interface $\sigma_{xz}^s(x)|_{z=h_s}$, represents the traction stress exerted by the adherent cell. Working in Fourier space with respect to x , we write all functions as $f(x, z) = \int_{-\infty}^{\infty} dq f(q, z) e^{iqx}$. Eq.(7.9) then becomes,

$$\left(\frac{1 - \nu_s}{1 + \nu_s} \right) \partial_z^2 v_x + iq \partial_z v_z - \left(\frac{2}{1 + \nu_s} \right) q^2 v_x = 0 , \quad (7.11a)$$

$$\left(\frac{2}{1 + \nu_s} \right) \partial_z^2 v_z + iq \partial_z v_x - \left(\frac{1 - \nu_s}{1 + \nu_s} \right) q^2 v_z = 0 . \quad (7.11b)$$

Eqs. (7.11a) and (7.11b) can now be conveniently solved for \mathbf{v} with the given boundary conditions. In particular we seek the traction stress at the cell-substrate interface given by $T_x(q) = \sigma_{xz}(q, z = h_s)$ as a function of u_x^s . The final result can be compactly written as, $T_x(q) = Q(q)u^s(q)$, where

$$Q(q) = \mu_s q \frac{(3 - \nu_s)(1 + \nu_s)(e^{4h_s q} + 1) + 2e^{2h_s q} [(5 - 2\nu_s + \nu_s^2) + 2h_s^2 q^2 (1 + \nu_s)^2]}{(3 - \nu_s)(e^{4h_s q} - 1) + 4e^{2h_s q} h_s q (1 + \nu_s)} , \quad (7.12)$$

where $\mu_s = E_s^{2d}/2(1 + \nu_s)$ is the shear modulus of the substrate. The stiffness function $Q(q)$ is related to the elastic Green's function at the top surface of the substrate as,

$$G(x) = \frac{1}{2\pi} \int dq Q^{-1}(q) e^{-iqx} . \quad (7.13)$$

For long wavelengths $qh_s \ll 1$, which corresponds to a thin substrate, we get $Q(q) \rightarrow \mu_s/h_s$. The Green's function is then given by,

$$G(x) = \frac{h_s}{\mu_s} \delta(x) . \quad (7.14)$$

For short wavelengths $qh_s \gg 1$, corresponding to an elastic half-plane we obtain $Q(q) \rightarrow \mu_s q(1 + \nu_s)$, and the Green's function is given by

$$G(|x|) = -\frac{2}{\pi E_s^{2d}} [\gamma + \log(|x|/L)] . \quad (7.15)$$

For an elastic slab of finite thickness we use the following approximate form interpolating between the limits of thin and infinitely thick substrates,

$$Q \simeq \frac{\mu_s}{h_s} \sqrt{1 + [qh_s(1 + \nu_s)]^2} . \quad (7.16)$$

Fig. 7.4 shows a comparison between the exact stiffness function given in Eq. (7.12) and the interpolated form given in Eq. (7.16). Using Eq. (7.16) we can perform the Fourier inversion analytically to obtain the Green's function in real space in terms of a modified Bessel function of the second kind, as

$$G(x) = \frac{2}{\pi E_s^{2d}} K_0 \left[\frac{|x|}{h_s(1 + \nu_s)} \right] . \quad (7.17)$$

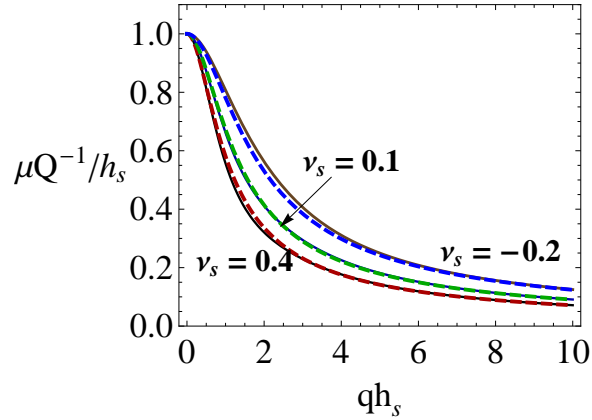


Figure 7.4: The inverse local stiffness $Q^{-1}\mu_s/h_s$ as a function of wavenumber qh_s , comparing the exact solution in Eq. (7.12) (solid lines) with the approximate form in Eq. (7.16) (dashed lines). Poisson ratios : $\nu_s = 0.1$ (green), $\nu_s = 0.4$ (red), $\nu_s = -0.2$ (blue).

Appendix 7.B One dimensional cell layer on elastic half plane

In this section we derive the solution for the internal stress distribution in a one-dimensional cell layer adhering to an elastic half plane, using the Green's function given by Eq. (7.15). The stress $\sigma(x)$ obeys the integro-differential equation,

$$\ell_a^2 \partial_x^2 \sigma + \sigma_a = \sigma + \frac{\ell_{s\infty}^2}{2L} \text{p.v.} \int_0^L dx' \frac{\sigma'(x')}{x-x'}, \quad (7.18)$$

where, $\ell_{s\infty} = \sqrt{4BhL/\pi E_s}$ and p.v. denotes principal value. We then expand $\sigma(x)$ in a Fourier sine series as $\sigma(x) = \sum_{n=1}^{\infty} \sigma_n \sin(n\pi x/L)$, which satisfies the boundary condition $\sigma|_{x=0} = \sigma|_{x=L} = 0$. Eq (7.18) then becomes,

$$\sigma_a = \sum_{n=1}^{\infty} \sigma_n \sin(\hat{n}x) [\hat{n}^2 \ell_a^2 + 1] + \frac{\ell_{s\infty}^2}{2L} \sum_{m=1}^{\infty} \hat{m} \sigma_m \int_0^L dx' \frac{\cos(\hat{m}x')}{x-x'}, \quad (7.19)$$

where $\hat{n} = n\pi/L$. We then integrate both sides of Eq. (7.19) by $\frac{2}{L} \int_0^L dx \sin(\hat{n}x)$ to reduce Eq. (7.18) to a linear system of algebraic equations for the Fourier mode amplitudes, σ_n , given by

$$\frac{2(1 - (-1)^n)}{n\pi} \sigma_a = (1 + \ell_a^2 \hat{n}^2) \sigma_n + \left(\frac{\ell_{s\infty}}{L}\right)^2 \sum_{m=1}^{\infty} H_{mn} \sigma_m, \quad (7.20)$$

where the dimensionless mode coupling matrix H_{mn} is given by,

$$H_{mn} = m\pi \int_0^1 dx' \int_0^1 dx \sin(n\pi x) \frac{1}{x-x'} \cos(m\pi x'). \quad (7.21)$$

H_{mn} can be analytically or numerically evaluated after regularizing the integral by providing a short-distance cut-off a as introduced earlier. Using computed values for H_{mn} , we solve numerically for the Fourier amplitudes σ_n , and then obtain $\sigma(x)$ by summing a series.

Appendix 7.C Two dimensional cell layers

For completeness we show here that the elastic deformation of a planar cell layer adhering to a two-dimensional substrate can also be described by a single equation

for the thickness-averaged stress tensor of the cellular material, although in general shear and compressional deformations are coupled. The case of a circular cell layer where spatial variation only occur along the radial direction can again be reduced to a one-dimensional problem. Considering a cell layer in the xy plane of thickness h in the z direction, with h small compared to the lateral dimension L of the layer, the force balance equation, averaged over the cell thickness, is

$$Y_a [u_i(\mathbf{x}) - u_i^s(\mathbf{x})] = h \partial_j \bar{\sigma}_{ij}(\mathbf{x}) , \quad (7.22)$$

where \mathbf{x} is a position in the xy plane, i, j denote in-plane cartesian components, Y_a describes the effective strength of the focal adhesions, $\mathbf{u}(\mathbf{x})$ is the two-dimensional displacement field of the cellular medium at $z = h_s$, and $\bar{\sigma}_{ij}$ is the in-plane cellular stress tensor averaged over the thickness of the cell, $\bar{\sigma}_{ij}(\mathbf{x}) = 1/h \int_{h_s}^{h_s+h} dz \sigma_{ij}(\mathbf{x}, z)$, given by $\bar{\sigma}_{ij}(\mathbf{x}) = B u_{kk} \delta_{ij} + 2\mu [u_{ij} - \delta_{ij} u_{kk}] + \sigma_a \delta_{ij}$, with B and μ the longitudinal and shear elastic moduli of the cell layer and σ_a is the isotropic active stress. Although we have neglected components of the cellular displacements along the cell thickness and spatial variations along z , the cell elastic constants are those of a three-dimensional cellular medium. The substrate deformation at the surface is

$$u_i^s(\mathbf{x}) = h \int d\mathbf{x}' G_{ij}(\mathbf{x} - \mathbf{x}') \partial'_k \bar{\sigma}_{jk}(\mathbf{x}') , \quad (7.23)$$

with \mathbf{G} the elastic Green's tensor of a substrate of infinite extent in the xy plane, occupying the region $0 \leq z \leq h_s$, evaluated at $z = h_s$. Eqs. (7.22)-(7.23) can be reduced to integro-differential equations for the cellular stress, as

$$\ell_a^2 [\partial_i \partial_k \bar{\sigma}_{kj}]^S + \delta_{ij} \sigma_a = \bar{\sigma}_{ij} + \frac{2\mu}{B - 2\mu} \delta_{ij} (\bar{\sigma}_{kk} - 2\sigma_a) - (B + 2\mu) h \int d\mathbf{x}' [\partial_i \partial_l G_{ik}(\mathbf{x} - \mathbf{x}') \bar{\sigma}_{kl}(\mathbf{x}')]^S , \quad (7.24)$$

where, $\ell_a = \sqrt{(B + 2\mu)h/Y_a}$, and $[\dots]^S$ denotes symmetrization with respect to indices that are not summed over, e.g., $[\partial_i \partial_k \bar{\sigma}_{kj}]^S = \frac{1}{2} [\partial_i \partial_k \bar{\sigma}_{kj} + \partial_j \partial_k \bar{\sigma}_{ki}]$. The one dimensional case can then be obtained by letting $\mu = 0$ and considering only spatial variations along x .

Chapter 8

Collective Mechanics of Adherent Cell Colonies

Mechanical interactions of individual cells play a crucial role in the spatial organization of tissues [220, 221] and in embryonic development [222–224]. The mechanical cooperation of cells is evident in dynamic processes such as flow-induced alignment of vascular endothelial cells [225] and muscle contraction [226]. However, mechanical interactions of cells within a tissue also affect the tissue’s static mechanical properties including elastic modulus [52], surface tension [227], and fracture toughness [228]. Little is known about how these tissue-scale mechanical phenomena emerge from interactions at the molecular and cellular levels [229].

In this chapter, we first describe measurements of traction forces in colonies of cohesive epithelial cells adherent to soft substrates. We find that the spatial distribution and magnitude of traction forces are more strongly influenced by the physical size of the colony than by the number of cells. For large colonies, the total traction force, \mathcal{F} , that the cell colony exerts on the substrate appears to scale as the equivalent radius, R , of the colony. This scaling suggests the emergence of a scale-free material property of the adherent tissue, an apparent surface tension of order 10^{-3} N/m. A simple physical model of adherent cell colonies as contractile elastic media captures

this behavior.

Next, we address the impact of intercellular adhesions on cell-ECM traction forces. We measure traction forces exerted by colonies of keratinocytes before, during, and after formation of cadherin-mediated intercellular adhesions. As cadherin-dependent junctions form, there is dramatic rearrangement of cell-ECM traction forces from a disorganized, punctate distribution underneath the colony to an organized concentration of force at the colony periphery. Through perturbations of cadherin-based adhesions, we demonstrate an essential role for cadherin in organizing cell-matrix mechanics. Finally, the spatial reorganization of cell-matrix forces is reproduced by a minimal physical model of a cell colony as two-dimensional objects connected by springs and adherent to a soft substrate. While downstream signaling pathways regulate responses to cadherin-based-junction formation, our experimental data and physical model suggest that the simple physical cohesion created by intercellular adhesions is sufficient to organize traction forces. These results have implications for intercellular adhesions' role in the mechanical relationship of tissues to their surroundings and the emergence of tissues' bulk material properties.

8.1 Cohesive epithelial cell colonies

8.1.1 Traction stress measurements

To measure traction stresses that the cells exert on their substrate, we used traction force microscopy (TFM) [46]. The TFM setup consisted of a film of highly elastic silicone gel with thickness $h_s = 27 \mu\text{m}$ on a rigid glass coverslip (Fig. 8.1A). Using bulk rheology, we estimated the Young's modulus of the gel to be 3 kPa. To quantify the gel deformation during the experiments, the substrates contained two dilute layers of fluorescent beads (radius 100 nm): one layer between the glass and gel and a second at height $z_o = 24 \mu\text{m}$ above the coverslip [58]. To image the fluorescent beads, spinning-disk confocal microscope was used. After determining bead positions using

centroid analysis in MATLAB [230], the deformation of the substrate was calculated, $u_i^s(\mathbf{r}, z_o)$, across its stressed (with cells) and unstressed (with cells removed) states. In Fourier space, the in-plane deformation field is related to the traction stresses at the surface of the substrate via linear elasticity, $\sigma_{iz}^s(\mathbf{k}, h_s) = Q_{ij}(\mathbf{k}, z_o, h_s)u_j^s(\mathbf{k}, z_o)$, where \mathbf{k} represents the in-plane wave vector. Here, $\sigma_{iz}^s(\mathbf{k}, h_s)$ and $u_j^s(\mathbf{k}, z_o)$ are the Fourier transforms of the in-plane traction stress on the top surface and the displacements just below the surface, respectively. The tensor, Q , depends on the thickness and modulus of the substrate, the location of the beads, and the wave vector [58, 231]. We calculated the strain energy density, $w(\mathbf{r}) = \frac{1}{2}\sigma_{iz}^s(\mathbf{r}, h_s)u_i^s(\mathbf{r}, h_s)$, which represents the work per unit area performed by the cell colony to deform the elastic substrate [47]. The deformation on the surface was determined using $u_i^s(\mathbf{k}, h_s) = Q_{ij}^{-1}(\mathbf{k}, h_s, h_s)Q_{jk}(\mathbf{k}, z_o, h_s)u_k^s(\mathbf{k}, z_o)$.

Primary mouse keratinocytes were isolated and cultured as described in [232]. We plated keratinocytes on fibronectin-coated TFM substrates. After the cells proliferated to the desired colony sizes over 6–72 hr, the concentration of CaCl_2 was raised in the growth medium from 0.05 mM to 1.5 mM. After 18–24 hr in the high-calcium medium, cadherin-based adhesions formed between adjacent keratinocytes, which organized themselves into cohesive single-layer cell colonies [233]. After imaging the beads in their stressed positions, we removed the cells by applying proteinase K and imaged the beads in their unstressed positions.

Stress fields and strain energy densities for representative colonies of one, two, and twelve keratinocytes are shown in Fig. 8.1. Traction stresses generically point inward, indicating that the colonies are adherent and contractile. Regions of high strain energy appear to be localized primarily at the periphery of the single- or multi-cell colony. For single cells, these findings are consistent with myriad previous reports on the mechanics of isolated, adherent cells [234–237]. Recent reports have also observed localization of high stress at the periphery of small cell colonies on micropatterned substrates [238] and at edges of cell monolayers [51, 206, 239]. To visualize cell–

cell and cell–matrix adhesions, we immunostained multi-cell colonies for E-cadherin and zyxin. Additionally, we stained the actin cytoskeleton with phalloidin. Actin stress fibers were concentrated at colony peripheries and usually terminated with focal adhesions, as indicated by the presence of zyxin at the fibers’ endpoints. In contrast, E-cadherin was localized at cell–cell junctions, typically alongside small actin fibers. Despite differences in the architecture of the relevant proteins, the stresses and strain energy distributions are remarkably similar in the single-cell and multi-cell colonies.

To explore these trends, traction stresses of 45 cohesive colonies of 1–27 cells were measured. For each colony, we defined an equivalent radius, R , as the radius of a disk with the same area. The equivalent radii ranged from 20 to 200 μm . We calculated the average strain energy density as a function of distance, Δ , from the colony edge (Fig. 8.2 inset). Figure 8.2 shows the normalized strain energy profiles, $\bar{w}(\Delta)/\bar{w}(0)$, of all 45 colonies. Usually, the strain energy density was largest near the colony edge ($\Delta = 0$). Because of the finite spatial resolution of the implementation of TFM, there were nonzero strain energy outside colony boundaries ($\Delta < 0$).

8.1.2 Effective surface tension

Next, we examined how global mechanical activity of the colony changes with the cell number and geometrical size of the colony. To this end, we calculated the “total traction force”,

$$\mathcal{F} = \int dA \sqrt{(\sigma_{xz}^s)^2 + (\sigma_{yz}^s)^2}, \quad (8.1)$$

exerted by the cell colony onto the substrate. This quantity is meaningful when stresses have radial symmetry and are localized at the colony edge, which is the case for the majority of colonies in this study. We observed a strong positive correlation between equivalent radius and total force over the range of colonies examined (Fig. 8.3). Similar trends have been seen for isolated cells over a smaller dynamic range of sizes [50, 240–242]. We see no systematic differences in \mathcal{F} for colonies of the

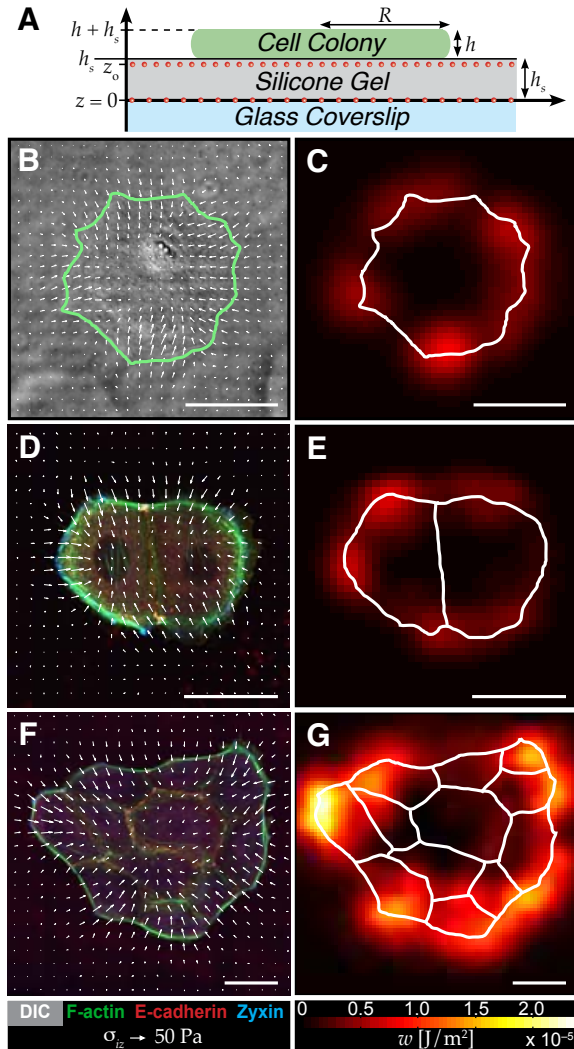


Figure 8.1: Traction stresses and strain energies for colonies of cohesive keratinocytes. (A) Schematic of experimental setup (not to scale) with a cell colony adherent to an elastic substrate embedded with two dilute layers of fluorescent beads. (B, D, F) Distribution of traction stresses, σ_{iz} , and (C, E, G) strain energy, w , for a representative single cell, pair of cells, and colony of 12 cells. Traction stress distribution is overlaid on a DIC image (B) or images of immunostained cells (D, F). Solid lines in (B–C, E, G) mark cell boundaries. For clarity, only one-quarter of the calculated stresses are shown in (B, D) and one-sixteenth of the stresses in (F). Scale bars in (B–G) represent $50 \mu\text{m}$.

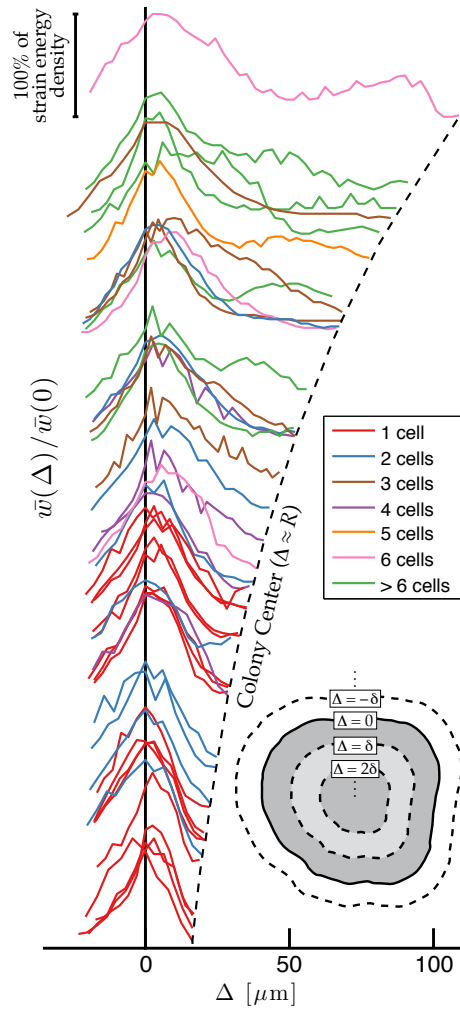


Figure 8.2: Spatial distribution of strain energy for colonies of different size. Each curve represents a colony's measured strain energy density as a function of distance from the edge of the colony, Δ . For clarity, the profiles are spaced vertically according to the size of the colony. Each profile terminates at the point where the inward erosion of the outer edge covers the entire area of the colony, at $\Delta \approx R$. The erosion proceeds in discrete steps of size δ , as illustrated in the inset.

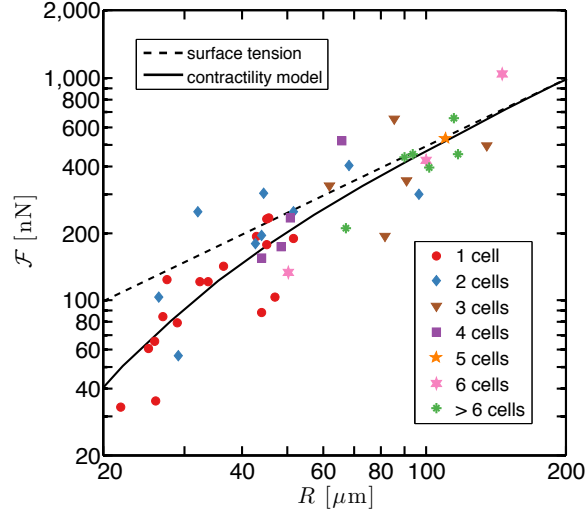


Figure 8.3: Mechanical output of keratinocyte colonies versus geometrical size. Total force transmitted to the substrate by the cell colonies, defined in Eq. (8.1), is plotted as a function of the equivalent radius of the colonies. The dashed line represents scaling expected for surface tension, $\mathcal{F} \sim R$. The solid line shows the a fit of the data to the minimal contractility model in Eq. (8.6).

same size having different numbers of cells, suggesting that cohesive cells cooperate to create a mechanically coherent unit.

The data in Fig. 8.3, while scattered, show clear monotonic growth of the mechanical output of cell colonies with their geometrical size, independent of the number of cells. For smaller colonies ($R < 60 \mu\text{m}$), the increase of total force with colony radius is superlinear. As the cell colonies get larger, the scaling exponent appears to approach unity. We hypothesize that the transition to an apparently consistent exponent for the large colonies reflects the emergence of a scale-free material property of a tissue, defined by the ratio $\mathcal{F}/(2\pi R) = (8 \pm 2) \times 10^{-4} \text{ N/m}$, with dimensions of surface tension.

Just as intermolecular forces yield the condensation of molecules into a dense phase, cohesive interactions between cells, mediated by cadherins, cause them to form dense colonies [81, 243]. For large ensembles of molecules, these molecular interactions manifest as an energy penalty per unit area for creating an interface between two phases, known as surface tension. It is tempting to think of the adherent colonies

studied here as aggregates of cohesive cells that have wet the surface [244]. Indeed, when matter wets a surface, the traction stresses are localized at the contact line [245], as we found in our cell colonies (Figs. 8.1 and 8.2).

Effective surface tension of cell agglomerates has been invoked to explain cell sorting and embryogenesis [246]. Previous measurements of non-adherent aggregates of cohesive cells reported effective surface tensions between 2 and 20 mN/m [227, 247, 248]. However, the origins of the effective surface tension of cohesive cells are distinct from conventional surface tension. Recently it was suggested that the surface tension is not only determined by contributions from cell–cell adhesions but also the contraction of acto-myosin networks [249, 250]. It is important to distinguish the effective surface tension due to active processes from the familiar surface tension defined in thermodynamic equilibrium. To elucidate the origin of the effective surface tension in these experiments, we consider the minimal physical model introduced in Chapter 5 and 7 to describe cell–substrate interactions.

8.1.3 Minimal physical model

We describe a cohesive colony as an active elastic disk of thickness h and radius R (Fig. 8.1A). The mechanical properties of the cell colony are assumed to be homogeneous and isotropic with Young’s modulus E and Poisson’s ratio ν . Acto-myosin contractility is modeled as a negative contribution to the local pressure. In our model, the strength of cell–cell adhesions is implicitly contained in the material parameters of the colony, E and ν . The constitutive equations for the stress tensor, σ_{ij} , of the colony are then given by

$$\sigma_{ij} = \frac{E}{2(1+\nu)} \left[\frac{2\nu}{1-2\nu} \nabla \cdot \mathbf{u} + \partial_i u_j + \partial_j u_i \right] + \sigma_a \delta_{ij}, \quad (8.2)$$

where \mathbf{u} is the displacement field of the cell colony and $\sigma_a > 0$ represents the active pressure due to actomyosin contractility. Mechanical equilibrium requires that $\partial_j \sigma_{ij} = 0$.

We use cylindrical coordinates and assume in-plane rotational symmetry. The top surface is stress-free, $\sigma_{rz}|_{z=h+h_s} = 0$, and we employ a simplified coupling of the colony to substrate. Ignoring all nonlocal effects arising from the substrate elasticity, $\sigma_{rz}|_{z=h_s} = Y u_r(z = h_s) \approx Y \bar{u}_r$. Here, u_r is the radial component of the displacement field, the bar denotes z -averaged quantities, and the rigidity parameter, Y , describes the coupling of the contractile elements of the cell to the substrate. The local equivalence of stress and displacement is accurate only when the substrate thickness is much smaller than the characteristic length scale of the stress distribution or when the cells are on substrates of soft posts [50].

With these assumptions, the equation of force-balance simplifies to

$$[\partial_r(r\bar{\sigma}_{rr}) - \bar{\sigma}_{\theta\theta}]/r = Y\bar{u}_r/h. \quad (8.3)$$

Combining Eqs. (8.2) and (8.3), we find the governing equation for the radial deformation, u_r :

$$r^2\partial_r^2 u_r + r\partial_r u_r - (1 + r^2/\ell_p^2) u_r = 0, \quad (8.4)$$

where the penetration length, ℓ_p , describing the localization of stresses near the boundary of the cell colony, is given by $\ell_p^2 = E(1 - \nu)h/[Y(1 + \nu)(1 - 2\nu)]$.

The solution of Eq. (8.4) with boundary conditions $u_r(r = 0) = 0$ and $\sigma_{rr}(r = R) = 0$ can be expressed in terms of modified Bessel functions as

$$u(r) = -\sigma_a \left[\frac{(1 + \nu)(1 - 2\nu)}{E(1 - \nu)} \right] R I_1(r/\ell_p) g(R/\ell_p), \quad (8.5)$$

with $[g(s)]^{-1} = sI_0(s) - (\frac{1-2\nu}{1-\nu}) I_1(s)$.

As in our experiments, the resulting deformations and traction stresses are localized near the colony edge (Fig. 8.2). To compare quantitatively to experiments, we calculate the total force,

$$\mathcal{F}(R) = 2\pi Y \left| \int_0^R r dr u_r(r) \right|. \quad (8.6)$$

In the large colony limit, for $R \gg \ell_p$, we find $\mathcal{F}(R) \simeq 2\pi\sigma_a h R \sim R$, yielding the anticipated linear growth of total force for large colonies. In this limit, the contractile active pressure dominates over internal elastic stresses and underlies the observed apparent surface tension.

The theory matches the scaling of the data reasonably well with $\ell_p = 11 \mu\text{m}$ and apparent surface tension $\sigma_a h \approx 8 \times 10^{-4} \text{ N/m}$, as shown by the solid line in Fig. 8.3. The penetration length, ℓ_p is comparable to the spatial resolution of the measurements. For single cells, recent measurements have suggested apparent surface tensions of $2 \times 10^{-3} \text{ N/m}$ in an endothelial cell [71] and $1 \times 10^{-4} \text{ N/m}$ in *Dictyostelium* cells [236]. From previously published data on a millimeter-scale adherent sheet of cohesive cells, we calculated the apparent surface tension by integrating the average stress profiles near the sheet edge and found a value of about $7 \times 10^{-4} \text{ N/m}$ [85]. For the keratinocyte cell colonies of thickness $h \approx 0.2 \mu\text{m}$, estimated from confocal imaging of phalloidin-stained colonies, the fitted value of the apparent surface tension implies $\sigma_a \approx 4 \text{ kPa}$. This value is consistent with that inferred from experiments in crawling keratocytes [32]. We can estimate the active pressure by assuming $\sigma_a \approx \rho_m k_m \Delta_m$, where ρ_m is the areal density of bound myosin motors, k_m the stiffness of motor filaments, and Δ_m their average stretch. Using $k_m \approx 1 \text{ pN/nm}$, $\Delta_m \approx 1 \text{ nm}$, and $\rho_m \approx 10^3 \mu\text{m}^{-2}$, we find $\sigma_a \approx 1 \text{ kPa}$.

8.2 Role of intercellular adhesions

8.2.1 Traction Stresses Systematically Reorganize in High-Calcium Medium

To investigate the relationship between cadherin-based intercellular adhesions and cell-matrix traction stresses, the formation of cadherin-based adhesions were induced in primary mouse keratinocytes by elevating extracellular-calcium concentrations. In low-calcium medium, keratinocytes plated at low density proliferated into colonies of

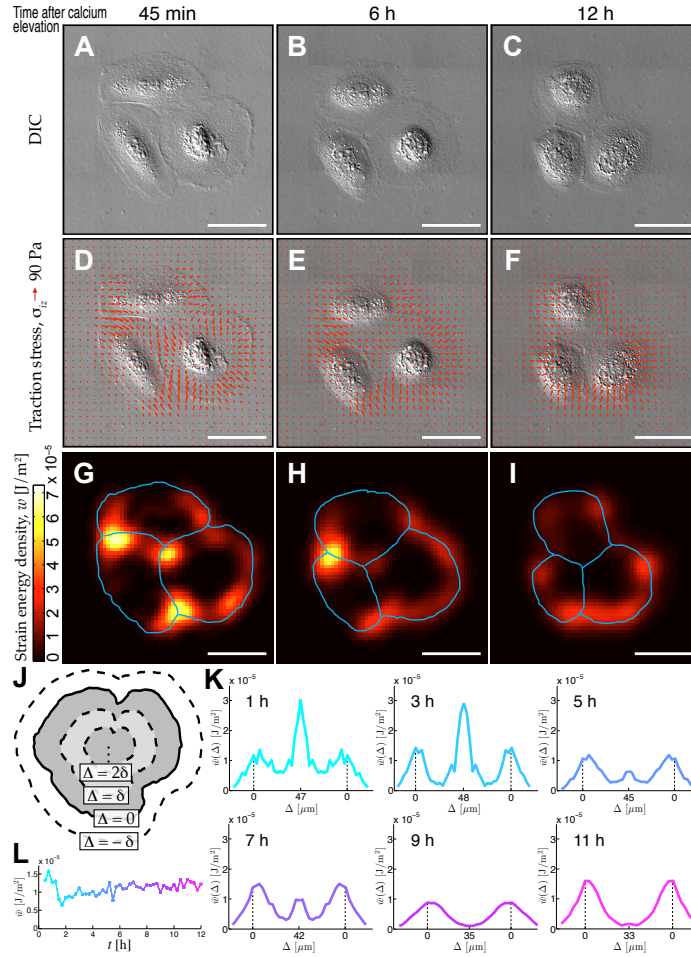


Figure 8.4: (A–C) DIC images of a three-cell colony at 45 min (A), 6 h (B), and 12 h (C) after calcium elevation. (D–F) Distribution of in-plane traction stresses (red arrows) for cell colony at timepoints in A–C overlaid on DIC images. For clarity, one-quarter of calculated traction stresses are shown. (G–I) Distribution of strain energy density, w , for cell colony at timepoints in A–C. Blue lines mark individual cell boundaries. (J) Schematic for calculating azimuthal-like averages for strain energy. Colony outline is eroded inward by distance, Δ , in discrete steps, δ , until entire colony area has been covered. Average strain energy density is then calculated for each concentric, annular-like region. (K) Strain energy profiles for three-cell colony at six timepoints after calcium elevation. Solid colored lines represent colony’s average strain energy density as a function of distance, Δ , from colony edge. Each profile is mirrored about $\Delta \approx R$, the effective colony radius. Colony periphery ($\Delta = 0$) is indicated by dashed vertical black lines. Strain energy at $\Delta < 0$ corresponds to regions outside colony periphery. (L) Average strain energy density for entire colony at 15 min intervals from 30 min to 12 h after calcium elevation. Plot colors in K and L are scaled according to time, t , after calcium elevation, from cyan at $t = 0$ to magenta at $t = 12$ h. Scale bars in A–I represent 50 μ m.

cells with weak cell–cell interactions. Exposing keratinocytes to high-calcium medium resulted in formation of cadherin-based cell–cell adhesions after 6–12 h.

Over 12 h in high-calcium medium, keratinocytes developed cell–cell junctions [233] and contracted [251] (Fig. 8.4 *A–C*). Prior to adhesion formation, in-plane traction stresses emanated from both the colony periphery and the interior junction of the three cells in a colony. Forces at the colony periphery pointed radially inward, while interior forces pointed in various directions (Fig. 8.4*D*). During the timecourse, traction stress in the middle of the colony gradually weakened (Fig. 8.4*E*), and by 12 h after calcium elevation, interior traction stress all but disappeared (Fig. 8.4*F*).

From substrate displacement and traction stresses, we calculated the strain energy density, w , the mechanical work per unit area performed by the colony to deform the substrate. Shortly after calcium elevation, high strain energy was localized both underneath and at the periphery of the colony (Fig. 8.4*G*). 12 h after calcium elevation, strain energy was limited to the colony edge (Fig. 8.4*I*).

To quantify these spatial changes, we calculated azimuthal-like averages of strain energy during the timecourse. We eroded the colony outline inward by distance, Δ , in discrete steps, δ , until the entire colony area was covered (Fig. 8.4*J*). We calculated the average strain energy, $\bar{w}(\Delta)$, in each of these concentric, annular-like regions and plotted it as a function of distance from the colony edge, Δ (Fig. 8.4*K*). During the first 3 h after calcium elevation, three peaks exist in the strain-energy profiles, corresponding to localization of strong strain energy at the colony periphery ($\Delta = 0$) and center. Between 5 and 9 h, the center strain-energy peak diminishes and disappears, and high strain energy is only at the colony periphery. We measured some strain energy outside the colony ($\Delta < 0$) due to the finite spatial resolution of our implementation of TFM.

Although strain-energy localization changed after calcium elevation, the colony’s overall average strain energy density was relatively consistent during the timecourse (Fig. 8.4*L*). Hotspots of strong strain energy (yellow regions in Fig. 8.4*G*) were no

longer present by the end of the experiment (Fig. 8.4I), but overall average strain energy density was compensated by a decrease in colony area.

To probe how intercellular adhesions alter traction forces across a large range of colony geometrical size and cell number, we analyzed the magnitude and localization of traction force in 32 keratinocyte colonies in low-calcium medium and 29 keratinocyte colonies after 24 h in high-calcium medium. A total of 117 low-calcium cells and 150 high-calcium cells comprised these colonies, each containing 2–27 cells, and spanned a geometrical dynamic range of nearly a factor of 100 in spread area.

In general, low-calcium colonies exhibited traction stresses throughout the colony, usually pointing radially inward from the colony edge and in various directions in the interior (Fig. 8.5A). Regions of high strain energy were found throughout the interior (Fig. 8.5B). In contrast, high-calcium colonies displayed traction stresses generically pointing radially inward from the colony edge (Fig. 8.5C) with hardly any strain energy beyond the colony edge (Fig. 8.5D). This observation is reminiscent of measurements on cohesive Madin-Darby canine kidney cells showing enhancement of traction force at the edges of cell pairs [86] and large cell sheets [85].

To quantify these spatial distributions, we plotted average strain energy density as a function of distance, Δ , from the colony edge (as depicted in Fig. 8.4J). Average strain energy densities, $\bar{w}(\Delta)$, were normalized by the average strain energy density at the colony periphery, $\bar{w}(0)$. These profiles (Fig. 8.5 E and F) terminate where inward erosion covered the entire area of the colony, at $\Delta \approx R$, where R is the effective radius of the colony, given by the radius of the disk with the same area as the colony.

In most low-calcium colonies, we observed some localization of strain energy at the colony periphery ($\Delta = 0$) and high amounts of strain energy throughout the colony ($\Delta > 0$), sometimes at the colony center ($\Delta \approx R$) (Fig. 8.5E). In contrast, the strain energy of nearly all the high-calcium colonies was strongly localized at the colony periphery, generally decaying to zero toward the colony center (Fig. 8.5F). Although this trend seems to hold regardless of number of cells in the colony, the

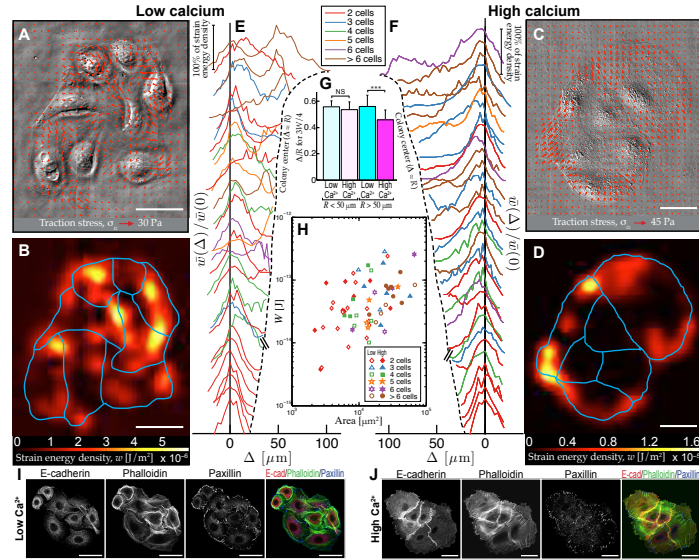


Figure 8.5: (A) Distribution of in-plane traction stresses (red arrows) of an eight-cell wildtype colony in low-calcium medium overlaid on DIC image of colony. For clarity, one-ninth of calculated traction stresses are shown. (B) Strain energy distribution, w , of low-calcium colony in C with individual cell outlines in blue. (C) Distribution of traction stresses (red arrows) of a six-cell wildtype colony in high-calcium medium for 24 h overlaid on DIC image of colony. For clarity, one-ninth of calculated traction stresses are shown. (D) Strain energy distribution, w , of high-calcium colony in E, with individual cell outlines in blue. (E) Strain energy profiles for $n = 32$ low-calcium colonies. (F) Strain energy profiles for $n = 29$ high-calcium colonies. In E and F, each solid curve represents a colony's average strain energy density as a function of distance, Δ , from colony edge. Each profile terminates where inward erosion covers entire colony area, at $\Delta \approx R$, the effective colony radius, indicated by dashed line. Average strain energy is normalized to value at colony periphery, $\bar{w}(0)$, giving each colony the same height on the graphs, indicated by the vertical scale bar. For clarity, profiles are spaced vertically according to colony size, with profiles for larger colonies (terminating at larger values of Δ) appearing higher up the y axis. Profile colors correspond to colony cell number given in the legend. (G) Quantification of relative distance from colony periphery (Δ/R) corresponding to 75% of total strain energy, $3W/4$, in colonies in low- or high-calcium medium. Small colonies ($R < 50 \mu\text{m}$, below hash marks in E and F), in low- ($n = 8$) or high-calcium ($n = 8$) medium showed no significant difference, whereas large ($R > 50 \mu\text{m}$) low-calcium colonies ($n = 24$) had significantly more strain energy closer to colony center than large high-calcium colonies ($n = 21$). (H) Relationship between total strain energy, W , and area, A , of colonies in low- and high-calcium medium. Open symbols correspond to low-calcium colonies, closed symbols to high-calcium colonies. Symbol colors indicate colony cell number, given in the legend. (I and J) Keratinocytes in low-calcium medium (I) or after 24 h in high-calcium medium (J) labeled with anti-E-cadherin and anti-paxillin antibodies and stained with phalloidin to mark F-actin. Scale bars in A–D, I, and J represent $50 \mu\text{m}$. Data for high-calcium colonies in F–H are adapted from [104].

difference is much less pronounced for the smallest colonies ($R \lesssim 50 \mu\text{m}$). The radii of small colonies are comparable to the traction-stress penetration length, ℓ_p , which measures how far from the periphery traction stresses penetrate the colony. Thus in small colonies, the stress measurements do not readily distinguish the colony center and periphery.

Next, we quantitatively compared the spatial distributions of strain energy across these two colony populations with and without cadherin-based intercellular adhesions. We calculated the total strain energy, W , exerted by each colony and the relative distance into the colony from its periphery, Δ/R , required to capture 75% of the total strain energy, $3W/4$. We separated larger colonies ($R \gg \ell_p$, or $R > 50 \mu\text{m}$) of the low- and high-calcium populations. Large, low-calcium colonies required on average 10% more inward erosion to achieve 75% of the total colony strain energy than large, high-calcium colonies, whereas there was no significant difference in strain energy distribution for the populations of small ($R < 50 \mu\text{m}$) colonies (Fig. 8.5*G*). These data suggest that formation of cadherin-based adhesions in high-calcium medium results in a shift in localization of traction stress from internal regions of the colony to the periphery.

The low- and high-calcium colonies did not seem to exhibit different amounts of average strain energy density. A plot of total strain energy versus colony area, A , while scattered, shows no apparent difference between these populations (Fig. 8.5*H*). In both cases, larger colonies tended to perform more work on the substrate.

Because low- and high-calcium keratinocyte colonies have different arrangements of cytoskeletal and adhesion proteins, we characterized spatial localizations of actin, E-cadherin-mediated cell–cell adhesions, and focal adhesions in keratinocyte colonies using phalloidin staining and immunohistochemistry. E-cadherin is highly expressed in keratinocytes, mediates adhesive activity, and is essential for adherens-junction formation. In high-calcium colonies, E-cadherin was localized at keratinocyte junctions (Fig. 8.5*I*). Positions of actin stress fibers were correlated with areas of strong

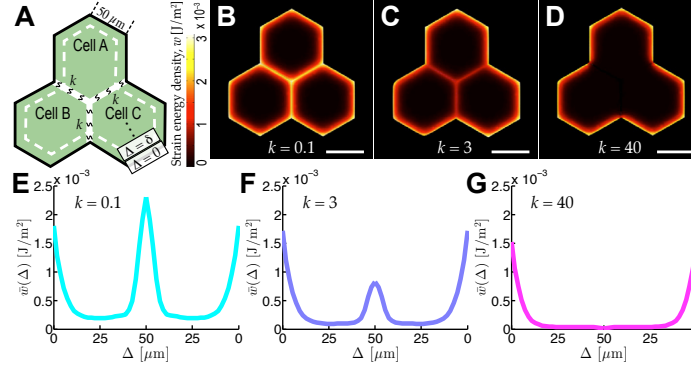


Figure 8.6: (A) Schematic of planar colony of three hexagonal cells. (B–D) Strain energy distributions for colony of three hexagonal cells with different spring stiffness, k , expressed in units of E/L , where E is the Young’s modulus of the cell and L the side length of each hexagon. (E–G) Spatial profiles of average strain energy as a function of distance, Δ , from colony edge for different values of k corresponding to data in B–D. Other parameters: $\ell_p/L = 0.2$, $E = 1$ kPa, $\nu = 0.4$, $\sigma_a = 4$ kPa, $h = 0.2$ μm , $Y = 2 \times 10^6$ N/m^3 (*SI Text*). Scale bars in B–D represent 50 μm .

E-cadherin localization, and there was coordination of the orientation of actin fibers across multiple cells, consistent with earlier reports on cytoskeletal rearrangement after calcium elevation [75]. While traction stresses of low- and high-calcium colonies had different spatial distributions, focal adhesions, marked by paxillin, were concentrated at the colony periphery in both cases.

8.2.2 Planar model of cell colonies as elastic media

Because of the simple spatial trends of traction stresses observed in colonies with and without intercellular adhesions, we examined whether a minimal physical model could reproduce the experimental results. We model each cell in a colony as a homogeneous and isotropic elastic material with constitutive relation given in Eq. (8.2) In our model, each cell exerts a contractile “pressure” σ_a opposed by strong adhesion to a compliant substrate. This model ignores all active processes modulated by cell–cell adhesions, including downstream signaling, and represents each intercellular adhesion as a purely physical connection described by linear springs. Cell–cell interactions are

then characterized by a spring constant k per unit area, exerting a harmonic force \mathbf{f} per unit area normal to the interface between two cells. The addition of springs translates into boundary conditions at the intercellular interfaces as $\sigma_{ij}n_j = f_i$, with \mathbf{n} denoting the outward unit normal. The edge of the colony, however, respects the stress-free boundary condition, $\sigma_{ij}n_j = 0$. We numerically solve the coupled elasticity equations subject to the aforementioned boundary conditions using the MATLAB PDE Toolbox. We evaluate strain energy density, w , given by $w = \frac{1}{2}\mathbf{T} \cdot \mathbf{u}$, where $\mathbf{T} = Y\mathbf{u}$ is the local traction stress exerted by the colony.

To mimic the cell geometry in the timecourse experiment (Fig. 8.4), we consider the case of three hexagonal cells (Fig. 8.6A). We find that, for increasing cell–cell-coupling strength, k , traction stress and strain energy disappear under cell–cell junctions (Fig. 8.6 B–D), recapitulating the transition seen in real cells stimulated by calcium elevation (Fig. 8.4 D–F). The similarity between model and experiment is also evident in plots of strain energy density as a function of distance from the colony edge (Fig. 8.6 E–G and Fig. 8.4K).

The model demonstrates the importance of intercellular-adhesion strength in spatially organizing cell-ECM forces. For weak cell–cell coupling (small k), individual cells deform the substrate independently of each other, with significant substrate deformation at all edges of each cell. On the other hand, strongly coupled colonies (large k) behave as a cohesive, contractile unit, with substrate deformation only at the colony periphery.

This planar model is an extension of an analytically tractable, one-dimensional model, described in detail below.

8.2.3 Model of cell colonies as elastic media in one dimension

As in the planar case, individual cells are described in one dimension as thin active elastic materials adherent to an elastic substrate. We consider N cells, each of rest length L/N and average height h , with cell–cell adhesions modeled by linear springs



Figure 8.7: Minimal one-dimensional picture of N cells adhering via cadherin-based adhesions, modeled as linear springs of stiffness k .

of stiffness k (Fig. 8.7). Let $\sigma^{(\alpha)}$ denote the internal stress in the α^{th} cell and $u^{(\alpha)}$ the corresponding displacement field. The one-dimensional constitutive relation and force-balance condition for the α^{th} cell are given by

$$\sigma^{(\alpha)}(x) = B\partial_x u^{(\alpha)} + \sigma_a \quad (8.7)$$

and

$$h\partial_x \sigma^{(\alpha)} = Y u^{(\alpha)}, \quad (8.8)$$

respectively, where B is the longitudinal elastic modulus of the cell. Internal stress distribution in the colony is then governed by equations

$$\ell_p^2 \partial_x^2 \sigma^{(\alpha)}(x) + \sigma_a = \sigma^{(\alpha)}(x) \text{ for } 1 \leq \alpha \leq N \quad (8.9)$$

subject to boundary conditions

$$\sigma^{(1)}|_{x=0} = 0, \quad (8.10a)$$

$$\begin{aligned} \sigma^{(\alpha)}|_{x=\alpha L/N} &= \sigma^{(\alpha+1)}|_{x=\alpha L/N} \\ &= k [u^{(\alpha+1)} - u^{(\alpha)}]|_{x=\alpha L/N} \text{ for } 1 \leq \alpha < N, \end{aligned} \quad (8.10b)$$

$$\sigma^{(N)}|_{x=L} = 0. \quad (8.10c)$$

For simplicity, we assume that the cell–cell adhesion springs have zero rest length and that the colony ends ($x = 0, L$) respect stress-free boundary conditions.

Explicit solutions for cellular stresses in an adherent cell-pair ($N = 2$) are given

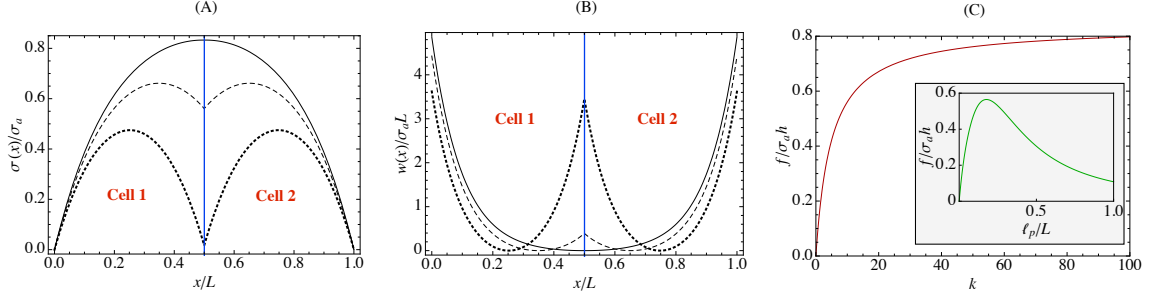


Figure 8.8: (A) Internal stress and (B) strain energy density in a one-dimensional adherent cell-pair for $kL/\sigma_a = 0.004$ (dotted), $kL/\sigma_a = 0.4$ (dashed), and $kL/\sigma_a = 40$ (solid). Parameters: $\ell_p/L = 0.2$, $B/\sigma_a = 2$, $h/L = 0.1$. (C) Intercellular force, f versus intercellular adhesion strength, k (in units of σ_a/L) for $\ell_p/L = 0.2$. Inset: f as a function of ℓ_p/L for $kL/\sigma_a = 10$.

by

$$\sigma^{(1)}(x)/\sigma_a = 1 - \exp\left(-\frac{x}{\ell_p}\right) \quad (8.11a)$$

$$+ \frac{2 \sinh\left(\frac{x}{\ell_p}\right) \left[\frac{2k\ell_p}{B} + \exp\left(\frac{L}{2\ell_p}\right) - 1 \right]}{\frac{2k\ell_p}{B} \left[1 + \exp\left(\frac{L}{\ell_p}\right) \right] + \exp\left(\frac{L}{\ell_p}\right) - 1},$$

$$\sigma^{(2)}(x)/\sigma_a = 2 \sinh\left(\frac{L-x}{2\ell_p}\right) \quad (8.11b)$$

$$\times \frac{\cosh\left(\frac{x}{2\ell_p}\right) - \cosh\left(\frac{L-x}{2\ell_p}\right) + \frac{2k\ell_p}{B} \sinh\left(\frac{x}{2\ell_p}\right)}{\frac{2k\ell_p}{B} \cosh\left(\frac{L}{2\ell_p}\right) + \sinh\left(\frac{L}{2\ell_p}\right)}.$$

For weak intercellular coupling, $k \ll B/\ell_p$, internal stresses are maximal at the center of individual cells and negligible at the cell–cell junction. For a strongly coupled cell-pair, $k \gg B/\ell_p$, internal stresses build up at the junction between the cells, which corresponds to the limit of a cohesive cell colony (Fig. 8.8A). In this case, internal stress takes the simple form

$$\frac{\sigma(x)}{\sigma_a} = 1 - \frac{\cosh\left(\frac{L-2x}{2\ell_p}\right)}{\cosh\left(\frac{L}{2\ell_p}\right)}. \quad (8.12)$$

Strain energy density, w , in the cell-pair is determined using $w(x) = \frac{1}{2}T(x)u(x)$, where the traction $T(x) = Yu(x)$. For a weakly coupled cell-pair ($k \rightarrow 0$), w is

localized at the edges of individual cells, and the net traction force on each individual cell vanishes. In contrast, a strongly cohesive cell-pair ($k \rightarrow \infty$) behaves as a single cell, with strain energy density localized at the edge of the pair and vanishing at the junction (Fig. 8.8B). For intermediate strengths of cell-cell adhesion, there is finite but small strain energy at the junction compared to the edges of the cell-pair. Traction force imbalance at each cell gives the estimate of the total force, f , transmitted to the intercellular adhesion,

$$\begin{aligned}
 f &= \left| \int_0^{L/2} dx T^{(1)}(x) \right| \\
 &= h |\sigma(0) - \sigma(L/2)| \\
 &= \frac{h\sigma_a \left| 1 - \cosh\left(\frac{L}{2\ell_p}\right) \right|}{\cosh\left(\frac{L}{2\ell_p}\right) + \frac{B}{2k\ell_p} \sinh\left(\frac{L}{2\ell_p}\right)} \\
 &\simeq h\sigma_a \frac{k}{k + B/2\ell_p} \text{ for } L \gg \ell_p.
 \end{aligned} \tag{8.13}$$

Intracellular force, f , grows monotonically with adhesion strength, k , before reaching a plateau when k is large (Fig. 8.8C). However, the dependence of f on penetration length, ℓ_p , which is inversely related to substrate stiffness, is non-monotonic (Fig. 8.8C, inset). This biphasic relation arises from the competition among different elastic components (cell, substrate, and the intercellular spring) connected in series. For small ℓ_p , the substrate is deformed less compared to the cells and to the intercellular spring, leading to a rise in intercellular force. A more compliant substrate with large ℓ_p is likely to accommodate larger cellular forces, reducing the net force transmitted to the intercellular adhesion.

In summary, our results show that cadherin-based cell-cell adhesions modulate force transmission to the ECM. In particular, our traction-force data on cohesive cell colonies suggest that intercellular-adhesion formation through classical cadherins reorganize the spatial distributions of traction stress. In colonies of cells with strong E-cadherin-based adhesions, cell-ECM traction stresses are localized in a ring around the colony periphery. In weakly cohesive colonies, regions of high traction stress ap-

pear throughout the colony. Comparison of our experimental data with our minimal physical model suggests that strong physical cohesion between cells is sufficient to drive the relocalization of cell-ECM forces to the periphery of cell colonies. While our data show that E-cadherin is necessary to reorganize traction forces, E-cadherin alone may not be sufficient. Further study is required to determine whether additional adhesive processes downstream of adherens junctions, such as the formation of desmosomes by nonclassical cadherins [252], are necessary to achieve sufficient cohesion.

Our findings resonate with recent studies on cellular adhesion pointing toward crosstalk of cadherin- and integrin-based adhesions. Focal adhesions have been observed to disappear underneath cell–cell contacts [88], but this effect may depend on substrate stiffness [90] and the extent of cell spreading [253]. Recent work has also suggested that forces transmitted through focal adhesions can modulate intercellular forces [86, 90], which in turn can modulate intercellular-junction assembly and disassembly [77]. Our study highlights intercellular adhesions’ ability to impact cell-ECM force generation, which allows for bidirectional feedback between cell–cell and cell-matrix forces. Indeed, tension at cadherin junctions [75] is known to elicit cell-signaling events and actin dynamics [254–256] and contribute to collective cell migration [87, 257]. In light of these prior results on integrin-cadherin feedback, it is somewhat surprising that a minimal physical model can capture the observed dependence of cell-matrix forces on the strength of cadherin-mediated cell–cell adhesions.

Reorganization of cell-ECM forces is likely one important mechanism by which cadherin-based adhesions drive tissue morphogenesis and homeostasis. In development, differential adhesion has been shown to play an important role in cell sorting [246], and the reorganization of intercellular forces in this context is entirely unexplored. Furthermore, in wound healing, we expect strong cell-ECM forces to be generated at a wound edge due to the local loss of intercellular adhesion. These forces could act as a signal, inducing migratory behavior in epithelial cells [85], activating

responses of stromal cells, and organizing the ECM [258, 259]. A key avenue for future investigations will be to explore how organization of force stimulates cellular responses within tissues.

Appendix 8.A Materials and Methods

Preparation of Substrates for Traction Force Microscopy

A borate buffer solution was made from deionized water with 3.8 mg/ml sodium tetraborate and 5 mg/ml boric acid. Silane (3-aminopropyl triethoxysilane) (Polysciences) was vapor-deposited onto 35 mm glass-bottom dishes (WillCo Wells) to allow fluorescent beads to be bonded to the surface. Beads were deposited by filling the dish with a solution containing dark-red fluorescent (660/680) carboxylate-modified microspheres with radius $0.1 \mu\text{m}$ (Life Technologies) at a volume ratio of 1:3,000 and 1 wt% 1-ethyl-3-(3-dimethylaminopropyl)carbodiimide (EDC) (Sigma-Aldrich) at a volume ratio of 1:100 in borate buffer. Silicone elastomer was then prepared by mixing a 1:1 weight ratio of CY52-276A and CY52-276B (Dow Corning Toray). After being degassed for 10 min, the elastomer was spin-coated onto the glass of the dish at 2,000 rpm for 60s. The dish was cured at 50°C for 3 min and resulted in an elastic film $\sim 21 \mu\text{m}$ thick. With the elastomer cross-linked, silane was vapor-deposited on the elastomer-coated dish. A second layer of fluorescent polystyrene beads was deposited at a higher concentration, volume ratios of 1:1,000 beads and 1:100 EDC in borate buffer. A second layer of fresh, degassed elastomer was spin-coated at 10,000 rpm for 90s resulting in a layer $\sim 3 \mu\text{m}$ thick. The sample was cured at RT overnight. We estimated the Young's modulus, E , of the cured elastomer to be $\sim 3 \text{ kPa}$ using bulk rheology. Before cells were plated, the elastomer surface was coated with fibronectin from bovine plasma (Sigma-Aldrich) at a concentration of 0.2 mg/ml, which sat for 20 min at RT before being washed off with PBS.

Confocal Microscopy

Images for TFM experiments were acquired using an Andor Revolution spinning-disk confocal system (Andor Technology) mounted on an inverted microscope (Nikon Eclipse Ti) with a Plan Apo 60 \times water-immersion objective lens with numerical aperture of 1.2 (Nikon). A 640 nm laser and DIC channel were used to image fluorescent beads and cells, respectively. Images were acquired with an iXon EMCCD camera with a resolution of 1,024 \times 1,024 pixels (Andor Technology). The field of view was 113 \times 113 μm^2 . Because a single field of view was too small to image an entire cell colony, between 9 and 42 fields of view per colony were acquired, with adjacent fields of view overlapping by $\sim 25\%$ and stitched together with sub-pixel precision by aligning bead positions in overlapping regions. The stage was controlled through Motion Controller/Driver SMC100CC high-speed motorized actuators (Newport). We imaged fluorescent beads with confocal image stacks of total thickness 5 μm to cover the beads' entire point-spread function in z . Confocal image slices were spaced 200 nm apart. These stacks were reduced to single images for particle-tracking by averaging the slices from five below to five above the slice with the highest total intensity.

Live-Cell Imaging

Confocal image stacks of the fluorescent beads were acquired for each cell condition. Control images of the beads in their unstressed state were acquired after removing the cells from the elastomer with proteinase K (Life Technologies) at 0.5 mg/ml for 5 min and then washing with PBS. The cells on the microscope were maintained at 37 $^\circ\text{C}$ using a heated microscope stage. pH was controlled using HEPES solution at 15mM (Sigma-Aldrich). To inhibit the formation of cadherin-based adhesions, we added anti-E-cadherin antibody DECMA-1 (Abcam) at 6 $\mu\text{g}/\text{ml}$ to the high-calcium medium. For consistency across cellular conditions, we controlled for colonies that deviated significantly from disk-shaped and contained cells with long protrusions by selecting for colonies whose actual perimeter, P , was no more than 1.5 times the

perimeter of a circle of the same area, A , as the colony ($P \leq 3\sqrt{\pi A}$).

Calculation of Traction Stresses and Strain Energies

After determining bead positions using centroid analysis in MATLAB [230], we calculated the deformation of the substrate, $u_i^s(\mathbf{r}, z_o)$, across its stressed (with cells) and unstressed (with cells removed) states, where z_o is the distance between the substrate bottom and the bead layer. In Fourier space, the deformation field is related to the traction stresses at the surface of the substrate, h_s , via linear elasticity, $\sigma_{iz}^s(\mathbf{k}, h_s) = Q_{ij}(\mathbf{k}, z_o, h_s)u_j^s(\mathbf{k}, z_o)$, where \mathbf{k} represents the in-plane wave vector. Here, $\sigma_{iz}^s(\mathbf{k}, h_s)$ and $u_j^s(\mathbf{k}, z_o)$ are the Fourier transforms of the traction stress on the top surface and the displacements of the bead layer just below the surface, respectively. The tensor, Q , depends on the thickness and modulus of the substrate, the location of the beads, and the wave vector [58, 231]. We calculated the strain energy density, $w(\mathbf{r}) = \frac{1}{2}\sigma_{iz}^s(\mathbf{r}, h_s)u_i^s(\mathbf{r}, h_s)$ [47]. The deformation on the surface was determined using $u_i^s(\mathbf{k}, h_s) = Q_{ij}^{-1}(\mathbf{k}, h_s, h_s)Q_{jk}(\mathbf{k}, z_o, h_s)u_k^s(\mathbf{k}, z_o)$. Because of their small size and immersion in a viscous medium, we expect the colonies of cells to be in mechanical equilibrium (net force of zero). Due to experimental error in determining substrate displacement fields, we occasionally calculated non-zero net traction forces on a colony. We discarded colonies with more than 15% residual force, $|\int dA (\sigma_{xz}^s \hat{x} + \sigma_{yz}^s \hat{y})| \geq 0.15 \int dA |\sigma_{xz}^s \hat{x} + \sigma_{yz}^s \hat{y}|$.

Primary Keratinocyte Culture

Primary wildtype keratinocytes were isolated as described [260]. Briefly, isolated backskin of newborn CD1 mice was floated on dispase overnight at 4°C. The epidermis was separated from the dermis with forceps and incubated in 0.25% trypsin for 10min at RT. Individual cells were released by trituration and plated on mitomycin-C-treated J2 fibroblasts in low-calcium medium (0.05mM CaCl₂). After 2–4 passages, cells were plated on plastic dishes without feeder cells. Primary keratinocytes were

also isolated as described [261] from newborn epidermis in which E-cadherin was conditionally deleted as described [262]. KO/KD cells were generated by lentiviral transduction of E-cadherin-deficient keratinocytes using shRNA directed against P-cadherin, as described [252]. Cadherin-junction formation was induced by raising the concentration of CaCl_2 of the low-calcium medium to 1.5mM.

Immunohistochemistry

Cells were fixed in 3.7% formaldehyde for 10min and then washed twice for 2min in PBS. A blocking solution of normal goat serum, normal donkey serum, bovine serum albumin, gelatin, and triton X in PBS was used to prevent non-specific binding. Cells were stained using 3,000 units/ μl Alexa Fluor 594 phalloidin (Life Technologies) and primary antibodies 8 ng/ μl monoclonal mouse anti-E-cadherin (TaKaRa) and 4 ng/ μl rabbit anti-paxillin (Sigma-Aldrich). After being washed in PBS, cells were incubated with secondary antibodies 8 ng/ μl goat anti-rabbit Alexa Fluor 488 (Life Technologies) and 8 ng/ μl goat anti-rat Alexa Fluor 647 (Life Technologies) and again with 3,000 units/ μl Alexa Fluor 594 phalloidin. Cells were then mounted in ProLong Gold with DAPI (Life Technologies).

Fluorescent images of immunohistochemical staining were acquired using confocal laser scanning microscopy on a Zeiss LSM 510 system equipped with Ar, HeNe 543, and HeNe 633 laser lines allowing imaging with lasers of wavelengths 488, 568, and 633 nm and a Plan Apo 40 \times oil-immersion objective with numerical aperture 1.3 (Zeiss). The field of view was $313 \times 313 \mu\text{m}^2$ with a maximum resolution of $2,048 \times 2,048$ pixels. The stage was controlled using an MCU 28 unit (Zeiss).

Statistical Analyses

Statistical significance for strain-energy distributions was assessed with p values determined by two-sided Student's t tests. Statistically significant p values were those lower than 0.05.

Bibliography

- [1] D. E. Discher, P. Janmey, and Y.-l. Wang, *Science* **310**, 1139 (2005).
- [2] J. Howard, *Mechanics of motor proteins and the cytoskeleton* (Sinauer Associates Sunderland, MA, 2001).
- [3] D. Bray, *Cell movements: from molecules to motility* (Routledge, 2000).
- [4] A. B. Verkhovsky, O. Y. Chaga, S. Schaub, T. M. Svitkina, J.-J. Meister, and G. G. Borisy, *Molecular biology of the cell* **14**, 4667 (2003).
- [5] M. Doi and S. F. Edwards, *The theory of polymer dynamics*, vol. 73 (Oxford University Press, USA, 1988).
- [6] F. Gittes, B. Mickey, J. Nettleton, and J. Howard, *The Journal of cell biology* **120**, 923 (1993).
- [7] F. Wottawah, S. Schinkinger, B. Lincoln, R. Ananthakrishnan, M. Romeyke, J. Guck, and J. Käs, *Physical review letters* **94**, 98103 (2005).
- [8] T. M. Svitkina and G. G. Borisy, *The Journal of cell biology* **145**, 1009 (1999).
- [9] J.-F. Joanny and J. Prost, *HFSP journal* **3**, 94 (2009).
- [10] F. Jülicher and J. Prost, *Physical review letters* **75**, 2618 (1995).
- [11] V. Schaller, C. Weber, C. Semmrich, E. Frey, and A. R. Bausch, *Nature* **467**, 73 (2010).

- [12] D. Riveline, A. Ott, F. Jülicher, D. A. Winkelmann, O. Cardoso, J.-J. Lacapère, S. Magnúsdóttir, J.-L. Viovy, L. Gorre-Talini, and J. Prost, *European biophysics journal* **27**, 403 (1998).
- [13] S. Banerjee, M. C. Marchetti, and K. Müller-Nedebock, *Physical Review E* **84**, 011914 (2011).
- [14] F. Ndlec, T. Surrey, A. C. Maggs, and S. Leibler, *Nature* **389**, 305 (1997).
- [15] S. Köhler, V. Schaller, and A. R. Bausch, *Nature materials* **10**, 462 (2011).
- [16] M. Gardel, J. Shin, F. MacKintosh, L. Mahadevan, P. Matsudaira, and D. Weitz, *Science* **304**, 1301 (2004).
- [17] P. M. Bendix, G. H. Koenderink, D. Cuvelier, Z. Dogic, B. N. Koeleman, W. M. Briehner, C. M. Field, L. Mahadevan, and D. A. Weitz, *Biophysical journal* **94**, 3126 (2008).
- [18] G. H. Koenderink, Z. Dogic, F. Nakamura, P. M. Bendix, F. C. MacKintosh, J. H. Hartwig, T. P. Stossel, and D. A. Weitz, *Proceedings of the National Academy of Sciences* **106**, 15192 (2009).
- [19] D. Mizuno, C. Tardin, C. Schmidt, and F. MacKintosh, *Science* **315**, 370 (2007).
- [20] A. Mansson, M. Balaz, N. Albet-Torres, K. J. Rosengren, et al., *Frontiers in bioscience: a journal and virtual library* **13**, 5732 (2008).
- [21] K. Kruse and F. Jülicher, *Current opinion in cell biology* **17**, 20 (2005).
- [22] T. Anazawa, K. Yasuda, and S. Ishiwata, *Biophysical journal* **61**, 1099 (1992).
- [23] D. G. Albertson et al., *Developmental biology* **101**, 61 (1984).
- [24] T. Sanchez, D. Welch, D. Nicastro, and Z. Dogic, *Science* **333**, 456 (2011).
- [25] S. Günther and K. Kruse, *New J. Phys.* **9**, 417 (2007).

- [26] R. Aditi Simha and S. Ramaswamy, *Physical review letters* **89**, 058101.1 (2002).
- [27] K. Kruse, J.-F. Joanny, F. Jülicher, J. Prost, and K. Sekimoto, *The European Physical Journal E: Soft Matter and Biological Physics* **16**, 5 (2005).
- [28] M. Marchetti, J.-F. Joanny, S. Ramaswamy, T. Liverpool, J. Prost, M. Rao, and R. A. Simha, arXiv preprint arXiv:1207.2929 (2012).
- [29] K. Kruse and F. Jülicher, *Physical review letters* **85**, 1778 (2000).
- [30] T. B. Liverpool and M. C. Marchetti, *EPL (Europhysics Letters)* **69**, 846 (2005).
- [31] P. Vallotton, G. Danuser, S. Bohnet, J.-J. Meister, and A. B. Verkhovsky, *Molecular biology of the cell* **16**, 1223 (2005).
- [32] K. Kruse, J. Joanny, F. Jülicher, and J. Prost, *Physical biology* **3**, 130 (2006).
- [33] R. J. Pelham and Y.-l. Wang, *Proceedings of the National Academy of Sciences* **94**, 13661 (1997).
- [34] M. Théry, A. Pépin, E. Dressaire, Y. Chen, and M. Bornens, *Cell motility and the cytoskeleton* **63**, 341 (2006).
- [35] U. S. Schwarz and M. L. Gardel, *Journal of Cell Science* **125**, 3051 (2012).
- [36] M. L. Gardel, I. C. Schneider, Y. Aratyn-Schaus, and C. M. Waterman, *Annual review of cell and developmental biology* **26**, 315 (2010).
- [37] D. Tsuruta, M. Gonzales, S. B. Hopkinson, C. Otey, S. Khuon, R. D. Goldman, and J. C. Jones, *The FASEB Journal* (2002).
- [38] K. K. Parker, A. L. Brock, C. Brangwynne, R. J. Mannix, N. Wang, E. Ostuni, N. A. Geisse, J. C. Adams, G. M. Whitesides, and D. E. Ingber, *The FASEB journal* **16**, 1195 (2002).

- [39] P. Roca-Cusachs, J. Alcaraz, R. Sunyer, J. Samitier, R. Farré, and D. Navajas, *Biophysical journal* **94**, 4984 (2008).
- [40] A. D. Rape, W.-h. Guo, and Y.-l. Wang, *Biomaterials* **32**, 2043 (2011).
- [41] A. J. Engler, S. Sen, H. L. Sweeney, and D. E. Discher, *Cell* **126**, 677 (2006).
- [42] T. Yeung, P. C. Georges, L. A. Flanagan, B. Marg, M. Ortiz, M. Funaki, N. Zahir, W. Ming, V. Weaver, and P. A. Janmey, *Cell motility and the cytoskeleton* **60**, 24 (2004).
- [43] A. Chopra, E. Tabdanov, H. Patel, P. A. Janmey, and J. Y. Kresh, *American Journal of Physiology-Heart and Circulatory Physiology* **300**, H1252 (2011).
- [44] A. K. Harris, P. Wild, D. Stopak, et al., *Science* **208**, 177 (1980).
- [45] D. Stopak and A. K. Harris, *Developmental biology* **90**, 383 (1982).
- [46] M. Dembo and Y.-L. Wang, *Biophysical Journal* **76**, 2307 (1999).
- [47] J. P. Butler, I. M. Tolić-Nørrelykke, B. Fabry, and J. J. Fredberg, *American Journal of Physiology-Cell Physiology* **282**, C595 (2002).
- [48] U. Schwarz, N. Balaban, D. Riveline, A. Bershadsky, B. Geiger, and S. Safran, *Biophysical journal* **83**, 1380 (2002).
- [49] W. R. Legant, C. K. Choi, J. S. Miller, L. Shao, L. Gao, E. Betzig, and C. S. Chen, *Proceedings of the National Academy of Sciences* **110**, 881 (2013).
- [50] J. L. Tan, J. Tien, D. M. Pirone, D. S. Gray, K. Bhadriraju, and C. S. Chen, *Proceedings of the National Academy of Sciences* **100**, 1484 (2003).
- [51] O. Du Roure, A. Saez, A. Buguin, R. H. Austin, P. Chavrier, P. Siberzan, and B. Ladoux, *Proceedings of the National Academy of Sciences of the United States of America* **102**, 2390 (2005).

- [52] A. Engler, L. Bacakova, C. Newman, A. Hategan, M. Griffin, and D. Discher, *Biophysical Journal* **86**, 617 (2004).
- [53] N. Zaari, P. Rajagopalan, S. K. Kim, A. J. Engler, and J. Y. Wong, *Advanced Materials* **16**, 2133 (2004).
- [54] A. Buxboim, K. Rajagopal, A. E. X. Brown, and D. E. Discher, *J. Phys.: Cond. Matt.* **22**, 194116 (2010).
- [55] N. Q. Balaban, U. S. Schwarz, D. Riveline, P. Goichberg, G. Tzur, I. Sabanay, D. Mahalu, S. Safran, A. Bershadsky, L. Addadi, et al., *Nature cell biology* **3**, 466 (2001).
- [56] M. Ghibaudo, A. Saez, L. Trichet, A. Xayaphoummine, J. Browaeys, P. Silberzan, A. Buguin, and B. Ladoux, *Soft Matter* **4**, 1836 (2008).
- [57] M. L. Gardel, B. Sabass, L. Ji, G. Danuser, U. S. Schwarz, and C. M. Waterman, *The Journal of cell biology* **183**, 999 (2008).
- [58] Y. Xu, W. C. Engl, E. R. Jerison, K. J. Wallenstein, C. Hyland, L. A. Wilen, and E. R. Dufresne, *Proceedings of the National Academy of Sciences* **107**, 14964 (2010).
- [59] A. Nicolas, B. Geiger, and S. A. Safran, *Proceedings of the National Academy of Sciences of the United States of America* **101**, 12520 (2004).
- [60] T. Shemesh, B. Geiger, A. D. Bershadsky, and M. M. Kozlov, *Proceedings of the National Academy of Sciences of the United States of America* **102**, 12383 (2005).
- [61] A. Nicolas and S. Safran, *Biophysical journal* **91**, 61 (2006).
- [62] A. Besser and S. A. Safran, *Biophysical journal* **90**, 3469 (2006).

- [63] I. L. Novak, B. M. Slepchenko, A. Mogilner, and L. M. Loew, *Physical review letters* **93**, 268109 (2004).
- [64] R. Bruinsma, *Biophysical journal* **89**, 87 (2005).
- [65] J. D. Eshelby, *Proceedings of the Royal Society of London. Series A. Mathematical and Physical Sciences* **241**, 376 (1957).
- [66] A. Zemel, F. Rehfeldt, A. Brown, D. Discher, and S. Safran, *Nature physics* **6**, 468 (2010).
- [67] B. M. Friedrich and S. A. Safran, *EPL (Europhysics Letters)* **93**, 28007 (2011).
- [68] V. S. Deshpande, R. M. McMeeking, and A. G. Evans, *Proceedings of the National Academy of Sciences* **103**, 14015 (2006).
- [69] U. Schwarz, T. Erdmann, and I. Bischofs, *Biosystems* **83**, 225 (2006).
- [70] R. Bar-Ziv, T. Tlusty, E. Moses, S. A. Safran, and A. Bershadsky, *Proceedings of the National Academy of Sciences* **96**, 10140 (1999).
- [71] I. B. Bischofs, S. S. Schmidt, and U. S. Schwarz, *Physical review letters* **103**, 48101 (2009).
- [72] C. A. Lemmon, N. J. Sniadecki, S. A. Ruiz, J. L. Tan, L. H. Romer, and C. S. Chen, *Mechanics & chemistry of biosystems: MCB* **2**, 1 (2005).
- [73] T. Yeung, P. C. Georges, L. A. Flanagan, B. Marg, M. Ortiz, M. Funaki, N. Zahir, W. Ming, V. Weaver, and P. A. Janmey, *Cell motility and the cytoskeleton* **60**, 24 (2005).
- [74] A. C. Martin, M. Gelbart, R. Fernandez-Gonzalez, M. Kaschube, and E. F. Wieschaus, *Journal of Cell Biology* **188**, 735 (2010).

- [75] A. Vaezi, C. Bauer, V. Vasioukhin, and E. Fuchs, *Developmental Cell* **3**, 367 (2002).
- [76] G. Fenteany, P. A. Janmey, and T. P. Stossel, *Current Biology* **10**, 831 (2000).
- [77] Z. J. Liu, J. L. Tan, D. M. Cohen, M. T. Yang, N. J. Sniadecki, S. A. Ruiz, C. M. Nelson, and C. S. Chen, *Proceedings of the National Academy of Sciences* **107**, 9944 (2010).
- [78] N. Borghi, M. Sorokina, O. G. Shcherbakova, W. I. Weis, B. L. Pruitt, W. J. Nelson, and A. R. Dunn, *Proceedings of the National Academy of Sciences* **109**, 12568 (2012).
- [79] J. H.-C. Wang and J.-S. Lin, *Biomechanics and Modeling in Mechanobiology* **6**, 361 (2007).
- [80] B. Sabass, M. L. Gardel, C. M. Waterman, and U. S. Schwarz, *Biophysical Journal* **94**, 207 (2008).
- [81] R. A. Foty and M. S. Steinberg, *Developmental Biology* **278**, 255 (2005).
- [82] B. Ladoux, E. Anon, M. Lambert, A. Rabodzey, P. Hersen, A. Buguin, P. Silberzan, and R. M. Mège, *Biophysical Journal* **98**, 534 (2010).
- [83] N. Borghi, M. Lowndes, V. Maruthamuthu, M. L. Gardel, and W. J. Nelson, *Proceedings of the National Academy of Sciences* **107**, 13324 (2010).
- [84] T. T. Onder, P. B. Gupta, S. A. Mani, J. Yang, E. S. Lander, and R. A. Weinberg, *Cancer Research* **68**, 3645 (2008).
- [85] X. Trepant, M. Wasserman, T. Angelini, E. Millet, D. Weitz, J. Butler, and J. Fredberg, *Nature physics* **5**, 426 (2009).
- [86] V. Maruthamuthu, B. Sabass, U. S. Schwarz, and M. L. Gardel, *Proceedings of the National Academy of Sciences* **108**, 4708 (2011).

- [87] D. Tambe, C. Hardin, T. Angelini, K. Rajendran, C. Park, X. Serra-Picamal, E. Zhou, M. Zaman, J. Butler, D. Weitz, et al., *Nature materials* **10**, 469 (2011).
- [88] S. Yamada and W. J. Nelson, *The Journal of cell biology* **178**, 517 (2007).
- [89] J. Tsai and L. Kam, *Biophysical Journal* **96**, L39 (2009).
- [90] M. L. McCain, H. Lee, U. Aratyn-Schaus, A. G. Kléber, and K. K. Parker, *Proceedings of the National Academy of Sciences* **109**, 9881 (2012).
- [91] J. de Rooij, A. Kerstens, G. Danuser, M. A. Schwartz, and C. M. Waterman-Storer, *Journal of Cell Biology* **171**, 153 (2005).
- [92] Q. Tseng, E. Duchemin-Pelletier, A. Deshiere, M. Balland, H. Guilloud, O. Filhol, and M. Théry, *Proceedings of the National Academy of Sciences* **109**, 1506 (2012).
- [93] C. Martinez-Rico, F. Pincet, J.-P. Thiery, and S. Dufour, *Journal of Cell Science* **123**, 712 (2010).
- [94] G. F. Weber, M. A. Bjerke, and D. W. DeSimone, *Journal of Cell Science* **124**, 1183 (2011).
- [95] A. Jasaitis, M. Estevez, J. Heysch, B. Ladoux, and S. Dufour, *Biophysical Journal* **103**, 175 (2012).
- [96] R. Krishnan, D. D. Klumpers, C. Y. Park, K. Rajendran, X. Trepate, J. van Bezu, V. W. van Hinsbergh, C. V. Carman, J. D. Brain, J. J. Fredberg, et al., *American Journal of Physiology – Cell Physiology* **300**, C146 (2011).
- [97] S. Banerjee and M. C. Marchetti, *Soft Matter* **7**, 463 (2010).
- [98] S. Banerjee, T. B. Liverpool, and M. C. Marchetti, *EPL (Europhysics Letters)* **96**, 58004 (2011).

- [99] S. Banerjee and M. C. Marchetti, *EPL (Europhysics Letters)* **96**, 28003 (2011).
- [100] C. M. Edwards and U. S. Schwarz, *Physical Review Letters* **107**, 128101 (2011).
- [101] S. Banerjee and M. C. Marchetti, *Physical Review Letters* **109**, 108101 (2012).
- [102] S. Banerjee and M. C. Marchetti, *New Journal of Physics* **15**, 035015 (2013).
- [103] S. Banerjee and L. Giomi, *Soft Matter* (2013).
- [104] A. F. Mertz, S. Banerjee, Y. Che, G. K. German, Y. Xu, C. Hyland, M. C. Marchetti, V. Horsley, and E. R. Dufresne, *Physical Review Letters* **108**, 198101 (2012).
- [105] A. F. Mertz, Y. Che, S. Banerjee, J. M. Goldstein, K. A. Rosowski, S. F. Revilla, C. M. Niessen, M. C. Marchetti, E. R. Dufresne, and V. Horsley, *Proceedings of the National Academy of Sciences* **110**, 842 (2013).
- [106] K. Guevorkian, M.-J. Colbert, M. Durth, S. Dufour, and F. Brochard-Wyart, *Physical review letters* **104**, 218101 (2010).
- [107] T. Butt, T. Mufti, A. Humayun, P. B. Rosenthal, S. Khan, S. Khan, and J. E. Molloy, *J. Biol. Chem.* **285**, 4964 (2010).
- [108] M. F. Copeland and D. B. Weibel, *Soft Matter* **5**, 1174 (2009).
- [109] T. Guérin, J. Prost, P. Martin, and J.-F. Joanny, *Curr. Op. Cell Biol.* **22**, 14 (2010).
- [110] F. Jülicher and J. Prost, *Phys. Rev. Lett.* **78**, 4510 (1997).
- [111] S. W. Grill, K. Kruse, and F. Jülicher, *Phys. Rev. Lett.* **94**, 108104 (2005).
- [112] A. Vilfan and E. Frey, *Journal of Physics: Condensed Matter* **17**, S3901 (2005).
- [113] S. Camalet and F. Jülicher, *New Journal of Physics* **2**, 24 (2000).

- [114] M. Badoual, F. Jülicher, and J. Prost, Proc. Natl. Acad. Sci. USA **99**, 6696 (2002).
- [115] P. Y. Plaçais, M. Balland, T. Guérin, J.-F. Joanny, and P. Martin, Phys. Rev. Lett. **103**, 158102 (2009).
- [116] F. Gibbons, J. F. Chauwin, M. Despósito, and J. V. José, Biophys. J. **80**, 2515 (2001).
- [117] P. Kraikivski, R. Lipowsky, and J. Kierfeld, Phys. Rev. Lett. **96**, 258103 (2006).
- [118] C. J. Brokaw, Proc. Natl. Acad. Sci. USA **72**, 3102 (1975).
- [119] A. Vilfan, E. Frey, and F. Schwabl, Europhys. Lett. **283**, 45 (1999).
- [120] D. Hexner and Y. Kafri, Phys Biol **6**, 036016 (2009).
- [121] T. Guérin, J. Prost, and J.-F. Joanny, Phys. Rev. Lett. **104**, 248102 (2010).
- [122] A. F. Huxley, Prog. Biophys. Chem. **7**, 255 (1957).
- [123] A. Vilfan, Biophys. J. **11301137**, 2515 (2009).
- [124] S. van Teeffelen and H. Löwen, Phys. Rev. E **78**, 020101 (2008).
- [125] A. Baskaran and M. C. Marchetti, Phys. Rev. Lett. **101**, 268101 (2008).
- [126] K. Svoboda and S. M. Block, Cell **77**, 773 (1994).
- [127] A. Parmeggiani, F. Jülicher, L. Peliti, and J. Prost, Europhys. Lett. **56**, 603 (2001).
- [128] K. Visscher, M. J. Schnitzer, and S. M. Block, Nature **400**, 184 (1999).
- [129] K. Tawada and K. Sekimoto, Journal of Theoretical Biology **150**, 193 (1991), ISSN 0022-5193.

- [130] N. Kikuchi, A. Ehrlicher, D. Koch, J. A. Käs, S. Ramaswamy, and M. Rao, Proceedings of the National Academy of Sciences **106**, 19776 (2009).
- [131] C. P. Brangwynne, G. H. Koenderink, F. C. MacKintosh, and D. A. Weitz, Phys. Rev. Lett. **100**, 118104 (2008).
- [132] Y. Han, A. Alsayed, M. Nobili, J. Zhang, T. C. Lubensky, and A. G. Yodh, Science **314**, 626 (2006).
- [133] D. Karpeev, I. S. Aranson, L. S. Tsimring, and H. G. Kaper, Phys. Rev. E **76**, 051905 (2007).
- [134] T. B. Liverpool, Phys. Rev. E **67**, 031909 (2003).
- [135] B. Alberts, A. Johnson, J. Lewis, M. Raff, K. Roberts, and P. Walter, *Molecular biology of the cell* (Garland, 2002), 4th ed., ISBN 0815332181.
- [136] K. Kruse, J. Joanny, F. Jülicher, J. Prost, and K. Sekimoto, Physical review letters **92**, 78101 (2004).
- [137] R. Voituriez, J. Joanny, and J. Prost, EPL (Europhysics Letters) **70**, 404 (2007).
- [138] L. Giomi, M. C. Marchetti, and T. B. Liverpool, Physical review letters **101**, 198101 (2008).
- [139] T. Surrey, F. Nédélec, S. Leibler, and E. Karsenti, Science **292**, 1167 (2001).
- [140] I. S. Aranson and L. S. Tsimring, Physical Review E **71**, 050901 (2005).
- [141] I. S. Aranson and L. S. Tsimring, Physical Review E **74**, 031915 (2006).
- [142] T. B. Liverpool and M. C. Marchetti, Physical review letters **90**, 138102 (2003).
- [143] A. Ahmadi, T. B. Liverpool, and M. C. Marchetti, Phys. Rev. E **72**, 060901 (2005).

- [144] Y. Hatwalne, S. Ramaswamy, M. Rao, and R. A. Simha, Physical review letters **92**, 118101 (2004).
- [145] T. Liverpool and M. C. Marchetti, Physical review letters **97**, 268101 (2006).
- [146] L. Giomi, T. B. Liverpool, and M. C. Marchetti, Physical Review E **81**, 051908 (2010).
- [147] M. Cates, S. Fielding, D. Marenduzzo, E. Orlandini, and J. Yeomans, Physical review letters **101**, 68102 (2008).
- [148] S. Pellegrin and H. Mellor, Journal of cell science **120**, 3491 (2007).
- [149] M. Rubinstein and R. Colby, *Polymer Physics (Chemistry)* (Oxford University Press, USA, 2003).
- [150] F. C. MacKintosh and A. J. Levine, Physical review letters **100**, 18104 (2008).
- [151] A. J. Levine and F. MacKintosh, The Journal of Physical Chemistry B **113**, 3820 (2009).
- [152] T. Liverpool, M. C. Marchetti, J.-F. Joanny, and J. Prost, EPL (Europhysics Letters) **85**, 18007 (2009).
- [153] A. J. Levine and T. C. Lubensky, Phys. Rev. E **63**, 041510 (2001).
- [154] A. J. Levine and T. C. Lubensky, Phys. Rev. Lett. **85**, 1774 (2000).
- [155] D. Head and D. Mizuno, Physical Review E **81**, 041910 (2010).
- [156] D. Humphrey, C. Duggan, D. Saha, D. Smith, and J. Kas, Nature **416**, 413 (2002).
- [157] J. Denoth, E. STÜSSI, G. Csucs, and G. Danuser, Journal of theoretical biology **216**, 101 (2002).

- [158] J. Murray and G. Oster, *Mathematical Medicine and Biology* **1**, 51 (1984).
- [159] G. M. Odell, G. Oster, P. Alberch, and B. Burnside, *Developmental biology* **85**, 446 (1981).
- [160] O. Thoumine and A. Ott, *Journal of cell science* **110**, 2109 (1997).
- [161] D. Mitrossilis, J. Fouchard, A. Guiroy, N. Desprat, N. Rodriguez, B. Fabry, and A. Asnacios, *Proceedings of the National Academy of Sciences* **106**, 18243 (2009).
- [162] A. S. Wineman and K. R. Rajagopal, *Mechanical response of polymers: an introduction* (Cambridge University Press, 2000).
- [163] R. Peter, V. Schaller, F. Ziebert, and W. Zimmermann, *New Journal of Physics* **10**, 035002 (2008).
- [164] P. Dalhaimer, D. E. Discher, and T. C. Lubensky, *Nature Physics* **3**, 354 (2007).
- [165] E. Yeh, C. Yang, E. Chin, P. Maddox, E. Salmon, D. J. Lew, and K. Bloom, *Molecular biology of the cell* **11**, 3949 (2000).
- [166] N. Okamura and S. Ishiwata, *Journal of muscle research and cell motility* **9**, 111 (1988).
- [167] T. Tanaka, *Physical Review Letters* **40**, 820 (1978).
- [168] L. Golubović and T. Lubensky, *Physical review letters* **63**, 1082 (1989).
- [169] C. Storm, J. J. Pastore, F. C. MacKintosh, T. C. Lubensky, and P. A. Janmey, *Nature* **435**, 191 (2005).
- [170] S. Strogatz, *Nonlinear dynamics and chaos: with applications to physics, biology, chemistry and engineering* (Perseus Books Group, 2001).
- [171] A. Magid, D. J. Law, et al., *Science* (New York, NY) **230**, 1280 (1985).

- [172] O. Chaudhuri, S. H. Parekh, and D. A. Fletcher, *Nature* **445**, 295 (2007).
- [173] T. Thoresen, M. Lenz, and M. L. Gardel, *Biophysical Journal* **100**, 2698 (2011).
- [174] Y. Shimamoto, M. Suzuki, and S. Ishiwata, *Biochemical and biophysical research communications* **366**, 233 (2008).
- [175] C. A. Reinhart-King, *Methods in enzymology* **443**, 45 (2008).
- [176] C. M. Lo, H. B. Wang, M. Dembo, and Y. Wang, *Biophysical Journal* **79**, 144 (2000).
- [177] W. Guo, M. T. Frey, N. A. Burnham, and Y. Wang, *Biophys. J.* **90**, 2213 (2006).
- [178] E. L. Barnhart, K. C. Lee, K. Keren, A. Mogilner, and J. A. Theriot, *PLoS Biology* **9**, e1001059 (2011).
- [179] N. Yoshinaga, J.-F. Joanny, J. Prost, and P. Marcq, *Phys. Rev. Lett.* **105**, 238103 (2010).
- [180] P. G. Torres, I. Bischofs, and U. Schwarz, *Physical Review E* **85**, 011913 (2012).
- [181] C. Lemmon and L. Romer, *Biophysical journal* **99**, L78 (2010).
- [182] A. Ahmadi, M. C. Marchetti, and T. Liverpool, *Physical Review E* **74**, 061913 (2006).
- [183] J. Y. Wong, A. Velasco, P. Rajagopalan, and Q. Pham, *Langmuir* **19**, 19081913 (2003).
- [184] C. S. Chen, M. Mrksich, S. Huang, G. M. Whitesides, and D. E. Ingber, *Science* **276**, 1425 (1997).
- [185] T. Wakatsuki, R. Wysolmerski, and E. Elson, *J Cell Sci* **116**, 1617 (2003).

- [186] N. Wang, I. Tolić-Nørrelykke, J. Chen, S. Mijailovich, J. Butler, J. Fredberg, and D. Stamenović, *American Journal of Physiology-Cell Physiology* **282**, C606 (2002).
- [187] S. Heidemann and D. Wirtz, *Trends in cell biology* **14**, 160 (2004).
- [188] C. Galbraith and M. Sheetz, *Curr Opin Cell Biol* **10**, 566 (1998).
- [189] D. Riveline, E. Zamir, N. Balaban, U. Schwarz, T. Ishizaki, S. Narumiya, Z. Kam, B. Geiger, and A. Bershadsky, *Science's STKE* **153**, 1175 (2001).
- [190] Y. Asano, A. Jiménez-Dalmaroni, T. Liverpool, M. Marchetti, L. Giomi, A. Kiger, T. Duke, and B. Baum, *HFSP journal* **3**, 194 (2009).
- [191] T. Lecuit and P. Lenne, *Nat Rev Mol Cell Bio* **8**, 633 (2007).
- [192] C. Mader, E. Hinchcliffe, and Y. Wang, *Soft Matter* **3**, 357 (2007).
- [193] R. Buchsbaum, *J Cell Sci* **120**, 1149 (2007).
- [194] I. Bischofs, F. Klein, D. Lehnert, M. Bastmeyer, and U. Schwarz, *Biophys J* **95**, 3488 (2008).
- [195] D. Mumford, in *Algebraic geometry and its applications*, edited by C. Bajaj (Springer-Verlag, New York, 1993), pp. 507–518.
- [196] L. Giomi and L. Mahadevan, *Proc R Soc A* **468**, 1851 (2012).
- [197] V. Vassilev, P. Djondjorov, and I. Mladenov, *J Phys A-Math Gen* **41**, 435201 (2008).
- [198] A. Gray, *Modern differential geometry of curves and surfaces with mathematica* (CRC-Press, Boca Raton, FL, 1997).
- [199] J. Flaherty, J. Keller, and S. Rubinow, *SIAM Journal on Applied Mathematics* **23**, 446 (1972).

- [200] P. Djondjorov, V. Vassilev, and I. Mladenov, *Int J Mech Sci* **53**, 355 (2011).
- [201] A. E. H. Love, *A Treatise on the Mathematical Theory of Elasticity* (Cambridge University Press, Cambridge, 1927), 4th ed.
- [202] M. A. Biot, *Mechanics of incremental deformations* (John Wiley and Sons, New York, 1965).
- [203] E. Hohlfeld and L. Mahadevan, *Phys. Rev. Lett.* **106**, 105702 (2011).
- [204] E. Hohlfeld and L. Mahadevan, *Phys. Rev. Lett.* **109**, 025701 (2012).
- [205] T. Tallinen, J. S. Biggins, and L. Mahadevan, *Phys. Rev. Lett.* **110**, 024302 (2013), URL <http://link.aps.org/doi/10.1103/PhysRevLett.110.024302>.
- [206] A. Saez, E. A. and M. Ghibaudo, O. du Roure, J.-M. D. Meglio, P. Hersen, P. Silberzan, A. Buguin, and B. Ladoux, *J. Phys.: Condens. Matter* **22**, 194119 (9pp) (2010).
- [207] Y. Lin, D. Tambe, C. Park, M. Wasserman, X. Trepate, R. Krishnan, G. Lenormand, J. Fredberg, and J. Butler, *Physical Review E* **82**, 041918 (2010).
- [208] S. Sen, A. Engler, and D. Discher, *Cellular and molecular bioengineering* **2**, 39 (2009).
- [209] R. Merkel, N. Kirchgeßner, C. Cesa, and B. Hoffmann, *Biophysical journal* **93**, 3314 (2007).
- [210] J. M. Maloney, E. B. Walton, C. M. Bruce, and K. J. van Vliet, *Phys. Rev. E* **78**, 041923 (2008).
- [211] I. Bischofs, S. Safran, and U. Schwarz, *Physical Review E* **69**, 021911 (2004).
- [212] R. De, A. Zemel, and S. Safran, *Nature Physics* **3**, 655 (2007).
- [213] I. B. Bischofs and U. S. Schwarz, *Phys. Rev. Lett.* **95**, 068102 (2005).

- [214] B. M. Friedrich and S. A. Safran, *Soft Matter* **8**, 3223 (2012).
- [215] M. Wozniak, K. Modzelewska, L. Kwong, and P. Keely, *Biochimica et Biophysica Acta (BBA)-Molecular Cell Research* **1692**, 103 (2004).
- [216] L. D. Landau, L. P. Pitaevskii, E. M. Lifshitz, and A. M. Kosevich, *Theory of Elasticity* (Butterworth-Heinemann, 1986), 3rd ed., ISBN 075062633X.
- [217] A. Saez, A. Buguin, P. Silberzan, and B. Ladoux, *Biophysical journal* **89**, L52 (2005).
- [218] A. Saez, M. Ghibaudo, A. Buguin, P. Silberzan, and B. Ladoux, *Proceedings of the National Academy of Sciences* **104**, 8281 (2007).
- [219] J. Barber, *Elasticity*, vol. 172 (Springer Verlag, 2010).
- [220] J. A. Zallen, *Cell* **129**, 1051 (2007).
- [221] R. Farhadifar, J.-C. Röper, B. Aigouy, S. Eaton, and F. Jülicher, *Current Biology* **17**, 2095 (2007).
- [222] N. Gorfinkiel, G. B. Blanchard, R. J. Adams, and A. Martinez Arias, *Development* **136**, 1889 (2009).
- [223] T. Mammoto and D. E. Ingber, *Development* **137**, 1407 (2010).
- [224] N. W. Goehring, P. K. Trong, J. S. Bois, D. Chowdhury, E. M. Nicola, A. A. Hyman, and S. W. Grill, *Science* **334**, 1137 (2011).
- [225] P. F. Davies, *Physiological Reviews* **75**, 519 (1995).
- [226] H. Iwamoto, *Biophysical Journal* **78**, 3138 (2000).
- [227] R. A. Foty, G. Forgacs, C. M. Pflieger, and M. S. Steinberg, *Physical review letters* **72**, 2298 (1994).

- [228] C. Gokgol, C. Basdogan, and D. Canadinc, *Medical Engineering and Physics* **34**, 882 (2012).
- [229] J. D. Humphrey, *Cell Biochemistry and Biophysics* **50**, 53 (2008).
- [230] J. Crocker and D. Grier, *Journal of Colloid and Interface Science* **179**, 298 (1996).
- [231] J. del Alamo, R. Meili, B. Alonso-Latorre, J. Rodriguez-Rodriguez, A. Aliseda, R. Firtel, and J. Lasheras, *Proceedings of the National Academy of Sciences* **104**, 13343 (2007).
- [232] Y. Barrandon and H. Green, *Proceedings of the National Academy of Sciences* **84**, 2302 (1987).
- [233] E. O’Keefe, R. Briggaman, and B. Herman, *Journal of Cell Biology* **105**, 807 (1987).
- [234] H.-B. Wang, M. Dembo, S. Hanks, and Y.-l. Wang, *Proceedings of the National Academy of Sciences* **98**, 11295 (2001).
- [235] N. Wang, E. Ostuni, G. Whitesides, and D. Ingber, *Cell Motility and the Cytoskeleton* **52**, 97 (2002).
- [236] H. Delanoë-Ayari and J. Rieu, *Physical Review Letters* **105**, 248103 (2010).
- [237] M. Fournier, R. Sauser, D. Ambrosi, J. Meister, and A. Verkhovsky, *Journal of Cell Biology* **188**, 287 (2010).
- [238] R. Krishnan, D. Klumpers, C. Park, K. Rajendran, X. Trepas, J. van Bezu, V. van Hinsbergh, C. Carman, J. Brain, J. Fredberg, et al., *American Journal of Physiology – Cell Physiology* **300**, C146 (2011).

- [239] C. M. Nelson, R. P. Jean, J. L. Tan, W. F. Liu, N. J. Sniadecki, A. A. Spector, and C. S. Chen, *Proceedings of the National Academy of Sciences* **102**, 11594 (2005).
- [240] I. Tolić-Nørrelykke and N. Wang, *Journal of Biomechanics* **38**, 1405 (2005).
- [241] J. Califano and C. Reinhart-King, *Cellular and Molecular Bioengineering* **3**, 68 (2010).
- [242] J. Fu, Y. Wang, M. Yang, R. Desai, X. Yu, Z. Liu, and C. Chen, *Nature Methods* **7**, 733 (2010).
- [243] P.-G. de Gennes, F. Brochard-Wyart, and D. Quèrè, *Capillarity and Wetting Phenomena: Drops, Bubbles, Pearls, Waves* (Springer-Verlag, New York, 2004).
- [244] S. Douezan, K. Guevorkian, R. Naouar, S. Dufour, D. Cuvelier, and F. Brochard-Wyart, *Proceedings of the National Academy of Sciences* **108**, 7315 (2011).
- [245] E. Jerison, Y. Xu, L. Wilen, and E. Dufresne, *Physical Review Letters* **106**, 186103 (2011).
- [246] M. Steinberg, *Current Opinion in Genetics & Development* **17**, 281 (2007).
- [247] R. Foty, C. Pflieger, G. Forgacs, and M. Steinberg, *Development* **122**, 1611 (1996).
- [248] K. Guevorkian, M. Colbert, M. Durth, S. Dufour, and F. Brochard-Wyart, *Physical Review Letters* **104**, 218101 (2010).
- [249] J. Käfer, T. Hayashi, A. F. M. Marée, R. W. Carthew, and F. Graner, *Proceedings of the National Academy of Sciences* **104**, 18549 (2007).
- [250] M. Manning, R. Foty, M. Steinberg, and E. Schoetz, *Proceedings of the National Academy of Sciences* **107**, 12517 (2010).

- [251] D. J. A. Thornton, C. A. Harrison, M. J. Heaton, A. J. Bullock, and S. MacNeil, *Journal of Burn Care and Research* **29**, 369 (2008).
- [252] C. Michels, T. Buchta, W. Bloch, T. Krieg, and C. M. Niessen, *Journal of Investigative Dermatology* **129**, 2072 (2009).
- [253] C. M. Nelson, D. M. Pirone, J. L. Tan, and C. S. Chen, *Molecular Biology of the Cell* **15**, 2943 (2004).
- [254] U. S. B. Potard, J. P. Butler, and N. Wang, *American Journal of Physiology – Cell Physiology* **272**, C1654 (1997).
- [255] L. Bard, C. Boscher, M. Lambert, R. . Mège, D. Choquet, and O. Thoumine, *Journal of Neuroscience* **28**, 5879 (2008).
- [256] S. Yonemura, Y. Wada, T. Watanabe, A. Nagafuchi, and M. Shibata, *Nature Cell Biology* **12**, 533 (2010).
- [257] G. F. Weber, M. A. Bjerke, and D. W. DeSimone, *Developmental Cell* **22**, 104 (2012).
- [258] S. Raghavan, C. Bauer, G. Mundschau, Q. Li, and E. Fuchs, *Journal of Cell Biology* **150**, 1149 (2000).
- [259] F. Grinnell, *Trends in Cell Biology* **10**, 362 (2000).
- [260] J. Nowak and E. Fuchs, *Methods in Molecular Biology* **482**, 215 (2009).
- [261] M. Pasparakis, G. Courtois, M. Hafner, M. Schmidt-Supprian, A. Nenci, A. Toksoy, M. Krampert, M. Goebeler, R. Gillitzer, A. Israel, et al., *Nature* **417**, 861 (2002).
- [262] J. A. Tunggal, I. Helfrich, A. Schmitz, H. Schwarz, D. Günzel, M. Fromm, R. Kemler, T. Krieg, and C. M. Niessen, *The EMBO journal* **24**, 1146 (2005).

VITA

AUTHOR: Shiladitya Banerjee

NATIONALITY: Indian

DATE OF BIRTH: September 17, 1986

DEGREES AWARDED:

- BSc. (Hons.), Physics, Chennai Mathematical Institute, India (2008)

PROFESSIONAL EMPLOYMENT:

Graduate Teaching/Research Assistant, Department of Physics, Syracuse University (2008-2013).

PUBLICATIONS:

- *Polymorphism and bistability in adherent cells*, S. Banerjee and L. Giomi, *Soft Matter*, doi: 10.1039/c3sm27791g (2013).
- *Controlling cell-matrix traction forces by extracellular geometry*, S. Banerjee and M.C. Marchetti, *New Journal of Physics* **15**, 035015 (2013).
- *Cadherin-based intercellular adhesions organize epithelial cell-matrix traction forces*, A.F. Mertz, Y. Che, S. Banerjee, J. Goldstein, S. Revilla, C. Niessen, M.C. Marchetti, E.R. Dufresne and V. Horsley, *Proc. Natl. Acad. Sci. USA* **110**, 842 (2013).
- *Contractile stresses in cohesive cell layers on finite-thickness substrates*, S. Banerjee and M.C. Marchetti, *Physical Review Letters* **109**, 108101 (2012).
- *Heterogeneous drying stresses in Stratum Corneum*, G.K. German, W.C. Engl, E. Pashkovski, S. Banerjee, Y. Xu, A.F. Mertz, C. Hyland and E.R. Dufresne, *Biophysical Journal* **102**, 2424 (2012).

- *Scaling of traction forces with the size of cohesive cell colonies*, A.F. Mertz, S. Banerjee, Y. Che, G. German, Y. Xu, C. Hyland, M.C. Marchetti, V. Horsley and E.R. Dufresne, *Physical Review Letters* **108**, 198101 (2012).
- *Generic phases of cross-linked active gels: Relaxation, oscillation and contractility*, S. Banerjee, T.B. Liverpool and M.C. Marchetti, *Europhysics Letters* **96**, 58004 (2011).
- *Substrate rigidity deforms and polarizes active gels*, S. Banerjee and M.C. Marchetti, *Europhysics Letters* **96**, 28003 (2011).
- *Motor-driven dynamics of cytoskeletal filaments in motility assays*, S. Banerjee, M.C. Marchetti and K.K. Müller-Nedebock, *Physical Review E* **84**, 011914 (2011).
- *Instabilities and oscillations in isotropic active gels*, S. Banerjee and M.C. Marchetti, *Soft Matter* **7**, 463 (2011).

AWARDS:

- All-University Doctoral Prize, Syracuse University (2013).
- Finalist, GSNP student speaker award, APS March Meeting (2012).
- I2CAM Junior Travel Award (2010).
- Graduate Assistantship, Department of Physics, Syracuse University (2008-2013).
- Gold Medal for Excellence in Physics, Chennai Mathematical Institute (2008).

TEACHING:

- PHY 360 : Vibrations, Waves and Optics (Fall 2012).
- PHY 305 : Solar Energy Science and Architecture (Fall 2012).

- PHY 312 : Relativity, Cosmology and Beyond (Spring 2011, Spring 2012).
- PHY 221 : General Physics I - Mechanics (Spring 2009).
- PHY 222 : General Physics II - Electricity, Magnetism and Light (Fall 2012).

INVITED PRESENTATIONS:

- *Dynamics of Suspensions, Gels, Cells and Tissues*, Isaac Newton Institute for Mathematical Sciences, Cambridge, UK (2013).
- American Physical Society March Meeting, Baltimore, USA (2013).
- Squishy Physics Seminar, Harvard University, Boston, USA (2013).
- Biophysics Seminar, Lewis-Sigler Institute for Integrative Genomics, Princeton University, USA (2012).
- Seminar, TIFR Center for Interdisciplinary Sciences, Hyderabad, India (2012).
- Condensed Matter and Biological Physics Seminar, Syracuse University, USA (2011).
- Theoretical Physics Seminar, Stellenbosch University, South Africa (2010).

CONTRIBUTED PRESENTATIONS:

- Talk, American Physical Society March Meeting, Baltimore, USA (2013).
- Soundbite, 13th New York Complex Matter Workshop, Syracuse University, Syracuse, USA (2013).
- Talk, American Physical Society March Meeting, Boston, USA (2012).
- Soundbite, 12th New York Complex Matter Workshop, Cornell University, Ithaca, USA (2011).

- Poster, Gordon Research Seminar and Gordon Research Conference, New London, NH, USA (2011).
- Soundbite, 11th New York Complex Matter Workshop, Syracuse University, USA (2011).
- Talk, American Physical Society March Meeting, Dallas, TX, USA (2011).
- Talk, Workshop on *Active Materials*, Stellenbosch, South Africa (2010).
- Soundbite, 10th New York Complex Matter Workshop, Cornell University, Ithaca, USA (2010).
- Soundbite, 9th New York Complex Matter Workshop, Rochester Institute of Technology, Rochester, USA (2009).
- Poster, Boulder School for condensed matter physics, Topic : *Nonequilibrium Statistical Mechanics*, Boulder, CO, USA (2009).
- Soundbite, 8th New York Complex Matter Workshop, Syracuse University, Syracuse, USA (2009).